Investigation of the Bauschinger Effect in forged Ti-6Al-4V under Cyclic Loading: Effects of Loading Direction, Temperature, and Strain-rate



Mr. Simranjeet Singh

Wadham College

University of Oxford

A thesis submitted for the degree of

Doctor of Philosophy

Hilary term 2026

Declaration

I declare that this thesis is entirely my own work and, except where stated, describes my own research.

Artificial intelligence tool, such as Grammarly, was utilised solely for grammar and sentence clarity.

Acknowledgments

First, I would like to express my sincere gratitude to my DPhil. advisors, Prof. Daniel Eakins and Dr. David Chapman, for their continuous support throughout my DPhil studies and research. Their guidance has been invaluable during my entire research journey. Over the past four years, their advice and encouragement have not only aided me in my research but have also nurtured me as an individual, teaching me how to think critically as a scientist, how to write scientific documents, and inspiring me to overcome the challenges I faced in my research.

I would also like to thank Dr. Phani Karamched for training me to operate the electron microscopes and for helping me understand some fundamental concepts of materials science relevant to my DPhil.

I am grateful to the members of the I12 (JEEP) Beamline at Diamond Light Source, UK, for accommodating my requests for beamtime on short notice, which allowed me to conduct residual stress measurement experiments. Special thanks to Prof. Felix Hofmann for his invaluable guidance on these measurements.

Additionally, I would like to extend my thanks to each member of the Impact and Shock Mechanics Laboratory, University of Oxford, for their kindness and support. Their assistance with academic, training, and logistical aspects made my time at the laboratory truly memorable.

Finally, I would like to express my gratitude to my friends and family for their unwavering support during my research journey. Their encouragement helped me through moments of frustration with my progress. Without their motivation, completing my degree would have been much more difficult. Thank you for standing by me.

Abstract

Titanium is widely used in the aerospace industry for manufacturing critical components of aircraft engines, including compressor blades, compressor discs, spacers, and fan blades. During operation, fan blades can be subjected to impacts from foreign objects or particulates, such as birds or volcanic ash. Following such impacts, the blades experience repeated cyclic loading that induces plastic strain with each cycle. This phenomenon is characteristic of low-cycle fatigue (LCF), where the blade deforms rapidly over a limited number of cycles due to cyclic plasticity. The impact site also generates a localised stress concentration, leading to the potential initiation of cracks within a few cycles. These cracks can then propagate with continued cycling, ultimately resulting in blade fracture. The detachment of a blade fragment can compromise engine integrity through secondary impacts, imbalances, and damage to surrounding components and containment structures. Therefore, it is crucial to comprehend the behaviour of titanium under these conditions to ensure the overall integrity of the system. However, predicting this response is complex, as titanium subjected to cyclic reverse loading can exhibit the Bauschinger effect. This effect indicates that prior plastic deformation reduces the yield strength upon load reversal and alters the subsequent cyclic stressstrain response.

This study aims to enhance understanding of the mechanisms responsible for the Bauschinger response of forged Ti-6Al-4V under reverse loading. The novelty of this work lies in investigating the influence of load direction, elevated temperature, and strain-rate on the Bauschinger effect. This includes measuring the

in-situ temperature rise of the specimen due to mechanical loading at increasing strain-rates. The investigation begins by characterising the Bauschinger response during cyclic reverse loading through the measurement of the 0.2% yield stress after each load step, along with the associated kinematic backstress derived from the hysteresis loops. The results indicate a clear Bauschinger effect in the tension-compression sequence, while it diminishes in the compression-tension sequence after the first cycle. Notably, the magnitude of the Bauschinger effect diminishes with increasing temperature, as elevated temperatures promote the recovery process and the relaxation of internal stress fields. Similarly, the magnitude of the Bauschinger effect decreases with increasing strain-rate due to the temperature rise in the specimen at higher strain-rates, which accelerates thermally activated recovery and facilitates backstress relaxation. Furthermore, kinematic backstress is minimal during compression-tension loading, but relatively significant during tension-compression loading.

Interrupted experiments were conducted to measure the evolution of microstructure and the accumulation of residual stress within the specimen as the number of load cycles increased. Additionally, residual stress accumulation was quantified using bulk X-ray diffraction to assess the internal stress state generated by cyclic plastic deformation. This stress state is expected to influence load reversal behaviour and the magnitude of the Bauschinger effect.

Electron Backscatter Diffraction (EBSD) analysis on interrupted test specimens reveals twinning-detwinning activity during the tension-compression load

sequence. However, this activity is not present in the compression-tension load sequence. The behaviour of the Schmid factor with an increasing number of load cycles for the prismatic slip system follows a trend similar to the Bauschinger effect. Fluctuations are observed in the tension-compression load sequence, but no fluctuations occur during the compression-tension load sequence as the number of load cycles increases. Additionally, residual stress accumulation was measured through X-ray diffraction to quantify the internal stress state generated by cyclic plastic deformation, which is anticipated to influence load reversal behaviour and the magnitude of the Bauschinger effect. The trend of residual stress accumulation in the material through the reflection via the prismatic plane also aligns with the behaviour observed in the Bauschinger effect. When considering these microscopic results alongside the macroscopic behaviour of the Bauschinger effect, it suggests that the interplay between twin and prismatic slip mechanisms contributes to the underlying causes of the Bauschinger effect. Consequently, the Bauschinger effect persists during the tension-compression load sequence, while it diminishes during the compression-tension load sequence, after the first load cycle, as the number of load cycles increases. The results of this study indicate that twin-prismatic slip interference contributes to the Bauschinger effect, leading to the accumulation of backstress.

Table of Contents

1 Introduction **1**

1.1 Background and Motivation 1

2 Literature Review **5**

2.1 Fundamental Stress, Strain, and Plasticity Theory 5

2.1.1 Engineering and true stress-strain measures 5

2.1.2 Tensor representation of stress and strain 7

2.1.3 Hydrostatic and deviatoric stress decomposition 9

2.1.4 Yield loci and hardening in deviatoric stress space 11

2.1.4.1 Yield surface, yield locus, and the deviatoric plane 11

2.1.4.2 Tresca yield criterion 12

2.1.4.3 von Mises yield criterion 13

2.1.4.4 Other yield criteria 14

2.1.4.5 Evolution of the yield locus under isotropic hardening 14

2.1.4.6 Evolution of the yield locus under kinematic hardening 15

2.1.4.7 Combined isotropic and kinematic hardening . . . 15

2.1.5 Formal definition of backstress 16

2.1.6 Constitutive modelling approaches for cyclic hardening behaviour 18

2.2 The Bauschinger effect 22

2.2.1 Explanation of the Bauschinger effect using yield surface evolution 24

2.2.2 Factors affecting the Bauschinger effect 26

2.2.3 Assessment and ranking of mechanisms for the Bausc-hinger effect 28

2.2.4 Experimental methods for uniaxial cyclic and reverse-loading tests 32

2.3 Mechanical behaviour in Titanium alloys 34
2.3.1 Deformation mechanisms in Ti-6Al-4V and Effects of Temperature and Strain-rate dependence 34
2.3.2 Bauschinger effect in Titanium alloys 38
2.4 Summary 42

3 Introduction to the As-received Material 44
3.1 Microstructure of the as-received material 45
3.1.1 Specimen preparation for EBSD 45
3.1.2 Phase-map of forged Ti-6Al-4V 48
3.1.3 Texture of α and β phases present in forged Ti-6Al-4V . . . 48
3.1.4 Error and uncertainty assessment for EBSD measurements . 50

4 Investigating the affect of Load Direction on the Bauschinger Response 56
4.1 Overview 56
4.2 Experimental methodology 57
4.3 Digital Image Correlation (DIC) for strain measurement 61
4.4 Error and uncertainty assessment for reverse loading tests 64
4.5 Experimental results 67
4.6 Microstructural analysis via Electron Backscatter Diffraction (EBSD) of sectioned interrupted specimens with increasing load cycles . . . 80
4.6.1 Twin evolution in forged Ti-6Al-4V 80
4.6.2 Schmid factor evolution of crystallographic slip systems in α and β phases in forged Ti-6Al-4V 83
4.7 Residual Stress accumulation in forged Ti-6Al-4V 94
4.7.1 Methodology to measure residual stress 94
4.7.2 Error and uncertainty assessment for synchrotron X-ray diffraction measurements 103
4.7.3 Residual stress evolution of crystallographic planes in α and β phases present in forged Ti-6Al-4V 107

4.8 Summary 115

5 Role of Increasing Temperature on the Bauschinger Response 117

5.1 Overview 117

5.2 Experimental conditions 118

5.3 Experimental results 118

5.4 Microstructural analysis via Electron Backscatter Diffraction (EBSD) of sectioned interrupted specimens at 100 °C and 200 °C with increasing load cycles 126

5.4.1 Twin evolution in forged Ti-6Al-4V 126

5.4.2 Schmid factor evolution of crystallographic slip systems in α and β phases in forged Ti-6Al-4V 128

5.5 Residual Stress accumulation in forged Ti-6Al-4V at 100 °C and 200 °C 145

5.5.1 Residual stress evolution of crystallographic planes in α and β phases present in forged Ti-6Al-4V 145

5.6 Summary 159

6 Behaviour of the Bauschinger effect as a Function of Strain-rate 161

6.1 Overview 161

6.2 Experimental methodology 162

6.3 Experimental results 164

6.4 Microstructural analysis via Electron Backscatter Diffraction (EBSD) of sectioned interrupted specimens at 1 s^{-1} and 10 s^{-1} with increasing load cycles 173

6.4.1 Twin evolution in forged Ti-6Al-4V 173

6.4.2 Schmid factor evolution of crystallographic slip systems in α and β phases in forged Ti-6Al-4V 176

6.5 Residual Stress accumulation in forged Ti-6Al-4V at 1 s^{-1} and 10 s^{-1} 193

6.5.1 Residual stress evolution of crystallographic planes in α and β phases present in forged Ti-6Al-4V 193

6.6 Summary 206

7 Discussion **208**

7.1 Macroscopic characterisation of the Bauschinger effect 208

7.2 Role of kinematic backstress 210

7.3 Role of twinning and detwinning 212

7.4 Assessment of slip favourability 214

7.5 Interference of twins with prismatic slip mechanism 215

7.6 Residual stress accumulation - Consequence of the twin-prismatic slip interference 218

7.7 Two-tailed correlation analysis of kinematic hardening behaviour and twin boundary length evolution 219

7.8 Summary of maximum MRD values obtained from pole figures for the α and β phases 221

8 Conclusion **223**

9 Future Work **227**

A Appendix **229**

B Appendix **240**

Bibliography **247**

List of Figures

1.1 Demonstration of a Rolls-Royce turbofan engine 2

2.1 Schematic stress-strain response illustrating the Bauschinger effect . 23
2.2 Schematic diagram of deformation twinning. 35
2.3 Main active slip planes in HCP titanium 36

3.1 Geometry of the dog-bone specimen used to conduct reverse loading. 44
3.2 Sectioned specimen for EBSD analysis. 46
3.3 IPF orientation maps of as-received forged Ti-6Al-4V. 46
3.4 EBSD phase map of as-received forged Ti-6Al-4V. 48
3.5 Pole figures of crystallographic planes in the as-received material. . 49

4.1 Specimen alignment during reverse compression 58
4.2 Set-up to conduct reverse loading under quasi-static conditions. . . 60
4.3 Speckled test specimen on the rig, with the gauge region highlighted. 62
4.4 Spatially resolved DIC strain maps of the specimen gauge region. . 62
4.5 Stress-Strain response of the material under quasi-static conditions. 69
4.6 Total and plastic strain energy in both loading sequences. 70
4.7 Repeat stress-strain responses at the 0.5-cycle loading step. 72
4.8 Behaviour of 0.2% effective yield stress in both sequences 73
4.9 Isotropic and Kinematic hardening behaviour of the material 77
4.10 Twin boundary length evolution for $\{10\bar{1}2\}$ and $\{10\bar{1}3\}$ twins 82
4.11 Basal slip system $\{0002\}\langle 11\bar{2}0\rangle$ (α) (T-C load sequence). The uncertainty associated with the median Schmid factor arises from bin-resolution, or quantisation uncertainty, which occurs when a continuous variable is discretised into finite bins of uniform width, denoted as Δ. When using uniform discretisation, the rounding or quantisation error is limited to half of the bin size. Therefore, the median is reported as $\tilde{m} \pm \frac{\Delta}{2}$ [138]. 87

4.12 Prismatic slip system $\{10\bar{1}0\}\langle\bar{1}2\bar{1}0\rangle$ (α) (T-C load sequence). 88
4.13 Pyramidal slip system $\{10\bar{1}1\}\langle\bar{1}2\bar{1}0\rangle$ (α) (T-C load sequence) 88
4.14 Pyramidal slip system $\{20\bar{2}1\}\langle\bar{1}2\bar{1}0\rangle$ (α) (T-C load sequence) 88
4.15 Second-order pyramidal slip system $\{11\bar{2}2\}\langle\bar{1}\bar{1}23\rangle$ (α) (T-C load sequence) 89
4.16 Pyramidal slip system $\{20\bar{2}2\}\langle\bar{1}\bar{1}23\rangle$ (α) (T-C load sequence) 89
4.17 $\{110\}\langle\bar{1}11\rangle$ slip system (β) (T-C load sequence) 89
4.18 $\{200\}\langle011\rangle$ slip system (β) (T-C load sequence) 90
4.19 $\{211\}\langle\bar{1}11\rangle$ slip system (β) (T-C load sequence) 90
4.20 Basal slip system $\{0002\}\langle11\bar{2}0\rangle$ (α) (C-T load sequence) 90
4.21 Prismatic slip system $\{10\bar{1}0\}\langle\bar{1}2\bar{1}0\rangle$ (α) (C-T load sequence). 91
4.22 Pyramidal slip system $\{10\bar{1}1\}\langle\bar{1}2\bar{1}0\rangle$ (α) (C-T load sequence) 91
4.23 Pyramidal slip system $\{20\bar{2}1\}\langle\bar{1}2\bar{1}0\rangle$ (α) (C-T load sequence) 91
4.24 Second-order pyramidal slip system $\{11\bar{2}2\}\langle\bar{1}\bar{1}23\rangle$ (α) (C-T load sequence) 92
4.25 Pyramidal slip system $\{20\bar{2}2\}\langle\bar{1}\bar{1}23\rangle$ (α) (C-T load sequence) 92
4.26 $\{110\}\langle\bar{1}11\rangle$ slip system (β) (C-T load sequence) 92
4.27 $\{200\}\langle011\rangle$ slip system (β) (C-T load sequence) 93
4.28 $\{211\}\langle\bar{1}11\rangle$ slip system (β) (C-T load sequence) 93
4.29 Set-up to conduct synchrotron X-ray diffraction experiment. 96
4.30 X-ray diffraction pattern of forged Ti-6Al-4V. 97
4.31 Residual stress in crystallographic planes of α phase during T-C load sequence. 111
4.32 Residual stress in crystallographic planes of β phase during T-C load sequence. 112
4.33 Residual stress in crystallographic planes of α phase during C-T load sequence. 113
4.34 Residual stress in crystallographic planes of β phase during C-T load sequence. 114

5.1 Set-up to conduct reverse loading under quasi-static conditions at elevated temperatures 119
5.2 Stress-Strain response of the material at quasi-static at 100 °C. . . . 119
5.3 Stress-Strain response of the material at quasi-static at 200 °C. . . . 120
5.4 0.2% effective yield strength behaviour at 100 °C 120
5.5 0.2% effective yield strength behaviour at 200 °C 121
5.6 Isotropic and Kinematic hardening behaviour at 100 °C 123
5.7 Isotropic and Kinematic hardening behaviour at 200 °C 124
5.8 Mean Kinematic hardening comparison at 100 °C and at 200 °C . . 125
5.9 Twin boundary length evolution of $\{10\bar{1}2\}$ and $\{10\bar{1}3\}$ twins at 100 °C127
5.10 Twin boundary length evolution of $\{10\bar{1}2\}$ and $\{10\bar{1}3\}$ twins at 200 °C128
5.11 Basal slip system $\{0002\}\langle 11\bar{2}0\rangle$ (α) (T-C load sequence) at 100 °C . 133
5.12 Prismatic slip system $\{10\bar{1}0\}\langle\bar{1}2\bar{1}0\rangle$ (α) (T-C load sequence) at 100 °C133
5.13 Pyramidal slip system $\{10\bar{1}1\}\langle\bar{1}2\bar{1}0\rangle$ (α) (T-C load sequence) at 100 °C133
5.14 Pyramidal slip system $\{20\bar{2}1\}\langle\bar{1}2\bar{1}0\rangle$ (α) (T-C load sequence) at 100 °C134
5.15 Second-order pyramidal slip system $\{11\bar{2}2\}\langle\bar{1}\bar{1}23\rangle$ (α) (T-C load sequence) at 100 °C 134
5.16 Pyramidal slip system $\{20\bar{2}2\}\langle\bar{1}\bar{1}23\rangle$ (α) (T-C load sequence) at 100 °C134
5.17 $\{110\}\langle\bar{1}11\rangle$ slip system (β) (T-C load sequence) at 100 °C 135
5.18 $\{200\}\langle 011\rangle$ slip system (β) (T-C load sequence) at 100 °C 135
5.19 $\{211\}\langle\bar{1}11\rangle$ slip system (β) (T-C load sequence) at 100 °C 135
5.20 Basal slip system $\{0002\}\langle 11\bar{2}0\rangle$ (α) (C-T load sequence) at 100 °C . 136
5.21 Prismatic slip system $\{10\bar{1}0\}\langle\bar{1}2\bar{1}0\rangle$ (α) (C-T load sequence) at 100 °C136
5.22 Pyramidal slip system $\{10\bar{1}1\}\langle\bar{1}2\bar{1}0\rangle$ (α) (C-T load sequence) at 100 °C136
5.23 Pyramidal slip system $\{20\bar{2}1\}\langle\bar{1}2\bar{1}0\rangle$ (α) (C-T load sequence) at 100 °C137
5.24 Second-order pyramidal slip system $\{11\bar{2}2\}\langle\bar{1}\bar{1}23\rangle$ (α) (C-T load sequence) at 100 °C 137
5.25 Pyramidal slip system $\{20\bar{2}2\}\langle\bar{1}\bar{1}23\rangle$ (α) (C-T load sequence) at 100 °C137
5.26 $\{110\}\langle\bar{1}11\rangle$ slip system (β) (C-T load sequence) at 100 °C 138
5.27 $\{200\}\langle 011\rangle$ slip system (β) (C-T load sequence) at 100 °C 138

5.28 $\{211\}\langle\bar{1}11\rangle$ slip system (β) (C-T load sequence) at 100 °C 138
5.29 Basal slip system $\{0002\}\langle11\bar{2}0\rangle$ (α) (T-C load sequence) at 200 °C . 139
5.30 Prismatic slip system $\{10\bar{1}0\}\langle\bar{1}2\bar{1}0\rangle$ (α) (T-C load sequence) at 200 °C139
5.31 Pyramidal slip system $\{10\bar{1}1\}\langle\bar{1}2\bar{1}0\rangle$ (α) (T-C load sequence) at 200 °C139
5.32 Pyramidal slip system $\{20\bar{2}1\}\langle\bar{1}2\bar{1}0\rangle$ (α) (T-C load sequence) at 200 °C140
5.33 Second-order pyramidal slip system $\{11\bar{2}2\}\langle\bar{1}\bar{1}23\rangle$ (α) (T-C load sequence) at 200 °C 140
5.34 Pyramidal slip system $\{20\bar{2}2\}\langle\bar{1}\bar{1}23\rangle$ (α) (T-C load sequence) at 200 °C140
5.35 $\{110\}\langle\bar{1}11\rangle$ slip system (β) (T-C load sequence) at 200 °C 141
5.36 $\{200\}\langle011\rangle$ slip system (β) (T-C load sequence) at 200 °C 141
5.37 $\{211\}\langle\bar{1}11\rangle$ slip system (β) (T-C load sequence) at 200 °C 141
5.38 Basal slip system $\{0002\}\langle11\bar{2}0\rangle$ (α) (C-T load sequence) at 200 °C . 142
5.39 Prismatic slip system $\{10\bar{1}0\}\langle\bar{1}2\bar{1}0\rangle$ (α) (C-T load sequence) at 200 °C142
5.40 Pyramidal slip system $\{10\bar{1}1\}\langle\bar{1}2\bar{1}0\rangle$ (α) (C-T load sequence) at 200 °C142
5.41 Pyramidal slip system $\{20\bar{2}1\}\langle\bar{1}2\bar{1}0\rangle$ (α) (C-T load sequence) at 200 °C143
5.42 Second-order pyramidal slip system $\{11\bar{2}2\}\langle\bar{1}\bar{1}23\rangle$ (α) (C-T load sequence) at 200 °C 143
5.43 Pyramidal slip system $\{20\bar{2}2\}\langle\bar{1}\bar{1}23\rangle$ (α) (C-T load sequence) at 200 °C143
5.44 $\{110\}\langle\bar{1}11\rangle$ slip system (β) (C-T load sequence) at 200 °C 144
5.45 $\{200\}\langle011\rangle$ slip system (β) (C-T load sequence) at 200 °C 144
5.46 $\{211\}\langle\bar{1}11\rangle$ slip system (β) (C-T load sequence) at 200 °C 144
5.47 Residual stress in crystallographic planes in α phase at 100 °C during the T-C load sequences 151
5.48 Residual stress in crystallographic planes in β phase at 100 °C during the T-C load sequences 152
5.49 Residual stress in crystallographic planes in α phase at 100 °C during the C-T load sequences 153
5.50 Residual stress in crystallographic planes in β phase at 100 °C during the C-T load sequences 154

5.51 Residual stress in crystallographic planes in α phase at 200 °C during the T-C load sequences 155
5.52 Residual stress in crystallographic planes in β phase at 200 °C during the T-C load sequences 156
5.53 Residual stress in crystallographic planes in α phase at 200 °C during the C-T load sequences 157
5.54 Residual stress in crystallographic planes in β phase at 200 °C during the C-T load sequences 158

6.1 Set-up to conduct reverse loading at intermediate strain rates . . . 163
6.2 Engineering stress-strain response of the material at $1\,s^{-1}$ 165
6.3 Engineering stress-strain response of the material at $10\,s^{-1}$ 165
6.4 Real-time temperature rise of the material at $1\,s^{-1}$ 166
6.5 Real-time temperature rise of the material at $10\,s^{-1}$ 166
6.6 Behaviour of the Taylor-Quinny factor at $10\,s^{-1}$ 168
6.7 0.2% effective yield strength behaviour at $1\,s^{-1}$ 169
6.8 0.2% effective yield strength behaviour at $10\,s^{-1}$ 169
6.9 Isotropic and Kinematic hardening behaviour at $1\,s^{-1}$ 170
6.10 Isotropic and Kinematic hardening behaviour at $10\,s^{-1}$ 171
6.11 Mean Kinematic hardening comparison at $1\,s^{-1}$ and $1\,s^{-1}$ 172
6.12 Twin boundary length evolution of $\{10\bar{1}2\}$ and $\{10\bar{1}3\}$ twins at $1\,s^{-1}$ 174
6.13 Twin boundary length evolution of $\{10\bar{1}2\}$ and $\{10\bar{1}3\}$ twins at $10\,s^{-1}$ 175
6.14 Basal slip system $\{0002\}\langle 11\bar{2}0\rangle$ (α) (T-C load sequence) at the strain-rate of 1 s^{-1} 180
6.15 Prismatic slip system $\{10\bar{1}0\}\langle\bar{1}2\bar{1}0\rangle$ (α) (T-C load sequence) at the strain-rate of 1 s^{-1} 180
6.16 Pyramidal slip system $\{10\bar{1}1\}\langle\bar{1}2\bar{1}0\rangle$ (α) (T-C load sequence) at the strain-rate of 1 s^{-1} 181
6.17 Pyramidal slip system $\{20\bar{2}1\}\langle\bar{1}2\bar{1}0\rangle$ (α) (T-C load sequence) at the strain-rate of 1 s^{-1} 181

6.18 Second-order pyramidal slip system $\{11\bar{2}2\}\langle\bar{1}\bar{1}23\rangle$ (α) (T-C load sequence) at the strain-rate of 1 s^{-1} 181
6.19 Pyramidal slip system $\{20\bar{2}2\}\langle\bar{1}\bar{1}23\rangle$ (α) (T-C load sequence) at the strain-rate of 1 s^{-1} 182
6.20 $\{110\}\langle\bar{1}11\rangle$ slip system (β) (T-C load sequence) at the strain-rate of 1 s^{-1} 182
6.21 $\{200\}\langle011\rangle$ slip system (β) (T-C load sequence) at the strain-rate of 1 s^{-1} 182
6.22 $\{211\}\langle\bar{1}11\rangle$ slip system (β) (T-C load sequence) at the strain-rate of 1 s^{-1} 183
6.23 Basal slip system $\{0002\}\langle11\bar{2}0\rangle$ (α) (C-T load sequence) at the strain-rate of 1 s^{-1} 183
6.24 Prismatic slip system $\{10\bar{1}0\}\langle\bar{1}2\bar{1}0\rangle$ (α) (C-T load sequence) at the strain-rate of 1 s^{-1} 183
6.25 Pyramidal slip system $\{10\bar{1}1\}\langle\bar{1}2\bar{1}0\rangle$ (α) (C-T load sequence) at the strain-rate of 1 s^{-1} 184
6.26 Pyramidal slip system $\{20\bar{2}1\}\langle\bar{1}2\bar{1}0\rangle$ (α) (C-T load sequence) at the strain-rate of 1 s^{-1} 184
6.27 Second-order pyramidal slip system $\{11\bar{2}2\}\langle\bar{1}\bar{1}23\rangle$ (α) (C-T load sequence) at the strain-rate of 1 s^{-1} 184
6.28 Pyramidal slip system $\{20\bar{2}2\}\langle\bar{1}\bar{1}23\rangle$ (α) (C-T load sequence) at the strain-rate of 1 s^{-1} 185
6.29 $\{110\}\langle\bar{1}11\rangle$ slip system (β) (C-T load sequence) at the strain-rate of 1 s^{-1} 185
6.30 $\{200\}\langle011\rangle$ slip system (β) (C-T load sequence) at the strain-rate of 1 s^{-1} 185
6.31 $\{211\}\langle\bar{1}11\rangle$ slip system (β) (C-T load sequence) at the strain-rate of 1 s^{-1} 186
6.32 Basal slip system $\{0002\}\langle11\bar{2}0\rangle$ (α) (T-C load sequence) at the strain-rate of 10 s^{-1} 186

6.33 Prismatic slip system $\{10\bar{1}0\}\langle\bar{1}2\bar{1}0\rangle$ (α) (T-C load sequence) at the strain-rate of 10 s^{-1} . . . 186
6.34 Pyramidal slip system $\{10\bar{1}1\}\langle\bar{1}2\bar{1}0\rangle$ (α) (T-C load sequence) at the strain-rate of 10 s^{-1} . . . 187
6.35 Pyramidal slip system $\{20\bar{2}1\}\langle\bar{1}2\bar{1}0\rangle$ (α) (T-C load sequence) at the strain-rate of 10 s^{-1} . . . 187
6.36 Second-order pyramidal slip system $\{11\bar{2}2\}\langle\bar{1}\bar{1}23\rangle$ (α) (T-C load sequence) at the strain-rate of 10 s^{-1} . . . 187
6.37 Pyramidal slip system $\{20\bar{2}2\}\langle\bar{1}\bar{1}23\rangle$ (α) (T-C load sequence) at the strain-rate of 10 s^{-1} . . . 188
6.38 $\{110\}\langle\bar{1}11\rangle$ slip system (β) (T-C load sequence) at the strain-rate of 10 s^{-1} . . . 188
6.39 $\{200\}\langle011\rangle$ slip system (β) (T-C load sequence) at the strain-rate of 10 s^{-1} . . . 188
6.40 $\{211\}\langle\bar{1}11\rangle$ slip system (β) (T-C load sequence) at the strain-rate of 10 s^{-1} . . . 189
6.41 Basal slip system $\{0002\}\langle11\bar{2}0\rangle$ (α) (C-T load sequence) at the strain-rate of 10 s^{-1} . . . 189
6.42 Prismatic slip system $\{10\bar{1}0\}\langle\bar{1}2\bar{1}0\rangle$ (α) (C-T load sequence) at the strain-rate of 10 s^{-1} . . . 189
6.43 Pyramidal slip system $\{10\bar{1}1\}\langle\bar{1}2\bar{1}0\rangle$ (α) (C-T load sequence) at the strain-rate of 10 s^{-1} . . . 190
6.44 Pyramidal slip system $\{20\bar{2}1\}\langle\bar{1}2\bar{1}0\rangle$ (α) (C-T load sequence) at the strain-rate of 10 s^{-1} . . . 190
6.45 Second-order pyramidal slip system $\{11\bar{2}2\}\langle\bar{1}\bar{1}23\rangle$ (α) (C-T load sequence) at the strain-rate of 10 s^{-1} . . . 190
6.46 Pyramidal slip system $\{20\bar{2}2\}\langle\bar{1}\bar{1}23\rangle$ (α) (C-T load sequence) at the strain-rate of 10 s^{-1} . . . 191
6.47 $\{110\}\langle\bar{1}11\rangle$ slip system (β) (C-T load sequence) at the strain-rate of 10 s^{-1} . . . 191

6.48 $\{200\}\langle 011\rangle$ slip system (β) (C-T load sequence) at the strain-rate of 10 s^{-1} . . . 191
6.49 $\{211\}\langle \bar{1}11\rangle$ slip system (β) (C-T load sequence) at the strain-rate of 10 s^{-1} . . . 192
6.50 Residual stress in crystallographic planes in α phase at 1 s^{-1} during the T-C load sequence . . . 198
6.51 Residual stress in crystallographic planes in β phase at 1 s^{-1} during the T-C load sequence . . . 199
6.52 Residual stress in crystallographic planes in α phase at 1 s^{-1} during the C-T load sequence . . . 200
6.53 Residual stress in crystallographic planes in β phase at 1 s^{-1} during the C-T load sequence . . . 201
6.54 Residual stress in crystallographic planes in α phase at 10 s^{-1} during the T-C load sequence . . . 202
6.55 Residual stress in crystallographic planes in β phase at 10 s^{-1} during the T-C load sequence . . . 203
6.56 Residual stress in crystallographic planes in α phase at 10 s^{-1} during the C-T load sequence . . . 204
6.57 Residual stress in crystallographic planes in β phase at 10 s^{-1} during the C-T load sequence . . . 205

7.1 Mean kinematic hardening behaviour with temperatures and strain-rates . . . 211
7.2 Mean Twin Boundary Length behaviour with temperatures and strain-rates . . . 213

9.1 Geometry of the specimens used to conduct reverse loading in the C-T load sequence. . . . 228

B.1 Pole figures for crystallographic planes in the α phase at low strain-rate during interrupted T-C loading show a weak-to-moderate, diffuse texture. . . . 240

B.2 Pole figures for crystallographic planes in the β phase at low strain-rate during interrupted T-C loading exhibit a weak diffuse texture. 241
B.3 Pole figures for crystallographic planes in the α phase at low strain-rate during interrupted C-T loading show a weak to moderate diffuse texture. 241
B.4 Pole figures for crystallographic planes in the β phase at low strain-rate during the C-T load sequence reveal a weak diffuse texture. . . 242
B.5 Pole figures for crystallographic planes in the α phase at 100 °C during interrupted T-C loading show a weak-to-moderate, diffuse texture. 242
B.6 Pole figures for crystallographic planes in the β phase at 100 °C during interrupted T-C loading reveal a weak, diffuse texture. . . . 243
B.7 Pole figures for crystallographic planes in the α phase at 100 °C during interrupted C-T loading show a weak-to-moderate, diffuse texture. 243
B.8 Pole figures for crystallographic planes in the β phase at 100 °C during interrupted C-T loading show a weak and diffuse texture. . . 244
B.9 Pole figures for crystallographic planes in the α phase at a strain rate of $1\,s^{-1}$ during interrupted T-C loading show a weak-to-moderate diffuse texture. 244
B.10 Pole figures for crystallographic planes in the β phase at a strain rate of $1\,s^{-1}$ during interrupted T-C loading show a weak and diffuse texture. 245
B.11 Pole figures for crystallographic planes in the α phase, measured at a strain rate of $1\,s^{-1}$ during interrupted C-T loading, show a weak-to-moderate diffuse texture. 245
B.12 $1\,s^{-1}$ during interrupted C-T loading show a weak diffuse texture . . 246

List of Tables

4.1 DaVis DIC parameters for low strain-rate reverse loading. 61

6.1 DaVis DIC parameters for intermediate strain-rate reverse loading. 163

7.1 Maximum MRD values obtained from pole figures for the α and β phases under as-received and tested conditions. 222

1 | Introduction

1.1 Background and Motivation

Titanium and its alloys play a crucial role in aerospace structures and propulsion systems due to their combination of high specific strength, excellent fatigue resistance, and impressive corrosion resistance. These characteristics make titanium particularly appealing for manufacturing components that require a high strength-to-weight ratio, damage tolerance, and long-term durability in aircraft operating environments. As a result, titanium is widely used in modern aircraft for various applications related to both the airframe and propulsion systems. Its uses include structural fittings and fasteners, landing gear components, and a diverse range of engine parts. These parts include compressor blades, compressor discs, spacers, cases, shafts, and fan blades. The key advantage of using titanium in these applications is its ability to provide a balance of low weight, high strength, and excellent fatigue resistance, which is essential for aircraft performance and safety. Among these materials, Ti-6Al-4V has emerged as a popular choice due to its well-established property profiles, including well-characterised strength, fatigue performance, and fracture behaviour. This enables its application in safety-critical parts that are subjected to complex thermo-mechanical loading histories. [1, 2].

Figure 1.1 displays a turbofan module of a Rolls-Royce engine, which contains components such as fan blades that rotate at high velocity during operation, with representative tip speeds of the order of several hundred metres per second [3]. During routine operation, a passenger aircraft undergoes different stages, including

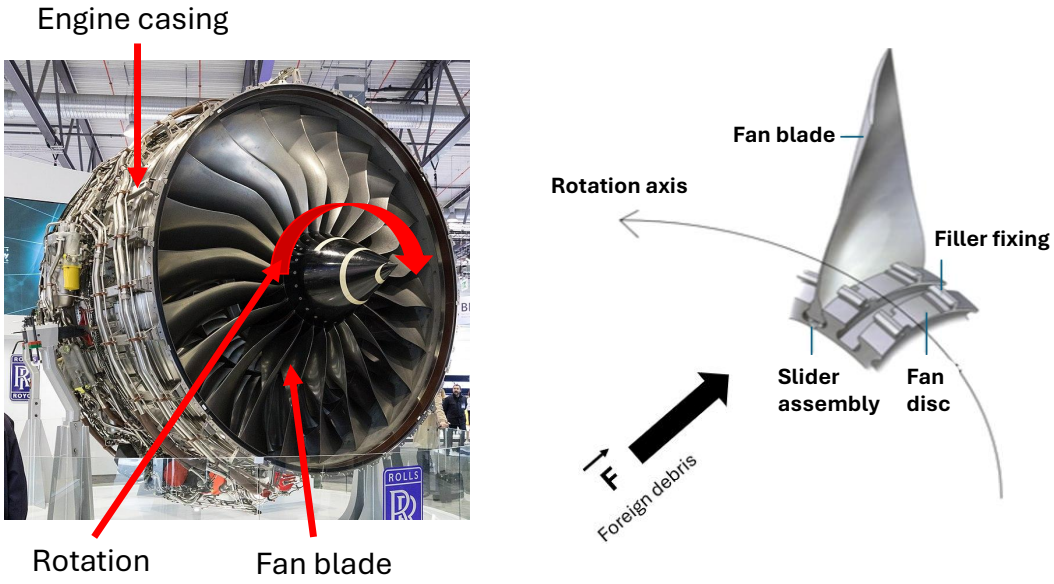


Figure 1.1: Demonstration of a Rolls-Royce turbofan engine (left) highlighting key components, including the fan and fan blades. Schematic showing a foreign-debris (such as a flying bird or ingestion of volcanic ash) trajectory directed toward a fan blade (right).

taxiing, climbing, cruising, and descending. The rotational speed of the fan, and therefore the fan blade tip speed, varies with engine model, thrust setting, flight condition, and aircraft mission phase. Upon descent, the temperature of the fan blades can increase up to 300 °C due to aerodynamic heating [4,5]. Therefore, fan blade materials may experience combined mechanical and thermal loading during service. During climbing or descending, foreign debris striking a fan blade is often reported [6–8]. Such impacts can impose a wide range of strain rates, depending on the relative impact velocity. This impact introduces various stress states and thermal effects within the engine blades. Historically, there have been numerous incidents where aircraft engines have been adversely affected by foreign debris [9,10]. In these cases, a flying bird may unexpectedly strike the fan blades while the engine is in operation, resulting in engine damage and raising concerns

for passenger safety. The impact induces local deformation and plasticity within the blade, subjecting it to high-amplitude fatigue loading that can lead to localised yielding and an increase in blade temperature. If this deformation persists, cracks may nucleate at the damaged region and potentially propagate under continued cyclic loading, ultimately resulting in catastrophic failure. A damaged or fractured blade can also cause secondary damage through rotor imbalance and fragment release, which may strike adjacent blades and damage downstream components. These events can jeopardise engine integrity and diminish aircraft performance, directly impacting operational safety. Therefore, it is critical to understand the mechanical behaviour of fan blades under cyclic reverse loading at elevated temperature and strain-rates to prevent such incidents from occurring in the future. Reverse loading refers to a loading history in which a specimen is first subjected to stress in one direction (such as tension) and then in the opposite direction (such as compression), and vice versa.

To understand the mechanical behaviour of the material, the current research investigates the influence of the loading direction (tension-compression and compression-tension load sequence) on the mechanical response of forged Ti-6Al-4V subjected to reverse loading at different temperatures and strain-rates. This study characterises the effect of increasing temperature and strain-rates on the Bauschinger response of the material. This study aims to develop an enhanced understanding of the mechanisms responsible for the macroscopic behaviour of the material. The investigation commences by characterising the Bauschinger response, i.e., the experimentally observed reduction in reverse yield stress following

prior plastic deformation. It further involves an analysis of the kinematic hardening behaviour of the material during cyclic reverse loading across both loading sequences. Kinematic hardening serves as the constitutive framework to describe this behaviour and is characterised by the evolution of backstressan internal stress-like variable that governs the translation of the yield surface in stress space as plastic deformation progresses [11]. These tests are interrupted to undergo microscopic analysis using Electron Backscatter Diffraction (EBSD) technique. This analysis aims to study the evolution of deformation mechanisms, twin activity, and slip behaviour based on the Schmid factor. Additionally, this study aims to understand the role of the residual stress accumulation within the interrupted specimens. In the future, the results of this research can be used to improve and extend our current constitutive models for titanium alloys, thereby enabling a deeper understanding and facilitating the design and manufacturing of industrial components from this material in a more effective manner.

2 | Literature Review

2.1 Fundamental Stress, Strain, and Plasticity Theory

The Bauschinger effect is a phenomenon related to cyclic plasticity, necessitating a precise explanation of stress, strain, yield behaviour, hardening, and back stress. While the experimental findings in this thesis are mainly illustrated through macroscopic stress-strain curves, understanding reverse yielding demands familiarity with tensorial stress, deviatoric stress, yield loci, and the evolution of yield surfaces. This section outlines the differences between engineering and true stress-strain measures, provides a tensor representation of stress and strain, and discusses the decomposition of hydrostatic and deviatoric stress, yield criteria, isotropic and kinematic hardening, and the definition of back stress used throughout this thesis. These concepts form a mechanical framework essential for interpreting the Bauschinger response in titanium alloys through the lens of cyclic plasticity theory.

2.1.1 Engineering and true stress-strain measures

Mechanical test results are commonly reported using engineering stress and engineering strain because these quantities are calculated directly from the initial specimen geometry and the measured force-displacement response. Engineering stress is defined as [12]:

$$\sigma_{\text{eng}} = \frac{F}{A_0}, \tag{2.1}$$

where F is the applied force and A_0 is the original cross-sectional area of the specimen. Engineering strain is defined as:

$$\varepsilon_{\text{eng}} = \frac{L - L_0}{L_0}, \tag{2.2}$$

where L_0 is the original gauge length and L is the instantaneous gauge length.

In contrast, true stress and true strain account for the instantaneous geometry of the deforming specimen. True stress is defined as:

$$\sigma_{\text{true}} = \frac{F}{A}, \tag{2.3}$$

where A is the instantaneous cross-sectional area. True strain is defined as:

$$\varepsilon_{\text{true}} = \ln\left(\frac{L}{L_0}\right). \tag{2.4}$$

Before the onset of necking, when deformation remains approximately uniform, engineering and true strain are related by [12]:

$$\varepsilon_{\text{true}} = \ln(1 + \varepsilon_{\text{eng}}). \tag{2.5}$$

Assuming plastic incompressibility during uniform deformation, the corresponding stress relationship is:

$$\sigma_{\text{true}} = \sigma_{\text{eng}}(1 + \varepsilon_{\text{eng}}). \tag{2.6}$$

This distinction is important in the context of this thesis because the Bauschinger effect is assessed after prior plastic deformation and is interpreted through changes in the forward and reverse yielding response. Engineering stress-strain curves are useful for presenting the measured macroscopic response during forward loading, unloading, and reverse loading, whereas true stress and true strain provide a more physically meaningful description of the evolving material state during plastic flow. The engineering-to-true stress-strain relationships given above are valid for uniform deformation before necking and are therefore used here as a theoretical basis for interpreting plastic deformation, rather than as a complete description of post-necking behaviour.

2.1.2 Tensor representation of stress and strain

In a general three-dimensional body, stress and strain cannot be fully represented by scalar quantities; instead, they are expressed using second-order tensors. Although the mechanical tests discussed in this thesis are primarily analysed through axial stress-strain curves, the fundamental theory of plasticity is tensorial in nature because yielding, plastic flow, and hardening depend on the complete stress state rather than on a single scalar stress value [13, 14]. This is particularly important when establishing yield criteria such as Tresca and von Mises, which are expressed using principal stresses, stress invariants, or stress-tensor components.

The Cauchy stress tensor can be written as [15]

$$\boldsymbol{\sigma} = \begin{bmatrix} \sigma_{11} & \sigma_{12} & \sigma_{13} \\ \sigma_{21} & \sigma_{22} & \sigma_{23} \\ \sigma_{31} & \sigma_{32} & \sigma_{33} \end{bmatrix}, \tag{2.7}$$

where the diagonal terms represent normal stresses and the off-diagonal terms represent shear stresses. In the absence of body couples, the stress tensor is symmetric, such that $\sigma_{ij} = \sigma_{ji}$.

For small deformation theory, the infinitesimal strain tensor is defined as [15]

$$\boldsymbol{\varepsilon} = \frac{1}{2}\left(\nabla \mathbf{u} + \nabla \mathbf{u}^T\right), \tag{2.8}$$

or, in index notation,

$$\varepsilon_{ij} = \frac{1}{2}\left(\frac{\partial u_i}{\partial x_j} + \frac{\partial u_j}{\partial x_i}\right), \tag{2.9}$$

where $\mathbf{u}$ is the displacement vector. The diagonal components of the strain tensor represent normal strains, while the off-diagonal components represent shear strains.

The principal stresses, denoted as σ_1, σ_2, and σ_3, are obtained in the coordinate system where the shear stresses are zero and the stress tensor is diagonal:

$$\boldsymbol{\sigma}_{\text{principal}} = \begin{bmatrix} \sigma_1 & 0 & 0 \\ 0 & \sigma_2 & 0 \\ 0 & 0 & \sigma_3 \end{bmatrix}. \tag{2.10}$$

Principal stresses are useful because many yield criteria can be expressed compactly in terms of σ_1, σ_2, and σ_3. Consequently, while the experimental findings presented in this thesis predominantly use axial stress-strain curves, the theoretical framework required to interpret yielding, hardening, and reverse yielding is rooted in tensorial stress and strain.

2.1.3 Hydrostatic and deviatoric stress decomposition

The stress tensor can be decomposed into hydrostatic and deviatoric components. The hydrostatic component represents the mean normal stress and is associated with volumetric loading, whereas the deviatoric component represents the distortional part of the stress state. This decomposition is commonly used in plasticity theory because yielding in ductile metals is governed primarily by distortional deformation rather than by hydrostatic pressure [13, 15].

The mean stress is defined as

$$\sigma_m = \frac{1}{3}\mathrm{tr}(\boldsymbol{\sigma}) = \frac{1}{3}\sigma_{kk}, \tag{2.11}$$

where $\mathrm{tr}(\boldsymbol{\sigma})$ is the trace of the stress tensor and σ_{kk} denotes the summation of the normal stress components using index notation. The hydrostatic stress tensor is then written as

$$\boldsymbol{\sigma}_{\mathrm{hyd}} = \sigma_m \mathbf{I}, \tag{2.12}$$

where $\mathbf{I}$ is the identity tensor.

The deviatoric stress tensor is obtained by subtracting the hydrostatic component from the total stress tensor:

$$\mathbf{s} = \boldsymbol{\sigma} - \sigma_m \mathbf{I}, \tag{2.13}$$

or, in index notation,

$$s_{ij} = \sigma_{ij} - \frac{1}{3}\sigma_{kk}\delta_{ij}, \tag{2.14}$$

where δ_{ij} denotes the Kronecker delta.

In matrix form, this decomposition can be expressed as

$$\begin{bmatrix} \sigma_{11} & \sigma_{12} & \sigma_{13} \\ \sigma_{21} & \sigma_{22} & \sigma_{23} \\ \sigma_{31} & \sigma_{32} & \sigma_{33} \end{bmatrix} = \begin{bmatrix} \sigma_m & 0 & 0 \\ 0 & \sigma_m & 0 \\ 0 & 0 & \sigma_m \end{bmatrix} + \begin{bmatrix} \sigma_{11} - \sigma_m & \sigma_{12} & \sigma_{13} \\ \sigma_{21} & \sigma_{22} - \sigma_m & \sigma_{23} \\ \sigma_{31} & \sigma_{32} & \sigma_{33} - \sigma_m \end{bmatrix}. \tag{2.15}$$

This matrix representation shows that the hydrostatic part contributes equally to the three normal stress directions and contains no shear components, while the deviatoric part contains the shear stresses and the departures of the normal stresses from the mean stress. The trace of the deviatoric stress tensor is zero, meaning that it represents shape-changing distortion without a net volumetric stress contribution.

The hydrostatic component is associated with changes in volume, while the deviatoric component is associated with changes in shape or distortion. For ductile metals, plastic yielding is typically governed mainly by the deviatoric stress state

rather than by the hydrostatic component [13, 14]. This is why yield criteria such as von Mises are usually formulated in terms of deviatoric stress invariants.

This decomposition is important in the present thesis because the Bauschinger effect is interpreted through changes in reverse yielding and yield-locus evolution during plastic deformation. Since yield loci for ductile metals are commonly represented in deviatoric stress space, the hydrostatic-deviatoric decomposition provides the link between the full tensorial stress state and the later discussion of kinematic hardening, backstress, and yield-surface translation [13, 16].

2.1.4 Yield loci and hardening in deviatoric stress space

2.1.4.1 Yield surface, yield locus, and the deviatoric plane

A yield criterion defines the stress states at which plastic deformation begins. In three-dimensional principal stress space, the yield surface separates elastic stress states from plastic stress states. The hydrostatic axis is defined by

$$\sigma_1 = \sigma_2 = \sigma_3, \tag{2.16}$$

where σ_1, σ_2, and σ_3 are the principal stresses. Stress states on this axis are purely hydrostatic.

The deviatoric plane, also referred to as the π-plane, is perpendicular to the hydrostatic axis and represents the distortional part of the stress state. For ductile metals, yielding is generally governed by distortional deformation rather

than by hydrostatic loading, and yield criteria are therefore commonly described in deviatoric stress space [13, 14].

The intersection of the yield surface with the deviatoric plane is referred to as the yield locus. This representation is useful because it shows the shape of the yield condition independently of hydrostatic stress. In the deviatoric plane, the von Mises yield locus appears as a circle, whereas the Tresca yield locus appears as a hexagon [13].

2.1.4.2 Tresca yield criterion

The Tresca yield criterion states that yielding begins when the maximum shear stress reaches a critical value. In terms of the principal stresses, the maximum shear stress is

$$\tau_{\max} = \frac{1}{2} \max \left(|\sigma_1 - \sigma_2|, |\sigma_2 - \sigma_3|, |\sigma_3 - \sigma_1| \right). \tag{2.17}$$

The Tresca yield condition may therefore be written as

$$\max \left(|\sigma_1 - \sigma_2|, |\sigma_2 - \sigma_3|, |\sigma_3 - \sigma_1| \right) = \sigma_y, \tag{2.18}$$

where σ_y is the uniaxial yield stress. In the deviatoric plane, the Tresca yield locus takes the form of a hexagon because yielding is controlled by the largest difference between the principal stresses [13].

2.1.4.3 von Mises yield criterion

The von Mises yield criterion states that yielding is governed by the second invariant of the deviatoric stress tensor, J_2, defined as [17]

$$J_2 = \frac{1}{2} s_{ij} s_{ij}. \tag{2.19}$$

The corresponding von Mises equivalent stress is [18]

$$\sigma_{\mathrm{v}} = \sqrt{3J_2} = \sqrt{\frac{3}{2} s_{ij} s_{ij}}, \tag{2.20}$$

and yielding occurs when

$$\sigma_{\mathrm{v}} = \sigma_y. \tag{2.21}$$

In terms of principal stresses, the equivalent stress may be written as

$$\sigma_{\mathrm{v}} = \sqrt{\frac{1}{2} \left[(\sigma_1 - \sigma_2)^2 + (\sigma_2 - \sigma_3)^2 + (\sigma_3 - \sigma_1)^2 \right]}. \tag{2.22}$$

In the deviatoric plane, the von Mises yield locus is circular because the equivalent stress depends only on the second invariant of the deviatoric stress tensor. This criterion is widely used for ductile metals because it is independent of hydrostatic stress and describes yielding as a condition governed by distortional stress [13, 14].

2.1.4.4 Other yield criteria

Other yield criteria may be required when additional material behaviour must be represented, such as pressure sensitivity or anisotropy. Pressure-dependent criteria include the influence of hydrostatic stress in the yield function, whereas anisotropic criteria modify the shape of the yield locus to account for direction-dependent yielding [14,19]. Nevertheless, the Tresca and von Mises criteria remain the fundamental engineering descriptions for yield loci in ductile metals and provide the basis for the present discussion.

2.1.4.5 Evolution of the yield locus under isotropic hardening

Plastic deformation modifies the yield locus through hardening. In isotropic hardening, the yield locus expands uniformly without any shift in its centre. For a von Mises material, the yield function may be written as [20]

$$f(\boldsymbol{\sigma}, R) = \sigma_{\mathrm{v}} - (\sigma_{y0} + R) = 0, \tag{2.23}$$

where σ_{y0} is the initial yield stress and R is the isotropic hardening variable. As plastic strain accumulates, R increases and the size of the yield locus grows. In the deviatoric plane, this corresponds to expansion of the circular von Mises yield locus without any change in its centre. Isotropic hardening therefore changes the size of the yield locus but not its position [13].

2.1.4.6 Evolution of the yield locus under kinematic hardening

In kinematic hardening, plastic deformation translates the yield locus in stress space without necessarily changing its size. This translation captures the directional nature of plastic deformation and is particularly important under reverse loading. For a von Mises material with pure kinematic hardening, the yield function may be written as

$$f(\boldsymbol{\sigma}, \boldsymbol{\alpha}) = \sqrt{\frac{3}{2}(\mathbf{s} - \boldsymbol{\alpha}) : (\mathbf{s} - \boldsymbol{\alpha})} - \sigma_{y0} = 0, \tag{2.24}$$

where $\mathbf{s}$ is the deviatoric stress tensor, $\boldsymbol{\alpha}$ represents the translation of the yield locus in deviatoric stress space, and σ_{y0} is the initial yield stress [13,16,21]. The term $(\mathbf{s} - \boldsymbol{\alpha})$ shows that yielding depends on the stress state relative to the translated centre of the yield locus.

Kinematic hardening is central to the interpretation of reverse yielding because translation of the yield locus reduces the stress required to yield in the reverse direction after prior plastic deformation. This provides the yield-surface basis for understanding the Bauschinger effect.

2.1.4.7 Combined isotropic and kinematic hardening

Real metals may exhibit both isotropic and kinematic hardening. A combined hardening form may therefore be written as

$$f(\boldsymbol{\sigma}, \boldsymbol{\alpha}, R) = \sqrt{\frac{3}{2}(\mathbf{s} - \boldsymbol{\alpha}) : (\mathbf{s} - \boldsymbol{\alpha})} - (\sigma_{y0} + R) = 0. \tag{2.25}$$

Here, R represents expansion of the yield locus, whereas $\boldsymbol{\alpha}$ represents translation of the yield locus. Isotropic hardening therefore changes the size of the yield locus, kinematic hardening changes its position, and combined hardening allows both effects to occur simultaneously.

This distinction is important in the present thesis because the Bauschinger effect is associated primarily with a reduction in reverse yield stress following prior plastic deformation. Such behaviour cannot be explained by isotropic hardening alone, since isotropic hardening expands the yield locus and would generally increase the resistance to yielding in both loading directions. Kinematic hardening, through translation of the yield locus, provides the mechanical framework needed to explain why reverse yielding can occur at a lower applied stress.

2.1.5 Formal definition of backstress

Backstress is a stress-like internal variable used in plasticity theory to describe the translation of the yield surface during kinematic hardening. It represents the displacement of the centre of the yield locus in stress space and accounts for the directional nature of plastic deformation under load reversal [13, 16, 21]. Unlike isotropic hardening, which changes the size of the yield surface, backstress changes the position of the yield surface.

For pressure-insensitive plasticity in ductile metals, the backstress tensor is commonly defined in deviatoric stress space. If $\mathbf{s}$ is the deviatoric stress tensor

and $\boldsymbol{\alpha}$ is the backstress tensor, the relative deviatoric stress may be written as

$$\boldsymbol{\eta} = \mathbf{s} - \boldsymbol{\alpha}, \tag{2.26}$$

where $\boldsymbol{\eta}$ is the stress state measured relative to the translated centre of the yield surface. In this framework, yielding is governed not by the absolute deviatoric stress $\mathbf{s}$, but by the shifted stress $\mathbf{s} - \boldsymbol{\alpha}$.

For a von Mises material with kinematic hardening, the yield function can be written as

$$f(\boldsymbol{\sigma}, \boldsymbol{\alpha}) = \sqrt{\frac{3}{2}(\mathbf{s} - \boldsymbol{\alpha}) : (\mathbf{s} - \boldsymbol{\alpha})} - \sigma_{y0} = 0, \tag{2.27}$$

where σ_{y0} is the initial yield stress. The symbol ":" denotes the double contraction of two second-order tensors. This expression shows that the backstress tensor shifts the centre of the yield surface in deviatoric stress space, while the radius of the yield surface remains unchanged for pure kinematic hardening [13, 21].

In uniaxial loading, the tensorial definition reduces to a scalar form. The relative stress is written as

$$\eta = \sigma - \alpha, \tag{2.28}$$

where σ is the applied uniaxial stress and α is the scalar backstress. Yielding occurs when

$$|\sigma - \alpha| = \sigma_y. \tag{2.29}$$

This scalar expression illustrates the physical significance of backstress during

reverse loading. After prior plastic deformation in one direction, the yield surface translates in stress space. As a result, a lower applied stress is required to cause yielding in the reverse direction, while a higher stress may be required to continue yielding in the original loading direction.

In the present thesis, backstress is therefore used as the internal variable that represents yield-surface translation associated with kinematic hardening. This provides the mechanical basis for interpreting the Bauschinger effect, where prior plastic deformation reduces the reverse yield stress. The concept is particularly relevant for the reverse-loading experiments considered in this work, because the measured reduction in reverse yield stress can be understood as a macroscopic manifestation of internal stress development and yield-surface translation [13, 16].

2.1.6 Constitutive modelling approaches for cyclic hardening behaviour

Constitutive plasticity models describe the evolution of stress, plastic strain, and internal variables during deformation. In classical rate-independent plasticity, the material response is commonly defined through three main components: a yield function, a flow rule, and hardening laws. The yield function defines the onset of plastic flow, the flow rule determines the direction of the plastic strain increment, and the hardening laws describe the evolution of internal variables such as the isotropic hardening variable R and the backstress tensor $\boldsymbol{\alpha}$ [13, 17]. These components provide the theoretical framework required to describe cyclic

hardening behaviour, reverse yielding, and the Bauschinger effect.

For isotropic hardening, plastic deformation causes the yield surface to expand without translating its centre. A von Mises yield function with isotropic hardening may be written as

$$f(\boldsymbol{\sigma}, R) = \sqrt{\frac{3}{2}\mathbf{s} : \mathbf{s}} - (\sigma_{y0} + R) = 0, \tag{2.30}$$

where $\mathbf{s}$ is the deviatoric stress tensor, σ_{y0} is the initial yield stress, and R is the isotropic hardening variable. The variable R represents the increase in the size of the yield surface due to accumulated plastic deformation. A simple isotropic hardening law may relate R to the accumulated equivalent plastic strain, $\bar{\varepsilon}^p$, through either a linear relationship or a saturating relationship. Although isotropic hardening can describe monotonic strengthening, it cannot by itself represent translation of the yield surface or the reduction in reverse yield stress after load reversal [13].

Kinematic hardening models introduce the backstress tensor, $\boldsymbol{\alpha}$, to describe translation of the yield surface in stress space. For a von Mises material with kinematic hardening, the yield function may be written as

$$f(\boldsymbol{\sigma}, \boldsymbol{\alpha}) = \sqrt{\frac{3}{2}(\mathbf{s} - \boldsymbol{\alpha}) : (\mathbf{s} - \boldsymbol{\alpha})} - \sigma_{y0} = 0. \tag{2.31}$$

Here, the term $\mathbf{s} - \boldsymbol{\alpha}$ represents the deviatoric stress measured relative to the translated centre of the yield surface. Kinematic hardening is therefore essential for describing load-path-dependent plasticity and reverse yielding.

The simplest kinematic hardening formulation is the linear Prager model, in which the backstress evolves proportionally to the plastic strain increment. This model captures the basic translation of the yield surface and can therefore represent the first-order features of the Bauschinger effect. However, because the backstress increases linearly and does not saturate, the model may overpredict hardening at larger plastic strains and is limited in its ability to describe cyclic stabilisation or nonlinear cyclic behaviour [13].

A more widely used nonlinear kinematic hardening formulation is the Armstrong–Frederick model. In this model, the backstress evolves through a hardening term and a dynamic recovery term. In rate form, the evolution law may be written as

$$d\boldsymbol{\alpha} = C\, d\boldsymbol{\varepsilon}^{p} - \gamma \boldsymbol{\alpha}\, d\bar{\varepsilon}^{p}, \tag{2.32}$$

where C controls the initial rate of kinematic hardening, γ controls dynamic recovery, $d\boldsymbol{\varepsilon}^{p}$ is the plastic strain increment, and $d\bar{\varepsilon}^{p}$ is the increment in accumulated equivalent plastic strain [13, 22]. The dynamic recovery term allows the backstress to approach a saturated value, making the model more suitable for cyclic loading than a purely linear kinematic hardening law.

Combined isotropic–kinematic hardening models allow both expansion and translation of the yield surface. A representative von Mises yield function may be written as

$$f(\boldsymbol{\sigma}, \boldsymbol{\alpha}, R) = \sqrt{\frac{3}{2}\,(\mathbf{s} - \boldsymbol{\alpha}) : (\mathbf{s} - \boldsymbol{\alpha})} - (\sigma_{y0} + R) = 0. \tag{2.33}$$

In this expression, R governs the expansion of the yield surface, while $\boldsymbol{\alpha}$ governs its translation. This combined framework is more appropriate for cyclic plasticity because real metals may exhibit both changes in yield-surface size and changes in yield-surface position during plastic deformation.

More advanced cyclic plasticity models, such as the Chaboche model, extend the Armstrong–Frederick approach by representing the total backstress as a sum of multiple backstress components:

$$\boldsymbol{\alpha} = \sum_{k=1}^{N} \boldsymbol{\alpha}^{(k)}. \tag{2.34}$$

Each component may evolve with different hardening and recovery parameters, allowing the model to capture different stages of kinematic hardening. This improves the description of cyclic hardening, cyclic stabilisation, mean-stress relaxation, ratcheting, and load-reversal behaviour [13].

These constitutive modelling approaches are relevant to the present thesis because the experimental programme investigates forward loading, unloading, and reverse loading in forged Ti-6Al-4V. The measured reduction in reverse yield stress is most directly associated with kinematic hardening and backstress development, whereas changes in the overall resistance to plastic flow may also involve isotropic hardening, thermal softening, and strain-rate effects. Therefore, the isotropic, kinematic, and combined hardening frameworks provide the theoretical basis for interpreting the observed Bauschinger response, even where full constitutive model calibration is beyond the scope of the present work.

2.2 The Bauschinger effect

Under reverse loading, certain materials, such as titanium, display a phenomenon known as the Bauschinger effect. It is essential to understand this effect in order to characterise it. The Bauschinger effect, first documented by Johann Bauschinger in 1881, refers to a behaviour observed in some metallic materials where the yield stress decreases when the direction of the load is reversed [23]. As shown in Figure 2.1, the stress-strain graph illustrates the reverse loading of a material. Initially, the material is subjected to a tensile load, moving from point O to point A, where it behaves elastically. With further application of stress, the material experiences plastic deformation until reaching point B. Further, the material is unloaded at point C. Furthermore, from point C, the load is reversed to compression and reaches point D, where the material would yield again in the reverse direction. However, for material that exhibits a Bauschinger effect, yielding occurs earlier at point D′. The load is reversed to compression, resulting in yield at point D′. This phenomenon suggests that the yield stress of the material decreases when the load is reversed. In other words, in materials exhibiting the Bauschinger effect, the yield stress upon load reversal is reduced: after prior tensile plastic deformation the compressive yield stress decreases to $\sigma'_{y,\mathrm{c}} < \sigma_{y,c}$, and after prior compressive plastic deformation the tensile yield stress decreases to $\sigma'_{y,\mathrm{t}} < \sigma_{y,t}$.

In microstructural terms, yielding corresponds to the onset of irreversible plastic deformation [12, 24]. Plastic flow during the initial loading direction causes

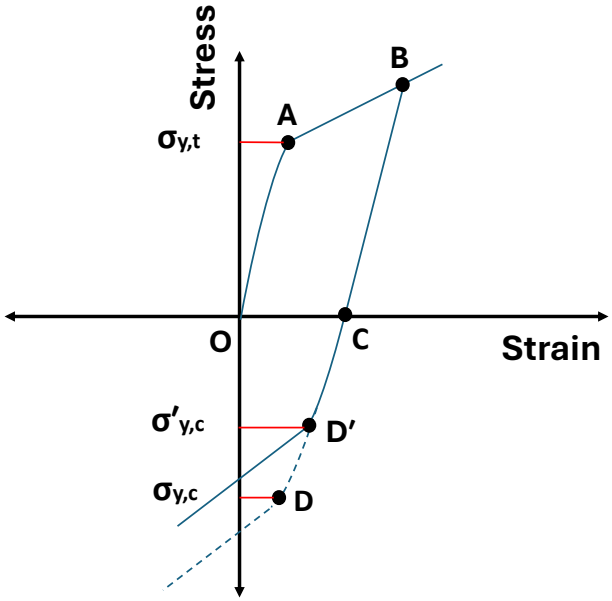


Figure 2.1: Schematic stress-strain response illustrating the Bauschinger effect under reverse axial loading (tension followed by compression). A material is initially loaded in tension from point O to point A, reaching the tensile yield stress, $\sigma_{y,t}$ (point A), and is plastically deformed to point B. The material is then unloaded from point B to point C. Upon load reversal in compression from point C, the material would typically yield at $\sigma_{y,c}$ (point D) in the reverse direction. However, if the material exhibits a Bauschinger effect, yielding occurs earlier at $\sigma'_{y,c}$ (point D′). This demonstrates a decrease in yield stress following load reversal.

the accumulation of dislocations and the formation of heterogeneous substructures, such as pile-ups at grain or phase boundaries, which generate internal stress fields that may persist after unloading [25]. When the load is reversed, these internal stresses can facilitate dislocation movement in the opposite direction within favourably oriented deformation systems, thus lowering the applied stress needed to reinitiate plasticity [25, 26]. This phenomenon is often characterised by a kinematic backstress [25, 27].

2.2.1 Explanation of the Bauschinger effect using yield surface evolution

The Bauschinger effect can be understood geometrically through the evolution of the yield surface during prior plastic deformation and subsequent load reversal. For an initially undeformed and approximately isotropic material, the yield surface may be considered to be centred at the origin of stress space. In this initial state, yielding in the forward and reverse loading directions occurs at approximately equal stress magnitudes. However, after plastic deformation in the forward direction, the yield surface may translate away from the origin due to the development of directional internal stresses [13, 21].

In continuum plasticity, these directional internal stresses are represented by the backstress tensor, $\boldsymbol{\alpha}$, which describes the translation of the yield surface in stress space. For a von Mises material with kinematic hardening, the yield condition may be written as [13, 16]

$$f(\boldsymbol{\sigma}, \boldsymbol{\alpha}) = \sqrt{\frac{3}{2}(\mathbf{s} - \boldsymbol{\alpha}) : (\mathbf{s} - \boldsymbol{\alpha})} - \sigma_y = 0, \tag{2.35}$$

where $\mathbf{s}$ is the deviatoric stress tensor, $\boldsymbol{\alpha}$ is the deviatoric backstress tensor, and σ_y represents the size of the yield surface. The symbol : denotes the double contraction of two second-order tensors. This expression shows that yielding is governed by the relative deviatoric stress, $\mathbf{s} - \boldsymbol{\alpha}$, rather than by the applied deviatoric stress $\mathbf{s}$ alone.

The backstress shifts the centre of the yield locus away from the origin. As a result, the stress required to yield in one loading direction becomes different from the stress required to yield in the opposite direction. This distinguishes kinematic hardening from isotropic hardening. In isotropic hardening, plastic deformation expands the yield surface uniformly, so the material becomes harder in both the forward and reverse loading directions. Isotropic hardening alone would therefore predict an increase in the reverse yield stress after prior plastic deformation, rather than the experimentally observed reduction. The reduction in reverse yield stress associated with the Bauschinger effect therefore requires yield-surface translation, which is represented through kinematic hardening and backstress development [13, 16].

In uniaxial loading, the same concept can be written in scalar form as

$$|\sigma - \alpha| = \sigma_y, \tag{2.36}$$

where σ is the applied axial stress, α is the uniaxial backstress, and σ_y is the current yield stress. After prior plastic deformation in tension, backstress develops in association with the forward loading direction and translates the yield locus in stress space. When the material is unloaded and reloaded in compression, the translated yield locus is reached at a lower compressive stress magnitude than would be expected for an unshifted yield surface. This earlier onset of reverse plasticity corresponds to the reduced reverse yield stress observed in the macroscopic stress–strain response.

This framework is important for the titanium alloy investigated in the present thesis because heterogeneous deformation between grains, phases, and slip systems can generate internal stresses that act as microstructural sources of continuum backstress. The experimentally measured Bauschinger effect can therefore be interpreted as the macroscopic consequence of yield-locus translation caused by internal stress development during prior plastic deformation [16].

2.2.2 Factors affecting the Bauschinger effect

The Bauschinger effect is influenced by factors such as the material's chemical composition, manufacturing process, crystal structure, grain size, nature of fatigue loading, and history of plastic strain. It has been studied in polycrystalline metals, particularly with FCC and BCC structures [28–36].In copper, the phenomenon arises from local hardening effects and the asymmetry of twinning and detwinning [28, 32]. In copper-silica alloys, it is linked to internal stresses in the copper matrix due to dislocation interactions with silica particles [37]. Relaxation through dislocation rearrangements reduces internal stresses, leading to softening upon load reversal [37]. A study on bi-directional microcantilever bending of single-crystal copper beams utilised *in situ* high-resolution electron backscatter diffraction to observe evolving dislocation structures [38]. The Bauschinger effect results from irreversible dislocation pile-up and high densities of geometrically necessary dislocations influenced by short-range interactions like junction formation [38]. A notable Bauschinger effect is also seen in Mn18Cr18N steel under pre-straining,

with increasing magnitude at higher pre-strain levels [39]. Additionally, dislocation accumulation near grain boundaries contributes to this effect [39]. In four-point bending cyclic tests of the 42CrMo4 alloy, asymmetric residual stresses from inhomogeneous deformation and dislocation rearrangement led to early yielding during reverse loading [40]. In nickel, local dislocation pile-ups cause the effect [30], while in ferrite, it arises from pile-ups at grain boundaries [34]. Research on stainless steel compositions has advanced understanding of this phenomenon. Hu et al. found that high-temperature pre-straining in austenitic stainless steel results in type II meso-scale residual stress accumulation and transient softening [33]. An increase in intragranular precipitates and pre-strain enhances type III micro-scale residual stresses, affecting the compressive curve during reloading [33]. Fajoui et al. used neutron diffraction on 316L austenitic steel, revealing that intragranular heterogeneities contribute to the Bauschinger effect [35]. Hu et al. studied Type 316H polycrystalline stainless steels and concluded that the Bauschinger effect arises from grain-scale residual stresses due to plastic anisotropy and dislocation recovery, impacting internal resistance via changes in dislocation junction density [41]. In experiments on pure Al with coarse and ultrafine grain sizes from ECAP and annealing, uniaxial tension-compression Bauschinger tests showed that the effect in Al is due to back stress from dislocation pile-ups at grain boundaries, with finer grains exhibiting stronger effects due to higher GND accumulation [42]. Ex-situ interrupted three-point bending tests on API X80 linepipe steels with acicular (fine, high-dislocation-density) and polygonal ferrite (coarser, low-dislocation-density) were also conducted [34]. The Bauschinger effect was more pronounced in

the acicular ferrite-rich steel, which exhibited notable dislocation pile-ups at grain boundaries, leading to stronger back stresses despite smaller reductions in mobile dislocation density [34]. However, the microstructural causes of the Bauschinger effect remain unclear in hexagonal close-packed (HCP) materials, particularly in titanium alloys. Previous studies have investigated this phenomenon in titanium and HCP materials [43–48], but have not fully elucidated its underlying causes.

2.2.3 Assessment and ranking of mechanisms for the Bauschinger effect

The Bauschinger effect is generally attributed to internal stress fields and microstructural changes generated during prior plastic deformation. These changes alter the stress required for yielding during subsequent reverse loading. Several mechanisms may contribute to this response, but their relative importance depends on the material, microstructure, deformation mode, temperature, strain rate, and level of pre-strain [13, 23, 36, 49]. In the present thesis, the mechanisms are ranked according to their relevance to reverse yielding in forged two-phase Ti-6Al-4V and to their usefulness for interpreting the macroscopic stress–strain response.

Rank 1: Long-range internal stresses and continuum backstress

The primary mechanism responsible for the Bauschinger effect is the development of long-range internal stresses during prior plastic deformation. These stresses arise when plastic deformation is spatially heterogeneous, for example between grains with different crystallographic orientations, regions with different slip

activity, or microstructural regions with different mechanical responses. Upon unloading and reverse loading, these internal stresses can assist plastic flow in the reverse direction and thereby reduce the apparent reverse yield stress [26, 36, 49].

In continuum plasticity, this mechanism is represented by the backstress tensor, $\boldsymbol{\alpha}$, which describes translation of the yield locus in stress space [13, 16, 21]. This mechanism is ranked first because it provides the most direct explanation for the defining feature of the Bauschinger effect: reduced yield stress during reverse loading after prior plastic deformation. It also links directly to the yield-locus framework used in this thesis, where kinematic hardening and backstress translate the yield surface rather than simply expanding it.

Rank 2: Dislocation pile-ups and short-range internal stresses

The second most important mechanism is the formation of dislocation pile-ups and short-range internal stresses at microstructural barriers such as grain boundaries, phase boundaries, and strong obstacles. During forward plastic deformation, dislocations can accumulate at these barriers and generate local internal stress fields. When the loading direction is reversed, these local stresses may assist reverse dislocation motion, reducing the stress required for reverse yielding [36, 50, 51].

This mechanism is ranked second because it provides a microstructural origin for the backstress used in continuum kinematic hardening models. In titanium alloys, slip incompatibility between neighbouring grains and across different phases

can promote the development of such local stress fields [50, 52]. However, at the macroscopic scale considered in the mechanical interpretation of this thesis, these effects are usually incorporated within the broader continuum backstress response rather than treated as a separate measurable variable.

Rank 3: Phase-level load partitioning

For two-phase titanium alloys, phase-level load partitioning is also an important mechanism. If the α and β phases deform differently during forward loading, residual internal stresses may develop between the phases after unloading. During reverse loading, these phase-level internal stresses can promote earlier reverse yielding. This mechanism is closely related to the development of long-range internal stresses, but it is specifically associated with the mechanical contrast between the phases and the redistribution of stress between them [50, 52, 53].

This mechanism is ranked third because it is likely to be relevant to the two-phase titanium alloy studied in this thesis, but its relative contribution depends on phase fraction, phase morphology, crystallographic texture, and the extent of strain partitioning. In the absence of phase-resolved measurements, it is difficult to separate this contribution from the broader internal stress and backstress response [50, 53].

Rank 4: Dislocation annihilation, rearrangement, and reversible dislocation motion

A further mechanism involves the annihilation, rearrangement, or reversible motion of dislocations during reverse loading. When the loading direction is reversed, some dislocations generated during forward plastic deformation may move back, reorganise, or interact with dislocations of opposite sign. This can reduce the resistance to reverse plastic flow and contribute to transient softening at the early stage of load reversal [25, 36, 54].

This mechanism is ranked fourth because it may contribute to the initial stages of reverse yielding, but it does not provide as direct a yield-locus-based explanation as long-range internal stress and kinematic hardening. It is therefore treated as a secondary mechanism in the present thesis [13].

Overall, the ranking adopted in this thesis places long-range internal stresses and continuum backstress as the dominant explanation for the measured Bauschinger effect, followed by dislocation pile-ups, phase-level load partitioning, and dislocation rearrangement processes. This ranking does not imply that only one mechanism operates. Instead, the experimentally measured reduction in reverse yield stress is interpreted as the combined macroscopic response of several microstructural mechanisms, with continuum backstress providing the most appropriate framework for linking these mechanisms to yield-locus translation and reverse yielding.

2.2.4 Experimental methods for uniaxial cyclic and reverse-loading tests

Uniaxial cyclic and reverse-loading tests are widely used experimental methods for investigating plasticity, hardening behaviour, and the Bauschinger effect. In these tests, a specimen is loaded along a single axis and then subjected to unloading, reloading, or complete load reversal. The resulting stress-strain response enables direct measurement of forward yield stress, reverse yield stress, cyclic hardening or softening, and hysteresis behaviour. This type of testing is particularly useful for studying the Bauschinger effect because the reduction in yield stress after load reversal can be identified from the reverse branch of the stress-strain curve [23, 36, 55, 56].

A typical uniaxial reverse-loading test first plastically deforms the specimen in one direction, unloads it, and then reloads it in the opposite direction. For example, a specimen may be plastically strained in tension before being reloaded in compression. The reverse yield stress is then compared with the initial yield stress or with the forward flow stress at the imposed pre-strain. If the reverse yield stress is lower than expected from isotropic hardening alone, the material is considered to exhibit the Bauschinger effect. This method provides a direct connection between the measured stress-strain response and the concepts of yield-locus translation, kinematic hardening, and backstress [13, 36, 55, 56].

Uniaxial cyclic tests can be conducted under either stress control or strain control. Strain-controlled testing is commonly used when the plastic strain his-

tory is important, because the imposed strain amplitude determines the level of plastic deformation in each cycle. Such tests produce hysteresis loops, which allow cyclic hardening, cyclic softening, mean-stress relaxation, and changes in unloading and reloading behaviour to be assessed. These features are important for linking experimental observations with constitutive descriptions based on isotropic and kinematic hardening [13, 57].

Several studies have used uniaxial cyclic or reverse-loading methods to investigate the Bauschinger effect in metals. Saleh and Margolin studied the Bauschinger effect during cyclic straining of two-phase titanium alloys, making their work particularly relevant to the present thesis [56]. Mamun et al. used uniaxial cyclic stress-strain tests to examine the relationship between internal residual strains and the macroscopic Bauschinger effect in polycrystalline stainless steel [36]. Atkinson et al. combined uniaxial reversed loading with high-resolution digital image correlation to quantify local plastic strain development during reverse loading in a nickel-based alloy [57]. Toribio et al. used cyclic tension-compression loading to evaluate the Bauschinger effect in cold-drawn pearlitic steels, demonstrating the effectiveness of uniaxial cyclic testing for quantifying reverse-yielding behaviour [58].

The main advantage of uniaxial cyclic and reverse-loading tests is that they provide a direct and interpretable measurement of the mechanical response before and after load reversal. However, careful experimental control is required. The measured response can be affected by specimen alignment, buckling during com-

pression, strain-measurement accuracy, grip compliance, friction, machine stiffness, pre-strain definition, and the method used to define reverse yield stress. Therefore, specimen geometry, strain-measurement method, loading rate, pre-strain level, unloading procedure, reloading path, and yield-stress definition must be reported clearly when comparing Bauschinger-effect measurements across different studies [36, 37, 55, 56].

The experimental methods employed in this thesis are detailed at the beginning of each pertinent experimental chapter. The uniaxial cyclic and reverse-loading procedures are outlined in the experimental methodology or experimental conditions in Chapters 4.2, 5.2, and 6.2. The methodologies for electron backscatter diffraction (EBSD) are discussed in Chapter 3.1.1, while the description of residual stress measurements is provided in Chapter 4.7.1. Consequently, these chapters offer a comprehensive explanation of the relevant uniaxial cyclic reverse-loading techniques employed at various temperatures and strain-rates, along with the methodology for conducting EBSD and residual stress measurements.

2.3 Mechanical behaviour in Titanium alloys

2.3.1 Deformation mechanisms in Ti-6Al-4V and Effects of Temperature and Strain-rate dependence

The macroscopic mechanical behaviour of a material is fundamentally influenced by its microstructural deformation mechanisms [59]. To accurately predict

the mechanical response of the material when subjected to uniaxial loading, it is crucial to comprehend the microscopic deformation mechanisms at play [59]. Ti-6Al-4V, a classic $\alpha + \beta$ titanium alloy, comprises a low volume fraction (5–10%) of the high-temperature body-centred cubic phase (β phase), with the remaining volume fraction consisting of the low-temperature hexagonal close-packed (α phase) allotropic form of titanium [59]. The intricate microstructure significantly impacts the plastic deformation characteristics of Ti-6Al-4V [60]. The predominant plastic deformation mechanisms in Ti-6Al-4V are dislocation glide and crystal twinning [61].

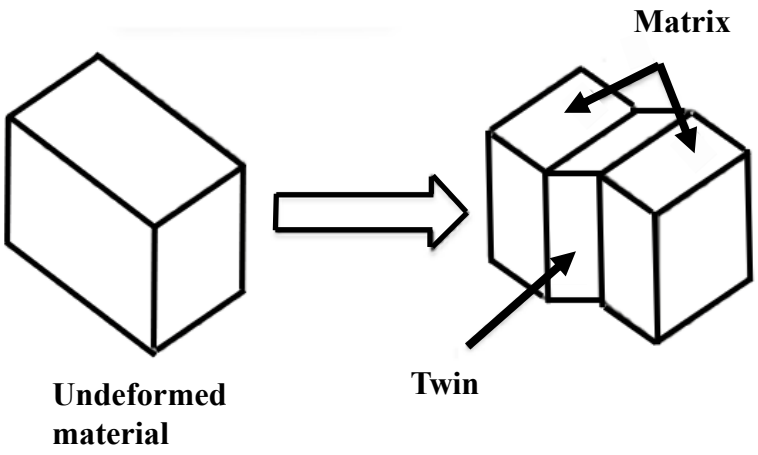


Figure 2.2: Schematic diagram of deformation twinning.

At a fixed, moderate strain rate, increasing temperature lowers the critical resolved shear stress (CRSS) for dislocation glide, facilitates cross-slip and climb, and enhances dynamic recovery. Consequently, plastic strain is preferentially accommodated by slip, while the incidence and thickening of twins decrease

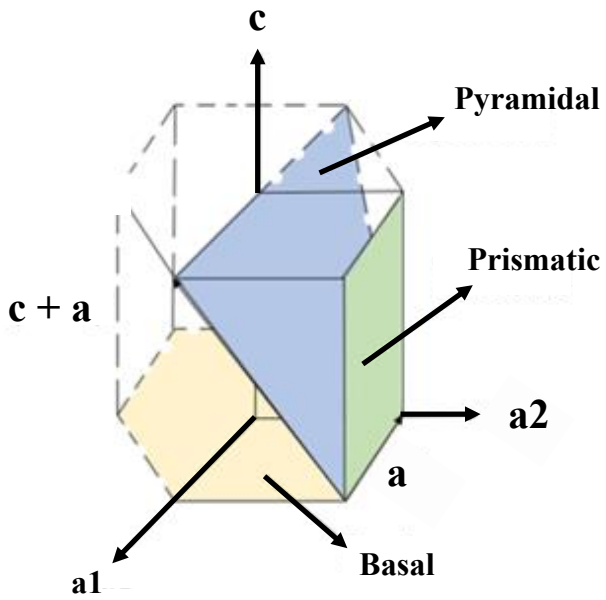


Figure 2.3: Main active slip planes in HCP titanium .

with temperature [59]. Classic Ti-6Al-4V data spanning wide rate-temperature windows exhibit a similar trend: twinning is more pronounced at lower temperatures where recovery is limited, whereas slip dominates the response at higher temperatures [62]. As the material approaches the β-transus, twinning is further suppressed because the increasing β (bcc) fraction is highly capable of slip, reducing the need for twin accommodation in the α matrix [59]. Conversely, cooling toward sub-ambient or cryogenic conditions promotes twinning in titanium, with high twin densities reported at low temperatures having associated effects on toughness [63]. Detailed studies indicate that the set of active twin systems shifts with temperature in titanium (e.g., {10-12}, {11-22}, {10-11} activity ranges with T), highlighting the significant temperature sensitivity of twinning modes [64]. Under reverse loading, detwinning occurs when the applied shear opposes the twin shear, and room-temperature *in situ* EBSD experiments demonstrate that re-

verse loading can drive twin reversion, confirming that detwinning is an accessible mechanism [63, 65]. Since recovery and interface mobility processes are thermally activated, higher temperatures can facilitate twin-boundary motion (promoting detwinning), whereas at lower temperatures, twins tend to persist and contribute to path-dependent hardening [63, 65].

At fixed temperature, an increase in strain-rate results in heightened flow stress and suppresses time-dependent recovery, thereby shifting plasticity toward higher-strength slip activity, which includes a greater reliance on pyramidal mechanisms [59, 66]. Foundational Ti-6Al-4V data covering approximately $10^{-3}10^{3}$ s^{-1} and a broad range of temperatures indicate systematic rate hardening as well as changes in associated mechanisms, framing most modern interpretations [62]. In commercially pure Ti, elevated stresses at high strain rates can encourage deformation twinning. In contrast, in Ti-6Al-4V, the twinning fraction is typically more constrained by α/β morphology and alloying elements (notably Al), leading to twinning being generally less prevalent than in CP-Ti at comparable strain rates [59]. Under extreme strain rates, local adiabatic heating and strain localization, such as the formation of adiabatic shear bands, further modify the active mechanisms and the resulting post-mortem microstructure [67, 68]. For reverse loading, higher strain rates tend to impede detwinning since twin-boundary motion has less time to proceed, unless local adiabatic heating facilitates this process. Conversely, at lower strain rates, detwinning occurs more fully and contributes to back-stress relaxation. These behaviours are documented by in-situ and cyclic studies across various Ti grades [69, 70].

During compression, twinning induces a strength differential (SD) within the material [71], with the SD effect attributed to the inhibiting influence of pressure on shear-activated slip within grains [72]. Previous research has primarily concentrated on the observation of SD; however, at high strain rates, these characteristics are expected to significantly influence the material's response under reverse loading due to the effects of the loading path [62, 73]. In commercially pure titanium, the detwinning phenomena resulting from load reversal are critical for the evolution of microstructure during cyclic deformation, impacting strain hardening within the material and serving as a back-stress relieving mechanism through the release of dislocations and stresses that accumulate at twin boundaries [74]. Thus, investigating the mechanical response of Ti-6Al-4V under reverse loading may necessitate the inclusion of detwinning as a potential deformation mechanism and a significant factor at high strain rates [60].

2.3.2 Bauschinger effect in Titanium alloys

Researchers are continuing to enhance their understanding of how titanium deforms under low-cycle fatigue conditions, particularly concerning the Bauschinger effect. This phenomenon can cause titanium to yield earlier than expected during fatigue loading. Furthermore, researchers are investigating how this effect evolves as the number of load cycles increases. Existing literature has reported on the Bauschinger effect in titanium and its alloys, providing various explanations for its occurrence. Recent studies, such as those by [44, 47], have detailed this effect

and its implications. [44] explored the Bauschinger effect in titanium alloys while performing reverse loading at both low and high strain rates. The study observed the Bauschinger effect in scenarios involving tension followed by compression and compression followed by tension loading, although it did not specify the underlying reasons for the occurrence of the Bauschinger effect. Similarly, [47] conducted fatigue tests by applying tensile loads on the material at very low strain levels, discovering that heterogeneous deformation contributed to the phenomenon. Additionally, studies by [43,46,75] have also identified the Bauschinger effect in titanium during cyclic loading at low strain levels. Interestingly, at the microscopic level, titanium exhibits an accumulation of residual stress during fatigue loading, as noted in studies by [76–78]. However, these studies did not specifically aim to investigate the Bauschinger effect.

In titanium alloys and Ti-aluminides, the behaviour of the backstress (BE) can manifest as transient softening during reloading and/or as permanent softening at the subsequent reverse yield, with this balance being controlled by microstructure, phase constitution, and loading path [79]. In hexagonal close-packed (HCP) Titanium, the prevailing mechanisms combine dislocation structures that store long-range internal stresses with twinning/detwinning processes that reorient the lattice and produce backstress, all of which is further influenced by the α/β morphology and texture in $\alpha+\beta$ alloys [80, 81]. Forward-reverse *in-situ* electron backscatter diffraction (EBSD) on commercially pure Ti directly links twin formation in the forward loading path and detwinning upon reversal to a pronounced, orientation-dependent (textural) BE [82]. For Ti-6Al-4V (Ti-64), uniaxial ten-

sioncompression datasets consistently demonstrate tension-compression asymmetry and measurable BE, thereby enabling the differentiation between isotropic and kinematic hardening when calibrating mixed-hardening models [81]. Representative quasi-static protocols utilize compression→tension and tension→compression sequences to several percent plastic strain to interrogate reverse yielding and isolate backstress evolution [83]. At high strain-rates, modified Split-Hopkinson torsion experiments illustrate a dynamic Bauschinger effect in Ti-64, underscoring the rate sensitivity of reverse yielding and the role of microstructural changes during very rapid reversals [80]. NASA reverse-loading tests on solution-treated and aged Ti-64 reveal immediate plasticity on the first reversal, presenting a clear practical signature of BE that motivates kinematic hardening in structural assessments [84]. Across a wide range of rate-temperature conditions, classic Ti64 studies indicate that increasing the strain rate raises flow stress and suppresses time-dependent recovery, effectively preserving backstress into the reverse path; conversely, higher temperatures activate recovery and cross-slip, diminishing twinning-assisted BE and favouring a slip-dominated kinematic response [62]. Under extreme rates, adiabatic heating and strain localization complicate the apparent BE by altering local microstructure and reloading softening, thus requiring careful interpretation of reverse-yield metrics [85]. Alloying and interfaces are critically important: β ligaments and α/β interfaces can limit twin transmission and modulate dislocation mean-free paths, thereby shifting the balance between kinematic and isotropic contributions at reverse yield [81]. Aluminium in the α phase tends to suppress specific twin modes (via short-range order and early Ti_3Al), reducing the twinning-

driven component of BE in Ti-64 relative to commercially pure titanium (CP-Ti) while leaving a substantial dislocation-backstress BE that remains texture- and path-dependent [86]. Grain size and prior strain history are also significant factors: generally, BE strengthens with refinement or heavy prior deformation in Ti, and trends differ from face-centred cubic (FCC) metals due to the slip/twin constraints inherent to HCP structures [45]. However, without paired microstructural characterization, it is challenging to unambiguously attribute the evolving stressstrain response to slip, twinning, and detwinning during quasi-static reversals [87]. Complementary studies in CP-Ti indicate that detwinning upon reversal can relieve backstress and alter hardening, which directly impacts the magnitude of the Bauschinger effect (BE) and cyclic life [82]. Comparative cyclic tests on differently processed titanium samples reveal distinct Bauschinger coefficients and fatigue lives, rationalized by varying detwinning fractions during displacement-controlled cycling [50]. Beyond monotonic reversals, creep-relevant loading also demonstrates asymmetry in near-α and α+β titaniums: for instance, Ti-6242 exhibits dramatic tensioncompression asymmetry in room-temperature creep, with tensile creep strains being several times greater than those in compression at comparable stress and time [88]. Micrographs from such studies illustrate intense slip-line morphology and significant shear offsets at β-laths in colonies oriented for α-basal slip, evidencing heterogeneous, interface-mediated plasticity during sustained loading [73]. Classical work further demonstrates that highly textured Ti-64 loaded along the α c-axis exhibits significantly higher compressive yield compared to tensile yield, which can be rationalized by the asymmetry in the resistance of $\langle c{+}a \rangle$

pyramidal slip (Peierls barrier) under opposing normal stresses [73]. Collectively, the literature indicates that accurate BE prediction in titanium alloys necessitates mixed-hardening constitutive models calibrated on reverse-loading sequences and supported by microstructure-resolved measurements of dislocation backstress, twin/detwin kinetics, and α/β interface constraints under relevant strain-rate and temperature conditions [81, 83].

2.4 Summary

The current literature has yet to provide a comprehensive understanding of the effects of loading direction, temperature, and strain-rate on the Bauschinger effect. Specifically, it lacks insights into the characterisation of the Bauschinger effect in relation to the increasing number of load cycles and the roles of the deformation mechanisms: slip and twinning, that contribute to this phenomenon. Additionally, the literature does not adequately address how backstress contributes to the Bauschinger effect. Moreover, there is a noticeable gap in information regarding how residual stress accumulates within the material during reverse loading experiments.

Therefore, this research is inspired by the existing gaps in the current literature to develop a deeper understanding of the Bauschinger effect. It investigates the Bauschinger effect in forged Ti-6Al-4V under uniaxial fatigue loading, with a focus on the tension-compression and compression-tension load sequences as the number of load cycles increases. This study characterises the response of the

Bauschinger effect under different temperatures and strain-rates. Furthermore, it aims to enhance the understanding of the role of kinematic backstress in the Bauschinger effect. Additionally, this research explores the microstructural mechanisms that give rise to the macroscopic response of the material under uniaxial loading in both directions, including the roles of deformation mechanisms, such as slip and twinning, in the Bauschinger effect. As these deformation pathways are the underlying mechanisms responsible for the backstress, which is responsible for the bulk Bauschinger behaviour of the material. Moreover, the study examines how residual stress accumulates within the material during reverse loading experiments. Overall, this work adopts a multi-length-scale approach that links macroscopic cyclic behaviour to microscopic deformation features, which collectively contribute to the observed measured Bauschinger response of the material.

The following chapters first outline the as-received forged Ti-6Al-4V microstructure, detailing grain orientation, phase distribution, and texture. The next chapter examines how load direction affects the Bauschinger response during tension-compression and compression-tension cycling at low strain rates. This is followed by an exploration of the combined impacts of elevated temperature and load direction, as well as the effects of increasing strain rate and load direction. Throughout these studies, the Bauschinger response and related kinematic backstress are characterised based on the number of load cycles. Interrupted tests are employed to evaluate microstructural evolution with increasing load cycles, focusing on slip propensity (via Schmid factor), twinning mechanisms contributing to the Bauschinger effect, and measuring residual stress accumulation.

3 | Introduction to the As-received Material

The material received is a forged Ti-6Al-4V cross-rolled plate supplied by Rolls-Royce plc. Due to the confidentiality surrounding their manufacturing process, the supplier did not provide detailed information about the rolling directions. Therefore, a geometric plate coordinate system has been established. The longitudinal direction (LD) is defined as the longest in-plane dimension of the plate, the transverse direction (TD) is the in-plane direction that is perpendicular to the LD, and the normal direction (ND) is the through-thickness direction.

Specimens were machined with their axes aligned parallel to the LD. The specimens are shaped like a cylindrical dog-bone, as illustrated in Figure 3.1. The gauge section of each specimen, which is the region of primary interest, has a diameter of 3 mm and a height of 3 mm. Each end of the specimen features a 12 mm long thread, allowing for a secure connection to the test rig when fastened tightly with M6 nuts.

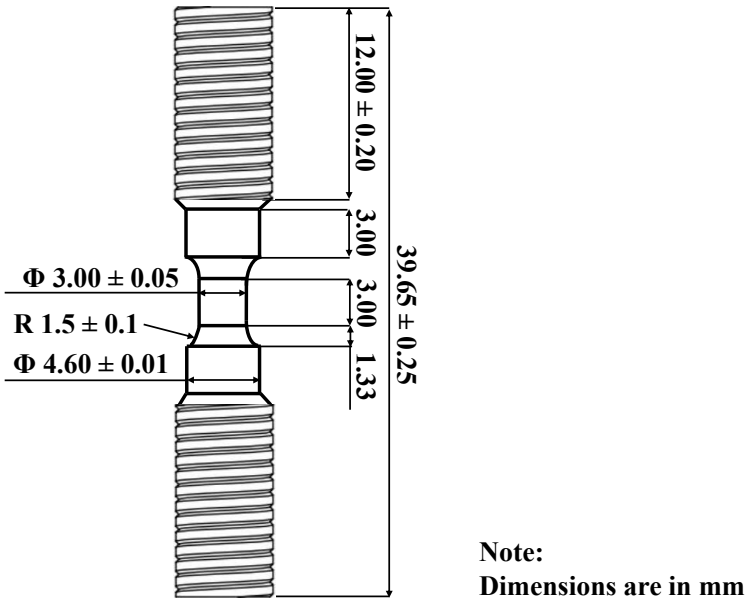


Figure 3.1: Geometry of the dog-bone specimen used to conduct reverse loading.

3.1 Microstructure of the as-received material

Characterisation of the microstructure, including grain size, phases, texture, twin boundary length (shown in the workable chapters), and Schmid factor (shown in the workable chapters), of the material, was conducted using Electron Backscatter Diffraction (EBSD). The following sub-section explains the specimen preparation procedure for the EBSD.

3.1.1 Specimen preparation for EBSD

The as-received specimen was sectioned, as shown in Figure 3.2, through the centre (X-Z plane), to prepare it for polishing and subsequent EBSD scanning. The sectioned specimen underwent a standard polishing procedure based on [89, 90]. Further, the polished mount was inserted and tilted at a 70° angle in a JEOL JSM-IT800 Schottky Field Emission Scanning Electron Microscope (FE-SEM), which is equipped with an EBSD detector. The microscope operated at an accelerating voltage of 20 kV and a probe current of 30 nA.

Electron backscatter diffraction (EBSD) mapping is performed on the sectioned plane of the sample, as shown in Figure 3.2, which is perpendicular to the axial load, using a step size of 0.15 μm.This sampling interval provides a sufficient number of data points to achieve the spatial resolution necessary for precise characterisation of intragranular deformation. A subsequent analysis of microstructural characteristics, such as phase quantification, texture of the material, twinning ac-

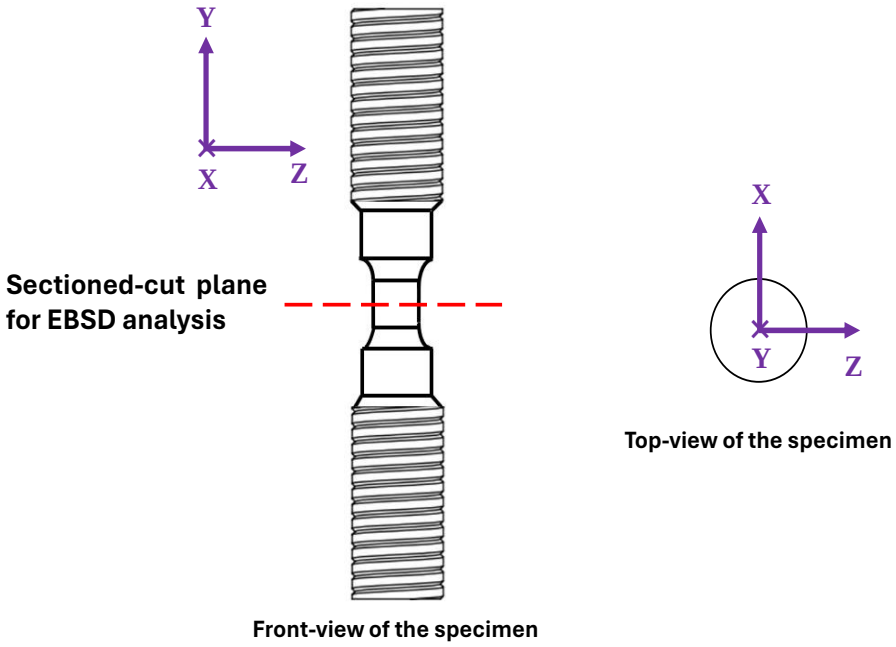


Figure 3.2: Sectioned specimen for EBSD analysis. During the test, the load was applied along the Y-direction.

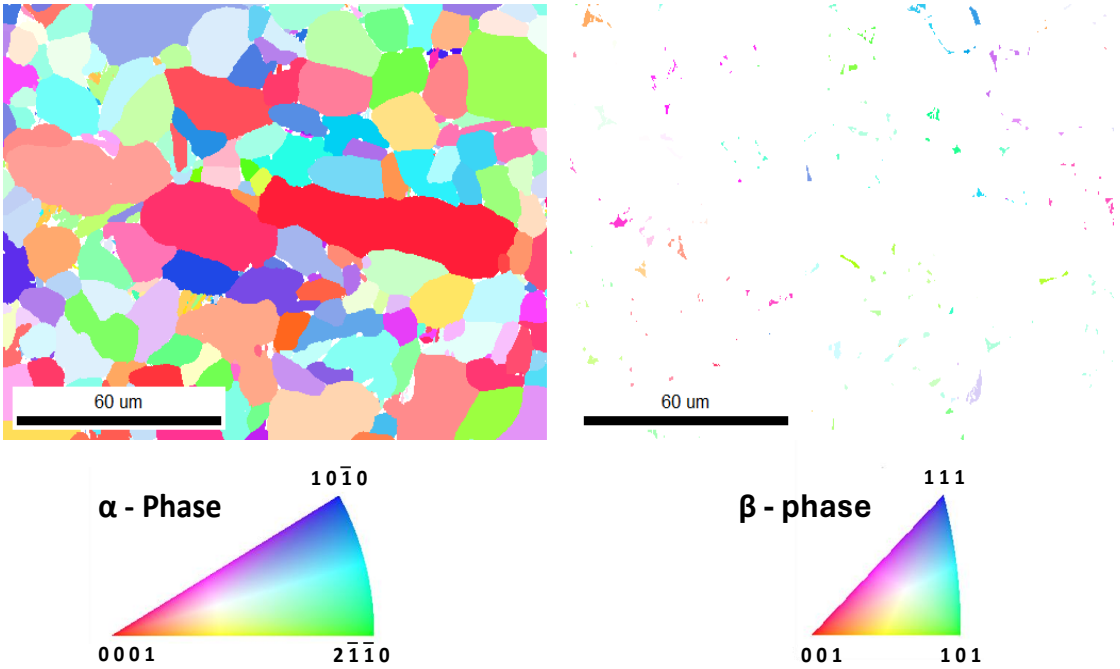


Figure 3.3: α (HCP) and β (BCC) IPF orientation maps of forged Ti-6Al-4V; colours indicate crystallographic orientation using the standard OIM IPF key, with colour changes between grains representing orientation differences within each phase.

tivity, and evolution of Schmid factor, in the EBSD data was conducted using EDAX OIM analysis software [91]. This revealed an average grain size, reported as mean grain perimeter, of approximately $17 \pm 2\,\mu$m in the as-received specimen. This measurement was taken from the grain-boundary image, as shown in Figure 3.4, using ImageJ. The pixel-to-length calibration was established using the embedded scale bar in micrometers in the micrograph. Individual grains were outlined, and their perimeters were measured. The reported grain size reflects the mean perimeter calculated across all measured grains. Each diffraction pattern was indexed using a maximum of nine Kikuchi bands for both the α and β phases, thereby minimising orientation-determination error. The scanned area measured $160\,\mu\text{m} \times 120\,\mu\text{m}$, capturing on the order of 10^2 grains, a similar number to previous studies [92–97]. Additionally, the IPF maps were coloured using the standard OIM IPF keys for α (HCP) and β (BCC), as illustrated in Figure 3.3. In each map, variations in colour among grains indicate that grains are oriented differently relative to one another within that phase, as defined by the relevant IPF key. Phase-specific IPF maps were extracted in EDAX OIM Analysis by applying phase masking, allowing for the separate export of α-only and β-only IPF maps. This separation is essential to avoid ambiguity, as the IPF colour keys vary between HCP and BCC crystal structures.

3.1.2 Phase-map of forged Ti-6Al-4V

The EBSD data analysis reveals an area fraction of approximately 98% of α and 2% of β present in forged Ti-6Al-4V, as shown in Figure 3.4. The β phase is present on the grain boundaries.

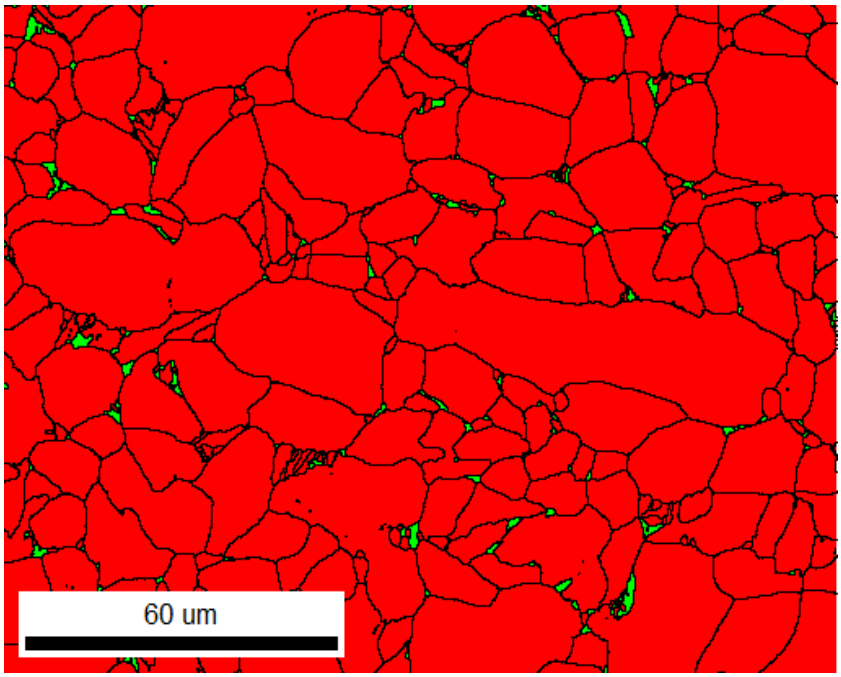


Figure 3.4: EBSD phase map quantifying area fractions shows that the α phase (red) comprises 98% and the β phase (green) 2% in the as-received forged Ti-6Al-4V specimen, with the β phase located at grain boundaries.

3.1.3 Texture of α and β phases present in forged Ti-6Al-4V

The pole figures for the crystallographic planes in the α and β phases of the as-received material are presented in Figure 3.5. The specimen's X and Z directions are indicated, with Y located at the centre of each pole figure. In the α phase, the (0002) plane is basal, $(10\bar{1}0)$ is prismatic, while $(10\bar{1}1)$, $(20\bar{2}1)$, and

$(11\bar{2}2)$ are classified as pyramidal planes.

In the as-received α phase, the (0002) pole figure reveals a maximum near the Y region, with the peak slightly off-centre, indicating mild tilting of the basal poles. The $(10\bar{1}0)$ prismatic pole figure shows intensity aligned along the X-Z axes, exhibiting a symmetric distribution. The pyramidal pole figures $(10\bar{1}1)$, $(20\bar{2}1)$, and $(11\bar{2}2)$ present broad lobes in symmetric pairs about the X-Z axes rather than a sharp orientation. Overall, the α phase displays a weak-to-moderate basal texture (max $\approx$ 2.56 MRD) alongside symmetric lobe distributions in the prismatic and pyramidal pole figures.

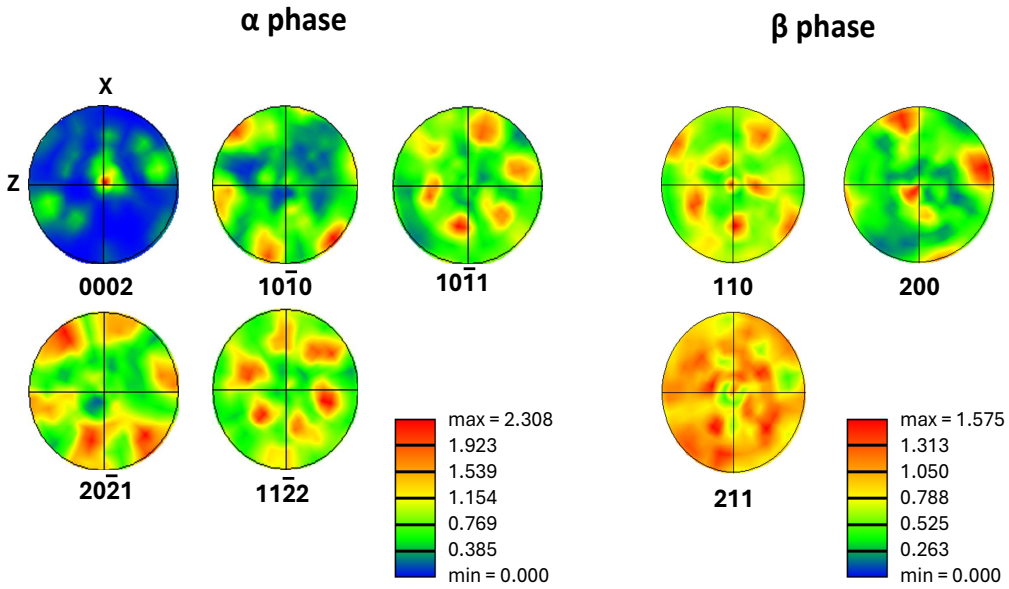


Figure 3.5: Pole figures of crystallographic planes in the α and β phases of the forged Ti-6Al-4V alloy in the as-received specimen are presented. The load is applied along the Y-axis. The α phase demonstrates a weak-to-moderate texture, while the β phase shows a weak, diffuse texture.

The β phase shows a weak, diffuse texture with a maximum of about 1.58 MRD. The (110) pole figure displays broad, low-intensity lobes without a

central maximum, while the (200) pole figure lacks a distinct peak, indicating a non-preferred orientation. Additionally, the (211) pole figure is diffuse, confirming the absence of a strong texture component.

3.1.4 Error and uncertainty assessment for EBSD measurements

The EBSD measurements contain uncertainties associated with specimen preparation, surface quality, indexing accuracy, step size, scan area, grain statistics, phase identification, grain-size measurement, and orientation-based quantities such as texture and Schmid factor. Since EBSD is a surface-based technique, the measured microstructure represents the polished sectioned plane and may not fully capture three-dimensional microstructural variation [98, 99]. The EBSD scan was performed with a step size of $\Delta x = 0.15$ μm. The spatial resolution of the map is therefore limited by the step size, and the number of points across a grain can be estimated as:

$$N_g \approx \frac{D}{\Delta x}, \tag{3.1}$$

where D is a characteristic grain size and Δx is the EBSD step size. A smaller step size improves the resolution of intragranular orientation gradients and boundary detection, whereas a larger step size may under-sample small grains, narrow β-phase regions, or local deformation features [98].

For the present EBSD analysis, the step size was taken as $\Delta x = 0.15$ μm.

The scan area was 160 μm $\times$ 120 μm. The spatial uncertainty associated with locating a feature or boundary in the EBSD map was taken as approximately one pixel, corresponding to ± 0.15 μm.

For measurements based on point-to-point distances or boundary locations, the half-step uncertainty may also be considered:

$$\pm\frac{\Delta x}{2} = \pm 0.075 \ \mu\text{m}. \tag{3.2}$$

The β-phase fraction was approximately $f_\beta = 2\% = 0.02$. This small phase fraction is sensitive to indexing quality, phase segmentation, and the treatment of non-indexed points. Therefore, the statistical counting uncertainty was calculated from the number of indexed pixels, while a larger practical uncertainty was considered to account for phase misindexing and segmentation effects.

The number of EBSD sampling points along the scan width is approximately:

$$N_x = \frac{160}{0.15} = 1067. \tag{3.3}$$

The number of EBSD sampling points along the scan height is approximately:

$$N_y = \frac{120}{0.15} = 800. \tag{3.4}$$

Therefore, the total number of sampled points is approximately: The total number of measurement points was $N_{\text{total}} = N_x N_y = 1067 \times 800 \approx 8.54 \times 10^5$. The area represented by each EBSD pixel is: The pixel area was $A_{\text{pixel}} = \Delta x^2 = 0.15^2 =$

0.0225 μm^2. The total mapped area was $A_{\text{map}} = 160 \times 120 = 19200$ μm^2. For a characteristic grain size of $D = 5$ μm, the number of EBSD points across a grain is:

$$N_g \approx \frac{D}{\Delta x} = \frac{5}{0.15} = 33.3. \tag{3.5}$$

Thus, a 5 μm grain was sampled by approximately $N_g \approx 33$ points. points across its diameter. This indicates that grains of this size are well resolved. However, features approaching 1 μm would only be sampled by:

$$N_g \approx \frac{1}{0.15} = 6.7,$$

or approximately 7 points across the feature, making boundary location and phase segmentation more sensitive to the selected step size.

The reported grain size was obtained from grain-boundary images using ImageJ and expressed as the mean grain perimeter. For n measured grains, the mean perimeter is:

$$\bar{P} = \frac{1}{n} \sum_{i=1}^{n} P_i, \tag{3.6}$$

and the scatter can be represented using the standard deviation:

$$s_P = \sqrt{\frac{1}{n-1} \sum_{i=1}^{n} \left(P_i - \bar{P}\right)^2}. \tag{3.7}$$

The uncertainty in the mean perimeter can be estimated from the standard

error:

$$\Delta \bar{P} = \frac{s_P}{\sqrt{n}}. \tag{3.8}$$

In addition to this statistical uncertainty, the spatial uncertainty from boundary placement contributes to the measured perimeter. Since the EBSD step size was 0.15 μm, the boundary-position uncertainty was taken as approximately ± 0.15 μm.

Therefore, grain-size and perimeter measurements are affected by both statistical scatter in the measured grains and spatial uncertainty from EBSD step size and boundary reconstruction.

The phase fraction was calculated from the EBSD phase map. For a phase containing N_{phase} indexed pixels out of a total of N_{total} indexed pixels, the area fraction is:

$$f_{\text{phase}} = \frac{N_{\text{phase}}}{N_{\text{total}}}. \tag{3.9}$$

For the β phase, $f_\beta = 0.02$. Using $N_{\text{total}} = 8.54 \times 10^5$, the number of β-phase pixels was approximately $N_\beta = f_\beta N_{\text{total}} = 0.02 \times 8.54 \times 10^5 \approx 1.71 \times 10^4$.

The statistical counting uncertainty in the phase fraction can be estimated as:

$$\Delta f_\beta = \sqrt{\frac{f_\beta(1 - f_\beta)}{N_{\text{total}}}}. \tag{3.10}$$

$$\Delta f_\beta = 1.5 \times 10^{-4}.$$

This corresponds to an absolute phase-fraction uncertainty of $\Delta f_\beta = 0.015\%$.

Therefore, the statistical uncertainty in the measured β-phase fraction is small. However, the practical uncertainty is expected to be larger because of misindexing, non-indexed points, pattern quality, phase segmentation, and overlap between weak α and β signals. For this reason, a practical β-phase fraction uncertainty of approximately $\pm$0.2-0.5 percentage points was adopted.

Orientation uncertainty affects texture, twin-boundary identification, and Schmid-factor calculations. The Schmid factor for a given slip system is defined as [100]:

$$m = \cos\phi \cos\lambda, \tag{3.11}$$

where ϕ is the angle between the loading direction and the slip-plane normal, and λ is the angle between the loading direction and the slip direction. Therefore, uncertainty in crystallographic orientation, loading-axis alignment, or phase indexing can affect the calculated Schmid factor. A practical EBSD orientation uncertainty of approximately $\pm 0.5°$–$1°$ was adopted for indexed points with good pattern quality. Larger local uncertainty may occur near grain boundaries, highly deformed regions, or low-confidence indexed pixels.

Overall, the EBSD measurements had a spatial resolution limited by the 0.15 μm step size, giving a boundary-position uncertainty of approximately $\pm$0.15 μm. The scan contained approximately 8.54×10^5 sampling points over an area of 19200 μm^2. For a 2% β-phase fraction, the statistical phase-fraction uncertainty was approximately 0.015%, but the practical uncertainty was taken as approximately $\pm$0.2-0.5 percentage points because phase segmentation and indexing errors

dominate over counting statistics. Therefore, the main quantitative uncertainties in the EBSD measurements came from step size, boundary reconstruction, phase indexing, scan-area representativeness, and orientation accuracy.

4 | Investigating the affect of Load Direction on the Bauschinger Response

4.1 Overview

In this chapter, the behaviour of forged Ti-6Al-4V is investigated when subjected to reverse loading in a quasi-static environment at room temperature. The material's response during reverse loading is observed in two distinct sequences: (i) cycles initiated in tension, in which the loading alternates between tension and compression, and (ii) cycles initiated in compression, in which the loading alternates between compression and tension. The Bauschinger effect is characterised, and the kinematic backstress behaviour is analysed in both loading sequences until material failure. To understand the microstructural evolution and the underlying causes of the Bauschinger effect under these test conditions, the reverse loading experiments are interrupted after each loading step, up to the second load cycle. This interruption allows for a detailed analysis of twin evolution, the distribution of the Schmid factor within the crystallographic planes using Electron Backscattered Diffraction (EBSD), and the measurement of residual stress accumulation using synchrotron X-ray diffraction.

4.2 Experimental methodology

Uniaxial reverse loading experiments were performed at room temperature on the cylindrical dog-bone-shaped specimens with a diameter of 3 mm and a gauge length of 3 mm, as shown in Figure 3.1. The tests were conducted using a Zwick Roell Z050 machine, as shown in Figure 4.2, capable of delivering loads up to ±50 kN. As a quasi-static experiment, the loading speed was set to $\pm 0.006\,\mathrm{mm\,s^{-1}}$. The video extensometer was utilised to measure the axial strain within the specimen through *in situ* Digital Image Correlation (DIC). Importantly, this video extensometer (Imetrum device: IMT-CONTR-VG5-ADV) enabled the load sequence to be strain-controlled.

Engineering stress was calculated from the force measured by the test machine load cell divided by the specimens initial cross-sectional area. Engineering strain data was measured from post-processing DIC of the video extensometer images, as discussed in section 4.3.

The experimental approach included two loading sequences: tension load followed by compression load steps (henceforth referred to as the T-C load sequence) and compression load followed by tension load steps (henceforth referred to as the C-T load sequence). In the T-C load sequence, specimens were initially subjected to tensile loading, reaching a target strain of +5%, before being reversed to compressive loading at a target strain of -4.6%. Conversely, in the C-T load sequence, specimens began with compressive loading, targeting -5%, and were sub-

sequently reversed to tensile loading at +4.6%. In other words, regardless of load sequence, the cycling protocol was identical in amplitude: each cycle consisted of a loading step to a target strain magnitude of 5%, followed by a reverse loading step to a target strain magnitude of 4.6%. This alternation between 5% and 4.6% was repeated for subsequent cycles, with the sign given by the loading mode ('+' in tension and '-' in compression).

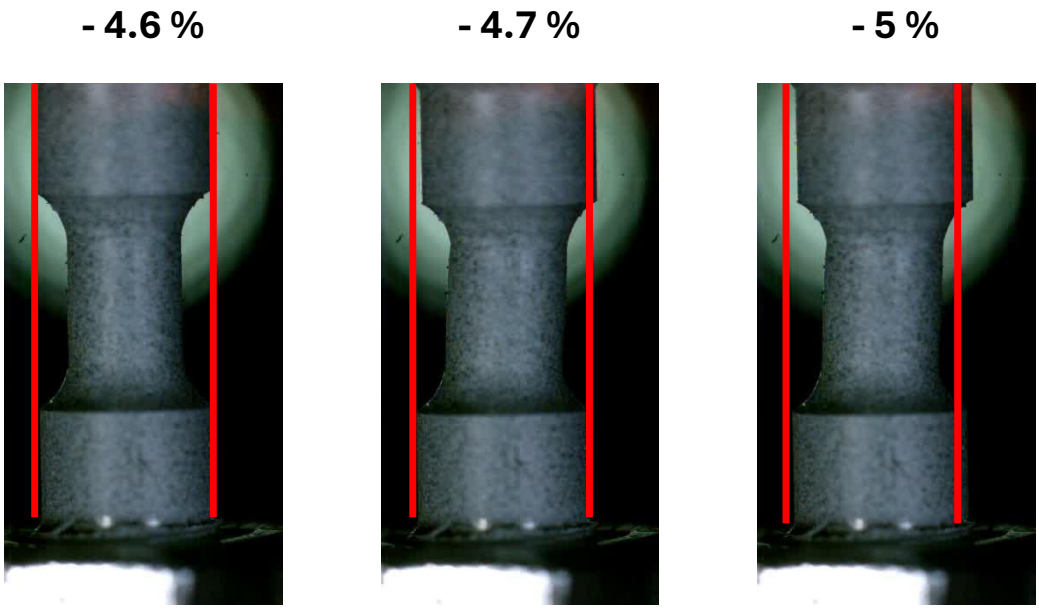


Figure 4.1: Representative camera images of the specimen during reverse compression at reverse strain levels of -4.6%, -4.7%, and -5%. The red vertical lines provide a visual reference for axial alignment. The specimen remains approximately straight at -4.6%, whereas specimen tilt becomes increasingly visible as the reverse compressive strain increases to -4.7% and -5%. These images support the interpretation that compression-related instability becomes more pronounced at higher reverse compressive strain levels.

The purpose of these strain levels is to ensure that the material exhibits sufficient plasticity and can withstand a good number of load cycles. The nature of the experiments also allows for a comprehensive analysis of the Bauschinger effect as loading cycles progress. Initial tests utilising a symmetric strain range of

±5% resulted in premature failures of some specimens, frequently occurring by the second cycle. During these tests, the compressive reversals displayed indications of instability associated with compression in the dog-bone geometry, as shown in Figure 4.1. In this context, compression-related instability signifies the disruption of a consistent axial compressive deformation mode during reverse loading, leading the specimen to begin deforming through bending rather than maintaining a straight, axial compression.

This behaviour was noted as slight bending of the gauge section during the compressive phase of the cycle. It was not linked to significant misalignment of the testing setup, as such an issue would be expected to influence all strain ranges similarly. Instead, it was interpreted as an instability dependent on the level of strain, driven by the combination of high reverse compressive strain, dog-bone geometry, end constraints, and minor unavoidable eccentricities in the loading path.

At higher levels of reverse strain, both the compressive displacement and load requirements increased. Under these circumstances, minor alignment sensitivities and fixture constraints can become exaggerated, leading the specimen to stray from uniform axial compression. This deviation can result in bending, localised stress concentrations, and premature failure, rendering the measured stress-strain response less reflective of uniform axial loading. This instability was observed even when the reverse compressive strain was decreased to -4.7%. However, when the reverse compressive strain was further reduced to -4.6%, stable and repeatable

axial cycling was successfully attained. This suggests that, while the lower strain range did not eliminate all alignment sensitivity from the apparatus, it did keep the specimen beneath the practical threshold at which bending and non-uniform compression became evident.

As a result, the magnitude of the reverse compressive strain was set at -4.6% to guarantee stable cyclic reverse loading while still inducing significant reverse plasticity, which is essential for assessing the Bauschinger effect. In these experiments, a complete load cycle is characterised as the procedure in which the applied reverse load on the specimen begins at zero stress and ultimately returns to zero stress.

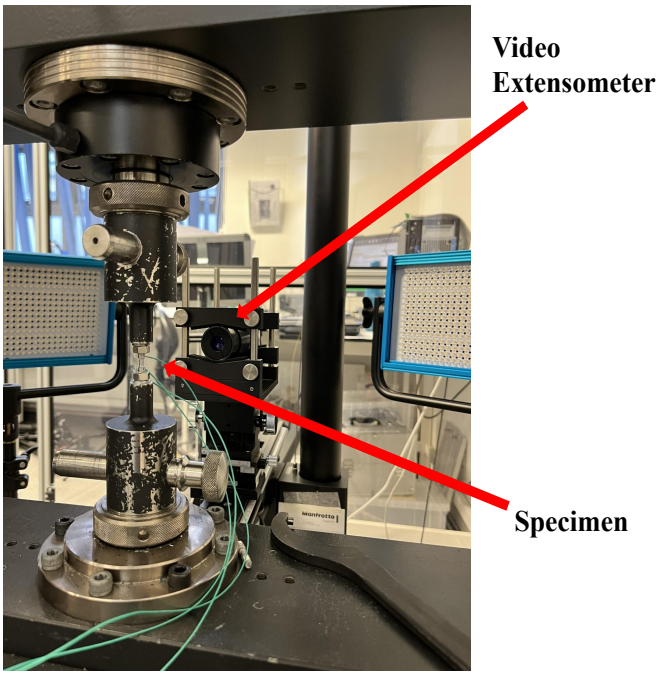


Figure 4.2: Set-up to conduct reverse loading under quasi-static conditions at room temperature. The video extensometer is utilised to measure strain within the speckled specimen through DIC.

4.3 Digital Image Correlation (DIC) for strain measurement

Digital Image Correlation (DIC) is a well-established technique for obtaining high-fidelity, full-field strain measurements on test specimens [101]. Reliable correlation requires a high-contrast speckle pattern on the region of interest, as shown in Figure 4.3. In this study, the pattern was produced by a two-step in-house procedure. First, the specimen surface was coated with a very thin, uniform layer of matte white, water-based acrylic paint to provide a reflective background. This base coat was then overlaid with a fine, stochastic spatter of black acrylic paint applied through a low-pressure airbrush, creating the requisite speckle distribution. The method has consistently delivered patterns with adequate spatial resolution and grey-scale contrast for accurate DIC analysis.

Table 4.1: DaVis DIC parameters for low strain-rate reverse loading.

Parameter	**Low strain-rate reverse loading**
Image properties: Image scale (pixels/mm)	159.15
Time-series settings: Correlation mode	Relative to first
Displacement-calculation settings: Subset size (pixels)	30
Displacement-calculation settings: Step size (pixels)	18
Calculation mode:	Gaussian 6^{th}-order spline
Virtual extensometer characteristics: Strain formulation	Engineering strain

A video extensometer was utilised to measure the axial strain within the specimen through *in situ* Digital Image Correlation (DIC). Additionally, the im-

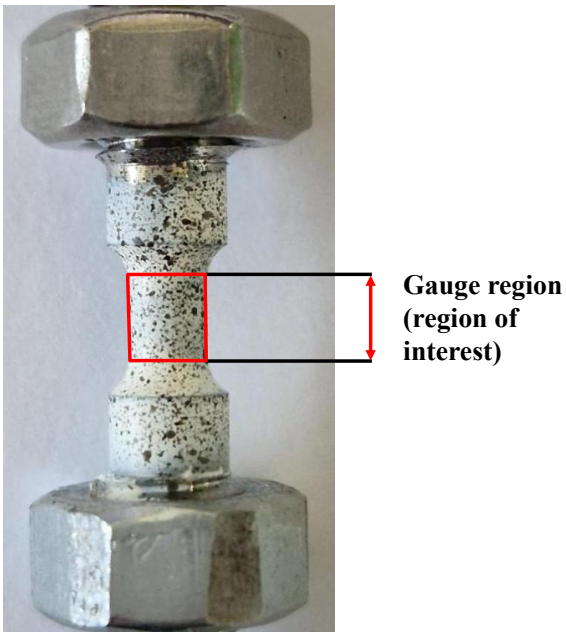


Figure 4.3: The speckled specimen was aligned with the experimental test-rig, highlighting the gauge region, which is the area of interest.

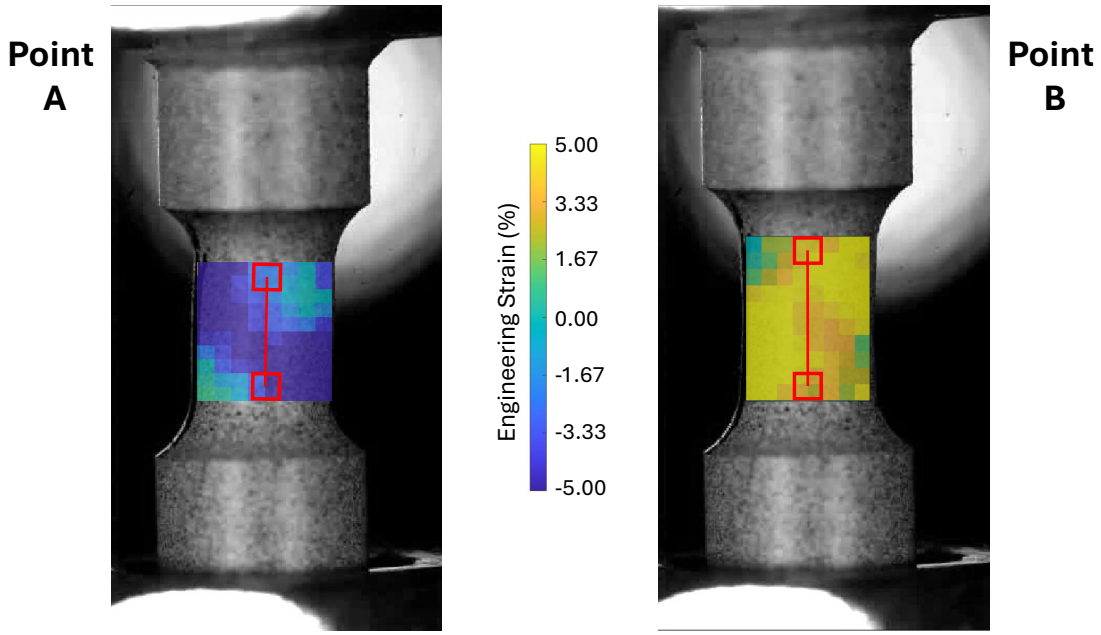


Figure 4.4: Spatially resolved DIC strain maps of the specimen gauge region highlighting non-homogeneous strain localisation. Strain maps correspond to points A and B on the hysteresis loop of the engineering stress-strain response of the material (see Figure 4.5(a)). The overlaid virtual extensometer (in red colour) defines the gauge length used to compute the average engineering strain.

ages captured by the extensometer were analysed using DaVis DIC software [102–104]. The parameters used in the DaVis software to calculate the strain field of the specimen presented in Table 4.1. The image scale provides the calibration factor required to convert measured displacements from pixels to physical units. The correlation mode was set to Relative to first, such that each deformed image is correlated with the initial reference image, yielding displacements and strains relative to the undeformed configuration throughout the reverse-loading sequence. The subset size defines the interrogation window used for correlation; a larger subset improves correlation robustness and reduces sensitivity to image noise but reduces spatial resolution and may smooth local strain gradients. The step size specifies the spacing between neighbouring subset centres and therefore controls the spatial sampling density of the displacement field, with smaller step sizes producing a denser displacement/strain map at increased computational cost. The calculation mode (Gaussian 6^{th}-order spline) governs the interpolation/smoothing and differentiation procedure used to obtain strains from displacement gradients, providing improved numerical stability and reduced noise amplification during differentiation. Finally, the strain formulation was set to engineering strain, consistent with the strain definition used in the global mechanical analysis. Examples of outputs derived from the DIC data display spatially resolved DIC strain maps of the specimen's gauge region, emphasising the non-homogeneous localisation of strain. These strain maps correspond to points A and B on the hysteresis loop of the engineering stress-strain response of the material (see Figure 4.5(a)). The overlaid virtual extensometer delineates the gauge length employed for computing

the average engineering strain.

4.4 Error and uncertainty assessment for reverse loading tests

The uncertainty in the experimental stress-strain response was estimated from force measurement, specimen diameter measurement, and DIC-based strain measurement. These uncertainties affect the measured engineering stress-strain response.

Engineering stress was calculated from the measured force divided by the initial cross-sectional area:

$$\sigma_{\text{eng}} = \frac{F}{A_0} \tag{4.1}$$

For a circular specimen, the initial cross-sectional area is:

$$A_0 = \frac{\pi d^2}{4} \tag{4.2}$$

The relative uncertainty in engineering stress was estimated as [105, 106]:

$$\frac{\Delta\sigma_{\text{eng}}}{\sigma_{\text{eng}}} = \sqrt{\left(\frac{\Delta F}{F}\right)^2 + \left(\frac{\Delta A_0}{A_0}\right)^2} \tag{4.3}$$

Since the area depends on the square of the diameter:

$$\frac{\Delta A_0}{A_0} = 2\frac{\Delta d}{d} \tag{4.4}$$

The numerical values used in the uncertainty calculation were selected from the experimental configuration and from typical values reported for calibrated mechanical testing and DIC measurements. The specimen gauge diameter was taken as $d = 3.0$ mm, consistent with the small cylindrical gauge geometry used in the tests. The diameter measurement uncertainty was taken as $\Delta d = \pm 0.005$ mm, corresponding to the resolution and reading uncertainty of a micrometre measurement on a small cylindrical specimen.

The load-cell force uncertainty was taken as $\Delta F/F = \pm 0.5\%$, corresponding to a Class 0.5 force-measuring system, where the permissible relative force indication error is approximately $\pm 0.5\%$ of the indicated force. The DIC displacement uncertainty was taken as 0.01 pixels, consistent with commonly reported DIC displacement resolution under controlled imaging and correlation conditions [107]. The calibrated image scale was taken as 25 μm/pixel, based on the imaging magnification used for the test. The virtual extensometer gauge length was taken as $L_0 = 3.0$ mm, corresponding to the gauge length selected for averaging the DIC displacement field.

The practical DIC-based strain uncertainty was taken as $\pm$83-500 $\mu\varepsilon$. The lower value comes from the ideal displacement-resolution calculation, while the upper value accounts for additional experimental effects such as speckle quality, lighting variation, image calibration, subset size, step size, strain smoothing, and local strain gradients.

For the present assessment, $d = 3.0$ mm and $\Delta d = \pm 0.005$ mm. Therefore:

$$\frac{\Delta A_0}{A_0} = 2\frac{0.005}{3.0} = 0.0033 \approx 0.33\% \tag{4.5}$$

The load-cell force uncertainty was $\frac{\Delta F}{F} = \pm 0.5\% = 0.005$. Therefore, the combined relative uncertainty in engineering stress is:

$$\frac{\Delta \sigma_{\text{eng}}}{\sigma_{\text{eng}}} = \sqrt{(0.005)^2 + (0.0033)^2} = 0.0060 \approx 0.6\%$$

Thus, the engineering stress uncertainty in the mechanical tests was estimated as $\Delta \sigma_{\text{eng}} \approx \pm 0.6\%$. At a stress level of 900 MPa, this corresponds to $\Delta \sigma_{\text{eng}} = 0.006 \times 900 = 5.4$ MPa. Thus, $\sigma_{\text{eng}} = 900 \pm 5.4$ MPa.

Engineering strain was measured using the video extensometer and DIC:

$$\varepsilon_{\text{eng}} = \frac{L - L_0}{L_0} \tag{4.6}$$

The DIC displacement uncertainty was taken as 0.01 pixels. Using a calibrated image scale of 25 μm/pixel, the displacement uncertainty is $\Delta u = 0.01 \times 25 = 0.25$ μm. For a virtual extensometer gauge length of $L_0 = 3.0$ mm, the corresponding strain uncertainty is:

$$\Delta \varepsilon_{\text{DIC}} = \frac{\Delta u}{L_0} = \frac{0.25 \times 10^{-3}}{3.0} = 8.33 \times 10^{-5} = 83\ \mu\varepsilon \tag{4.7}$$

Therefore, the DIC-based average strain uncertainty was $\Delta \varepsilon_{\text{DIC}} \approx \pm 83\ \mu\varepsilon$. Over-

all, the mechanical tests had an estimated engineering stress uncertainty of approximately ±0.6%, corresponding to approximately ±5.4 MPa at a stress level of 900 MPa. The ideal DIC-based strain uncertainty was estimated as ±83 $\mu\varepsilon$, while the practical DIC-based average strain uncertainty was taken as ±83-500 $\mu\varepsilon$. Therefore, the main quantitative uncertainty in the experimental stress-strain response came from the combined effect of force measurement and specimen diameter measurement, while the strain uncertainty was mainly governed by DIC resolution, calibration, and the selected virtual extensometer gauge length.

4.5 Experimental results

The engineering stress-strain response under reversed loading was analysed for both load sequences, as shown in Figure 4.5. In the first loading step, the specimen was subjected to monotonic loading until a target plastic strain of 5% was achieved. The loading direction was then reversed, and loading continued in the reverse direction until a target plastic strain of 4.6% was reached. After this, the loading direction was reversed again. In this context, one complete load cycle is defined as a sequence in which the applied cyclic load on the specimen starts at zero stress and returns to zero stress after loading in both tension and compression. For example, if the loading commences in tension, is unloaded to zero stress, then is reversed into compression and subsequently unloaded back to zero stress, this is considered one complete cycle (and vice versa for compression followed by tension). Thus, two successive load steps (one in tension and one in compression) constitute

a single load cycle. This cyclic process was repeated, resulting in a hysteresis in the stress-strain response until the specimen ultimately failed. It is interesting to note that the failure occurred during the tension load step in both cases after necking.

The strain-time histories were examined around the turning points in the loading curves (Figure 4.5), particularly near load reversal. To assess the origin of the rounded strain response, the corresponding machine signals were examined over the same time interval. In particular, the crosshead displacement-time and load-time histories were compared with the strain-time histories. This comparison showed that the crosshead displacement and load also changed smoothly through reversal, rather than undergoing an ideal abrupt transition. The smoothing observed in the strain-time histories is therefore attributed mainly to the finite response of the test system during load reversal. This interpretation is supported by Zhao et al., who showed that servovalve and actuator dynamics can influence displacement-controlled testing and affect the achieved actuator response during dynamic or reversed loading conditions [108]. Similarly, Sivaselvan et al. showed that hydraulic actuator force control is affected by system compliance and displacement compensation, demonstrating that the measured force response can be influenced by the actuator-control system and the compliance of the testing arrangement [109].

Although intrinsic material effects cannot be completely ruled out, the available evidence suggests that they were not the dominant cause of the rounding

observed here. Similar smoothing was observed in the crosshead displacement and load histories, indicating that the reversal was also smoothed by the test system. This interpretation is consistent with studies showing that actuator dynamics, servovalve response, system compliance, and displacement compensation can influence measured responses in servo-hydraulic testing systems [108, 109].

Therefore, the rounded turning points in the stress-strain hysteresis loops are interpreted mainly as an experimental system effect associated with finite machine response during load reversal, rather than as direct evidence of intrinsic viscous material behaviour. Any intrinsic material contribution is considered secondary under the present testing conditions.

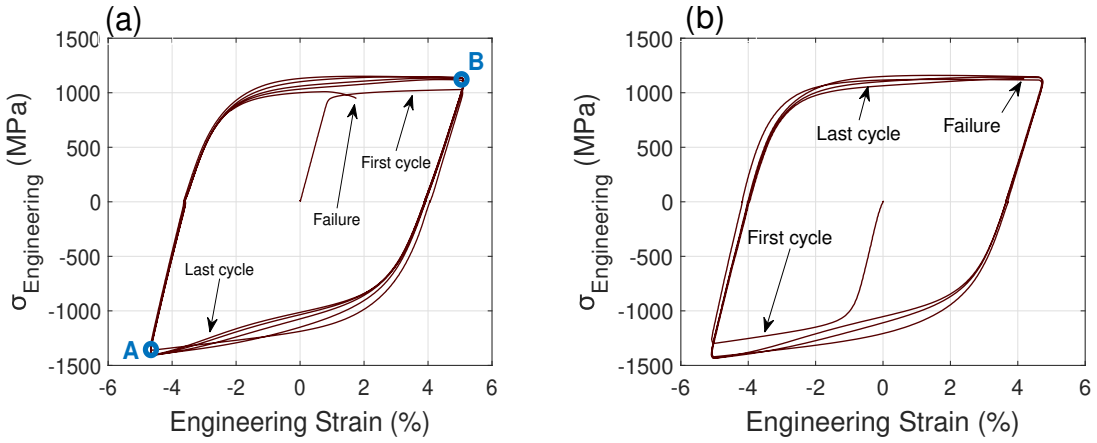


Figure 4.5: The engineering stress-strain response of forged Ti-6Al-4V under reverse loading during T-C load sequence (a), and C-T load sequence (b) was examined at controlled strain levels of 5% for the first load and 4.6% for the reverse load.

During the reverse loading, the plastic strain energy density and total strain energy density are calculated as illustrated in Figure 4.6. The total strain energy density, U_{total}, was determined as the area under the true stress-true strain curve

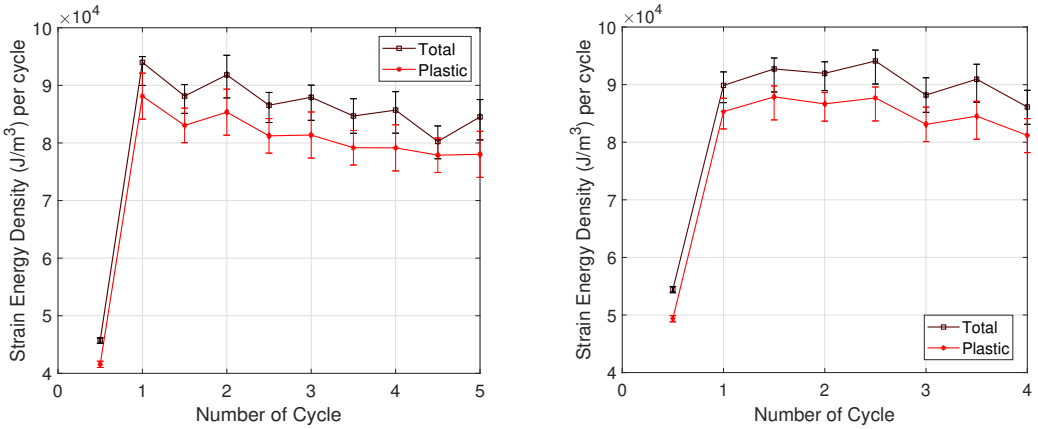


Figure 4.6: The total and plastic strain energy required by the material to deform during, T-C load sequence (left), C-T load sequence (right), are depicted. The black colour represents the total strain energy, while the red colour corresponds to plastic strain energy. Overall, in both cases, the strain energy density is observed to decrease. Additionally, it is noted that the strain energy density is smaller during tension load steps compared to that of compression load steps. The error in this data was calculated using the propagation of error method [105, 106] in light of motivation from assessing error in Chapter 4.4.

up to the maximum applied strain:

$$U_{\text{total}} = \int_0^{\varepsilon_{\max}} \sigma(\varepsilon)\, \mathrm{d}\varepsilon$$

where $\sigma(\varepsilon)$ is the true stress as a function of true strain ε, and $\varepsilon_{\max}$ is the maximum strain reached during loading.

The plastic strain energy density, U_{p}, was obtained from the area under the true stress-strain curve beyond the yield point:

$$U_{\text{p}} = \int_{\varepsilon_{y,0.2\%}}^{\varepsilon_{\max}} \sigma(\varepsilon)\, \mathrm{d}\varepsilon,$$

where $\varepsilon_{y,0.2\%}$ is the true strain at the 0.2% offset yield point. In this formulation, U_{p} represents the energy associated with plastic deformation, while the elastic

contribution is contained in the interval $0 \leq \varepsilon \leq \varepsilon_{y,0.2\%}$.

The conversion from engineering stress and strain to true stress and strain was performed using the following equations [12]:

$$\varepsilon_{\text{true}} = \ln(1 + \varepsilon_{\text{engineering}})$$

$$\sigma_{\text{true}} = \sigma_{\text{engineering}} (1 + \varepsilon_{\text{engineering}})$$

During the T-C loading sequence, there is a noticeable decrease in both the total and plastic strain energy density per cycle as the number of load cycles increases. This trend indicates that the material tends to soften with more load cycles.

In the initial loading step, where the material experienced only 5% strain, the strain increased to 9.6% in the first load cycle (load cycle 1). As a result, the strain energy density in load cycle 1 is almost double that of load cycle 0.5. From load cycle 1 onwards, it can be observed that the strain energy density fluctuates; specifically, the strain energy density is lower during tension loading steps compared to compression loading steps, and it continues to decrease overall. A similar trend is evident in the C-T loading sequence, where the strain energy density during compression loading steps is greater than that during tension loading steps. Even when comparing the first load step in the T-C loading cycle (load cycle 0.5), the strain energy density for the initial tension loading is smaller than that of the first compression loading step in the C-T loading cycle. Notably, to reach the same

target strain, the compression load steps required more mechanical work than the tension load steps. This asymmetry is consistent with the well-known non-Schmid behaviour of α-Ti: under compression, the unfavourable normal stress on $\frac{1}{3}\langle 11\bar{2}0\rangle$ screw dislocations constricts the core off the easy prismatic plane toward a compact pyramidal configuration, deepening the Peierls barrier and raising lattice friction; under tension, the opposite normal stress dilates the core back onto the prismatic plane, restoring low glide resistance [88, 110]. Consequently, the critical resolved shear stress for pyramidal $\langle c+a\rangle$ slip is greater in compression than in tension to achieve the same macroscopic strain [111, 112].

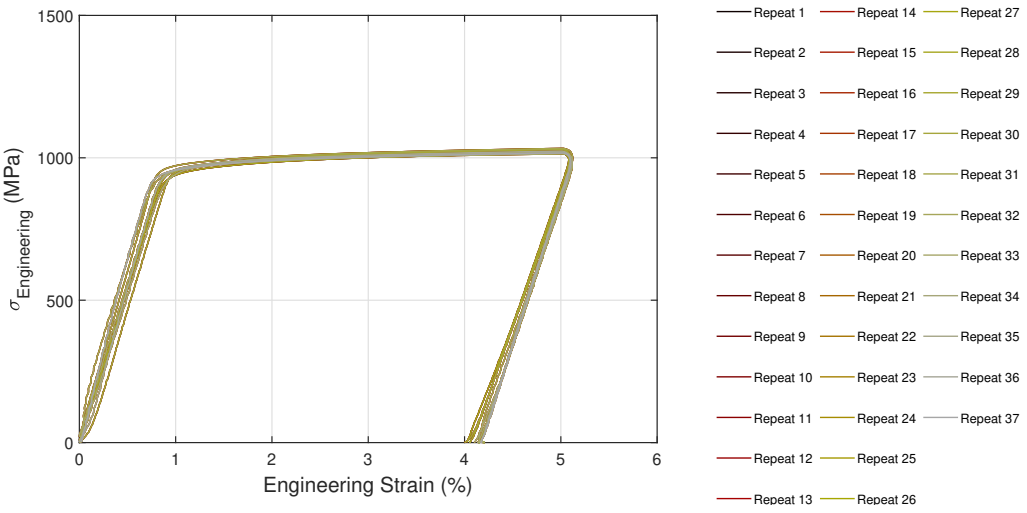


Figure 4.7: To assess the repeatability of the 0.2% effective yield stress at cycle 0.5 during the T-C loading sequence, the repeat stress-strain responses were examined. A total of 37 stress-strain curves for cycle 0.5 are presented. Of these, 33 curves were generated from three repeated full cyclic reverse-loading tests, with each complete test extending to 5.5 cycles, leading to 11 half-cycle yield-stress measurements, which resulted in $3 \times 11 = 33$ total measurements. Additionally, four curves were derived from interrupted tests conducted up to cycle 2. Therefore, the cycle 0.5 loading step contained a total of $33 + 4 = 37$ yield-stress measurements. The 0.2% effective yield stress for each curve was determined using the strain-offset method, and the mean yield stress and sample standard deviation were computed from these values. The same methodology was applied to the other common loading steps in the T-C and C-T loading sequences.

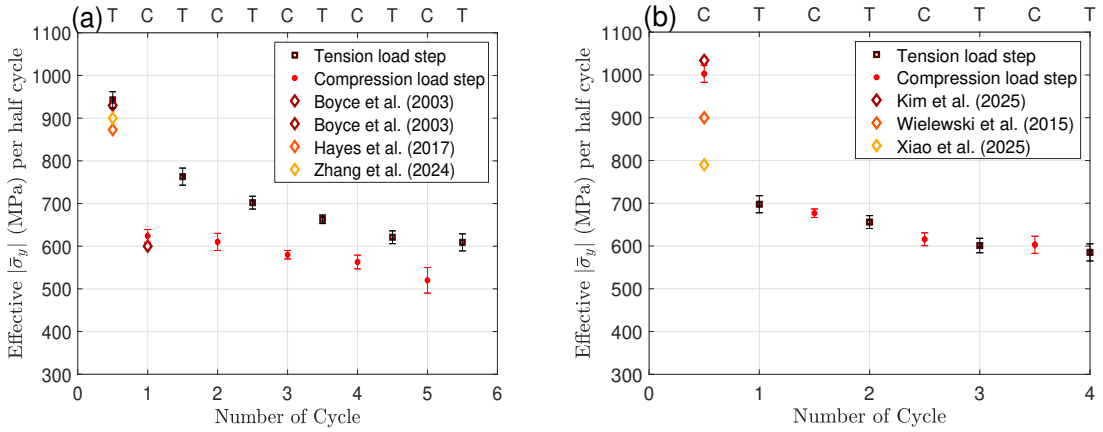


Figure 4.8: Behaviour of the 0.2% effective yield stress determined from the stress-strain curve at each loading step during both loading sequences: (a) T-C loading sequence and (b) C-T loading sequence. A significant Bauschinger effect is observed in both loading sequences. However, it persists during the T-C loading sequence but diminishes after the first loading cycle in the C-T loading sequence. For each loading step, the yield stress, $|\sigma_y|$, was averaged over repeated measurements, and the spread was quantified using the sample standard deviation, $S_{|\sigma_y|}$. The error bars therefore represent $|\bar{\sigma}_y| \pm S_{|\sigma_y|}$ [113].

Recent studies have used a 0.2% strain-offset method to quantify the Bauschinger effect by determining the yield stress at each loading step during successive loading cycles [47, 114]. In this method, the yield stress for a given loading step is defined as the stress corresponding to the intersection between the measured stress-strain response and a line drawn parallel to the initial linear elastic portion of the curve, but offset by 0.2% strain. The stress at this intersection is taken as the 0.2% offset yield stress for that loading step. In the present study, this approach was adopted to evaluate the Bauschinger effect in both T-C and C-T loading sequences, as shown in Figure 4.8.

Repeatability was assessed by comparing the 0.2% effective yield stress values obtained at common loading steps across the T-C and C-T loading sequences. The analysis incorporated both full hysteresis tests and interrupted tests, wherein

the same loading step was attained. The full hysteresis tests were repeated three times, while the interrupted tests were conducted once, reaching up to two cycles. Consequently, the number of available yield stress measurements varied with each loading step, contingent upon how many full and interrupted tests had reached that particular loading stage. For each loading step, the yield stress, denoted as $|\sigma_y|$, was averaged based on the available repeated measurements, and the spread was quantified using the sample standard deviation, $S_{|\sigma_y|}$. Thus, the error bars are represented as $|\bar{\sigma}_y| \pm S_{|\sigma_y|}$, where $|\bar{\sigma}_y|$ signifies the mean absolute 0.2% effective yield stress, and $S_{|\sigma_y|}$ represents the sample standard deviation of the repeated yield stress measurements.

For instance, during the T-C loading sequence, the full cyclic reverse-loading tests were conducted over 5.5 cycles and repeated three times. Each full hysteresis test yielded 11 half-cycle yield stress measurements, resulting in a total of 33 available measurements from the repeated full hysteresis tests. Additionally, interrupted tests were carried out up to cycle 2, yielding four further yield-stress measurements at cycle 0.5. Consequently, the yield stress at cycle 0.5 was calculated from a total of $33 + 4 = 37$ available measurements, while the yield stress at cycle 1 was calculated from the 33 available measurements obtained from the repeated full hysteresis tests. This methodology was similarly applied to other common loading steps in the T-C and C-T loading sequences. This allowed the repeatability and scatter of the 0.2% effective yield stress to be quantified at each common loading step, while avoiding the incorrect interpretation that each measurement corresponds to a separate independent test. The same statistical ap-

proach was also employed for all subsequent stress-strain analyses where repeated measurements were available.

During the T-C load sequence (see Figure 4.8(a)), a significant Bauschinger effect is observed between the first two load steps, tension and compression. Furthermore, this effect slightly decreases but remains persistent until the specimen fails at load cycle 5.5. Boyce et al. investigated Ti-6Al-4V supplied as a 20 mm-thick forged plate [115]. The plate underwent solution treatment for 1 hour at 925 °C and was subsequently vacuum annealed for 2 hours at 700 °C. Test specimens were machined into a threaded tensile dog-bone geometry. The material exhibited a bimodal $\alpha + \beta$ microstructure comprising approximately 60 vol.% primary α and 40 vol.% lamellar α/β colonies. The initial tensile load step is 930 MPa, reducing to 600 MPa upon load reversal, with a targeted plastic strain of $\pm 3\%$. Hayes et al. (2017) calculated the tensile yield stress of the material to be 873 MPa after studying a fabricated Ti-6Al-4V component utilising directed energy deposition through electron beam additive manufacturing [116]. The material exhibited a robust $\{001\}_\beta$ texture, as indicated by pole figures. Zhang et al. (2024) investigated a wrought Ti-6Al-4V rolled plate and determined the tensile yield stress to be 900 MPa [117]. The α-phase $\{0001\}$ pole figures revealed a pronounced through-thickness texture.

In contrast, during the C-T load sequence (see Figure 4.8(b)), a notable Bauschinger effect occurs during the initial two load steps, which involve compression and tension. This effect diminishes after the first load cycle and remains until

the material fails in load cycle 4. Kim et al. (2025) measured the compressive yield stress of Ti-6Al-4V to be 1034 MPa, as it was fabricated using a hot-rolled wrought process [118]. Compression tests were conducted from room temperature up to approximately 700°C to assess the temperature-dependent yield behaviour. The material shows a pronounced basal (0001) fibre texture. Wielewski et al. (2015) researched a cross-rolled Ti-6Al-4V plate characterised by a strong texture, with numerous α grains having their c-axes aligned with the orthogonal rolling directions [119]. The compressive yield stress was measured as 900 MPa. Xiao et al. (2025) investigated Ti-6Al-4V and measured the compressive yield stress to be 790 MPa [120]. The material underwent Gleeble-simulated thermal cycles to produce an α/β microstructure. They reported no significant macroscopic preferred-orientation texture.

This indicates that the Bauschinger effect continued to persist throughout the T-C load sequence until material failure occurred. In contrast, during the C-T load sequence, following the first cycle, the difference in yield stresses appeared to be diminished with the increasing number of load cycles.

During reverse loading in both loading sequences, the isotropic and kinematic hardening behaviour of the material is also explored in Figure 4.9. The isotropic and kinematic hardening behaviours are determined from the 0.2% yield stress response of the material during the T-C and C-T loading sequences. Isotropic hardening is defined as the increase in the size (diameter), D, of the yield sur-

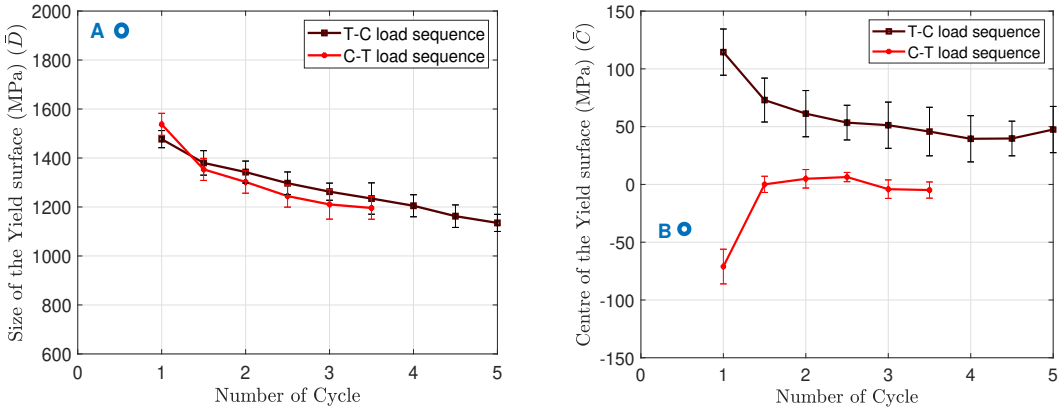


Figure 4.9: Isotropic hardening (Size of the yield surface) (on the left) and Kinematic hardening (Centre of the yield surface) (on the right) of both the loading sequences. Point A shows the size of the yield surface (D) at load cycle 0.5 for both the T-C and C-T load sequences. The size of the yield surface decreases progressively with each cycle in both load sequences. Point B shows the centre of the yield surface (C) at load cycle 0.5 for both the T-C and C-T load sequences. The centre of the yield surface, during the T-C load sequence, gradually decreases until just before failure. During the C-T load sequence, the centre of the yield surface increased positively after load cycle 1 and remained around the range of ± 5 MPa, which is very close to 0 MPa, until failure. For each condition, the Isotropic hardening (D) and Kinematic hardening (C) were averaged over repeated measurements, and the spread was quantified by the corresponding sample standard deviations (S_D and S_C); error bars show $\bar{D} \pm S_D$ and $\bar{C} \pm S_C$ [113].

face [121], and is given by:

$$D = \left|\sigma_y^{(\text{Tension})}\right| + \left|\sigma_y^{(\text{Compression})}\right|.$$

Kinematic hardening, which describes the translation of the yield surface due to backstress evolution and thereby captures the shift in yielding associated with the Bauschinger effect during load reversal [122], may be characterised by the position of the yield-surface centre, C, and is calculated using:

$$C = \frac{1}{2}\left(\sigma_y^{(\text{Tension})} + \sigma_y^{(\text{Compression})}\right).$$

Additionally, this study employed a linear interpolation method to track the isotropic and kinematic hardening responses across all load steps. The 0.2% yield stresses in tension and compression were identified at alternating half-cycles (e.g., tension at cycles n and compression at $n + 0.5$ in the T-C load sequence, and compression at cycles n and tension at $n + 0.5$ in the C-T load sequence). Consequently, each yield-stress series was linearly interpolated onto a common half-cycle index $(n, n + 0.5)$. This approach ensured that $\sigma_y^{(\text{Tension})}$ and $\sigma_y^{(\text{Compression})}$ were available at the same cycle index, enabling the consistent evaluation of the yield-surface size, D, and centre, C, at each load step rather than from mismatched points in the loading history.

At the beginning of the reverse loading (i.e. load cycle 0.5), for both the T-C and C-T load sequences, the size of the yield surface is measured at 1945 MPa, as indicated by point A. This value is obtained by adding the first yield stress in tension from the T-C load sequence and the first yield stress in compression from the C-T load sequence. In both loading sequences, the size of the yield surface progressively decreases with an increasing cycle number, indicating cyclic softening, as shown in Figure 4.9. This reduction is caused by material softening under successive load cycles [123, 124].

At the start of the reverse loading for both sequences, the centre of the yield surface is located at -30 MPa, as indicated by point B, also determined from the initial yield stress in the T-C and C-T load sequence. The centre of the yield surface demonstrated an interesting behaviour as shown in Figure 4.9. During

the T-C load sequence, the centre of the yield surface gradually decreases with successive loading cycles. Whereas, during the C-T load cycles, the centre of the yield surface increased positively after load cycle 1 and remained around the range of ± 5 MPa, which is very close to 0 MPa, until failure.

4.6 Microstructural analysis via Electron Backscatter Diffraction (EBSD) of sectioned interrupted specimens with increasing load cycles

To enhance understanding of microstructural evolution, including texture, twin boundary length, and Schmid factor during reverse loading, EBSD was performed on interrupted specimens from load cycles 0.5 to 2 for both loading sequences, even though the material can withstand more cycles beyond load cycle 2. The primary goal of the microscopy is to identify the mechanisms responsible for the Bauschinger response, rather than to monitor incremental changes in each cycle. Notably, the Bauschinger response of the material has been observed to remain unchanged after load cycle 2, as illustrated in Figure 4.8. Therefore, the microstructural characterisation conducted up to load cycle 2 is considered sufficient to provide a representative microstructural state for the mechanistic interpretation of the Bauschinger response in the material.

4.6.1 Twin evolution in forged Ti-6Al-4V

In this material, the presence of $\{10\bar{1}2\}$ and $\{10\bar{1}3\}$ twins was observed. The $\{10\bar{1}2\}$ twins, known as extension (tension) twins, are typically associated with a lattice reorientation of approximately 86° about the a-axis, $\langle 11\bar{2}0\rangle$ [125,126]. These twins are usually activated when tensile stress is applied parallel to the c-axes or when compressive stress is applied perpendicular to the c-axes. Whereas, $\{10\bar{1}3\}$ twins are typically classified as contraction (compression) twins, which are

associated with a compressive strain component along the c-axes [127, 128]. This type of twins are generally activated under compressive loading parallel to the c-axis (or tensile loading perpendicular to the c-axes) and are usually observed at higher strains than $\{10\bar{1}2\}$ extension twins. Furthermore, $\{10\bar{1}3\}$ twins are linked to a lattice reorientation of approximately 64° about the a-axis, $\langle 11\bar{2}0\rangle$. The evolution of twin boundary length for these twins is depicted in Figure 4.10. In OIM Analysis, twin boundaries were identified using an axis-angle misorientation criterion for $\{10\bar{1}2\}$ and $\{10\bar{1}3\}$ twins, summing the lengths of all classified twin boundary segments. A tolerance of $\pm 5°$ was applied to accommodate typical EBSD measurement uncertainty and minor local orientation variations near twin boundaries [129], effectively distinguishing twins from general grain boundaries. Segment lengths were converted to μm based on the EBSD step size, with results reported per mapped area. This illustrates the trend of $\{10\bar{1}2\}$ and $\{10\bar{1}3\}$ across both loading sequences as load cycles increase. In the as-received specimen, twin boundary lengths were measured at 134 μm for twin $\{10\bar{1}2\}$ and 145 μm for twin $\{10\bar{1}3\}$.

In the T-C load sequence, both twins $\{10\bar{1}2\}$ and $\{10\bar{1}3\}$ display asymmetric fluctuations in the Twin Boundary Length, characterised by a sequence of increasing (twin), decreasing (detwin), increasing (twin), and subsequently decreasing values with increasing number of load cycles. Conversely, in the C-T load sequence, fluctuation is primarily noticeable until the material is loaded in compression (load cycle 0.5), after this period, both twins $\{10\bar{1}2\}$ and $\{10\bar{1}3\}$ gradually decrease. Interestingly, this trend highlights a notable load-path de-

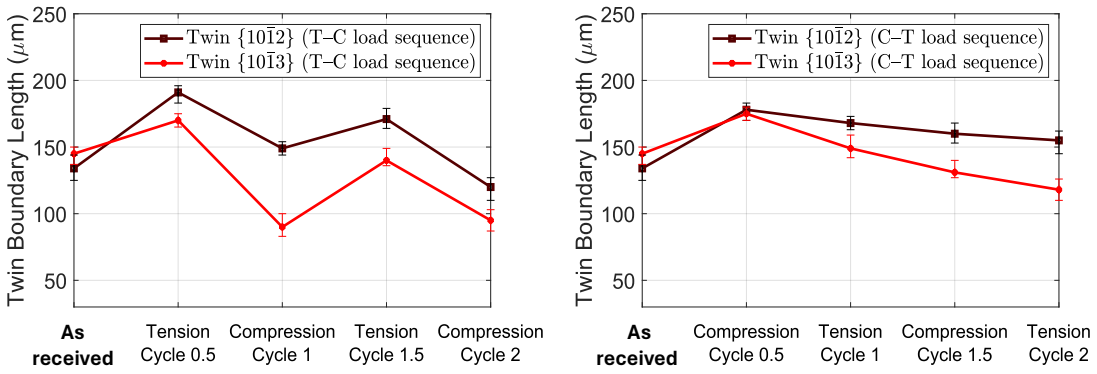


Figure 4.10: Twin boundary length evolution for $\{10\bar{1}2\}$ and $\{10\bar{1}3\}$ twins during interrupted T-C (left) and C-T (right) loading reveals distinct behaviours. In the T-C loading cycle, there are asymmetric fluctuations in detwinning and twinning across the cycles, while the C-T loading exhibits a significant change in the initial load, followed by a gradual decrease in twin boundary length. This suggests that the twin microstructure stabilises early, with subsequent deformation increasingly accommodated by non-twinning mechanisms, likely slip. The uncertainty was estimated from the EBSD scan spatial resolution, based primarily on the step size and the criteria used for twin boundary identification in OIM. The calculation of error is based on a methodology similar to the one described in Chapter 3.1.4.

pendence in twinning evolution. During the T-C load sequence, twinning and detwinning remain active for subsequent cycles, though with reduced amplitude. Conversely, the C-T load sequence shows a progressive decrease in twinning activity. This suggests that the twin microstructure stabilises early, with subsequent deformation increasingly accommodated by non-twinning mechanisms, likely slip. The twinning-detwinning behaviour is in agreement with previous studies indicating that twinning-detwinning phenomena contribute to the Bauschinger effect behaviour in HCP materials at low strain-rate [74, 130–134].

4.6.2 Schmid factor evolution of crystallographic slip systems in α and β phases in forged Ti-6Al-4V

To study the Schmid factor distribution within the crystallographic slip systems of the material, the Schmid factor [100] was applied:

$$m = \cos\phi \, \cos\lambda$$

The Schmid factor, m, relates an applied uniaxial stress, σ, to the resolved shear stress on a crystallographic slip system through the equation $\tau_{\mathrm{r}} = \sigma m$. Here, ϕ is the angle between the loading axis and the slip plane normal, while λ is the angle between the loading axis and the slip direction. Using the EBSD orientation data, the Schmid factors for each slip system were computed in EDAX OIM by defining the specimen loading axis and evaluating $m = \cos\phi\cos\lambda$ for all crystallographic variants at each measurement point. From this, the Schmid factor distributions were exported for plotting. According to the Schmid law, slip initiates when the resolved shear stress equals the critical resolved shear stress [100]; therefore, systems with higher m-values are preferentially activated under a given macroscopic stress state [100].

In titanium, the Schmid factor serves as a geometric measure of slip favourability relative to the macroscopic loading axis, with the implicit assumption of a uniform uniaxial stress state, such that $\tau_r = \sigma m$. However, in practice, the local driving stress can significantly deviate from this estimation due to non-Schmid

effects. These effects include (but not limited to), (i) grain-grain interaction and load redistribution, whereby heterogeneous, often multiaxial local stresses are produced by elastic-plastic anisotropy and neighbourhood constraint [135]; (ii) local stress gradients near twins and grain boundaries, for which titanium twin variant selection and growth have been shown to correlate more strongly with the maximum local driving condition than with the global Schmid factor derived from the remote load [136]; and (iii) non-glide stress effects, whereby stress components with little or no resolved shear can nevertheless modify dislocation core structure and glide barriers, such that activation is not governed solely by the Schmid projection [110]. Accordingly, the resolved shear stress relevant to activation should be evaluated from the local stress tensor, and the Schmid factor should be interpreted as identifying geometrically favourable candidates rather than uniquely predicting first activation. Quantitative observations in titanium reveal both amplification and shielding of local driving stress due to non-Schmid effects: (i) In commercially pure titanium, HR-EBSD measurements at a grain boundary with a prismatic slip band showed local resolved shear stresses of approximately $\sim$600 MPa, significantly higher than the far-field value of $\sim$115 MPa [137]. In contrast, grain-resolved 3D-XRD at 0.94% applied strain reported a macroscopic stress of 198 MPa exceeding the grain-weighted mean axial stress of 148 MPa by about 25%, indicating local stress shielding relative to σm [135]. In the current work, a pixel-wise Schmid factor was computed to identify the most geometrically favourable slip systems, based on the simplifying assumption of a uniform uniaxial stress state and negligible non-Schmid effects.

For all the slip systems present in the material, such as the $\langle a \rangle$ basal slip system, the $\langle a \rangle$ prismatic slip system, the $\langle a \rangle$ pyramidal slip system, and the $\langle c+a \rangle$ pyramidal slip system, the distribution of the Schmid factor, m, and its median, $\tilde{m}$, is plotted. In these plots, the Blue colour represents tension load steps, the Red colour denotes compression load steps, and the Grey colour indicates the as-received specimen. The median, $\tilde{m}$, is plotted in green. The distributions of the Schmid factor, m, along with their medians $\tilde{m}$, are illustrated for different slip systems. as cycling progresses for various grain orientations in the α and β phases under two distinct loading sequences, as shown in Figures 4.11 to 4.28. The uncertainty associated with the median Schmid factor arises from bin-resolution, or quantisation uncertainty, which occurs when a continuous variable is discretised into finite bins of uniform width, denoted as Δ. When using uniform discretisation, the rounding or quantisation error is limited to half of the bin size. Therefore, the median is reported as $\tilde{m} \pm \frac{\Delta}{2}$ [138].

In the α phase during the T-C load sequence (Figures 4.11 to 4.16), $\tilde{m}$ exhibits oscillations with load reversals across all slip families as the cycle number increases. Notably, the basal slip system shows modest oscillations, while the prismatic slip system shows fluctuations, and remains relatively favourable in the early stages but experiences a significant decline later. In contrast, the pyramidal slip systems demonstrate smaller amplitude oscillations coupled with an overall mild reduction. The second-order pyramidal slip system displays the most pronounced redistribution with increaisng load cycles. Collectively, the favourability of slip modes fluctuates with tension-compression reversals, highlighting a cyclic

and asymmetric redistribution of deformation propensity rather than a progressive stabilisation towards a single dominant slip mode.

In the β phase during the T-C load sequence, figures from 4.17 to 4.19, demonstrate the behaviour of $\tilde{m}$ shows a remarkable insensitivity to cycling: the $\{110\}\langle\bar{1}11\rangle$ and $\{211\}\langle\bar{1}11\rangle$ systems remain essentially constant, whereas the $\{200\}\langle011\rangle$ system exhibits only minor oscillations around its initial value. Overall, the β phase undergoes minimal cycle-dependent reorientation, indicating that slip favourability in β remains effectively unchanged throughout the T-C loading process.

In the α phase of the C-T load sequence (Figures 4.20 to 4.25), the back-and-forth movement, denoted as $\tilde{m}$, typically exhibits oscillations during load reversals across most slip families. However, this behaviour is not observed in the prismatic slip system. In this case, $\tilde{m}$ diminishes at Cycle 0.5 and then remains relatively stable through Cycle 2. In contrast, the $\tilde{m}$ values for the other slip systems exhibit an oscillating trend throughout the cycles. Overall, under the C-T load cycle, slip favourability is particularly sensitive to reversals in basal, pyramidal, and second-order pyramidal systems. In contrast, the prismatic slip system remains relatively unaffected by the cycles, indicating a more stable propensity for prismatic activity compared to the other modes.

Similarly, in the β phase during the C-T load sequence, the figures ranging from 4.26 to 4.28 show that $\tilde{m}$ remains largely stable throughout cycling for the $\{110\}\langle\bar{1}11\rangle$, $\{200\}\langle011\rangle$, and $\{211\}\langle\bar{1}11\rangle$ slip systems. The slip formability in the β phase of the C-T load cycle remains effectively unchanged across cycles.

In summary, in the α phase, differences are observed in the prismatic slip system, which exhibit fluctuations in the $\tilde{m}$ value during the T-C loading sequence, but not in the C-T loading sequence. During the T-C loading sequence, the variation in the $\tilde{m}$ value with different load directions indicates that the favourability of slip is dependent on the load direction. Conversely, during the C-T loading sequence, the $\tilde{m}$ values remain constant across different load directions, suggesting that the favourability of slip is independent of the load direction. No statistically significant differences are observed in the β phase between the two loading sequences. With an estimated area fraction of 2%, the β phase is assumed to be unlikely to have a substantial impact on the observed behaviour.

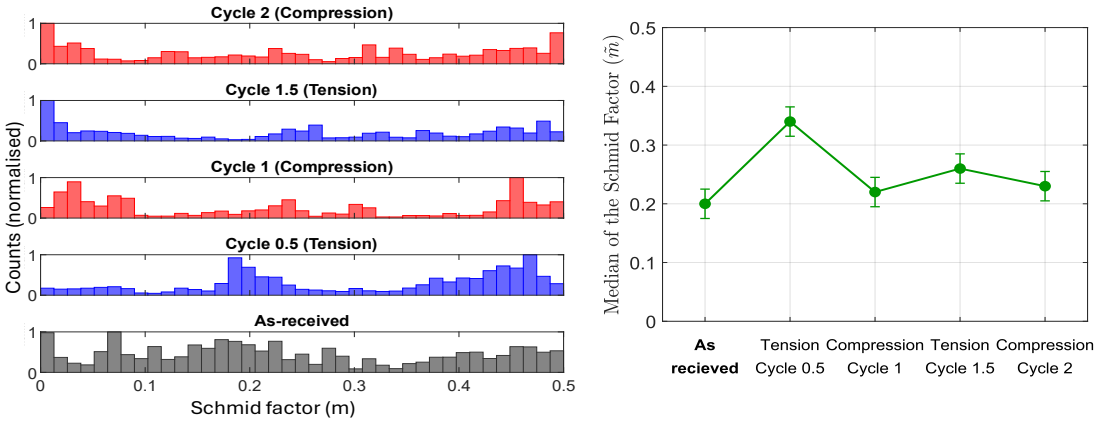


Figure 4.11: Basal slip system $\{0002\}\langle 11\bar{2}0\rangle$ (α) (T-C load sequence). The uncertainty associated with the median Schmid factor arises from bin-resolution, or quantisation uncertainty, which occurs when a continuous variable is discretised into finite bins of uniform width, denoted as Δ. When using uniform discretisation, the rounding or quantisation error is limited to half of the bin size. Therefore, the median is reported as $\tilde{m} \pm \frac{\Delta}{2}$ [138].

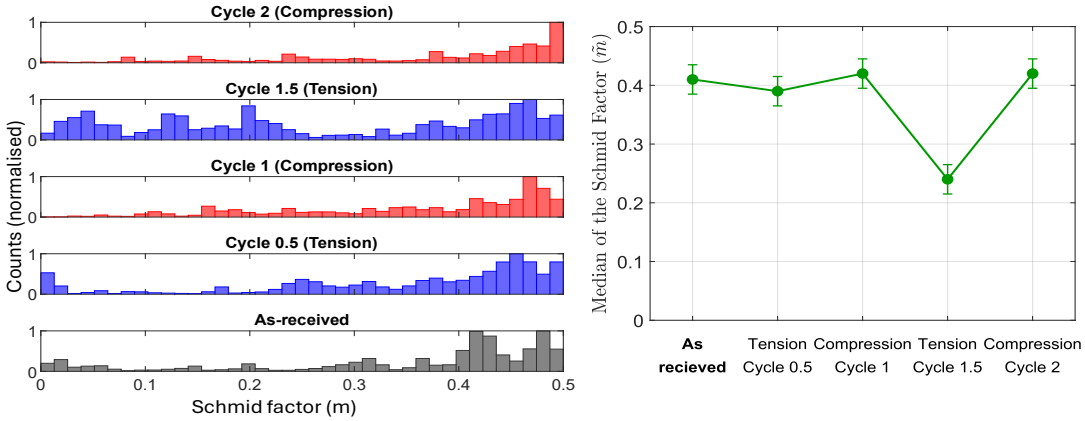


Figure 4.12: Prismatic slip system $\{10\bar{1}0\}\langle\bar{1}2\bar{1}0\rangle$ (α) (T-C load sequence).

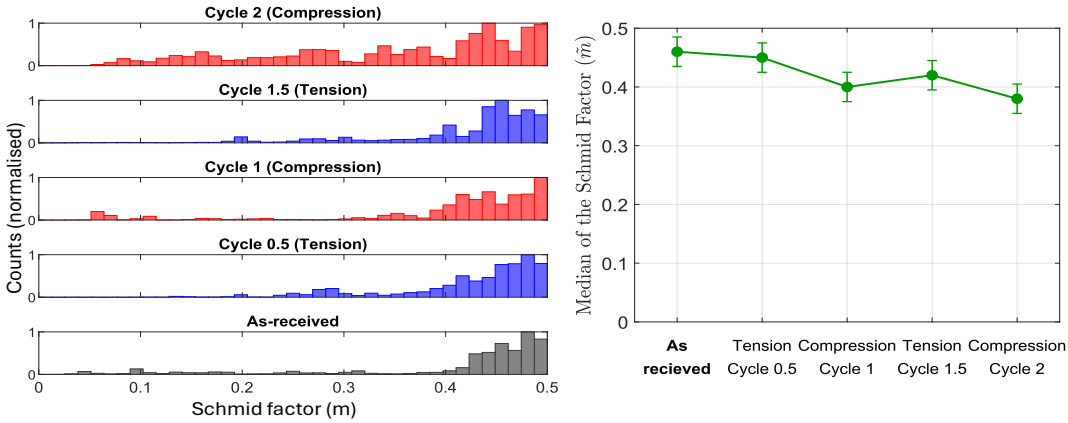


Figure 4.13: Pyramidal slip system $\{10\bar{1}1\}\langle\bar{1}2\bar{1}0\rangle$ (α) (T-C load sequence)

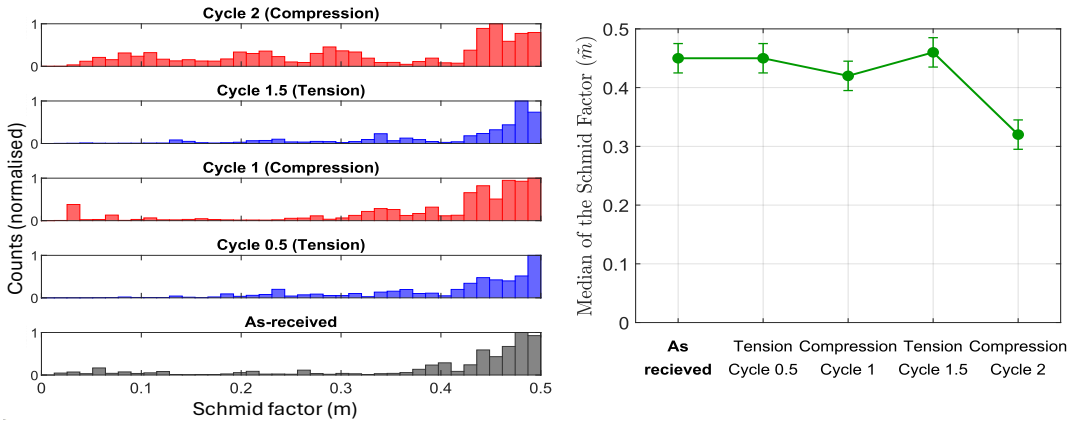


Figure 4.14: Pyramidal slip system $\{20\bar{2}1\}\langle\bar{1}2\bar{1}0\rangle$ (α) (T-C load sequence)

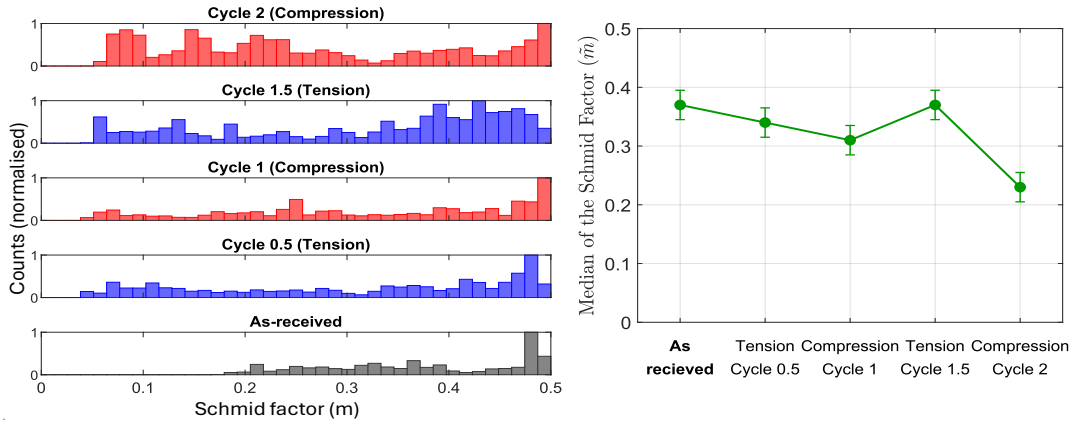


Figure 4.15: Second-order pyramidal slip system $\{11\bar{2}2\}\langle\bar{1}\bar{1}23\rangle$ (α) (T-C load sequence)

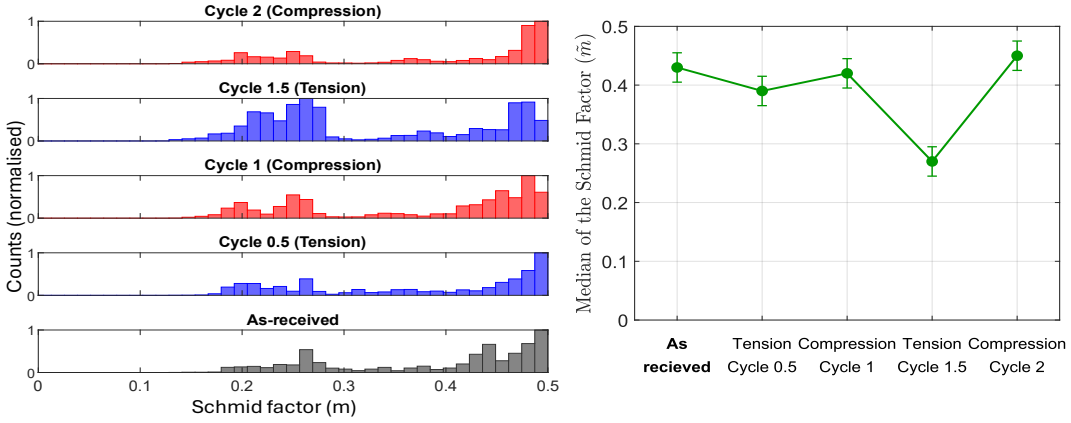


Figure 4.16: Pyramidal slip system $\{20\bar{2}2\}\langle\bar{1}\bar{1}23\rangle$ (α) (T-C load sequence)

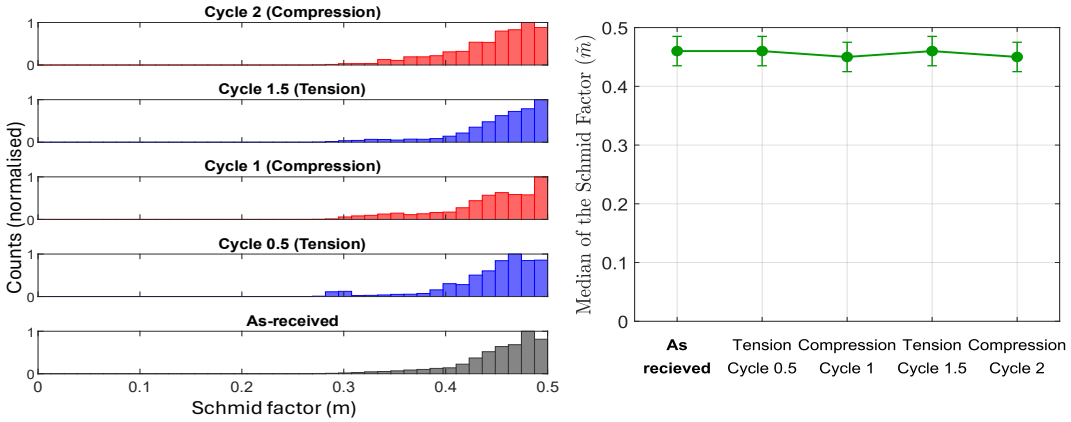


Figure 4.17: $\{110\}\langle\bar{1}11\rangle$ slip system (β) (T-C load sequence)

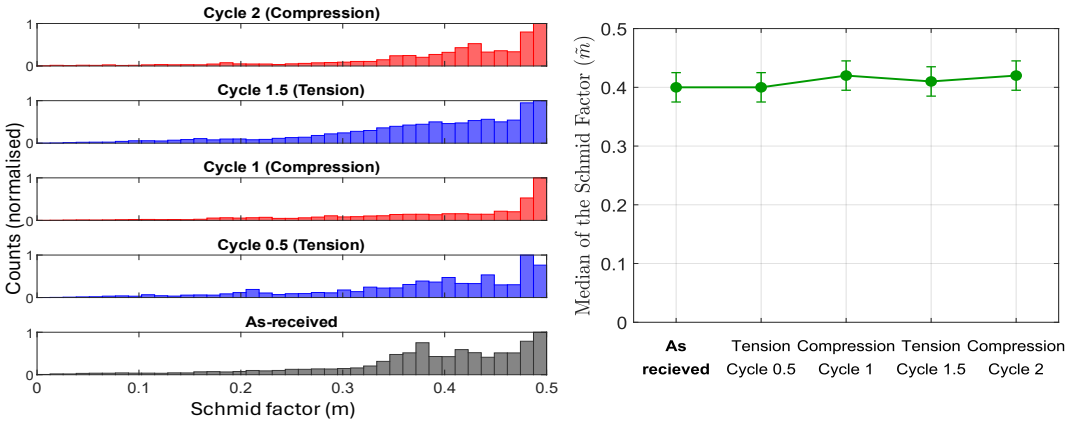


Figure 4.18: $\{200\}\langle 011\rangle$ slip system (β) (T-C load sequence)

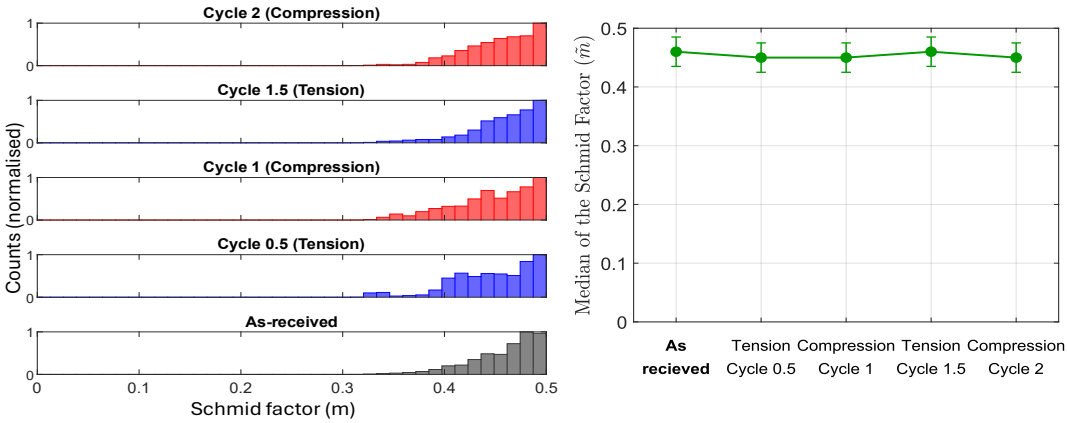


Figure 4.19: $\{211\}\langle \bar{1}11\rangle$ slip system (β) (T-C load sequence)

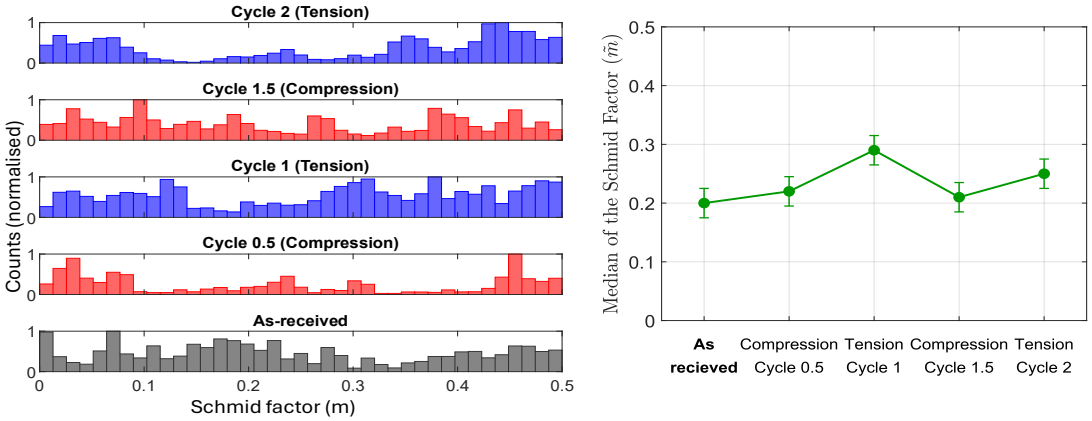


Figure 4.20: Basal slip system $\{0002\}\langle 11\bar{2}0\rangle$ (α) (C-T load sequence)

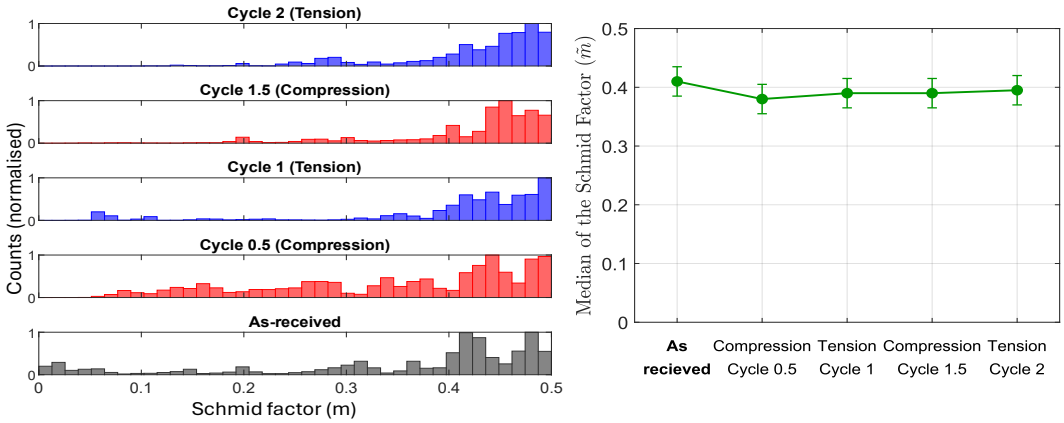


Figure 4.21: Prismatic slip system $\{10\bar{1}0\}\langle\bar{1}2\bar{1}0\rangle$ (α) (C-T load sequence).

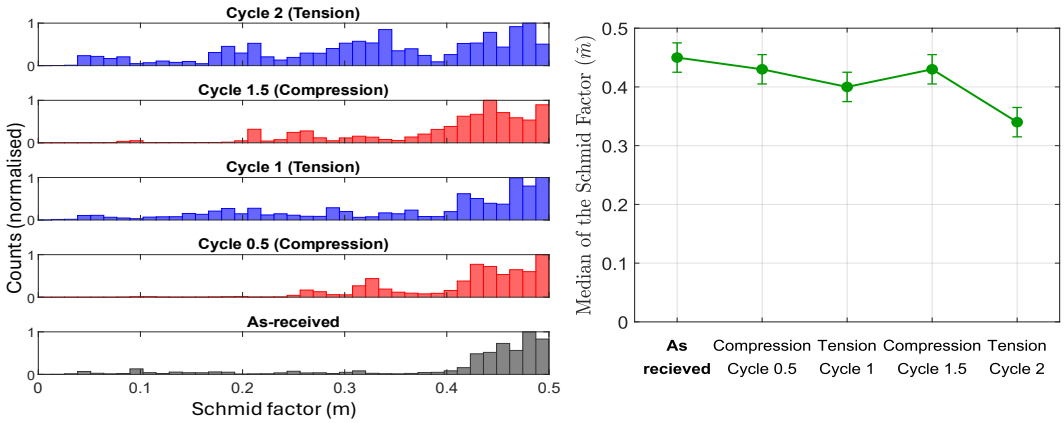


Figure 4.22: Pyramidal slip system $\{10\bar{1}1\}\langle\bar{1}2\bar{1}0\rangle$ (α) (C-T load sequence)

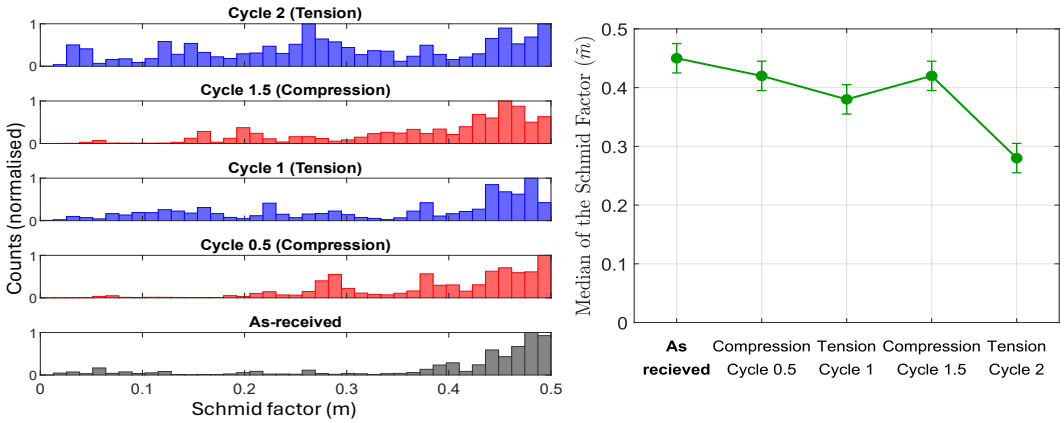


Figure 4.23: Pyramidal slip system $\{20\bar{2}1\}\langle\bar{1}2\bar{1}0\rangle$ (α) (C-T load sequence)

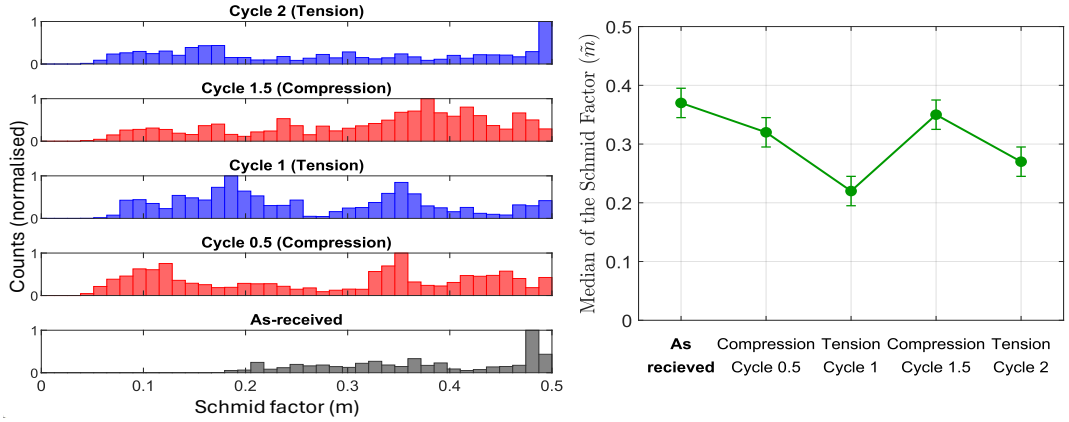


Figure 4.24: Second-order pyramidal slip system $\{11\bar{2}2\}\langle\bar{1}\bar{1}23\rangle$ (α) (C-T load sequence)

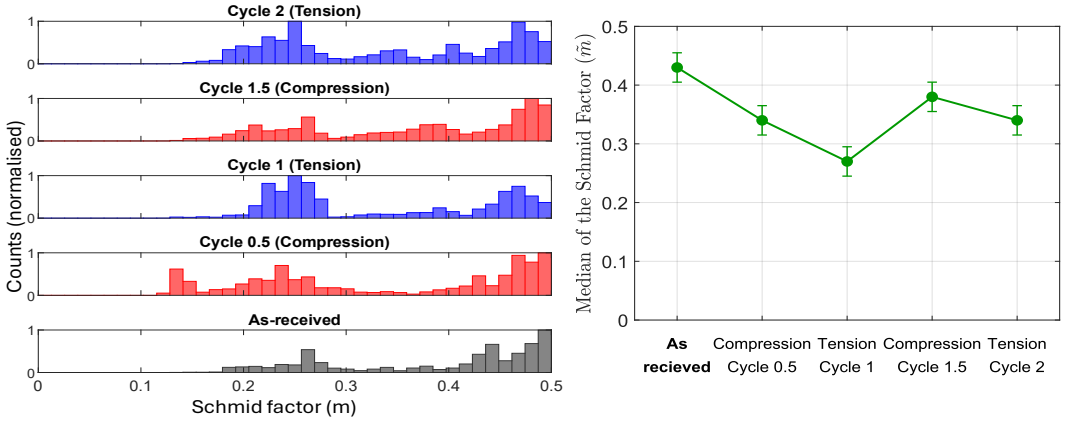


Figure 4.25: Pyramidal slip system $\{20\bar{2}2\}\langle\bar{1}\bar{1}23\rangle$ (α) (C-T load sequence)

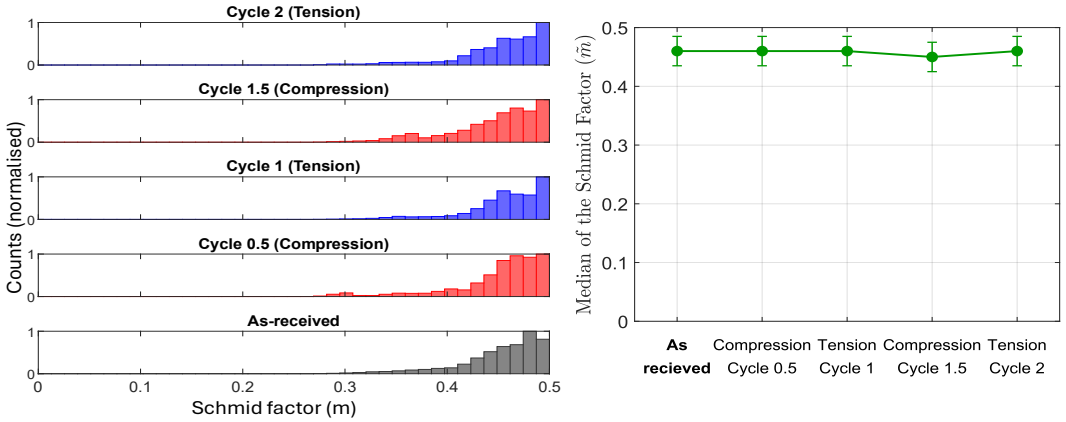


Figure 4.26: $\{110\}\langle\bar{1}11\rangle$ slip system (β) (C-T load sequence)

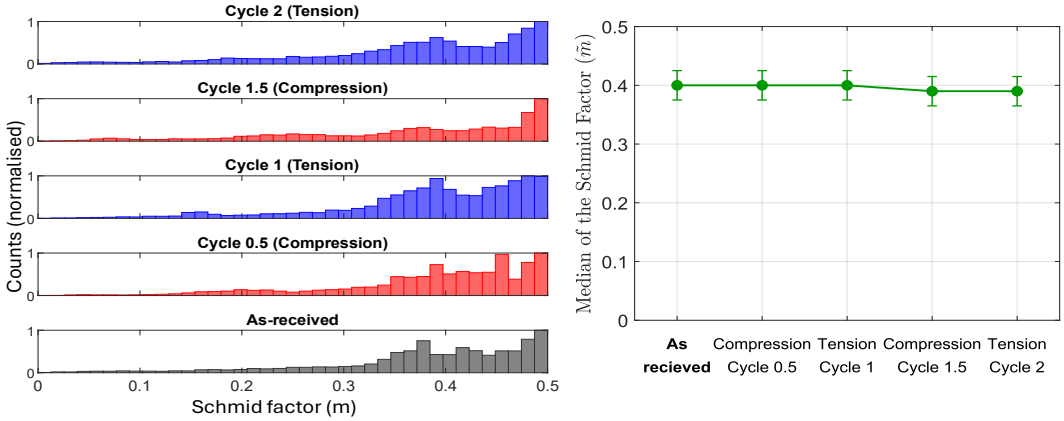


Figure 4.27: $\{200\}\langle 011\rangle$ slip system (β) (C-T load sequence)

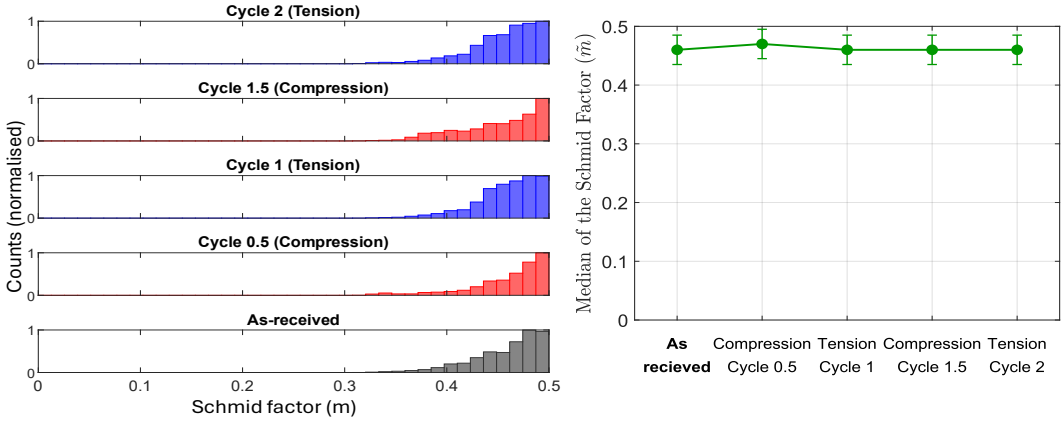


Figure 4.28: $\{211\}\langle \bar{1}11\rangle$ slip system (β) (C-T load sequence)

4.7 Residual Stress accumulation in forged Ti-6Al-4V

The evolution of residual stress accumulation in the material during reverse loading was assessed through the evaluation of interrupted unsectioned specimens. These specimens were analysed after each load step, which ranged from 0.5 to 2 load cycles, in both loading sequences, using X-ray diffraction. Residual stress is measured to quantify the internal stress state that remains after load reversal. The residual stress fields that develop within the specimen under cyclic reverse loading are expected to influence the subsequent Bauschinger response and assist in correlating the observed microstructural changes with macroscopic hysteresis [25, 26]. In Ti-6Al-4V, anisotropy and microstructural constraints can encourage heterogeneous plastic deformation during load reversal, resulting in the retention of internal stresses [81, 139]. The evolution of these internal stresses establishes a mechanistic link between microstructural changes, such as dislocation interactions with slip activity and twinning-related barriers, which may either facilitate or hinder motion and the resultant hysteresis characteristics, including the Bauschinger effect [139, 140].

4.7.1 Methodology to measure residual stress

The interrupted unsectioned specimens were analysed to measure the residual stress after each loading step during the first two cycles of reverse loading.

Specimens were chosen for residual stress measurement up to the second load cycle because the trend of the yield strength behaviour did not change significantly beyond that point, as illustrated in Figure 4.8. Synchrotron X-ray diffraction measurements took place at the I12-JEEP Beamline at the Diamond Light Source in Didcot, Oxfordshire, United Kingdom [141]. A monochromatic X-ray beam with a wavelength of 1.540 Å (79.104 keV) was collimated to a beam size of 0.075 mm x 0.075 mm, exposing on the order of 10^4 grains. This is in agreement with previous studies in the literature regarding the number of scattering grains analysed in the X-ray diffraction in titanium [142–144]. Residual stress measurements were conducted without rotating the cylindrical specimen around its axis. This approach assumes an approximately axisymmetric stress state and microstructure, meaning there is negligible circumferential variation. It also requires sufficient grain statistics with limited texture. As a result, the measured peak positions reflect an average lattice strain, rather than being influenced predominantly by a small group of favourably oriented grains. Two-dimensional diffraction patterns were azimuthally divided into 36 equal segments ("caked") and radially integrated to obtain one-dimensional intensity curves, $I(\eta, \vec{q})$, as a function of azimuthal angle, η, and the magnitude of the scattering vector, $\vec{q}$. In Figure 4.29, X, Y, and Z, are in the reference frame of the detector, and X_s, Y_s, and Z_s, are in the sample reference frame, respectively. As previously noted in Figure 3.4, the material consists of 98% α phase, which has a hexagonal close-packed (HCP) crystal structure, and 2% β phase. A representative crystal from each of the α and β phases, among many randomly oriented HCP and BCC crystals, is illustrated in Figure 4.29.

HCP and BCC data caking and integration were carried out by a data analysis software DAWN [145]. This transformed the intensity data from detector coordinates into polar coordinates, specifically plotting the azimuthal angle, η, against the magnitude of the scattering vector. The precise X-ray energy and geometry calibration were realised by measuring a NIST standard specimen, CeO_2 and LaB_6.

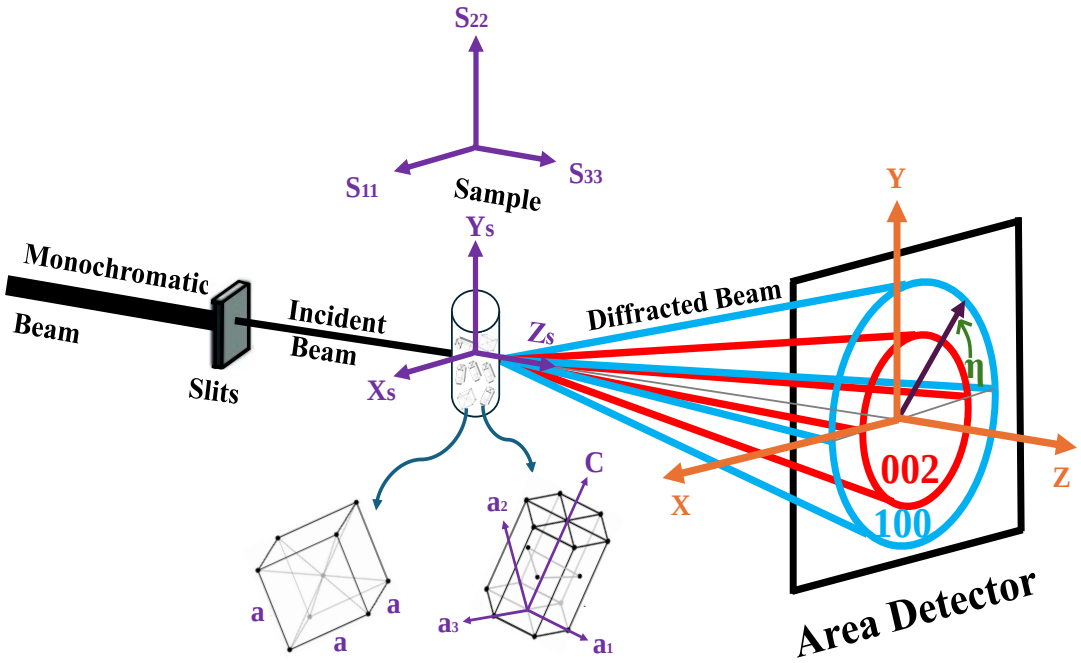


Figure 4.29: Set-up to conduct synchrotron X-ray diffraction experiment at I12-JEEP Beamline at Diamond Light Source, UK, demonstrating relevant coordinate systems and highlighting one of many randomly oriented HCP and BCC crystals within the sample.

An integrated diffraction pattern $I(\vec{q})$ with the corresponding Miller indices of the Bragg peaks is shown in Figure 4.30. These peaks were indexed using Bragg's law together with the scattering-vector relation (and also verified with the previous

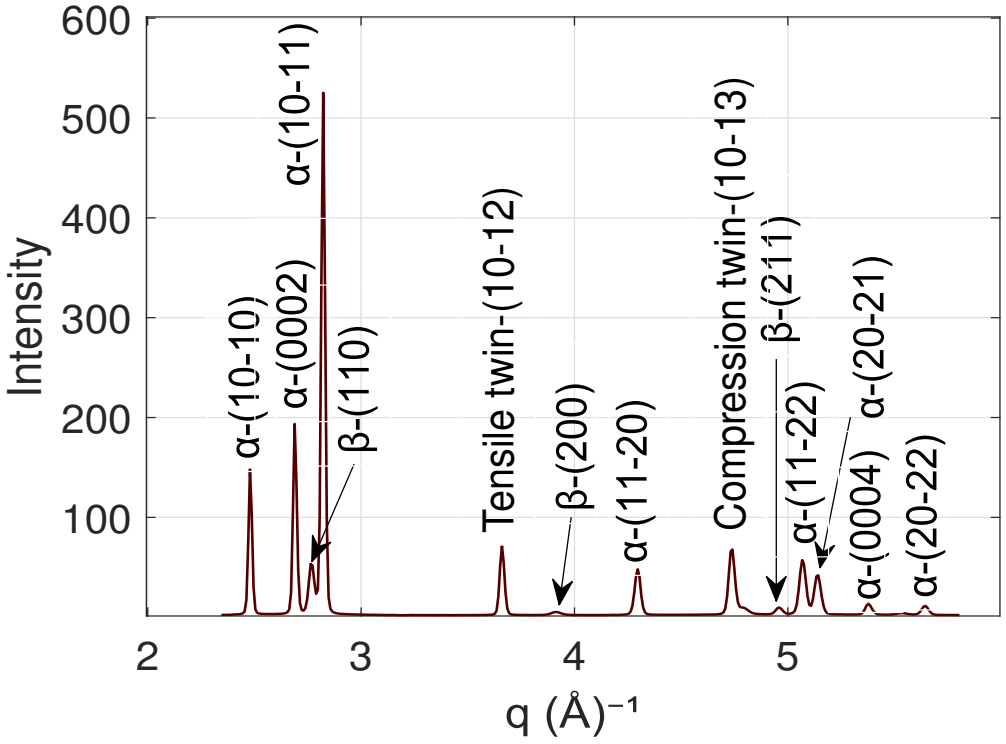


Figure 4.30: X-ray diffraction pattern of forged Ti-6Al-4V, illustrating indexed diffracted peaks corresponding to the crystallographic planes in both the α-phase and β-phase, along with twins associated with various crystallographic planes present within the material.

literature [146–149]), assuming first-order diffraction ($n = 1$):

$$2d_{hkl} \sin\theta = \lambda, \qquad q = \frac{4\pi \sin\theta}{\lambda} \Rightarrow d_{hkl} = \frac{2\pi}{q}.$$

For the hexagonal close-packed (HCP) phase, the interplanar spacings are computed using [150]:

$$\frac{1}{d_{hkl}^2} = \frac{4}{3}\frac{h^2 + hk + k^2}{a^2} + \frac{l^2}{c^2},$$

where, a and c are lattice parameters. For the body-centred cubic (BCC) phase,

the interplanar spacings are computed using [150]:

$$\frac{1}{d_{hkl}^2} = \frac{h^2 + k^2 + l^2}{a^2}$$

The diffraction pattern displays distinct peaks associated with various families of crystallographic planes. These include crystallographic planes in both, α and β phases. In α phase, it contains, Basal planes, represented by (0002) and (0004); Prismatic planes, represented by $(10\bar{1}0)$ and $(11\bar{2}0)$; and Pyramidal planes, which include $(11\bar{1}0)$, $(20\bar{2}1)$, $(11\bar{2}2)$, and $(20\bar{2}2)$. In β phase, crystallographic planes are (110), (200), and (211).

Individual Bragg peaks were fitted using a Gaussian function to determine the peak position in reciprocal space for each reflection and azimuthal sector, $q^{\{hkl\}}(\eta_i)$. The corresponding interplanar spacing, $d^{\{hkl\}}(\eta_i)$, was then calculated using $d^{\{hkl\}}(\eta_i) = 2\pi/q^{\{hkl\}}(\eta_i)$ [151]. The experimental directional lattice strain was computed as $\varepsilon_{\text{exp}}^{\{hkl\}}(\eta_i) = \left(d^{\{hkl\}}(\eta_i) - d_0^{\{hkl\}}\right)/d_0^{\{hkl\}}$, where $d_0^{\{hkl\}}$ is the lattice-plane spacing measured in the as-received specimen. Thus, experimental directional strains were obtained as a function of azimuthal angle, $\varepsilon_{\text{exp}}^{\{hkl\}}(\eta_i)$. The sample-frame strain tensor components ε_{11}, ε_{12}, ε_{13}, ε_{22}, ε_{23}, and ε_{33} were then determined from $\varepsilon_{\text{exp}}^{\{hkl\}}(\eta_i)$ using a least-squares fit to the angular strain transformation relation [152, 153], as follows:

(i) Peak fitting for each azimuthal sector: For each azimuthal sector η_i, the diffraction peak was fitted to obtain the lattice spacing $d_{hkl}(\eta_i)$ directly. The

corresponding Bragg angle $\theta(\eta_i)$ (available from the fit as $\sin\theta$) is used below only to construct the diffraction geometry and unit directions. For reference, Braggs law is $n\lambda = 2d\sin\theta$ (here $n = 1$, λ the X-ray wavelength), but d_{hkl} is not computed from θ in this work.

(ii) Experimental directional lattice strain: For each azimuthal sector and reflection, the experimental directional lattice strain was calculated from the fitted lattice spacing as

$$\varepsilon_{\mathrm{exp}}^{\{hkl\}}(\eta_i) = \frac{d^{\{hkl\}}(\eta_i) - d_0^{\{hkl\}}}{d_0^{\{hkl\}}},$$

where $d_0^{\{hkl\}}$ is the corresponding lattice-plane spacing measured in the as-received specimen.

(iii) Diffraction geometry and unit scattering vector direction: To determine the diffraction measurement direction for each azimuthal sector, detector coordinates (X, Y) were converted into the sample-frame geometry using the detector distance dd and ring radius $r = \sqrt{X^2 + Y^2}$, such that

$$\tan(2\theta) = \frac{r}{dd}.$$

The scattered-beam unit vector was written as

$$\hat{\mathbf{s}} = \frac{[-\tan(2\theta)\cos\eta,\ -\tan(2\theta)\sin\eta,\ 1]}{\sqrt{1 + \tan^2(2\theta)}}.$$

With the incident-beam vector defined as $\mathbf{s}_0 = [0, 0, 1]$, the unit scattering vector

direction was obtained from

$$\hat{\mathbf{q}} = \frac{\hat{\mathbf{s}} - \mathbf{s}_0}{|\hat{\mathbf{s}} - \mathbf{s}_0|}.$$

For each azimuthal sector η_i, this direction is denoted $\hat{\mathbf{q}}(\eta_i)$, with component form

$$\hat{\mathbf{q}}(\eta_i) = \big[q_x(\eta_i),\, q_y(\eta_i),\, q_z(\eta_i)\big].$$

(iv) Reconstruction of the sample-frame strain tensor: For each azimuthal sector η_i, the diffraction geometry defines a unit measurement direction $\hat{\mathbf{q}}(\eta_i)$. The lattice strain obtained from the peak shift in that sector is interpreted as the normal strain component along this direction (i.e., along the scattering vector direction).

Under the small-strain approximation, the experimental directional strain is given by the standard directional-strain relation (normal strain along a unit direction), namely the projection of the sample-frame strain tensor $\boldsymbol{\varepsilon}^{(s)}$ onto $\hat{\mathbf{q}}(\eta_i)$:

$$\varepsilon_{\mathrm{exp}}^{\{hkl\}}(\eta_i) = \hat{\mathbf{q}}(\eta_i)^T \boldsymbol{\varepsilon}^{(s)} \hat{\mathbf{q}}(\eta_i).$$

Since the strain tensor is symmetric, it contains six independent components and can be written as

$$\boldsymbol{\varepsilon}^{(s)} = \begin{bmatrix} \varepsilon_{11} & \varepsilon_{12} & \varepsilon_{13} \\ \varepsilon_{12} & \varepsilon_{22} & \varepsilon_{23} \\ \varepsilon_{13} & \varepsilon_{23} & \varepsilon_{33} \end{bmatrix}.$$

Expanding the projection for $\hat{\mathbf{q}}(\eta_i) = [q_x(\eta_i), q_y(\eta_i), q_z(\eta_i)]$ gives:

$$\varepsilon_{\mathrm{exp}}^{\{hkl\}}(\eta_i) = q_x(\eta_i)^2\,\varepsilon_{11} + 2q_x(\eta_i)q_y(\eta_i)\,\varepsilon_{12} + 2q_x(\eta_i)q_z(\eta_i)\,\varepsilon_{13} + q_y(\eta_i)^2\,\varepsilon_{22} + 2q_y(\eta_i)q_z(\eta_i)\,\varepsilon_{23} + q_z(\eta_i)^2\,\varepsilon_{33}.$$

Thus, each azimuthal sector provides one linear equation in the six unknown strain components. Collecting the coefficients associated with $\hat{\mathbf{q}}(\eta_i)$ defines one row of the design matrix:

$$A_i = \big[q_x(\eta_i)^2,\ 2q_x(\eta_i)q_y(\eta_i),\ 2q_x(\eta_i)q_z(\eta_i),\ q_y(\eta_i)^2,\ 2q_y(\eta_i)q_z(\eta_i),\ q_z(\eta_i)^2\big].$$

Stacking all azimuthal sectors for a given reflection yields the overdetermined linear system

$$A\,\boldsymbol{\varepsilon}^{(s)} = \boldsymbol{\varepsilon}_{\mathrm{exp}}^{\{hkl\}},$$

where

$$\boldsymbol{\varepsilon}^{(s)} = [\varepsilon_{11}, \varepsilon_{12}, \varepsilon_{13}, \varepsilon_{22}, \varepsilon_{23}, \varepsilon_{33}]^T,$$

and $\boldsymbol{\varepsilon}_{\mathrm{exp}}^{\{hkl\}}$ is the column vector formed by stacking the experimental directional strains $\varepsilon_{\mathrm{exp}}^{\{hkl\}}(\eta_i)$ over all azimuthal sectors. In this way, the azimuthal strain variation is recast as a linear inverse problem for the sample-frame strain tensor components.

(v) Least-squares solution of the overdetermined system: The six independent components of the symmetric strain tensor were obtained by solving the

overdetermined system in a least-squares sense. Specifically,

$$A\,\boldsymbol{\varepsilon}^{(s)} \approx \boldsymbol{\varepsilon}_{\mathrm{exp}}^{\{hkl\}}$$

This returns the least-squares estimate of the unknown strain vector,

$$\boldsymbol{\varepsilon}^{(s)} = \begin{bmatrix} \varepsilon_{11} \\ \varepsilon_{12} \\ \varepsilon_{13} \\ \varepsilon_{22} \\ \varepsilon_{23} \\ \varepsilon_{33} \end{bmatrix}.$$

(vi) Conversion from residual strain to residual stress: After determination of the residual strain tensor in the sample frame, the residual stress tensor was obtained by applying generalised Hookes law,

$$\boldsymbol{S}^{(s)} = \mathbf{C}^{(s)} : \boldsymbol{\varepsilon}^{(s)}$$

where $\mathbf{C}^{(s)}$ is the stiffness tensor expressed in the sample coordinate system (X_s, Y_s, Z_s). The stress conversion was performed using the stiffness tensor adopted for the relevant material response in the sample frame.

The unique components of the resulting residual stress tensor are

$$\{S_{11},\, S_{22},\, S_{33},\, S_{12},\, S_{23},\, S_{13}\},$$

where S_{11}, S_{22}, S_{33} are the normal stresses along X_s, Y_s, Z_s, respectively, and S_{12}, S_{23}, S_{13} are the shear stresses on the X_sY_s, Y_sZ_s, and X_sZ_s planes. The tensor is written as

$$\boldsymbol{S}^{(s)} = \begin{bmatrix} S_{11} & S_{12} & S_{13} \\ S_{12} & S_{22} & S_{23} \\ S_{13} & S_{23} & S_{33} \end{bmatrix}.$$

4.7.2 Error and uncertainty assessment for synchrotron X-ray diffraction measurements

The synchrotron X-ray diffraction measurements contain uncertainties from detector calibration, peak fitting, peak-position determination, azimuthal integration, grain statistics, specimen positioning, and the conversion from fitted peak position to interplanar spacing. Since the measured interplanar spacing was obtained indirectly from the diffraction peak position, uncertainty in the fitted scattering vector propagates into uncertainty in d_{hkl}.

The interplanar spacing was obtained from the fitted peak position in reciprocal space using:

$$d_{hkl} = \frac{2\pi}{q}. \tag{4.8}$$

Therefore, uncertainty in peak position, Δq, gives an uncertainty in lattice spacing:

$$\frac{\Delta d_{hkl}}{d_{hkl}} = \frac{\Delta q}{q}. \tag{4.9}$$

For the present analysis, the representative diffraction peak position was taken as $q = 2.4$ Å^{-1}. The peak-position uncertainty from the fitted diffraction peak was taken as $\Delta q = 3.0 \times 10^{-4}$ Å^{-1}. The peak-position uncertainty accounts for detector calibration, azimuthal integration, peak fitting, background subtraction, and local scatter in the fitted diffraction peak position. Additional uncertainty may arise from peak overlap between α and β reflections, limited grain statistics within the illuminated volume, specimen positioning, and possible local strain heterogeneity. For the present assessment, $q = 2.4$ Å^{-1} and $\Delta q = 3.0 \times 10^{-4}$ Å^{-1}. Therefore:

$$\frac{\Delta d_{hkl}}{d_{hkl}} = \frac{\Delta q}{q} = \frac{3.0 \times 10^{-4}}{2.4} = 1.25 \times 10^{-4}. \tag{4.10}$$

Thus, the relative uncertainty in interplanar spacing is:

$$\frac{\Delta d_{hkl}}{d_{hkl}} = 1.25 \times 10^{-4}.$$

or equivalently:

$$\frac{\Delta d_{hkl}}{d_{hkl}} = 0.0125\%.$$

The corresponding interplanar spacing at $q = 2.4$ Å^{-1} is:

$$d_{hkl} = \frac{2\pi}{2.4} = 2.618 \text{ Å}.$$

The absolute uncertainty in d_{hkl} is therefore:

$$\Delta d_{hkl} = d_{hkl} \left(\frac{\Delta d_{hkl}}{d_{hkl}} \right). \tag{4.11}$$

$$\Delta d_{hkl} = 2.618 \times 1.25 \times 10^{-4}.$$

$$\Delta d_{hkl} = 3.27 \times 10^{-4} \text{ Å}. \tag{4.12}$$

Therefore, the interplanar spacing may be reported as $d_{hkl} = 2.618 \pm 0.00033$ Å.

Overall, the synchrotron X-ray diffraction measurement had an estimated relative d-spacing uncertainty of approximately 1.25×10^{-4}, equivalent to 0.0125%. For a representative peak at $q = 2.4$ Å^{-1}, this corresponds to an absolute d-spacing uncertainty of approximately $\pm 3.3 \times 10^{-4}$ Å. The main quantitative uncertainty in the measured interplanar spacing therefore arises from the fitted peak-position uncertainty, while detector calibration, azimuthal integration, peak overlap, grain statistics, specimen positioning, and local strain heterogeneity contribute to the uncertainty in the fitted q-value.

The uncertainty in the measured interplanar spacing also propagates into the calculated lattice strain and residual stress. The lattice strain for a given reflection is calculated by comparing the measured interplanar spacing, d_{hkl}, with the stress-free reference spacing, $d_{0,hkl}$:

$$\varepsilon_{hkl} = \frac{d_{hkl} - d_{0,hkl}}{d_{0,hkl}}. \tag{4.13}$$

Therefore, uncertainty in both the measured spacing and the reference spacing contributes to the uncertainty in the calculated lattice strain.

Using standard uncertainty propagation [105,106], the uncertainty in lattice strain can be expressed as

$$\Delta\varepsilon_{hkl} = \sqrt{\left(\frac{\Delta d_{hkl}}{d_{0,hkl}}\right)^2 + \left(\frac{d_{hkl}\Delta d_{0,hkl}}{d_{0,hkl}^2}\right)^2}. \tag{4.14}$$

The first term represents the contribution from uncertainty in the measured interplanar spacing, while the second term represents the contribution from uncertainty in the stress-free reference spacing. If the uncertainty in the reference spacing is small compared with the uncertainty in the measured spacing, this expression may be approximated as

$$\Delta\varepsilon_{hkl} \approx \frac{\Delta d_{hkl}}{d_{0,hkl}}. \tag{4.15}$$

The uncertainty in lattice strain then propagates into the residual stress through the elastic relationship used for stress calculation:

$$\sigma_{hkl} = E_{hkl}\varepsilon_{hkl}, \tag{4.16}$$

where E_{hkl} is the diffraction elastic modulus for the relevant reflection and loading direction. The corresponding residual stress uncertainty is therefore

$$\Delta\sigma_{hkl} = E_{hkl}\Delta\varepsilon_{hkl}. \tag{4.17}$$

If uncertainty in the diffraction elastic modulus is also considered, the propagated residual stress uncertainty can be written as

$$\Delta\sigma_{hkl} = \sqrt{\left(E_{hkl}\Delta\varepsilon_{hkl}\right)^2 + \left(\varepsilon_{hkl}\Delta E_{hkl}\right)^2}. \tag{4.18}$$

Thus, uncertainty in peak fitting first propagates into the measured d-spacing, then into the calculated lattice strain, and finally into the residual stress estimate.

4.7.3 Residual stress evolution of crystallographic planes in α and β phases present in forged Ti-6Al-4V

The geometry of the specimen indicates a nearly axisymmetric residual stress state; however, the stresses derived from reflections represent a texture-weighted average of lattice strain rather than an ideal random aggregate. The material displays an anisotropic texture (as demonstrated in Sections 3.1.3 and **??**), such that the grain populations contributing to each $\{hkl\}$ peak vary with the azimuth η for both the α (HCP) and β (BCC) phases. Consequently, the inferred stress components from individual reflections may diverge from the ideal axisymmetric expectation (e.g., $S_{11} \neq S_{33}$) due to non-uniform sampling of orientations.

Further, the reconstructed values of S_{13} and S_{23} were indistinguishable from zero for all reflections and are therefore omitted; robust determination of

these components typically requires additional specimen tilts and/or orientations to increase sensitivity to the out-of-plane component of the scattering vector (i.e., greater variation in q_z) [154, 155]. By contrast, a small non-zero S_{12} is consistent with azimuthal distortion of the Debye–Scherrer rings, to which multi-η ring-based reconstructions are highly sensitive [154]. The material's anisotropic texture can additionally influence the effective azimuthal weighting and the contributing grain subsets for a given $\{hkl\}$, which can enhance the detectability of S_{12} through reflection-dependent sampling [155, 156].

The evolution of residual stress in the α phase during the T-C loading sequence is illustrated in Figure 4.32. The basal (0002) plane demonstrates a fluctuating trend in residual stress accumulation from load cycles 0.5 to 2 (Figure 4.32(a)). In the prismatic $(10\bar{1}0)$ plane, the components S_{11}, S_{22}, and S_{33} accumulate less during tensile loading than during compressive loading, while S_{12} exhibits minimal variation (Figure 4.32(b)). Conversely, the pyramidal $(10\bar{1}1)$ and $(20\bar{2}1)$ planes display greater accumulation of residual stress under compression than under tension (Figures 4.32(c,d)). For the second-order pyramidal $(11\bar{2}2)$ plane, the stress components remain close to their earlier-step values, with a tendency for higher accumulation under compression compared to tension (Figure 4.32(e)). In summary, the residual stresses fluctuate with load reversal, exhibiting a greater build-up in compression and a relaxation in tension-indicative of an asymmetric internal stress evolution that aligns with reversal-sensitive behaviour.

The residual-stress accumulation in β is much lower than in α (Figure 4.32).

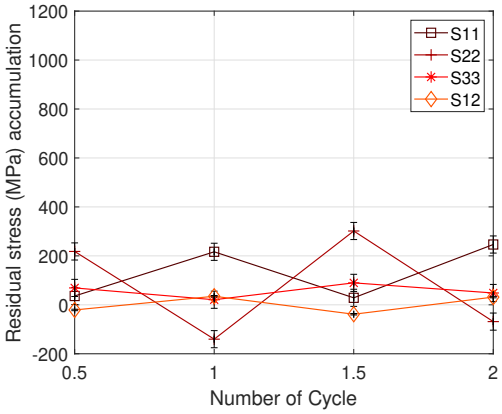
In the (110) plane, S_{12} stays near zero, while other components decrease after the first two load steps. In the (200) plane, S_{12} is consistently 0 MPa, and the other components accumulate to about -18 MPa. Similarly, in the (211) plane, S_{12} remains at 0 MPa, and the other components stabilise around -10 MPa as cycling continues. Overall, the residual stresses in β show minimal reversal-driven fluctuation and remain low, indicating that the β phase contributes weakly to the evolving internal stress state compared with the α phase.

As shown in Figure 4.33, during the C-T loading sequence the α-phase residual stresses evolve asymmetrically across planes. In the basal (0002) plane (Figure 4.33(a)), S_{11}, S_{22}, S_{33}, and S_{12} increase and then decrease from load cycle 0.5 to 2. In the prismatic $(10\bar{1}0)$ plane (Figure 4.33(b)), S_{11}, S_{22}, and S_{33} drop sharply at the first load step of cycle 1 and then remain nearly constant to cycle 2, while S_{12} remains almost constant throughout. The pyramidal $(10\bar{1}1)$ and $(20\bar{2}1)$ planes (Figures 4.33(c,d)) show increasing-decreasing behaviour with higher accumulation in compression than tension, and the second-order pyramidal $(11\bar{2}2)$ plane (Figure 4.33(e)) shows an overall decrease but remains higher in compression than tension. Overall, residual stresses evolve asymmetrically and dependently on the plane. Basal and pyramidal planes exhibit rise-fall behaviour and show greater accumulation in compression than tension, whereas the prismatic plane drops sharply at cycle 1 before stabilising until load cycle 2.

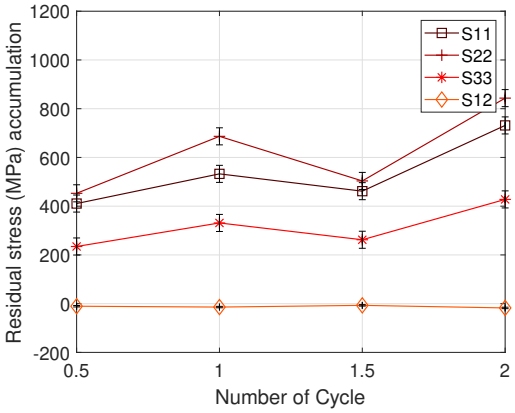
Similarly, residual stress accumulation in the β phase is shown in Figure 4.34. In the (110) plane (Figure 4.34(a)), S_{12} shows little accumulation, while

other components decrease initially and then sharply increase. In the (200) plane (Figure 4.34(b)), S_{12} remains near zero, with other components reaching about -18 MPa. In the (211) plane (Figure 4.34(c)), S_{12} stays at 0 MPa, while other components stabilise near -10 MPa as load cycles increase.

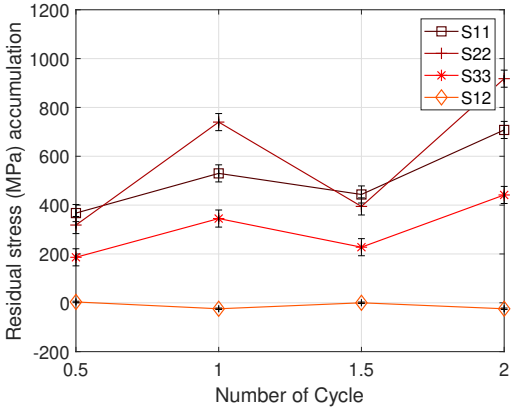
Overall, the residual stress response in the α phase exhibits fluctuations across the crystallographic planes for both loading sequences, with the notable exception of the prismatic planes. A clear directional dependence is observed in the residual stress inferred from prismatic reflections: during the T-C loading sequence, it displays significant fluctuations, while in the C-T loading sequence, it remains relatively stable from the first load cycle onward. The variation in residual stress inferred from prismatic reflections with load direction in the T-C sequence indicates a strong directional sensitivity of the α phase response to the applied loading path. In contrast, the nearly constant values across different load directions in the C-T sequence after the first load cycle suggest a reduced dependence on load direction, which corresponds to a more uniform redistribution and retention of stress as indicated by the prismatic reflections. Further, the corresponding changes in β phase residual stress are comparatively very small relative to the α phase across both loading sequences. With an estimated area fraction of $\sim$2%, it is assumed that the β phase is unlikely to significantly influence the overall residual stress behaviour.



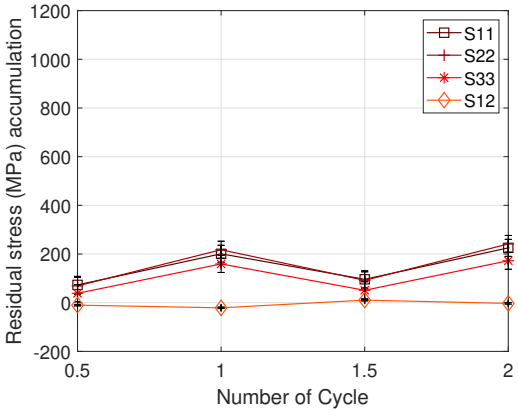
(a) Basal plane (0002) (α) (T-C load sequence)



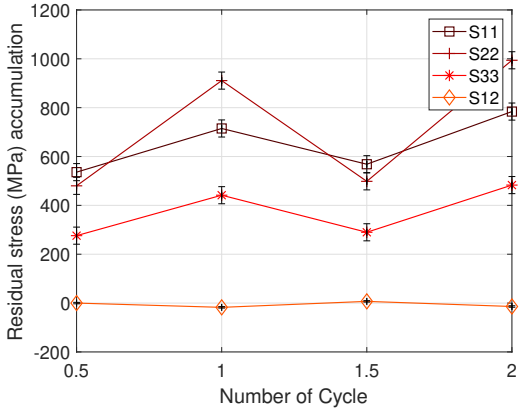
(b) Prismatic plane ($10\bar{1}0$) (α) (T-C load sequence)



(c) Pyramidal plane ($10\bar{1}1$) (α) (T-C load sequence)

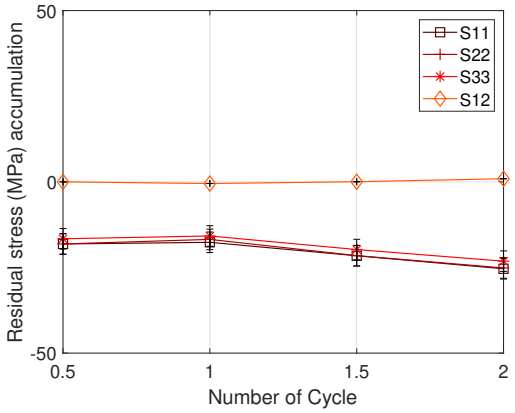


(d) Pyramidal plane ($20\bar{2}1$) (α) (T-C load sequence)

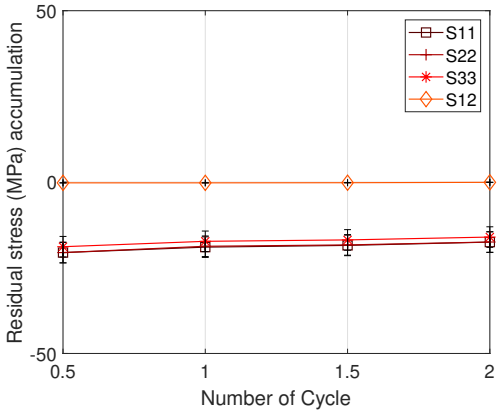


(e) Second-order Pyramidal plane ($11\bar{2}2$) (α) (T-C load sequence)

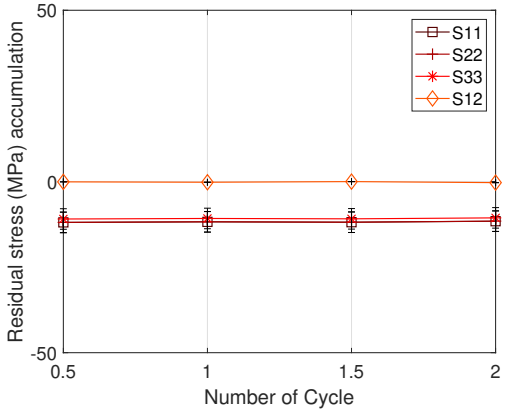
Figure 4.31: Residual stress accumulation in crystallographic planes in α phase during the T-C loading sequences, from load cycle 0.5 (Tension) to load cycle 2 (Compression). Each data point's uncertainty was estimated using the methodology outlined in Chapter 4.7.2, based on the synchrotron X-ray diffraction [141].



(a) (110) (β) (T-C load sequence)

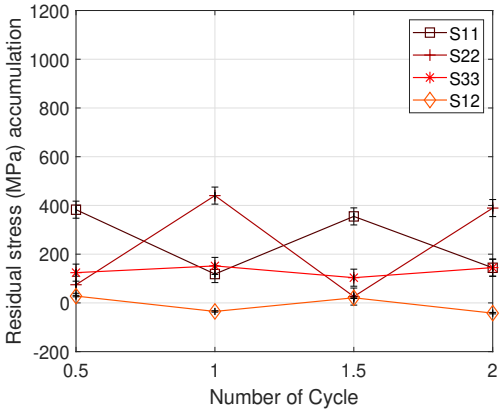


(b) (200) (β) (T-C load sequence)

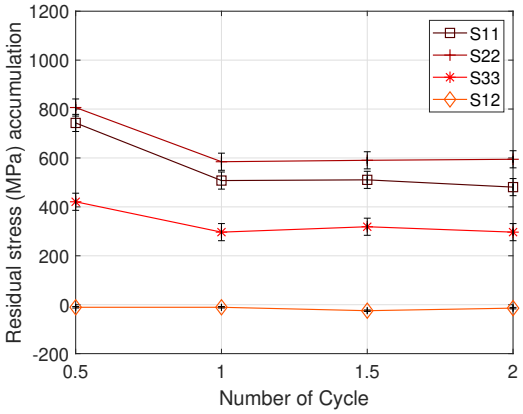


(c) (211) (β) (T-C load sequence)

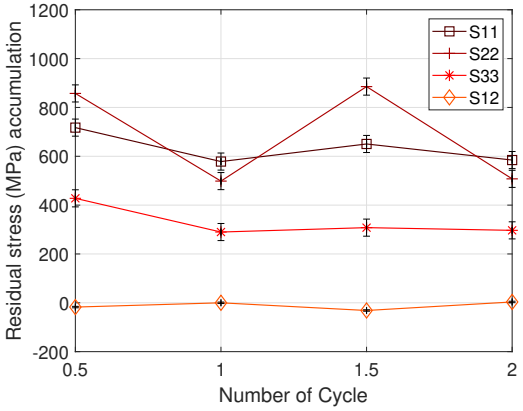
Figure 4.32: Residual stress accumulation in crystallographic planes in β phase during the T-C loading sequences, from load cycle 0.5 (Tension) to load cycle 2 (Compression). Each data point's uncertainty was estimated using the methodology outlined in Chapter 4.7.2, based on the synchrotron X-ray diffraction [141].



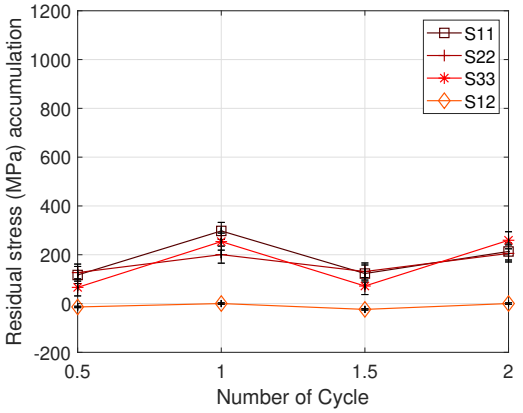
(a) Basal plane (0002) (α) (C-T load sequence)



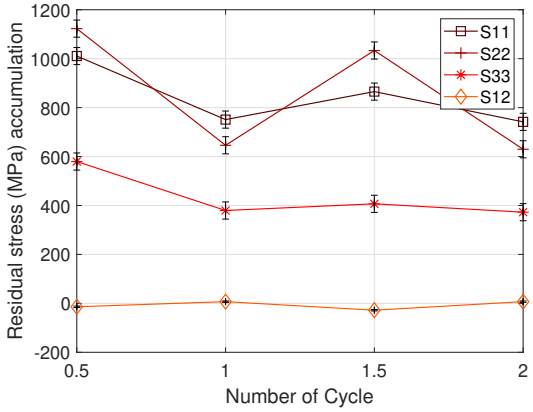
(b) Prismatic plane ($10\bar{1}0$) (α) (C-T load sequence)



(c) Pyramidal plane ($10\bar{1}1$) (α) (C-T load sequence)

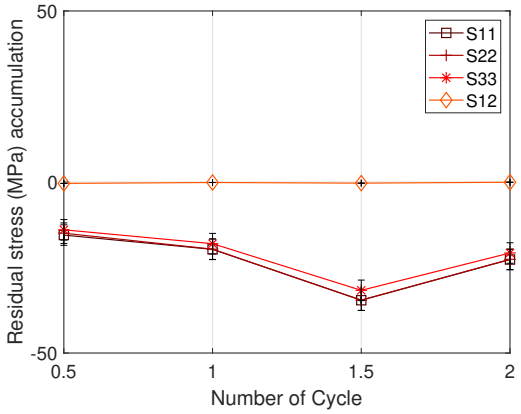


(d) Pyramidal plane ($20\bar{2}1$) (α) (C-T load sequence)

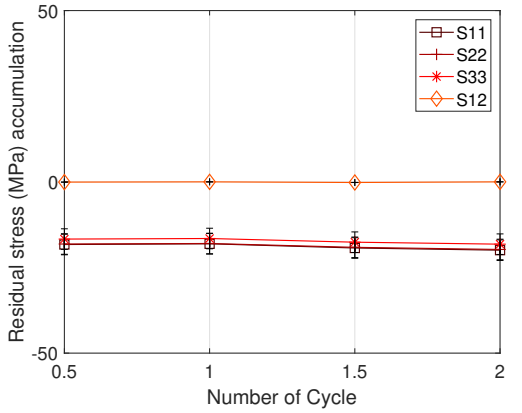


(e) Second-order Pyramidal plane ($11\bar{2}2$) (α) (C-T load sequence)

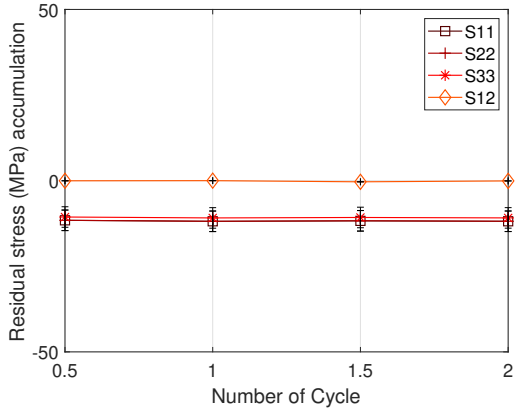
Figure 4.33: Residual stress accumulation in crystallographic planes in α phase during the T-C loading sequences, from load cycle 0.5 (Compression) to load cycle 2 (Tension). Each data point's uncertainty was estimated using the methodology outlined in Chapter 4.7.2, based on the synchrotron X-ray diffraction [141].



(a) (110) (β) (C-T load sequence)



(b) (200) (β) (C-T load sequence)



(c) (211) (β) (C-T load sequence)

Figure 4.34: Residual stress accumulation in crystallographic planes in β phase during the C-T loading sequences, from load cycle 0.5 (Compression) to load cycle 2 (Tension). Each data point's uncertainty was estimated using the methodology outlined in Chapter 4.7.2, based on the synchrotron X-ray diffraction [141].

4.8 Summary

During the low strain-rate reverse loading at room temperature, the reverse loading response of forged Ti-6Al-4V is investigated in two distinct sequences: tension followed by compression and compression followed by tension. The material exhibited a persistent Bauschinger effect during the T-C load sequence; however, this effect nearly diminished during the C-T load sequence after the first loading cycle. The observed kinematic backstress, as shown in Figure 4.9, in the T-C load sequence is noted to decrease with an increasing number of load cycles. Conversely, during the C-T load sequence, the kinematic backstress remains around 0 MPa after the initial loading cycle.

The microstructural behaviour of the material was analysed using interrupted specimens after each load step until load cycle 2. The microstructural analysis revealed the twinning-detwinning behaviour of twins, specifically twin $\{10\bar{1}2\}$ and twin $\{10\bar{1}3\}$. During the T-C load sequence, both twins exhibited asymmetric fluctuations in the twinning-detwinning trend with the increasing number of load cycles. In contrast, during the C-T load sequence, the material experienced an overall detwinning trend as the number of load cycles increased. Furthermore, the Schmid factor behaviour for all slip systems demonstrated a fluctuating increasing-decreasing trend in the median of Schmid factor values during both loading sequences, except for the Prismatic slip system during the C-T load sequence, which exhibited an almost constant median of the Schmid factor value. Interestingly, it was observed that, during the load step in which the twin boundary

length decreases, indicating detwinning, the corresponding median Schmid factor for the prismatic slip system increases, indicating a greater propensity for slip. The interrupted unsectioned specimens were also analysed for the measurement of accumulated residual stress within the material using synchrotron X-ray diffraction. The residual stress accumulation in the material revealed an asymmetrical behaviour in both loading sequences, with the exception of the Prismatic plane. Notably, the measurement indicated an intriguing trend in the Prismatic plane, which showed an asymmetric rise in residual stress accumulation during the T-C load sequence. However, during the C-T load sequence, the residual stress was observed to decrease in the first load cycle and then remained almost constant.

5 | Role of Increasing Temperature on the Bauschinger Response

5.1 Overview

In the preceding chapter, an investigation was undertaken to analyse the effects of load direction on the Bauschinger response of forged Ti-6Al-4V subjected to reverse loading at low strain-rate. This chapter aims to broaden this analysis by investigating the effect of elevated temperatures (100°C and 200°C), as well as the influence of thermal softening and load direction on the Bauschinger response of the material during reverse loading at a low strain-rate. Additionally, the Bauschinger effect is characterised, and the kinematic backstress behaviour is evaluated through successive loading cycles in both loading sequences at both temperatures. To enhance the understanding of microstructural changes and the fundamental causes of the Bauschinger effect under elevated temperatures, the reverse loading experiments are interrupted after each loading step, continuing up to the second load cycle. This interruption allows for an in-depth analysis of twin evolution, the distribution of the Schmid factor within the crystallographic planes, and the measurement of residual stress accumulation within the material.

5.2 Experimental conditions

Uniaxial reverse loading experiments were performed at elevated temperatures, 100 °C and 200 °C, on the cylindrical dog-bone-shaped specimens, as shown in Figure 3.1. The tests were conducted using a Zwick Roell Z250 machine, as shown in Figure 5.1, which is capable of delivering loads of up to ±250 kN. The experiments commenced once the temperature of the chamber reached the targeted 100 °C and 200 °C. The thermocouple wire inside the chamber confirmed that the desired temperature had been reached, as illustrated in the setup. Before the test begins, it is ensured that the temperature of the chamber matches that of the specimen. A thermocouple is attached directly to the specimen to measure its temperature, confirming that it aligns with the chamber temperature in both instances. The methodology follows the same approach as described in Chapter 4.

5.3 Experimental results

The stress-strain behaviour was examined under reverse loading at 100 °C and 200 °C in both loading sequences, as shown in Figures 5.2 and 5.3. The material withstood approximately three times more number of load cycles at 200 °C compared to 100 °C. At equivalent strain levels, the material tested at 200 °C showed a greater degree of softness compared to when it was at 100 °C. As a result, it experiences lower stress per cycle. This behaviour is consistent with the well-established principle that flow stress generally decreases as temperature increases [157, 158]. At 200 °C, dislocation movement and rearrangement occur more easily,

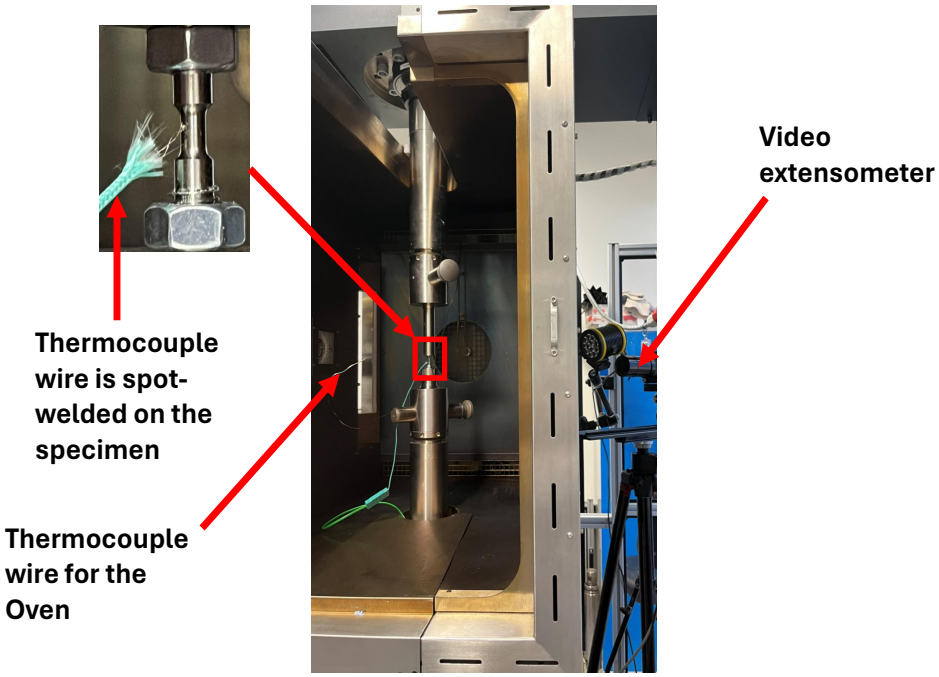


Figure 5.1: Set-up to conduct reverse loading under quasi-static conditions at elevated temperatures, 100 °C and 200 °C. The test commences when the chamber temperature, measured by the thermocouple wire, aligns with the specimen temperature, measured using the thermocouple welded to the specimen. The video extensometer is utilised to measure strain within the speckled specimen through DIC.

which facilitates dynamic recovery and stress relaxation between cycles, effectively delaying crack initiation [159].

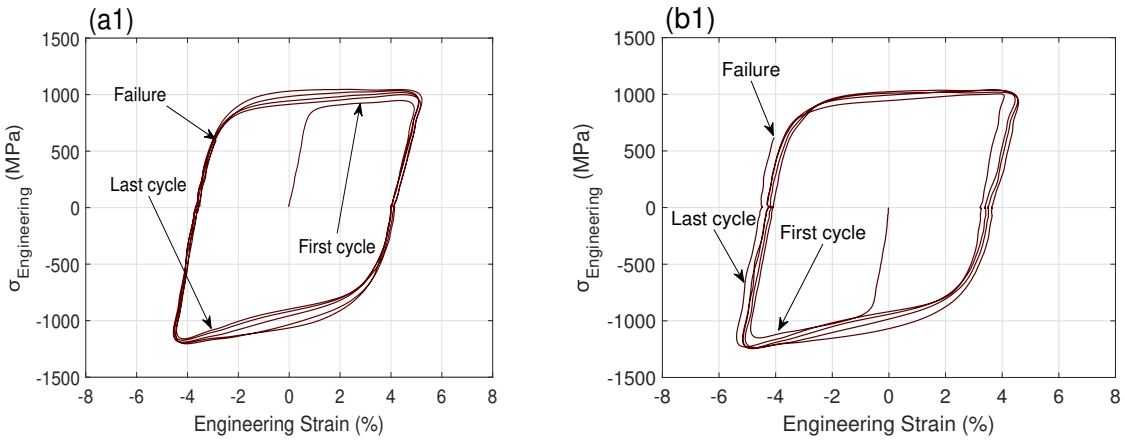


Figure 5.2: Engineering stress-strain response of forged Ti-6Al-4V during reverse deformation: (a1) T-C load sequence, (b1) C-T load sequence. These tests were conducted at controlled strain levels of 5% for the first load and 4.6% for the reverse load at a temperature of 100 °C.

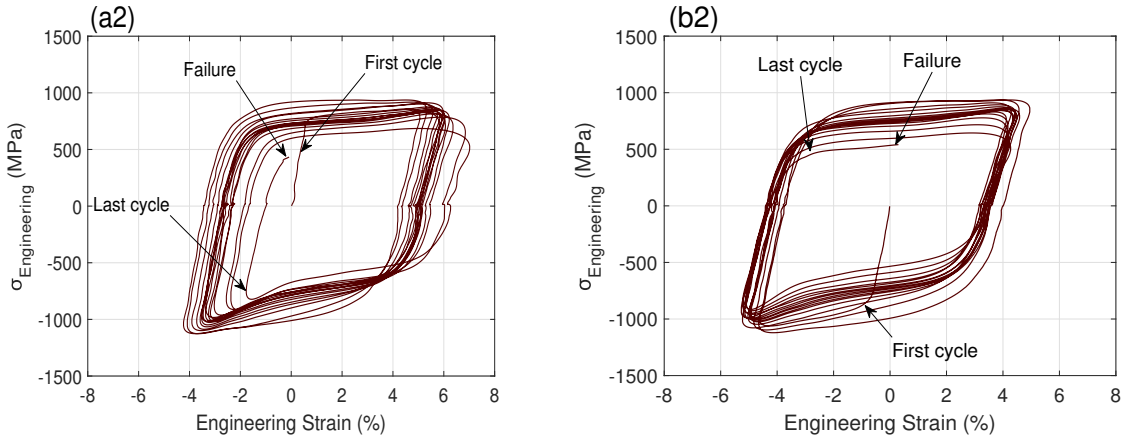


Figure 5.3: Engineering stress-strain response of forged Ti-6Al-4V during reverse deformation: (a1) T-C load sequence, (b1) C-T load sequence. These tests were conducted at controlled strain levels of 5% for the first load and 4.6% for the reverse load at a temperature of 200 °C.

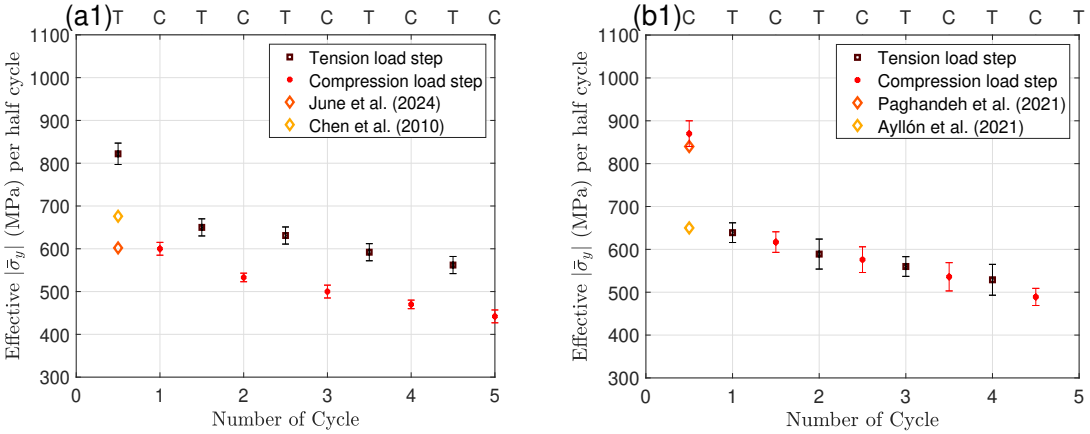


Figure 5.4: Behaviour of 0.2% effective yield strength determined from the stress-strain curve at each loading step during both the load sequences, (a1) T-C load sequence, (b1) C-T load sequence, at 100 °C. During the T-C load sequence, the Bauschinger effect persists throughout until the material failure. During the C-T load sequence, the Bauschinger effect diminishes after the first load cycle. For each load step, the yield stress ($|\sigma_y|$) was averaged over repeated measurements, and the spread was quantified by the sample standard deviation ($S_{|\sigma_y|}$); error bars show $|\bar{\sigma}_y| \pm S_{|\sigma_y|}$ [113].

As explained in Chapter 4, 0.2% strain offset method to identify the Bauschinger effect by measuring the yield stresses at each load step during successive load cycles. Consequently, this study will adopt the same methodology to examine the Bauschinger effect in both load sequences at both temperatures.

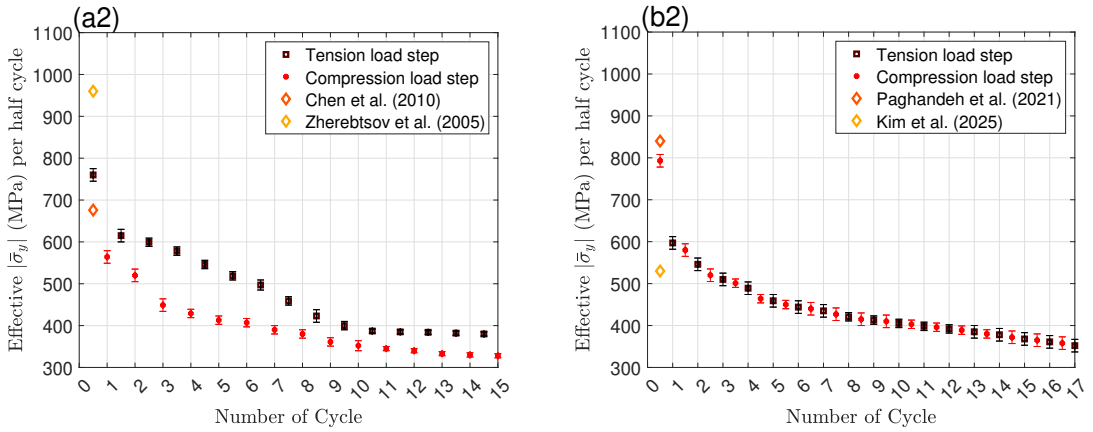


Figure 5.5: Behaviour of 0.2% effective yield strength determined from the stress-strain curve at each loading step during both the load sequences, (a2) T-C load sequence, (b2) C-T load sequence, at 200 °C. During the T-C load sequence, the Bauschinger effect persists throughout until the material failure, although magnitude of the effect tends to decrease towards the end of the test. During the C-T load sequence, the Bauschinger effect diminishes after the first load cycle. For each load step, the yield stress ($|\sigma_y|$) was averaged over repeated measurements, and the spread was quantified by the sample standard deviation ($S_{|\sigma_y|}$); error bars show $|\bar{\sigma}_y| \pm S_{|\sigma_y|}$ [113].

In Figure 5.4(a1), the Bauschinger effect is observed throughout the T-C load sequence at 100 °C until the material fails. Previous studies conducted by June et al. (2024) measured the tensile yield stress of Ti-6Al-4V produced by laser powder bed fusion to be 602 MPa, with tests conducted at a temperature of 250°C [160]. Notably, the material does not exhibit any strong texture. Chen et al. (2010) measured the tensile yield stress of cast-and-extruded Ti-6Al-4V at 455°C to be 676 MPa [161]. The X-ray diffraction (XRD) pole figures indicate that it is a basal-textured material.

In the C-T load sequence, as shown in Figure 5.4(b1), the Bauschinger effect was observed until load cycle 1; after that, this effect diminishes. Paghandeh et al. (2021) measured the compressive yield stress of Ti-6Al-4V at 100°C to be 840

MPa [162]. The microstructures are strongly textured, with most α grains oriented around the midline of (0001). Ayllón et al. (2021), in their study published in Metals, measured the compressive yield stress of Ti-6Al-4V, which was mill-annealed [163]. The test was conducted at 300°C, yielding a value of 650 MPa. However, they did not explicitly mention the texture in their paper.

Similarly, in Figure 5.5(a2), during the T-C load sequence at 200 °C, the Bauschinger effect remained consistent throughout the test; however, towards the end, the magnitude of the effect seemed to decrease. In the C-T load sequence, as shown in Figure 5.5(b2), the Bauschinger effect is observed in the first load cycle; however, it diminishes in subsequent cycles. Previous studies conducted by Zherebtsov et al. (2005) measured the tensile yield stress of Ti-6Al-4V at elevated temperatures, obtaining a value of 960 MPa at 600°C [164]. The material exhibited a weak texture. Kim et al. (2025) measured the compressive yield stress of wrought Ti-6Al-4V to be 530 MPa at 500°C [118]. EBSD pole figures ({0001}, $\{10\bar{1}0\}$, $\{11\bar{2}0\}$) indicate that the wrought Ti-6Al-4V displays an overall weak texture.

During reverse loading in both loading sequences at both temperatures, the isotropic and kinematic hardening behaviour of the material is also explored in Figures 5.6 and 5.7. Isotropic and Kinematic hardening behaviours are determined with the same process as described in the Chapter 4.

At the beginning of the test (i.e., load cycle 0.5), the size of the yield surface is 1692 MPa for both loading sequences at 100 °C, as indicated by point

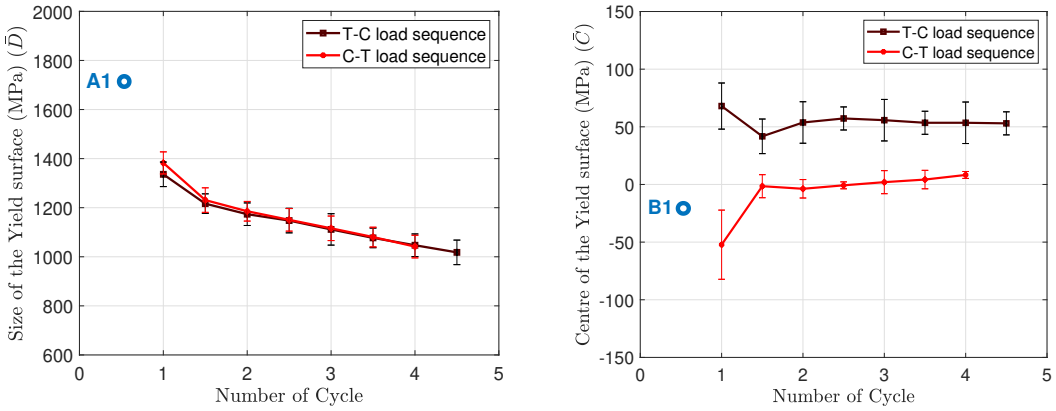


Figure 5.6: Isotropic hardening (Size of the yield surface) (on the left) and Kinematic hardening (Centre of the yield surface) (on the right) of both the loading sequences at 100 °C. Point A1 shows the size of the yield surface (D) at load cycle 0.5 for both the T-C and C-T load sequences. The size of the yield surface decreases as the number of cycles increases in both load sequences. Point B1 shows the centre of the yield surface (C) at load cycle 0.5 for both the T-C and C-T load sequences. The centre of the yield surface gradually shifts downward after the first load cycle and then remains constant during the T-C load sequence. In contrast, during the C-T load sequence, it moves significantly upwards towards zero before stabilising. For each condition, the Isotropic hardening (D) and Kinematic hardening (C) were averaged over repeated measurements, and the spread was quantified by the corresponding sample standard deviations (S_D and S_C); error bars show $\bar{D} \pm S_D$ and $\bar{C} \pm S_C$ [113].

A1 in Figure 5.6, and 1553 MPa at 200 °C, as shown by point A2 in Figure 5.7. It is observed to contract at both temperatures and load sequences as the number of load cycles increases. This contraction suggests that softening occurs within the material due to fatigue loading [165].

Similarly, the centre of the yield surface in both loading sequences is -24 MPa as indicated by point B1 at 100 °C, while the centre of the yield surface in both loading sequences is -16.5 MPa, represented by point B2 at 200 °C. During the T-C load sequence at 100 °C, the centre of the yield surface experiences a substantial decrease of approximately 25 MPa from load cycle 1 to 1.5, after which

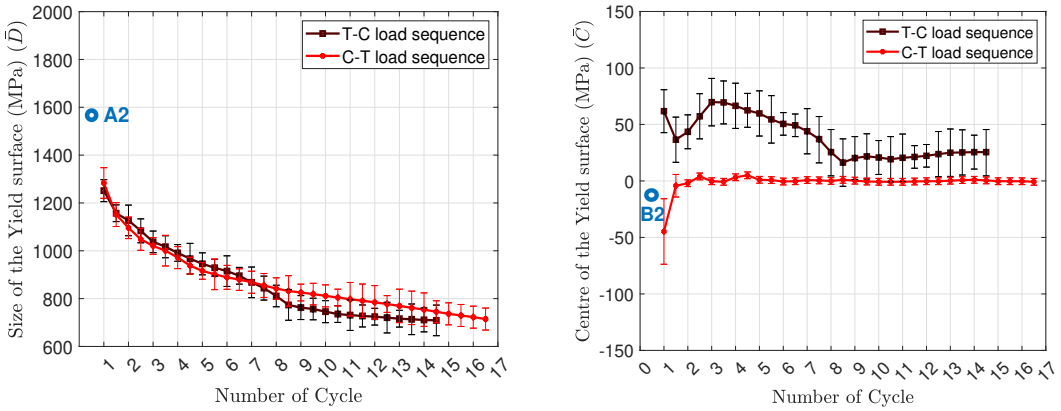


Figure 5.7: Isotropic hardening (Size of the yield surface) (on the left) and Kinematic hardening (Centre of the yield surface) (on the right) of both the loading sequences at 200 °C. Point A2 shows the size of the yield surface (D) at load cycle 0.5 for both the T-C and C-T load sequences. The size of the yield surface is observed to be decreasing with the increasing number of load cycles in both loading sequences. Point B2 shows the centre of the yield surface (C) at load cycle 0.5 for both the T-C and C-T load sequences. The centre of the yield surface during the T-C load sequence is observed to vary and globally decrease with the increasing number of load cycles. During the C-T load sequence, the centre moved drastically positive and stayed very close to zero until the material fails. For each condition, the Isotropic hardening (D) and Kinematic hardening (C) were averaged over repeated measurements, and the spread was quantified by the corresponding sample standard deviations (S_D and S_C); error bars show $\bar{D} \pm S_D$ and $\bar{C} \pm S_C$ [113].

it remains relatively constant. In contrast, during the C-T load sequence, the centre of the yield surface shifts positively from load cycle 1 to 1.5, subsequently stabilising closer to 0 MPa until material failure occurs. At 200 °C, during the T-C load sequence, the centre of the yield surface is observed to decrease globally, fluctuating until load cycle 8.5, before stabilising around 25 MPa until material failure. In contrast, during the C-T load sequence, the centre of the yield surface remains close to 0 MPa following the first load cycle.

The behaviour of the mean kinematic hardening in both loading sequences at both temperatures is demonstrated in Figure 5.8. For each condition, the kine-

matic hardening parameter (C) was averaged over repeated measurements and the spread was quantified using the sample standard deviation (S_C); error bars indicate $\bar{C} \pm S_C$ [113]. In both load sequences, it is observed that the mean kinematic hardening decreases with increasing temperature; although the change in the C-T load sequence is minimal. This reduction in mean kinematic hardening occurs in both loading sequences because elevated temperatures facilitate the recovery process and the relaxation of internal stress fields through mechanisms such as dislocation climb, rearrangement, and annihilation [166].

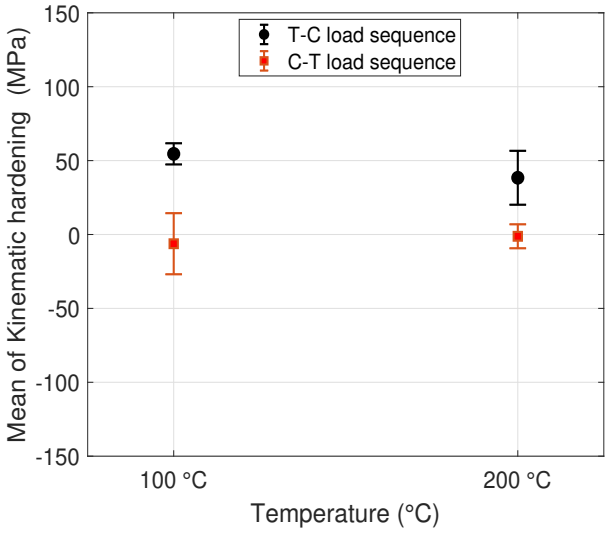


Figure 5.8: The mean kinematic hardening $\bar{C}$ behaviour at both temperatures and loading sequences is demonstrated. In the T-C load sequence, the mean kinematic hardening decreases as the temperature increases. Similarly, in the C-T load sequence, the mean kinematic hardening approaches 0 MPa with increasing temperature, although the change is very minimal. For each condition, kinematic hardening (C) is averaged over repeated measurements and the spread was quantified by the sample standard deviation (S_C); error bars show $\bar{C} \pm S_C$ [113].

5.4 Microstructural analysis via Electron Backscatter Diffraction (EBSD) of sectioned interrupted specimens at 100 °C and 200 °C with increasing load cycles

To gain a better understanding of the Bauschinger response with increasing load cycles at 100 °C and 200 °C, microstructural analysis using Electron Backscatter Diffraction (EBSD) was conducted on interrupted specimens from load cycle 0.5 to 2 in both loading sequences. The method used for this investigation is the same as described in Chapter 4.

5.4.1 Twin evolution in forged Ti-6Al-4V

The evolution of Twin Boundary Length for $\{10\bar{1}2\}$ and $\{10\bar{1}3\}$ at 100 °C and 200 °C twins is shown in Figures 5.9 and 5.10, comparing both T-C and C-T load sequences as the number of load cycles increases. At both temperatures, the T-C load sequence exhibits asymmetric fluctuations in Twin Boundary Length, characterised by a decrease (detwinning), followed by an increase (twinning), and then a further decrease with increasing cycle number, indicating that twinning and detwinning remain active beyond the initial load step, although with reduced amplitude as cycling progresses. In contrast, the C-T load sequence at both 100 °C and 200 °C shows changes primarily during the initial transient phase (up to cycle 1). After this point, the twin boundary lengths evolve more gradually, reflecting early microstructural stabilisation and suggesting that subsequent deformation is

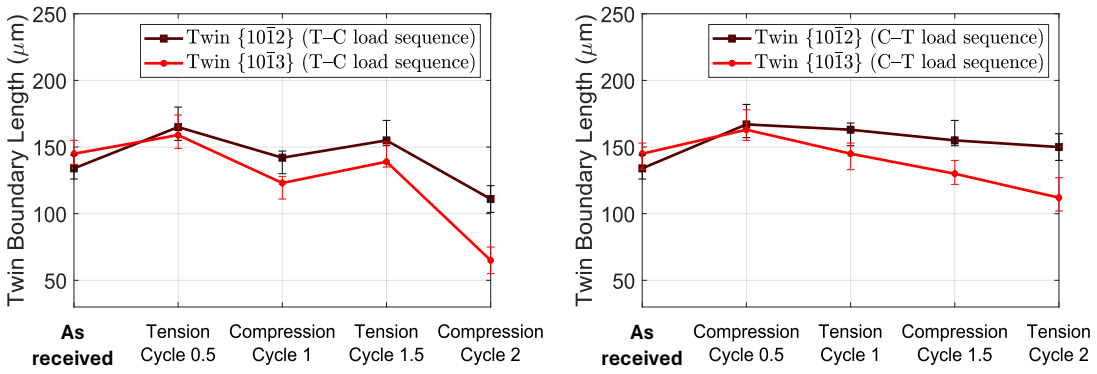


Figure 5.9: The evolution of twin boundary length for {10$\bar{1}$2} and {10$\bar{1}$3} twins during interrupted T-C (left) and C-T (right) loading demonstrates distinct behaviour under the two loading paths. Throughout the T-C cycle, twinning and detwinning exhibit asymmetric variations across successive cycles, with the twin boundary length in tension consistently greater than that in compression. Conversely, the C-T cycle displays marked changes during the initial load, followed by a gradual decrease in twin boundary length. This suggests that the twin microstructure stabilises at an early stage, with subsequent deformation primarily accommodated by non-twinning mechanisms, most likely slip. The uncertainty was estimated from the EBSD scan spatial resolution, based primarily on the step size and the criteria used for twin boundary identification in OIM. The calculation of error is based on a methodology similar to the one described in Chapter 3.1.4.

increasingly accommodated by slip rather than continued twinning activity [167].

The trend observed in both twins, {10$\bar{1}$2} and {10$\bar{1}$3}, across both loading sequences at 100 °C and 200 °C, reveals an interesting load directional dependence behaviour. This observation suggests that the twinning-detwinning phenomena significantly contribute to the Bauschinger effect at elevated temperatures. Moreover, as the temperature increases, the twinning boundary length during the first loading step shows a slight reduction. This decrease can be attributed to the thermal activation of additional slip systems at higher temperatures [64, 167–169]. These slip systems can accommodate c-axis strain that would otherwise be absorbed by twinning [64, 167–169]. As a result, deformation becomes increasingly

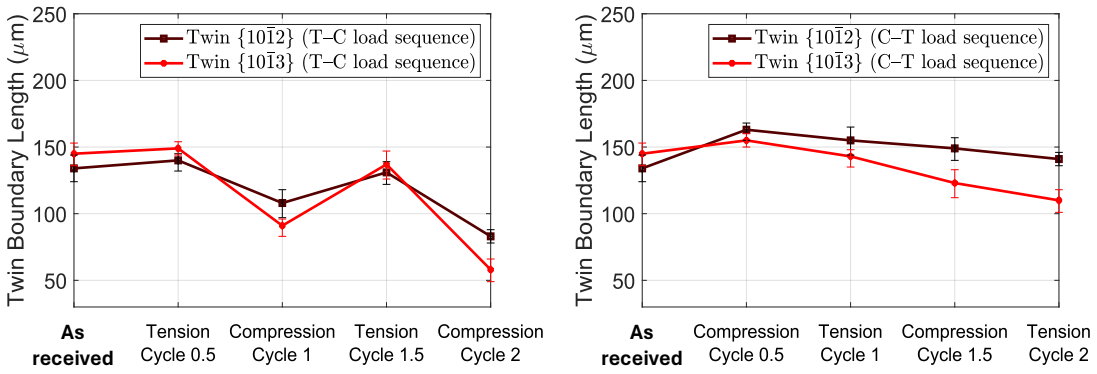


Figure 5.10: The evolution of twin boundary lengths for $\{10\bar{1}2\}$ and $\{10\bar{1}3\}$ twins during interrupted T-C and C-T loading exhibits distinct trends under the two loading pathways. In the T-C cycle, the processes of twinning and detwinning demonstrate asymmetrical variation from one load step to the next. In contrast, the C-T cycle shows the most significant changes occurring during the initial loading steps, followed by a gradual reduction in twin boundary length. The uncertainty was estimated from the EBSD scan spatial resolution, based primarily on the step size and the criteria used for twin boundary identification in OIM. The calculation of error is based on a methodology similar to the one described in Chapter 3.1.4.

dominated by slip, thereby diminishing the role of twinning.

5.4.2 Schmid factor evolution of crystallographic slip systems in α and β phases in forged Ti-6Al-4V

Similar to Chapter 4, the behaviour of the Schmid factor for the interrupted specimens is examined from load cycle 0.5 to load cycle 2 at elevated temperatures of 100 °C and 200 °C. This analysis is conducted in both the α and β phases, as well as under two different load sequences, as illustrated in Figures 5.11 to 5.46. These figures depict the distribution of the Schmid factor, m, alongside its median, $\tilde{m}$, as the number of load cycles increases across the grains oriented in different directions.

Figures 5.11 to 5.16 summarise the evolution of the median Schmid factor, $\tilde{m}$, for the dominant α phase slip families during the T-C load sequence at 100 °C. For the basal slip system, the response is characterised by asymmetric oscillation. In contrast, the prismatic slip system is not favourable during the first load step (tension), but it becomes favourable when the load is reversed (compression). The Pyramidal slip systems show smaller-amplitude oscillations, consistent with limited but persistent rebalancing of the propensity of slip. The strongest redistribution occurs for the second-order pyramidal systems, where $\tilde{m}$ exhibits the most pronounced asymmetric changes across reversals, including a marked dip followed by recovery in the later cycles. Overall, these trends highlight that T-C cycling drives an asymmetric, cycle-dependent redistribution of slip favourability across α-phase slip families, rather than stabilising towards a single dominant slip mode.

The evolution of the median Schmid factor, $\tilde{m}$, for the β phase slip families during the T-C load sequence at 100 °C is depicted in Figures 5.17 to 5.19. Unlike the α phase, the β phase shows minimal sensitivity to load reversal and cycle progression. The dominant slip systems, $\{110\}\langle\bar{1}11\rangle$, $\{200\}\langle011\rangle$, and $\{211\}\langle\bar{1}11\rangle$, remain stable, with $\tilde{m}$ demonstrating only slight variations. This stability indicates no redistribution of slip favourability within the β phase during the cyclic load sequence, suggestive of a consistent deformation propensity among the main β slip families.

The evolution of the median Schmid factor, $\tilde{m}$, for the α phase slip families

during the C-T load sequence at 100 °C is shown in Figures 5.20 to 5.25. The basal slip system exhibits modest, asymmetric oscillations and returns close to its initial level. The prismatic slip system stabilises after the first reversal, suggesting limited redistribution beyond the initial transient. In contrast, the pyramidal families show stronger reversal sensitivity: the pyramidal slip systems display larger asymmetric swings with partial recovery, while the second-order pyramidal system undergo the most pronounced early-cycle redistribution and only partial recovery thereafter. Overall, $\tilde{m}$ responds to load reversal across all families, indicating a cyclic redistribution of slip favourability that is largely transient-dominated in C-T, with the largest changes occurring early.

The evolution of the median Schmid factor, $\tilde{m}$, for the β phase slip families during the C-T load sequence at 100 °C is shown in Figures 5.26 to 5.28. Overall, the β phase exhibits only minor, transient changes in $\tilde{m}$ following the first reversal, after which the principal $\{110\}\langle\bar{1}11\rangle$, $\{200\}\langle011\rangle$, and $\{211\}\langle\bar{1}11\rangle$ systems remain essentially stable up to load cycle 2. This near-constant behaviour indicates limited redistribution of slip favourability within the β phase under C-T cycling at 100 °C.

The evolution of the median Schmid factor, $\tilde{m}$, for the α-phase slip families during the T-C load sequence at 200 °C is shown in Figures 5.29 to 5.34. The basal slip system shows pronounced reversal sensitivity, with $\tilde{m}$ shifting markedly between tension and compression. The prismatic slip system displays strong asymmetric swings, including a clear reduction under tension followed by recovery on reloading in compression. The pyramidal slip systems exhibit smaller-amplitude

oscillations superimposed on a mild overall reduction, suggesting a more limited redistribution than basal and prismatic slip. The largest reversal-driven redistribution occurs for the second-order pyramidal slip system, which show the most substantial asymmetric changes across reversals and only partial recovery with continued cycling. Overall, these trends highlight an asymmetric, cycle-dependent redistribution of deformation propensity among α-slip families during T-C cycling at 200 °C.

The evolution of the median Schmid factor, $\tilde{m}$, for the β phase slip families during the T-C load sequence at 200 °C is shown in Figures 5.35 to 5.37. Overall, the β phase exhibits weak sensitivity to load reversal and cycle progression, with $\tilde{m}$ remaining essentially stable across the dominant $\{110\}\langle\bar{1}11\rangle$, $\{200\}\langle011\rangle$, and $\{211\}\langle\bar{1}11\rangle$ systems. Only minor, transient variation is observed after the first loading step, indicating limited redistribution of slip favourability within the β phase during cyclic T-C loading at 200 °C.

The evolution of the median Schmid factor, $\tilde{m}$, for the α phase slip families during the C-T load sequence at 200 °C is shown in Figures 5.38 to 5.43. The basal slip system shows modest oscillations. The prismatic slip system evolves smoothly with only minor changes, suggesting weak redistribution after the initial transient. The pyramidal slip system display clearer asymmetric swings across reversals, with partial recovery on reloading. The strongest reversal sensitivity is observed for the second-order slip pyramidal systems, which undergo the largest redistribution and only partial recovery with continued cycling. Collectively, these

trends show that C-T cycling at 200 °C preferentially redistributes deformation propensity among the pyramidal families, while basal and prismatic slip systems remain comparatively less affected. Overall, $\tilde{m}$ shows asymmetric, reversal-driven oscillations across all slip systems, except for the prismatic slip system, where cyclic redistribution of slip favourability is greater than in others.

The evolution of the median Schmid factor, $\tilde{m}$, for the β phase slip families during the C-T load sequence at 200 °C is shown in Figures 5.44 to 5.46. Overall, the β phase shows minimal sensitivity to load reversal and cycle progression, with $\tilde{m}$ remaining essentially stable across the dominant $\{110\}\langle\bar{1}11\rangle$, $\{200\}\langle011\rangle$, and $\{211\}\langle\bar{1}11\rangle$ slip systems. This near-constant behaviour indicates limited redistribution of slip favourability within the β phase during cyclic C-T loading at 200 °C.

In conclusion, both temperatures show differences in the prismatic slip system within the α phase, where the $\tilde{m}$ value fluctuates during the T-C loading sequence but remains stable during the C-T loading sequence. The variation in the $\tilde{m}$ value with different loading directions during the T-C sequence indicates that slip favourability is influenced by the direction of the load. In contrast, during the C-T loading sequence, the $\tilde{m}$ values stay consistent across various load directions, implying the slip favourability is not affected by the load direction. There are no significant differences found in the β phase between the two loading sequences, and with an estimated area fraction of 2%, it is unlikely that the β phase has a major effect on the observed behaviour.

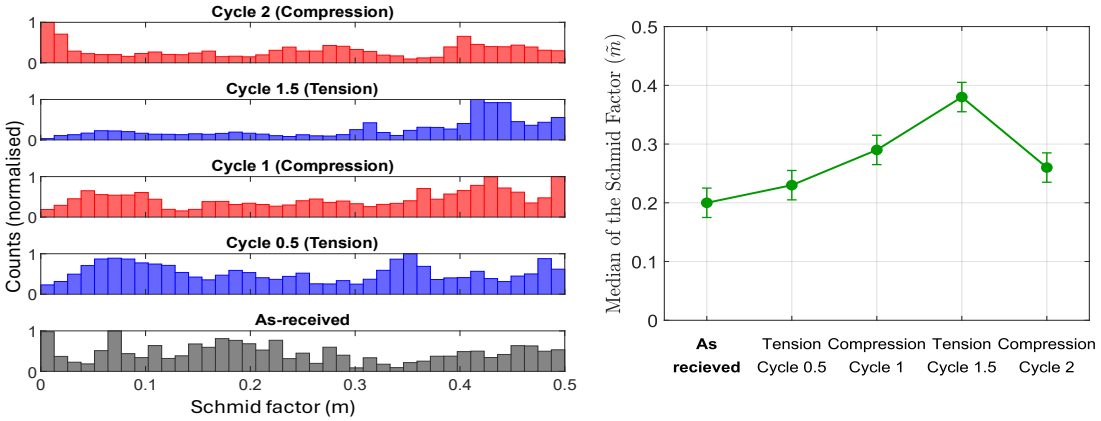


Figure 5.11: Basal slip system $\{0002\}\langle 11\bar{2}0\rangle$ (α) (T-C load sequence) at 100 °C

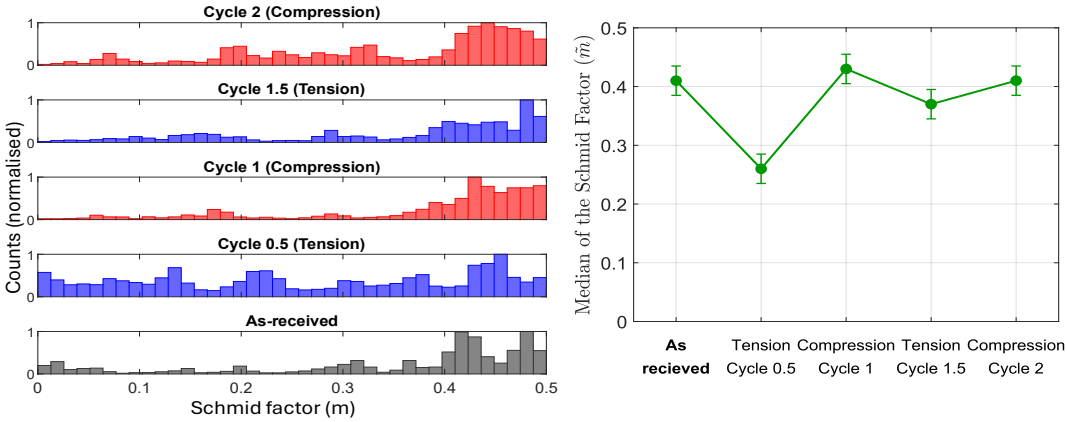


Figure 5.12: Prismatic slip system $\{10\bar{1}0\}\langle\bar{1}2\bar{1}0\rangle$ (α) (T-C load sequence) at 100 °C

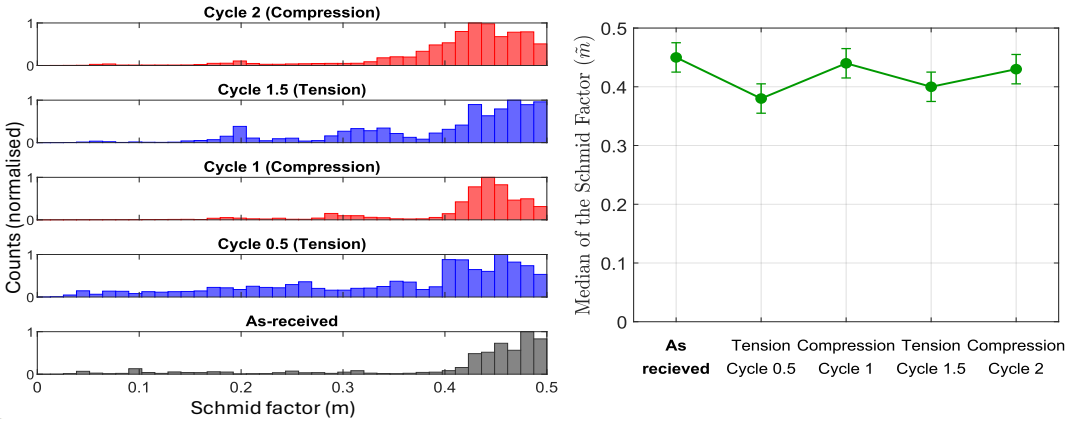


Figure 5.13: Pyramidal slip system $\{10\bar{1}1\}\langle\bar{1}2\bar{1}0\rangle$ (α) (T-C load sequence) at 100 °C

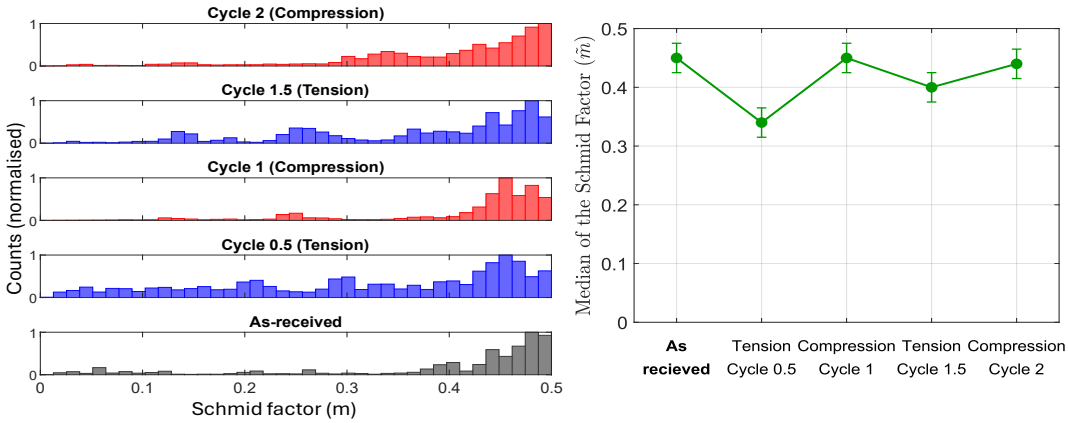


Figure 5.14: Pyramidal slip system $\{20\bar{2}1\}\langle\bar{1}2\bar{1}0\rangle$ (α) (T-C load sequence) at 100 °C

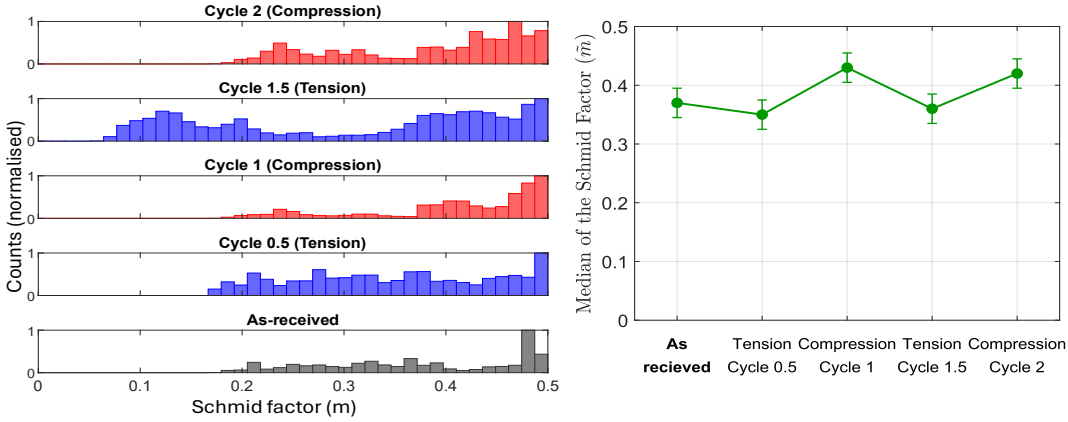


Figure 5.15: Second-order pyramidal slip system $\{11\bar{2}2\}\langle\bar{1}\bar{1}23\rangle$ (α) (T-C load sequence) at 100 °C

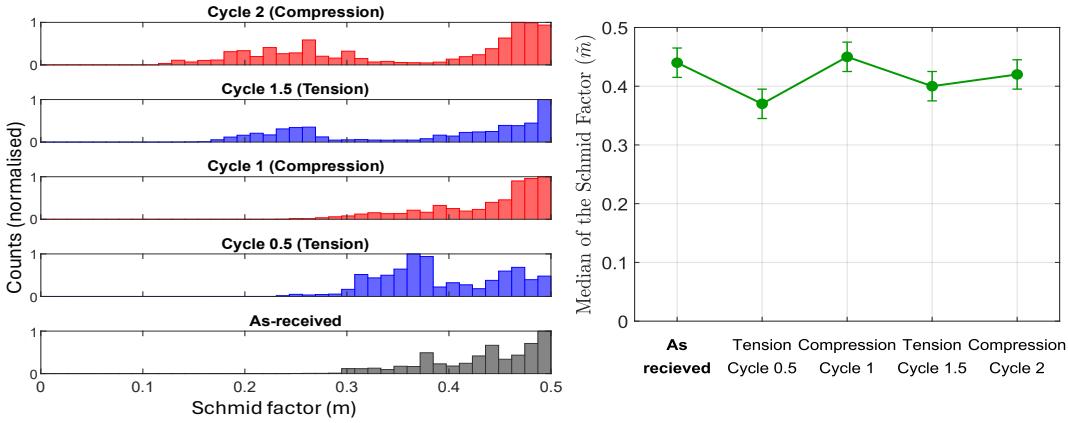


Figure 5.16: Pyramidal slip system $\{20\bar{2}2\}\langle\bar{1}\bar{1}23\rangle$ (α) (T-C load sequence) at 100 °C

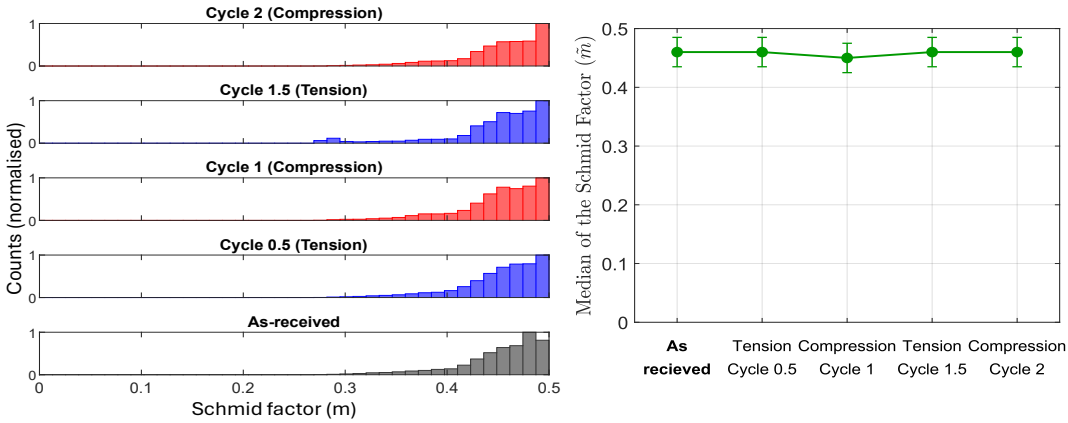


Figure 5.17: $\{110\}\langle\bar{1}11\rangle$ slip system (β) (T-C load sequence) at 100 °C

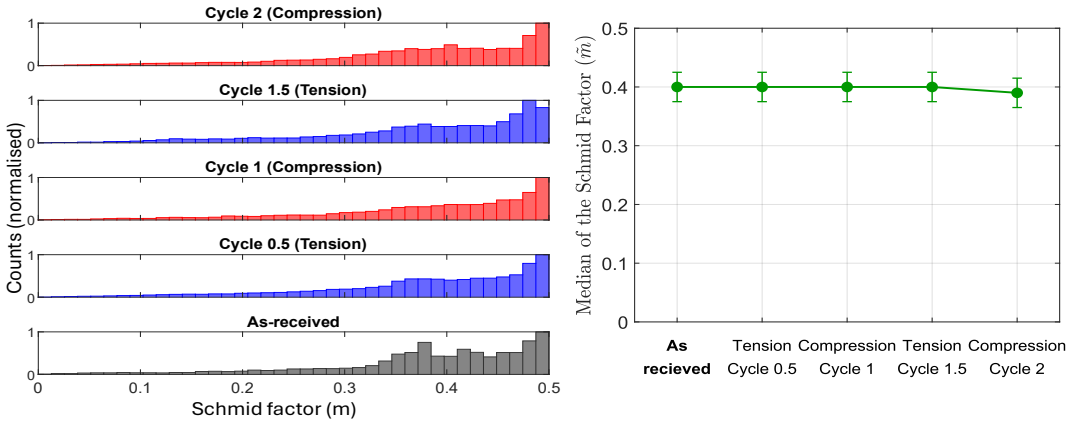


Figure 5.18: $\{200\}\langle011\rangle$ slip system (β) (T-C load sequence) at 100 °C

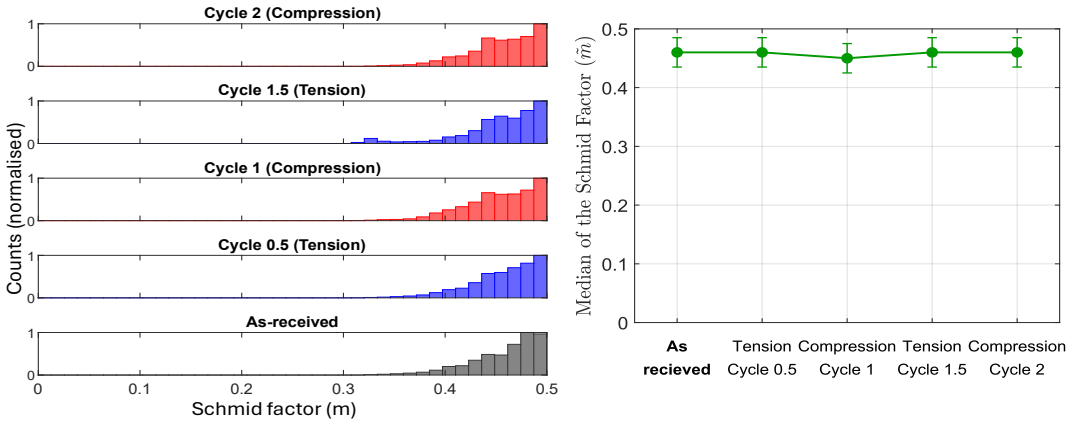


Figure 5.19: $\{211\}\langle\bar{1}11\rangle$ slip system (β) (T-C load sequence) at 100 °C

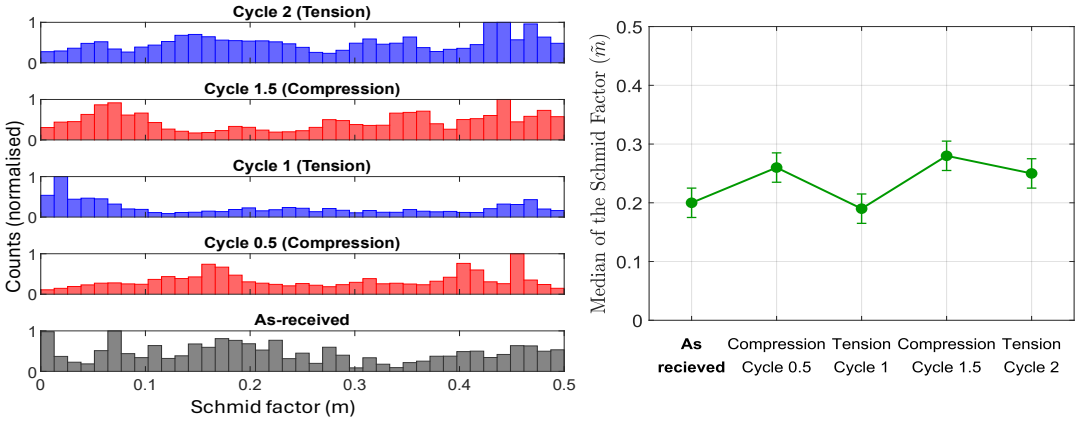


Figure 5.20: Basal slip system $\{0002\}\langle 11\bar{2}0\rangle$ (α) (C-T load sequence) at 100 °C

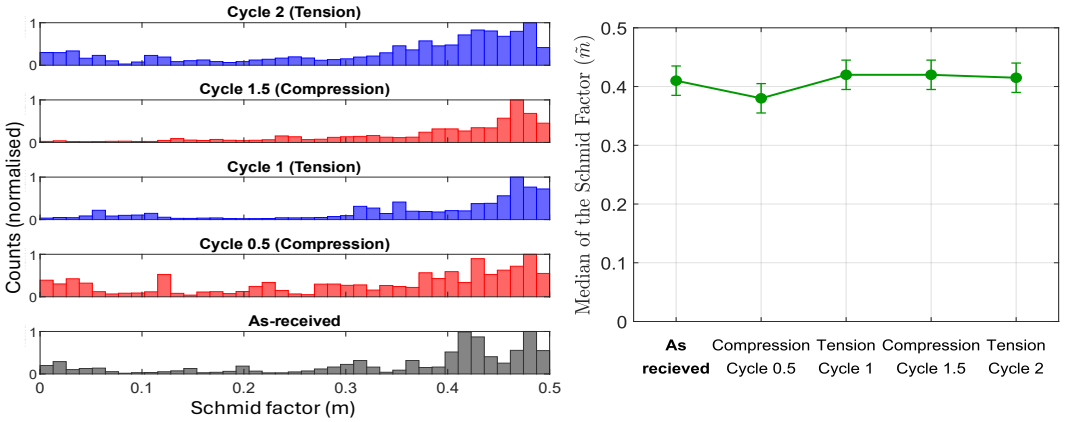


Figure 5.21: Prismatic slip system $\{10\bar{1}0\}\langle\bar{1}2\bar{1}0\rangle$ (α) (C-T load sequence) at 100 °C

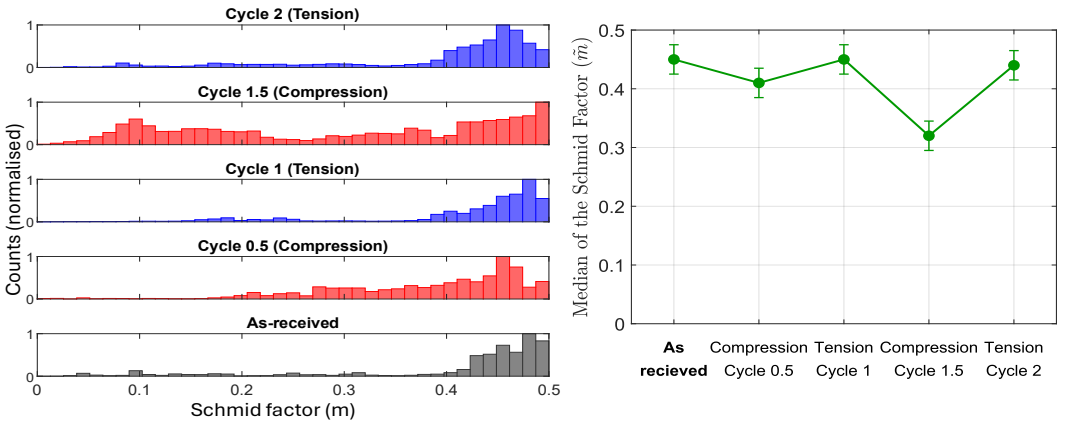


Figure 5.22: Pyramidal slip system $\{10\bar{1}1\}\langle\bar{1}2\bar{1}0\rangle$ (α) (C-T load sequence) at 100 °C

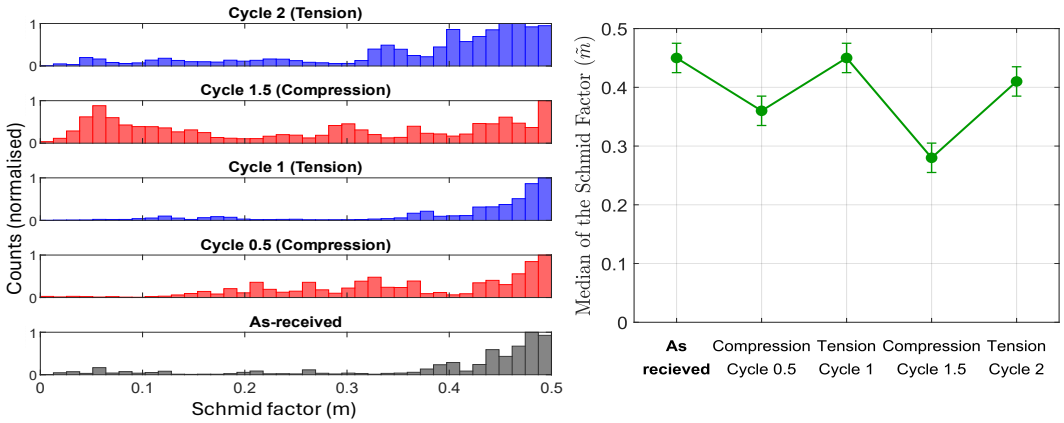


Figure 5.23: Pyramidal slip system $\{20\bar{2}1\}\langle\bar{1}2\bar{1}0\rangle$ (α) (C-T load sequence) at 100 °C

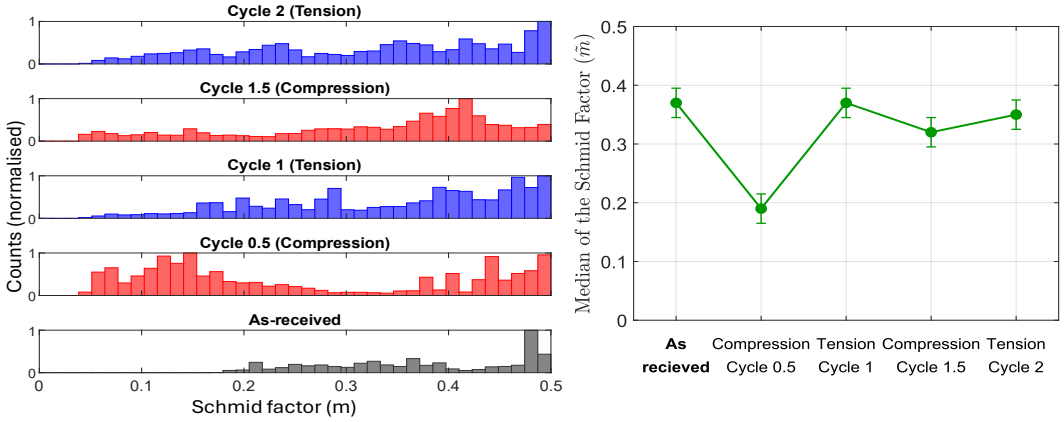


Figure 5.24: Second-order pyramidal slip system $\{11\bar{2}2\}\langle\bar{1}\bar{1}23\rangle$ (α) (C-T load sequence) at 100 °C

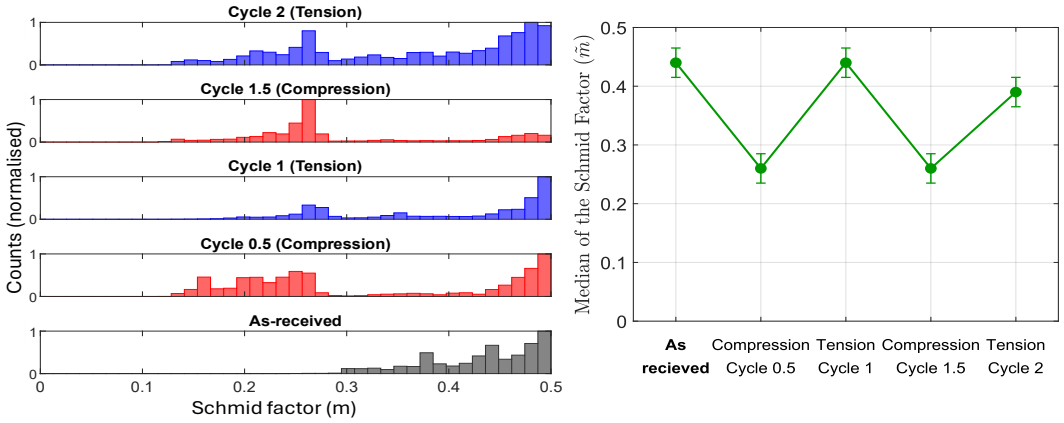


Figure 5.25: Pyramidal slip system $\{20\bar{2}2\}\langle\bar{1}\bar{1}23\rangle$ (α) (C-T load sequence) at 100 °C

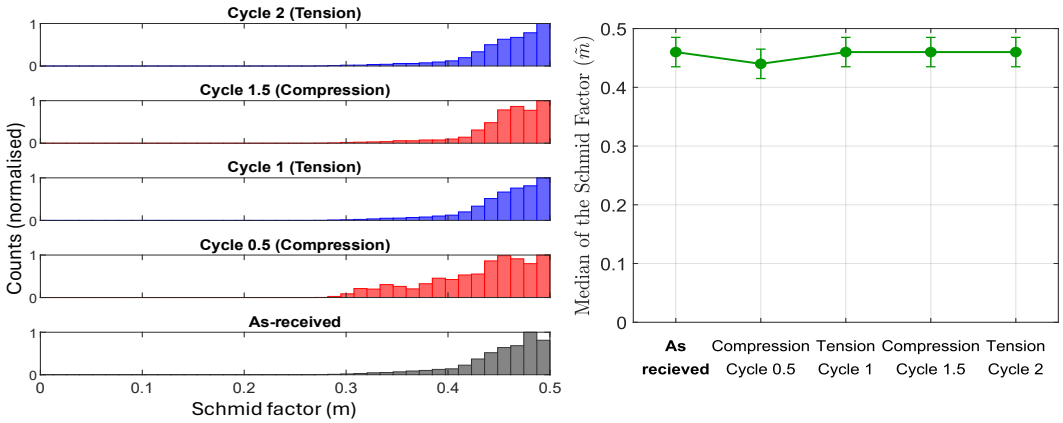


Figure 5.26: $\{110\}\langle\bar{1}11\rangle$ slip system (β) (C-T load sequence) at 100 °C

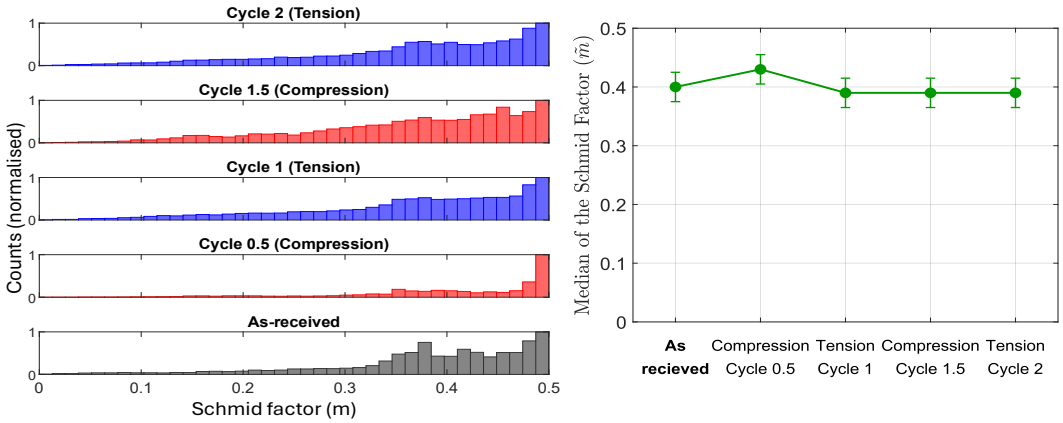


Figure 5.27: $\{200\}\langle011\rangle$ slip system (β) (C-T load sequence) at 100 °C

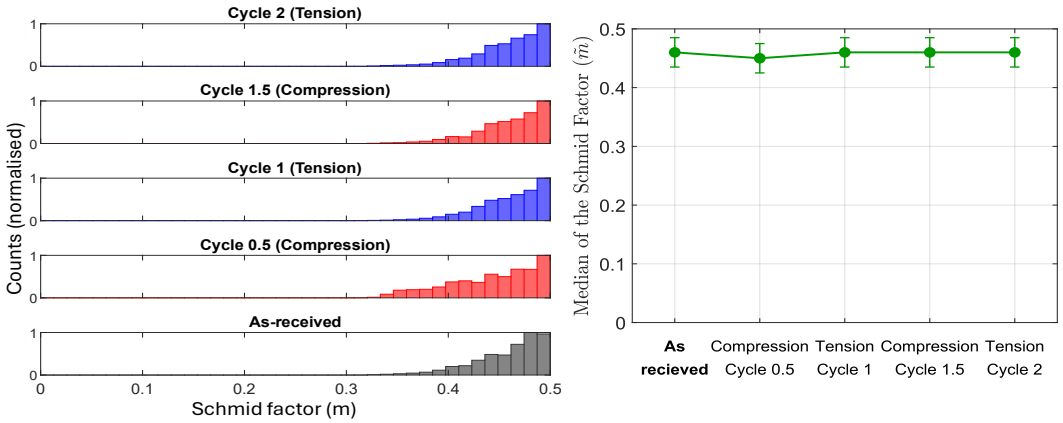


Figure 5.28: $\{211\}\langle\bar{1}11\rangle$ slip system (β) (C-T load sequence) at 100 °C

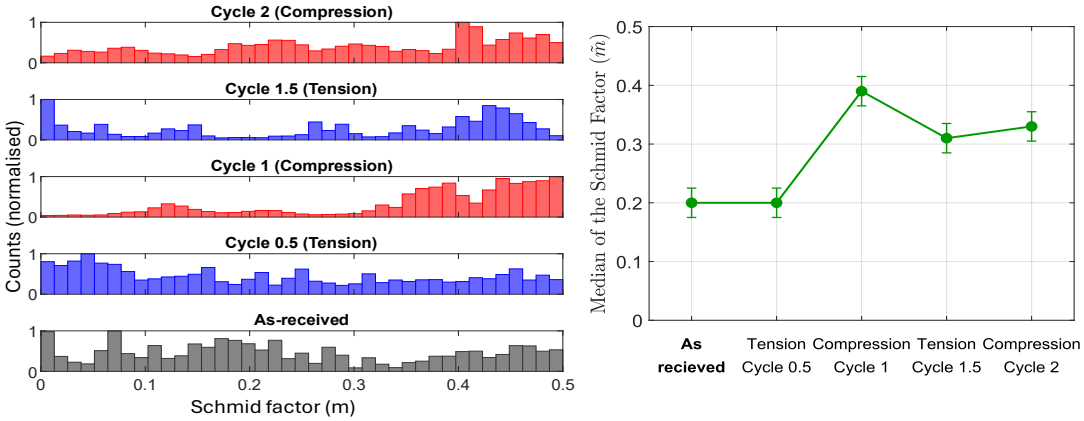


Figure 5.29: Basal slip system $\{0002\}\langle 11\bar{2}0\rangle$ (α) (T-C load sequence) at 200 °C

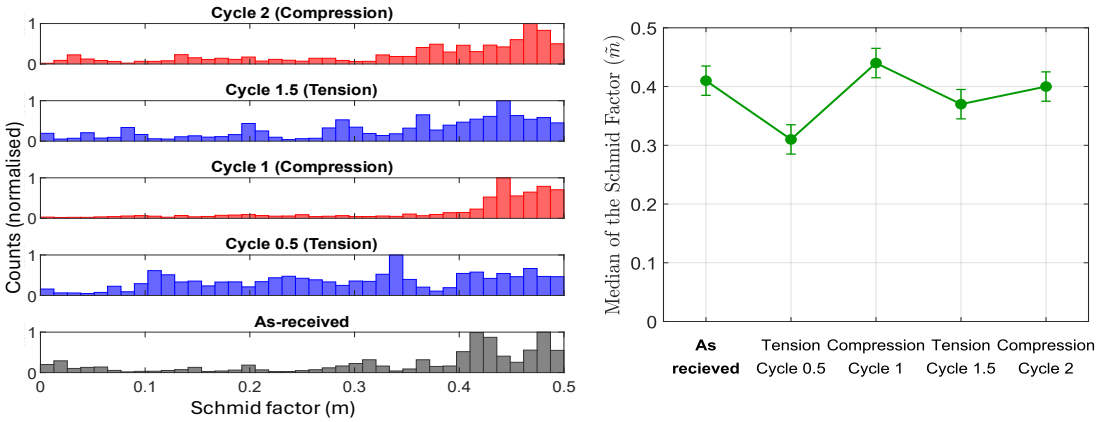


Figure 5.30: Prismatic slip system $\{10\bar{1}0\}\langle\bar{1}2\bar{1}0\rangle$ (α) (T-C load sequence) at 200 °C

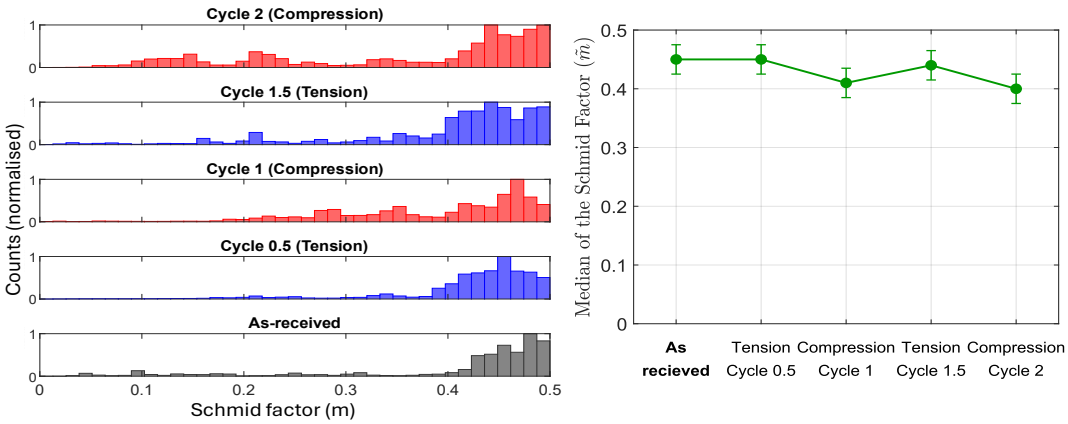


Figure 5.31: Pyramidal slip system $\{10\bar{1}1\}\langle\bar{1}2\bar{1}0\rangle$ (α) (T-C load sequence) at 200 °C

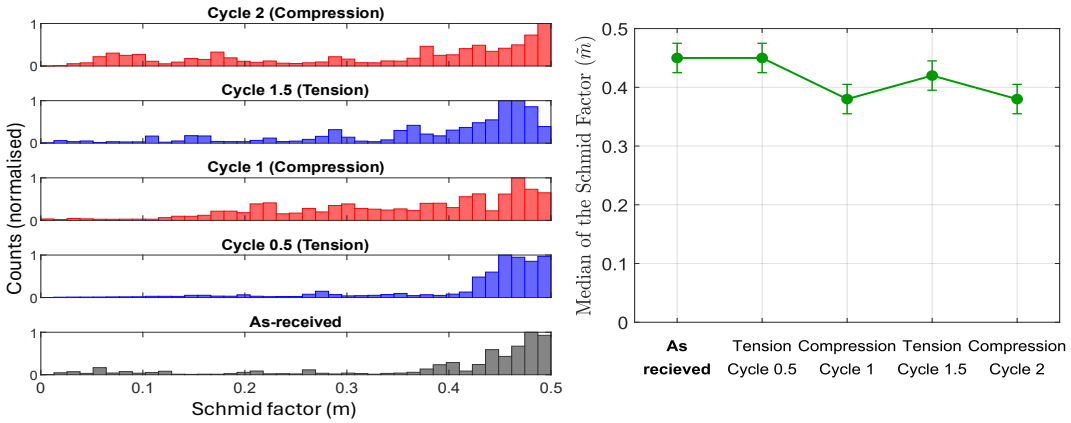


Figure 5.32: Pyramidal slip system $\{20\bar{2}1\}\langle\bar{1}2\bar{1}0\rangle$ (α) (T-C load sequence) at 200 °C

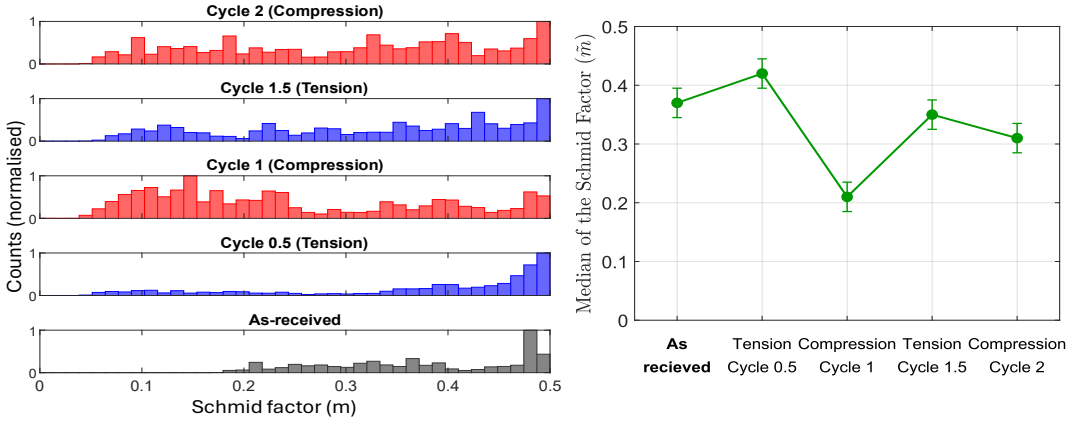


Figure 5.33: Second-order pyramidal slip system $\{11\bar{2}2\}\langle\bar{1}\bar{1}23\rangle$ (α) (T-C load sequence) at 200 °C

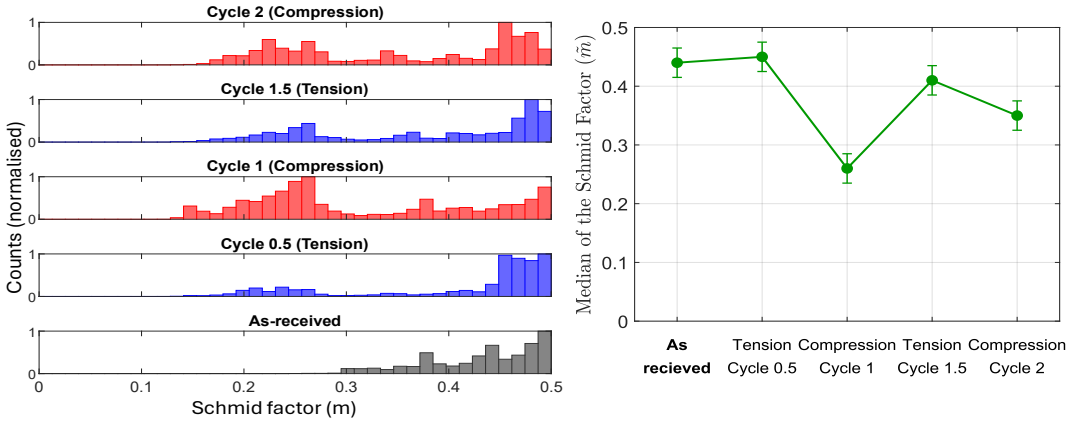


Figure 5.34: Pyramidal slip system $\{20\bar{2}2\}\langle\bar{1}\bar{1}23\rangle$ (α) (T-C load sequence) at 200 °C

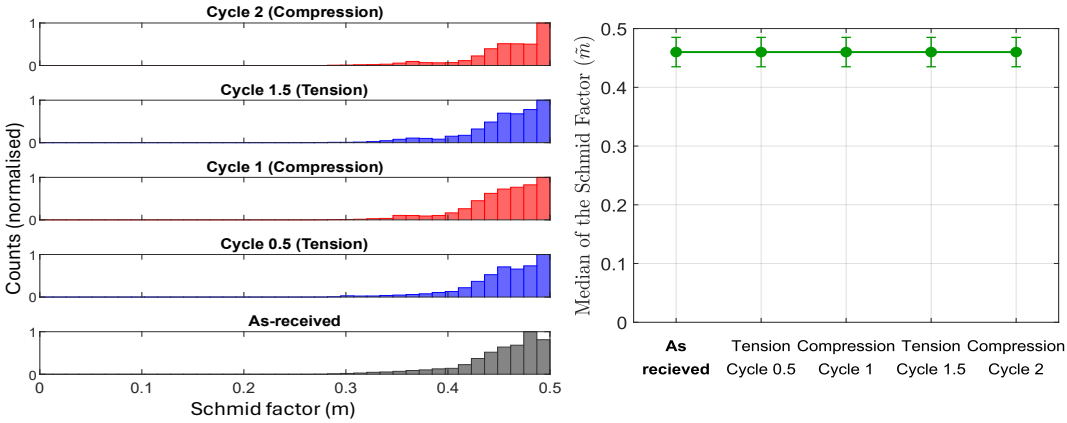


Figure 5.35: $\{110\}\langle\bar{1}11\rangle$ slip system (β) (T-C load sequence) at 200 °C

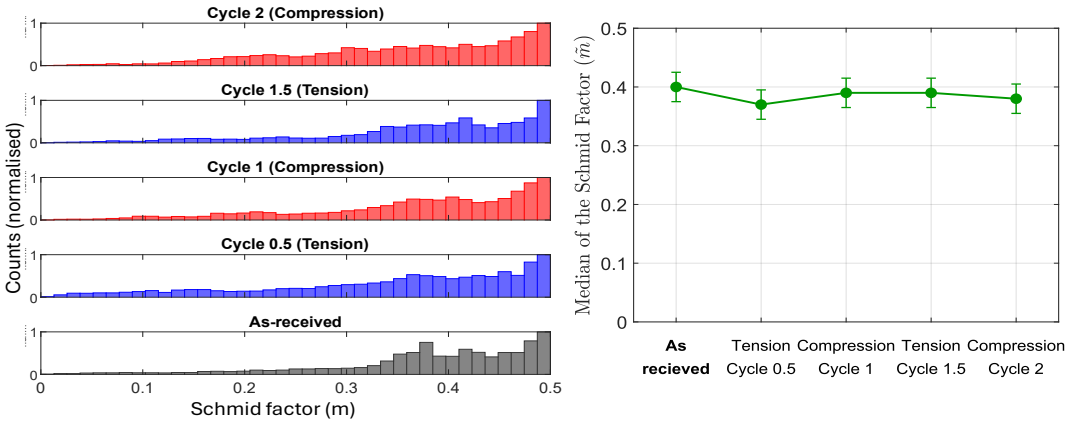


Figure 5.36: $\{200\}\langle011\rangle$ slip system (β) (T-C load sequence) at 200 °C

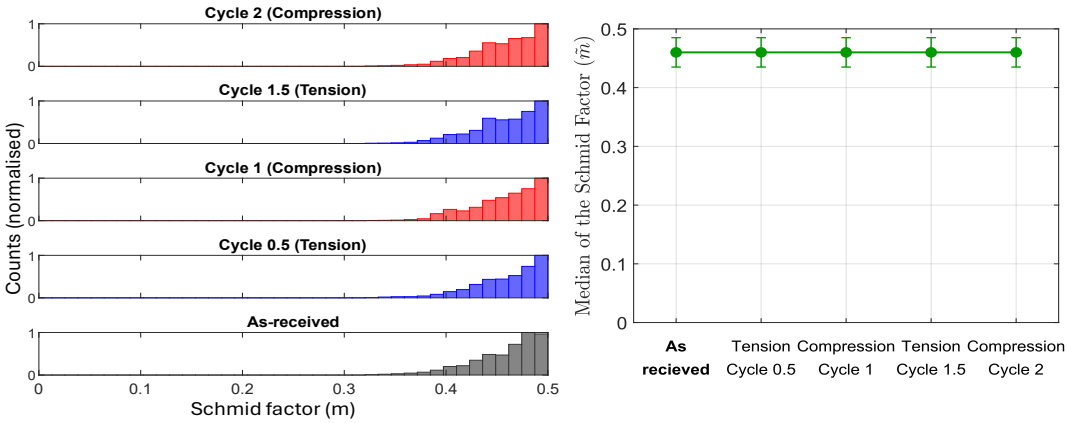


Figure 5.37: $\{211\}\langle\bar{1}11\rangle$ slip system (β) (T-C load sequence) at 200 °C

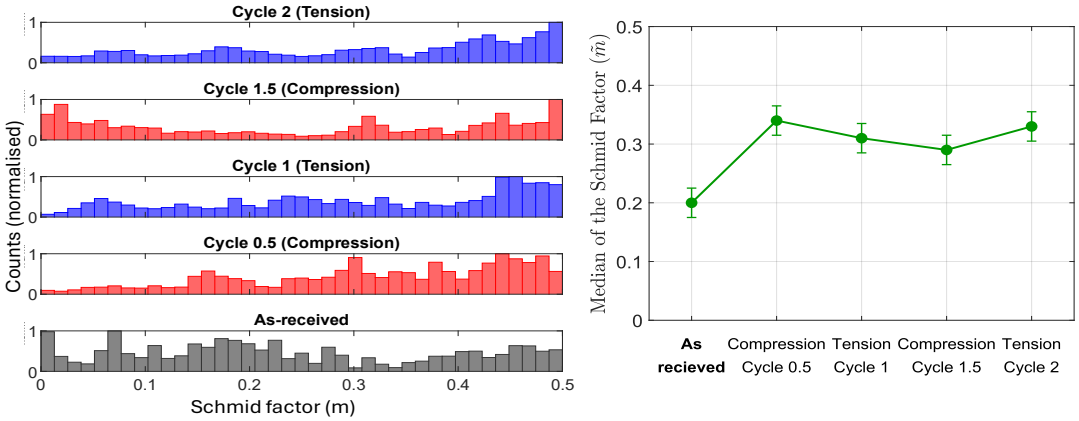


Figure 5.38: Basal slip system $\{0002\}\langle 11\bar{2}0\rangle$ (α) (C-T load sequence) at 200 °C

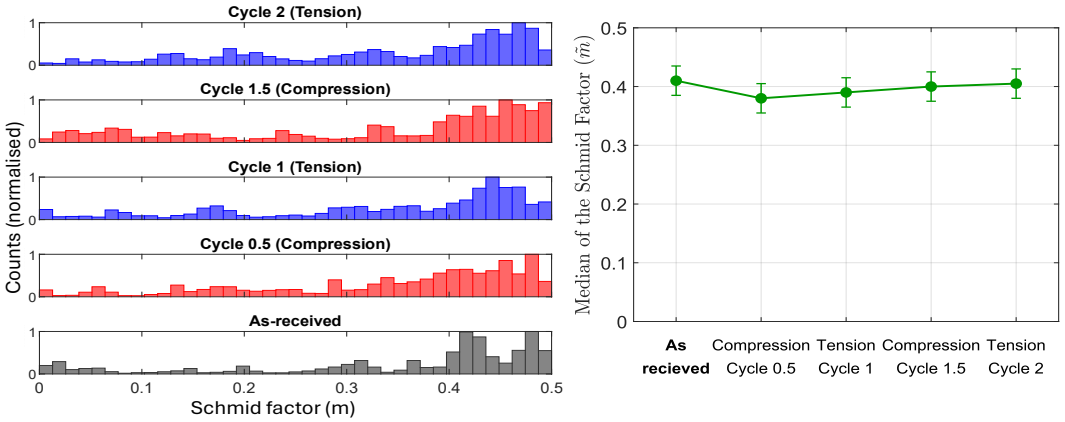


Figure 5.39: Prismatic slip system $\{10\bar{1}0\}\langle\bar{1}2\bar{1}0\rangle$ (α) (C-T load sequence) at 200 °C

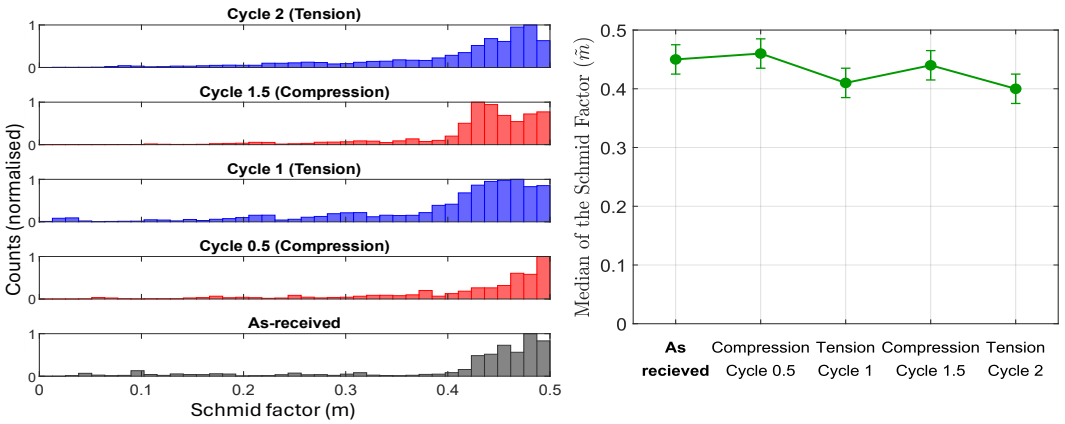


Figure 5.40: Pyramidal slip system $\{10\bar{1}1\}\langle\bar{1}2\bar{1}0\rangle$ (α) (C-T load sequence) at 200 °C

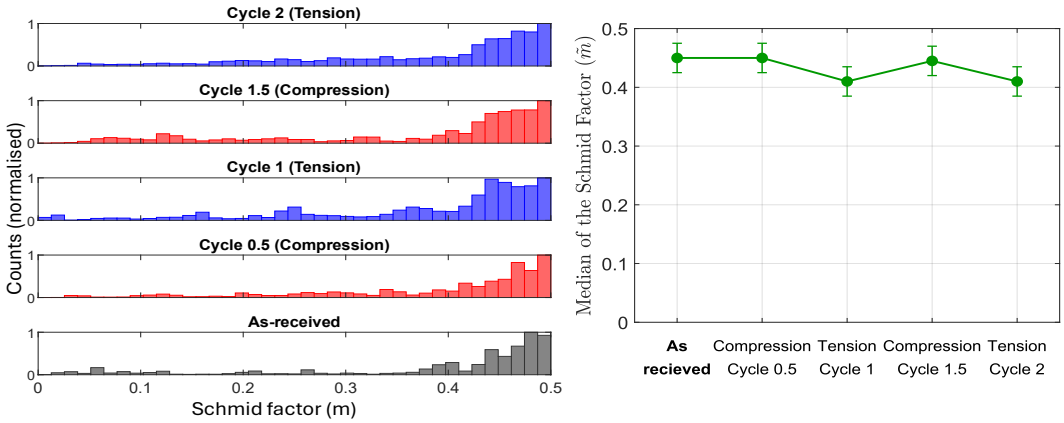


Figure 5.41: Pyramidal slip system $\{20\bar{2}1\}\langle\bar{1}2\bar{1}0\rangle$ (α) (C-T load sequence) at 200 °C

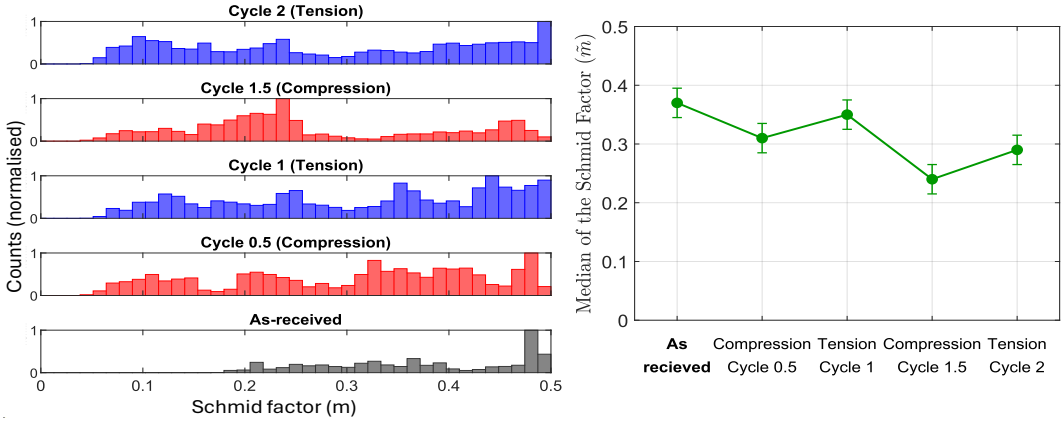


Figure 5.42: Second-order pyramidal slip system $\{11\bar{2}2\}\langle\bar{1}\bar{1}23\rangle$ (α) (C-T load sequence) at 200 °C

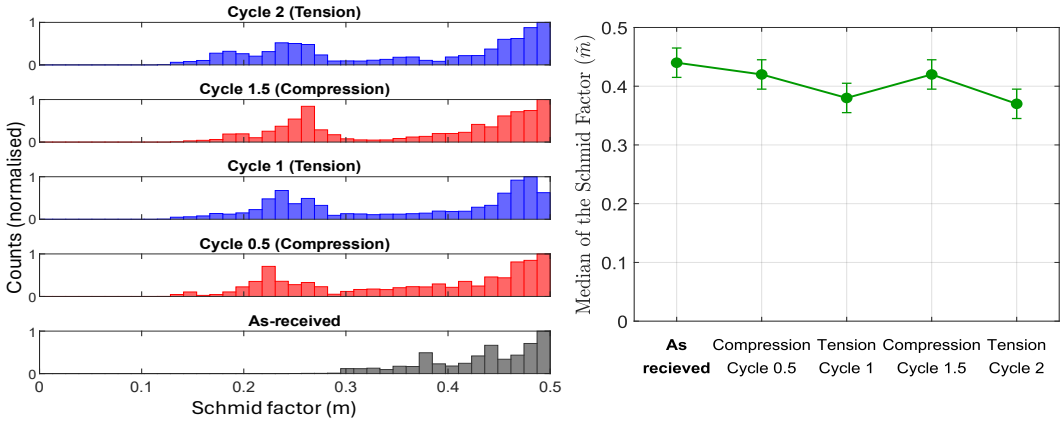


Figure 5.43: Pyramidal slip system $\{20\bar{2}2\}\langle\bar{1}\bar{1}23\rangle$ (α) (C-T load sequence) at 200 °C

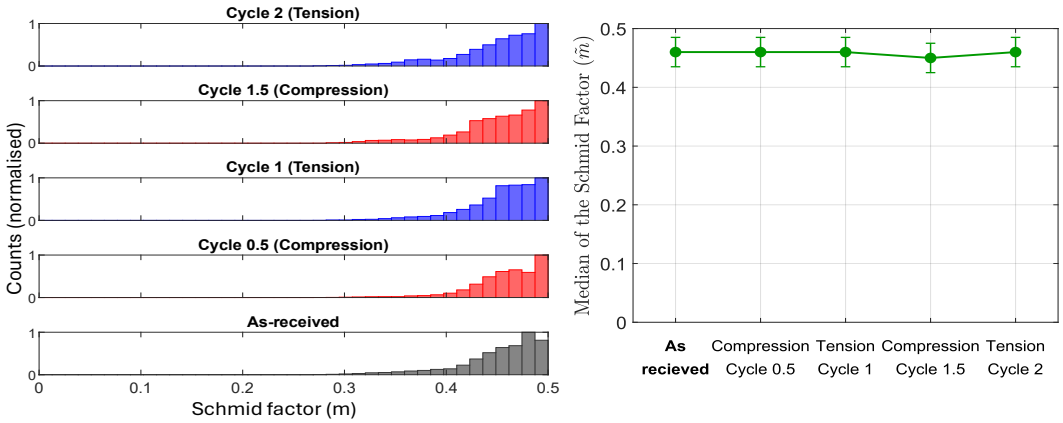


Figure 5.44: $\{110\}\langle\bar{1}11\rangle$ slip system (β) (C-T load sequence) at 200 °C

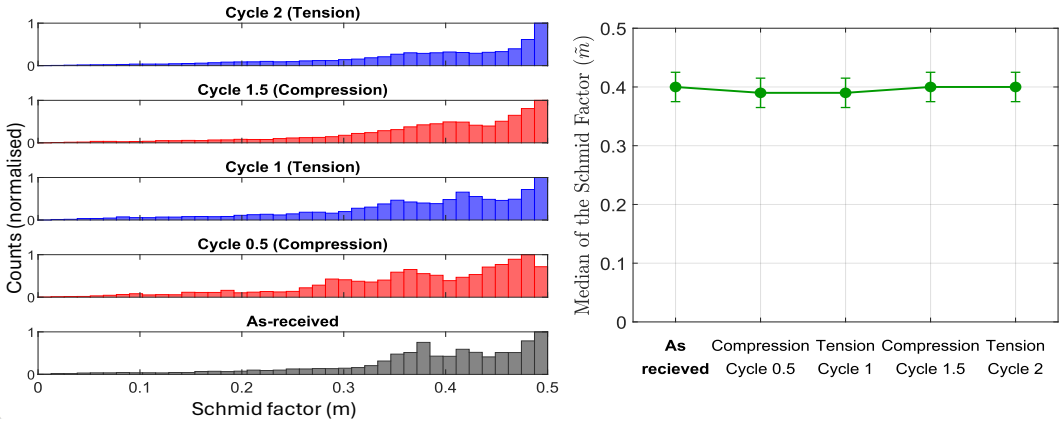


Figure 5.45: $\{200\}\langle011\rangle$ slip system (β) (C-T load sequence) at 200 °C

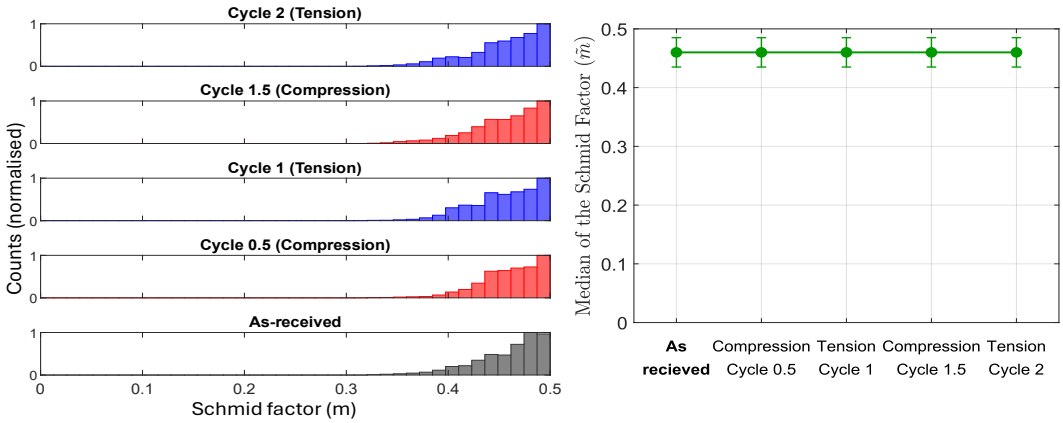


Figure 5.46: $\{211\}\langle\bar{1}11\rangle$ slip system (β) (C-T load sequence) at 200 °C

5.5 Residual Stress accumulation in forged Ti-6Al-4V at 100 °C and 200 °C

The evolution of residual stress accumulation in the crystallographic planes of the material during reverse loading at 100 °C and 100 °C was assessed through the evaluation of interrupted unsectioned specimens. These specimens were analysed after each load step, which ranged from 0.5 to 2 load cycles, in both loading sequences, using X-ray diffraction techniques.

5.5.1 Residual stress evolution of crystallographic planes in α and β phases present in forged Ti-6Al-4V

The interrupted, unsectioned specimens were analysed to measure the bulk residual stress after each loading step during the first two cycles of reverse loading for both loading sequences at 100 °C and 200 °C. Figures 5.47, 5.48, 5.49, 5.50, 5.51, 5.52, 5.53, and 5.54 demonstrate the evolution of the residual stress components, S_{11}, S_{22}, S_{33}, and S_{12}, within the crystallographic planes during the T-C loading in the α phase at 100 °C, during the T-C loading in the β phase at 100 °C, during the C-T loading in the α phase at 100 °C, during the C-T loading in the β phase at 100 °C, during the T-C loading in the α phase at 200 °C, during the T-C loading in the β phase at 200 °C, during the C-T loading in the α phase at 200 °C, and during the C-T loading in the β phase at 200 °C. The calculated values for S_{23} and S_{13} are zero in all the planes and are therefore not shown in the plots.

The accumulation of residual stress in the α phase at 100 °C during the T-C loading sequence is illustrated in Figure 5.47. Figure 5.47(a) demonstrates an asymmetrical trend in the behaviour of residual stress components within the basal plane (0002) as the load cycle progresses from 0.5 to 2. In the prismatic plane $(10\bar{1}0)$, Figure 5.47(b) reveals that the residual stress components S_{11}, S_{22}, and S_{33} also exhibit an asymmetrical trend as the number of cycles increases, while S_{12} demonstrates minimal variation. In the pyramidal plane $(10\bar{1}1)$, as depicted in Figure 5.47(c), the accumulation of residual stress is more pronounced during compression load steps in comparison to tension load steps. For the pyramidal plane $(20\bar{2}1)$, illustrated in Figure 5.47(d), it is evident that all residual stress components during compression load steps are relatively greater than those in tension load steps. Finally, for the second-order pyramidal plane $(11\bar{2}2)$, Figure 5.47(e) indicates that the residual stress components exhibit an asymmetrical fluctuation trend as the number of cycles increases.

Given that the presence of the β phase in the sample is only 2%, the accumulation of residual stress within the crystallographic planes is significantly lower than that of the α phase. Figure 5.48 illustrates the accumulation of residual stress in the β phase at 100 °C during the T-C loading sequence. In the (110) plane, as depicted in Figure 5.48(a), all residual stress components remain nearly constant with the increasing number of load cycles. In the (200) plane, shown in Figure 5.48(b), all stress components, except for S_{22}, also remain steady as the number of load cycles increases. Notably, S_{22} decreases by 20 MPa during the first cycle, after which it stabilises until load cycle 2. In the (211) plane, illustrated in Figure

5.48(c), the accumulation of residual stress in all components remains constant since the onset of loading.

As shown in Figure 5.49, in the α phase during the C-T loading sequence at 100 °C, the accumulation of residual stress in the basal plane (0002), depicted in Figure 5.49(a), exhibits an asymmetrical trend as well. Specifically, an increasing residual stress value is followed by a decreasing value, a trend that can be observed from load cycle 0.5 to cycle 2. In the prismatic plane $(10\bar{1}0)$, as illustrated in Figure 5.49(b), the residual stress components exhibit a relaxation of stress as the number of load cycles increases, transitioning from higher negative values toward zero. In contrast, S_{12} remains constant throughout. In the pyramidal plane $(10\bar{1}1)$, illustrated in Figure 5.49(c), the residual stress components show a similar trend, exhibiting both increasing and decreasing values as the number of load cycles increases. The pyramidal plane $(20\bar{2}1)$ shown in Figure 5.49(d) exhibits a similar trend in residual stress values, displaying more positive values during tension load steps and more negative values during compression load steps. A similar asymmetrical trend in residual stress values is observed in the second-order pyramidal plane $(11\bar{2}2)$, illustrated in Figure 5.49(e).

In the β phase of the material during the C-T loading sequence at 100 °C, the accumulation of residual stress is illustrated in Figure 5.50. Across all planes, namely (110), (200), and (211), as depicted in Figures 5.50(a), 5.50(b), and 5.50(c) respectively, the residual stress values remain almost constant until the second load cycle.

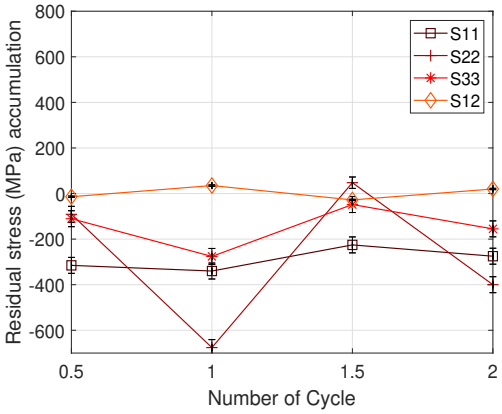
The accumulation of residual stress in the α phase at 200 °C during the T-C loading sequence is illustrated in Figure 5.51. Figure 5.51(a) demonstrates an asymmetrical trend in the behaviour of residual stress components within the basal plane (0002) as the load cycle progresses from 0.5 to 2. In the prismatic plane $(10\bar{1}0)$, Figure 5.51(b) reveals that the residual stress components S_{11}, S_{22}, and S_{33} also exhibit an asymmetrical trend as the number of cycles increases, while S_{12} demonstrates minimal variation. In the pyramidal plane $(10\bar{1}1)$, as depicted in Figure 5.51(c), the accumulation of residual stress is more pronounced during compression load steps in comparison to tension load steps. For the pyramidal plane $(20\bar{2}1)$, illustrated in Figure 5.51(d), it is evident that all residual stress components during compression load steps are relatively greater than those in tension load steps. Finally, for the second-order pyramidal plane $(11\bar{2}2)$, Figure 5.51(e) indicates that the residual stress components exhibit an asymmetrical fluctuation trend as the number of cycles increases.

Figure 5.52 illustrates the accumulation of residual stress in the β phase at 200 °C during the T-C loading sequence. In the (110) plane, as depicted in Figure 5.52(a), all residual stress components remain nearly constant with the increasing number of load cycles. In the (200) plane, shown in Figure 5.52(b), all stress components, except for S_{33}, also remain steady as the number of load cycles increases. Notably, S_{33} moves from around -30 MPa to around -20 MPa during the first cycle, after which it stabilises until load cycle 2. In the (211) plane, illustrated in Figure 5.52(c), the accumulation of residual stress in all components remains constant since the onset of loading.

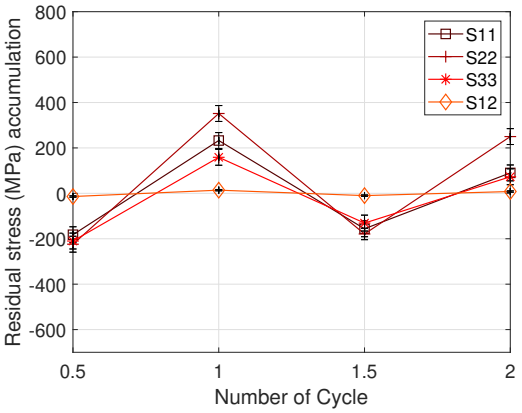
As shown in Figure 5.53, the α phase during the C-T loading sequence at 200 °C, the accumulation of residual stress in the basal plane (0002), depicted in Figure 5.53(a), exhibits an asymmetrical trend as well. Specifically, an increasing residual stress value is followed by a decreasing value, a trend that can be observed from load cycle 0.5 to cycle 2. In the prismatic plane $(10\bar{1}0)$, as illustrated in Figure 5.53(b), the residual stress components exhibit a relaxation of stress as the number of load cycles increases, transitioning from higher negative values toward zero. In contrast, S_{12} remains constant throughout. In the pyramidal plane $(10\bar{1}1)$, illustrated in Figure 5.53(c), the residual stress components show a similar trend, exhibiting both increasing and decreasing values as the number of load cycles increases. However, the accumulation of residual stress is more significant during compression load steps compared to tension load steps. The pyramidal plane $(20\bar{2}1)$ shown in Figure 5.53(d) exhibits a similar trend in residual stress values, displaying more positive values during tension load steps and more negative values during compression load steps. A similar asymmetrical trend in residual stress values is observed in the second-order pyramidal plane $(11\bar{2}2)$, illustrated in Figure 5.53(e).

In the β phase of the material during the C-T loading sequence at 200 °C, the accumulation of residual stress is illustrated in Figure 5.54. Across all planes, namely (110), (200), and (211), as depicted in Figures 5.54(a), 5.54(b), and 5.54(c) respectively, the residual stress values remain almost constant until the second load cycle.

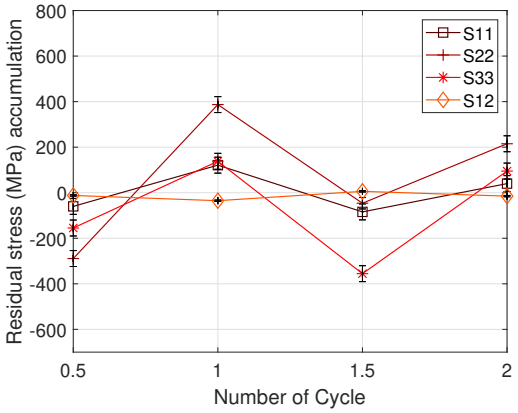
Interestingly, in all the planes at both temperatures, the accumulation of residual stress decreases with an increasing number of load cycles at elevated temperatures of 100 °C and 200 °C. This happens because higher temperatures make it easier for dislocations to rearrange and relieve internal backstress [170–172]. As a result, the build-up of residual stress per cycle diminishes across all planes during cyclic loading.



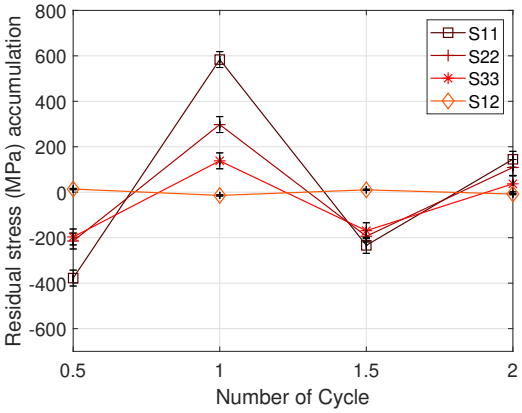
(a) Basal plane (0002) (α) (T-C load sequence)



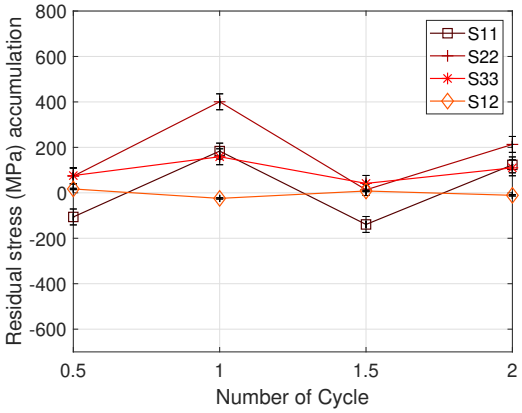
(b) Prismatic plane ($10\bar{1}0$) (α) (T-C load sequence)



(c) Pyramidal plane ($10\bar{1}1$) (α) (T-C load sequence)

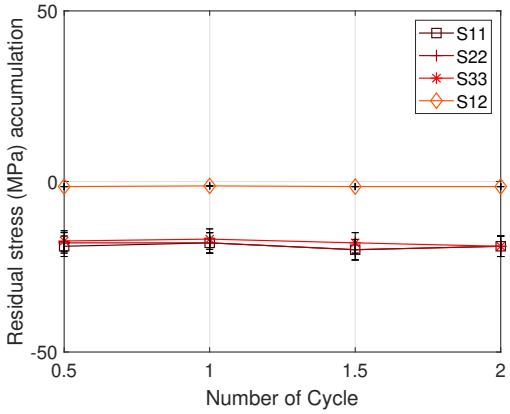


(d) Pyramidal plane ($20\bar{2}1$) (α) (T-C load sequence)

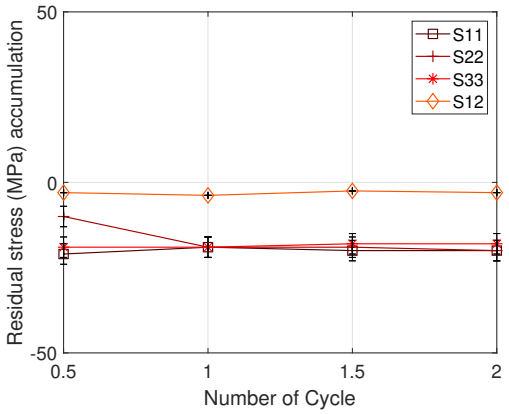


(e) Second-order Pyramidal plane ($11\bar{2}2$) (α) (T-C load sequence)

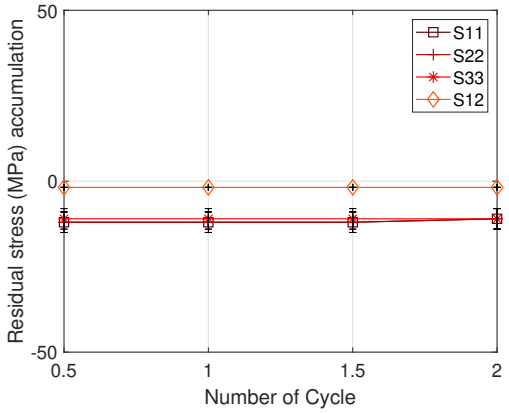
Figure 5.47: Residual stress accumulation in crystallographic planes in α phase at 100 °C during the T-C loading sequences, from load cycle 0.5 (Tension) to load cycle 2 (Compression). Each data point's uncertainty was estimated using the methodology outlined in Chapter 4.7.2, based on the synchrotron X-ray diffraction [141].



(a) (110) (β) (T-C load sequence)

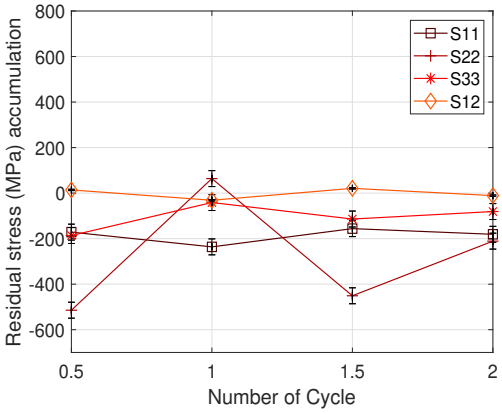


(b) (200) (β) (T-C load sequence)

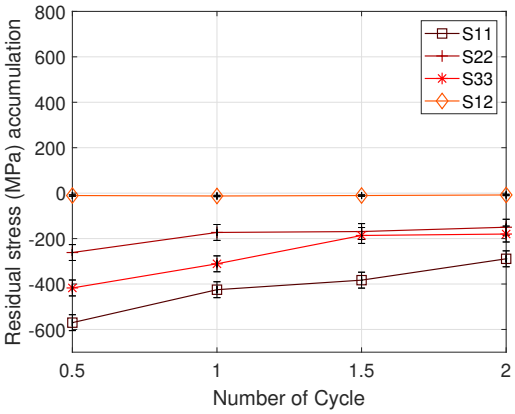


(c) (211) (β) (T-C load sequence)

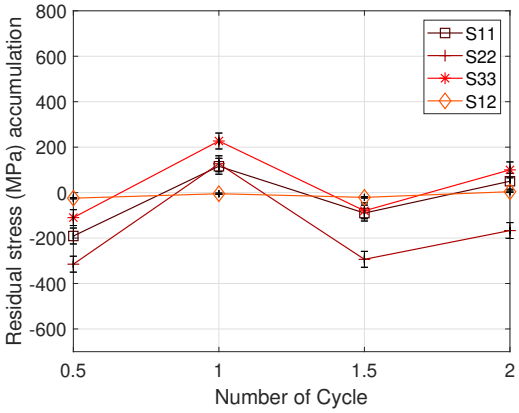
Figure 5.48: Residual stress accumulation in crystallographic planes in β phase at 100 °C during the T-C loading sequences, from load cycle 0.5 (Tension) to load cycle 2 (Compression). Each data point's uncertainty was estimated using the methodology outlined in Chapter 4.7.2, based on the synchrotron X-ray diffraction [141].



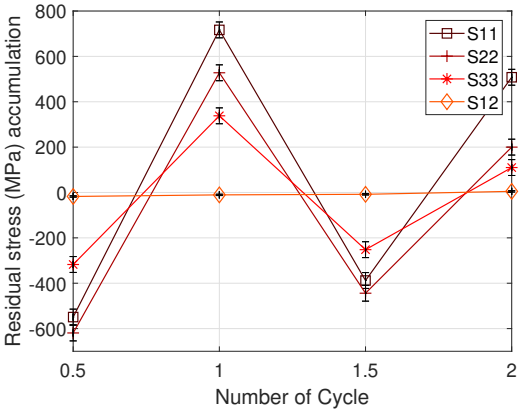
(a) Basal plane (0002) (α) (C-T load sequence)



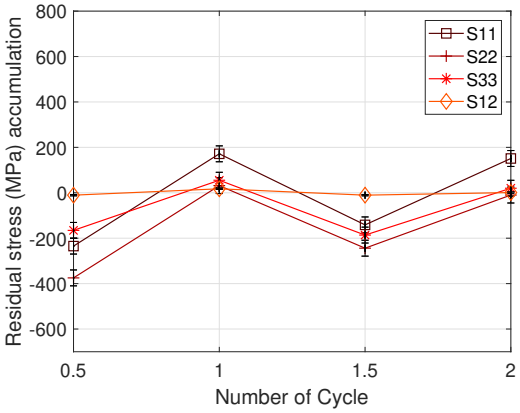
(b) Prismatic plane ($10\bar{1}0$) (α) (C-T load sequence)



(c) Pyramidal plane ($10\bar{1}1$) (α) (C-T load sequence)

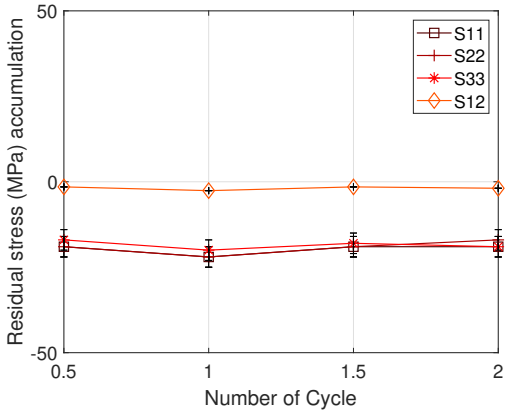


(d) Pyramidal plane ($20\bar{2}1$) (α) (C-T load sequence)

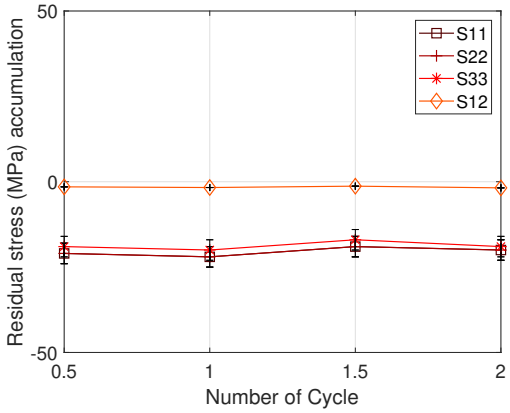


(e) Second-order Pyramidal plane ($11\bar{2}2$) (α) (C-T load sequence)

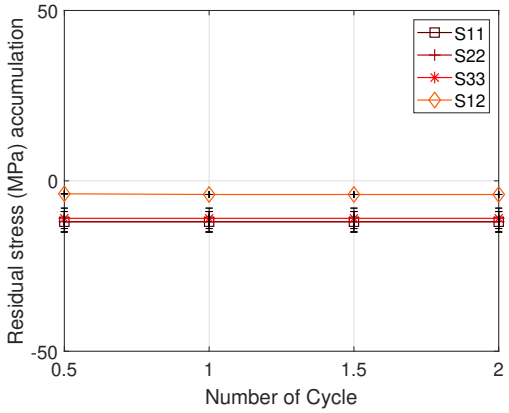
Figure 5.49: Residual stress accumulation in crystallographic planes in α phase at 100 °C during the C-T loading sequences, from load cycle 0.5 (Tension) to load cycle 2 (Compression). Each data point's uncertainty was estimated using the methodology outlined in Chapter 4.7.2, based on the synchrotron X-ray diffraction [141].



(a) (110) (β) (C-T load sequence)

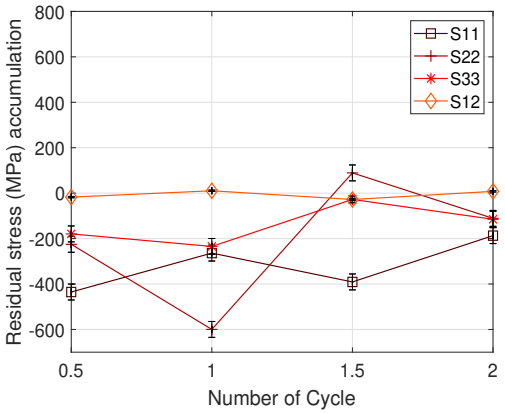


(b) (200) (β) (C-T load sequence)

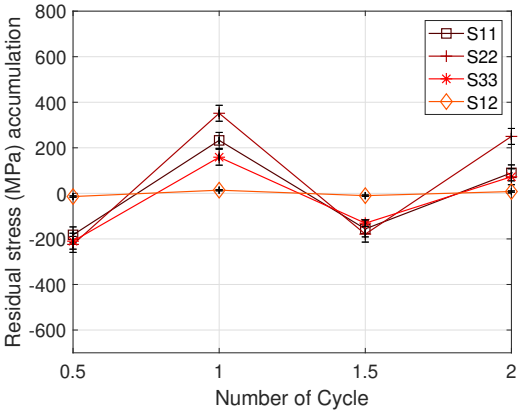


(c) (211) (β) (C-T load sequence)

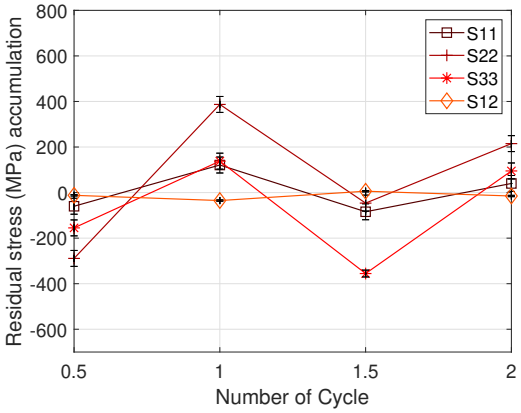
Figure 5.50: Residual stress accumulation in crystallographic planes in β phase at 100 °C during the C-T loading sequences, from load cycle 0.5 (Tension) to load cycle 2 (Compression). Each data point's uncertainty was estimated using the methodology outlined in Chapter 4.7.2, based on the synchrotron X-ray diffraction [141].



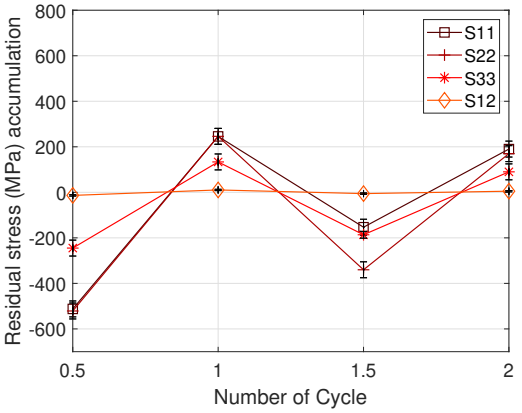
(a) Basal plane (0002) (α) (T-C load sequence)



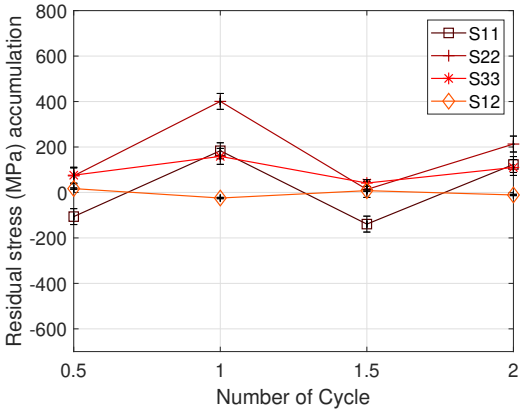
(b) Prismatic plane ($10\bar{1}0$) (α) (T-C load sequence)



(c) Pyramidal plane ($10\bar{1}1$) (α) (T-C load sequence)

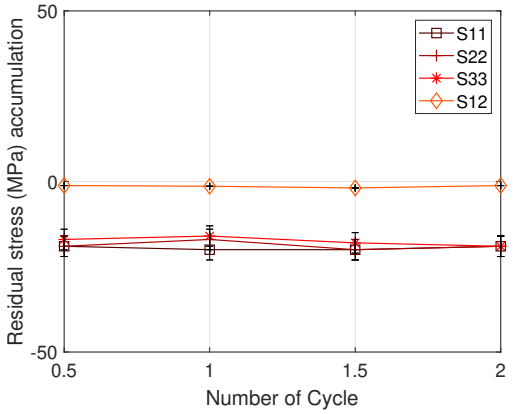


(d) Pyramidal plane ($20\bar{2}1$) (α) (T-C load sequence)

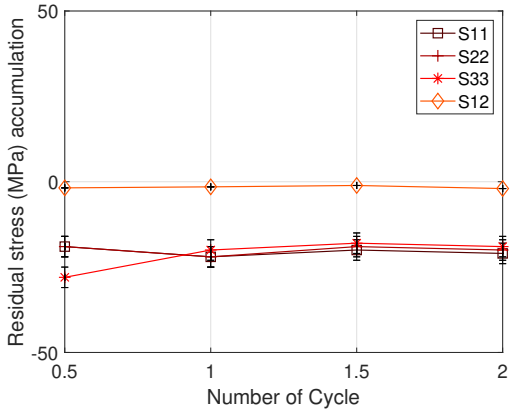


(e) Second-order Pyramidal plane ($11\bar{2}2$) (α) (T-C load sequence)

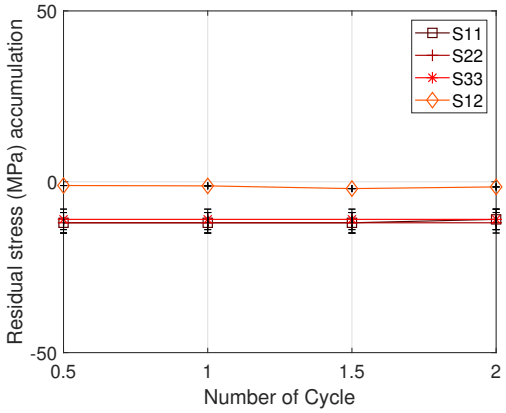
Figure 5.51: Residual stress accumulation in crystallographic planes in α phase at 200 °C during the T-C loading sequences, from load cycle 0.5 (Tension) to load cycle 2 (Compression). Each data point's uncertainty was estimated using the methodology outlined in Chapter 4.7.2, based on the synchrotron X-ray diffraction [141].



(a) (110) (β) (T-C load sequence)

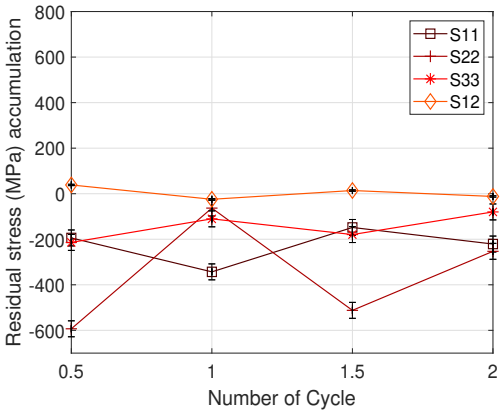


(b) (200) (β) (T-C load sequence)

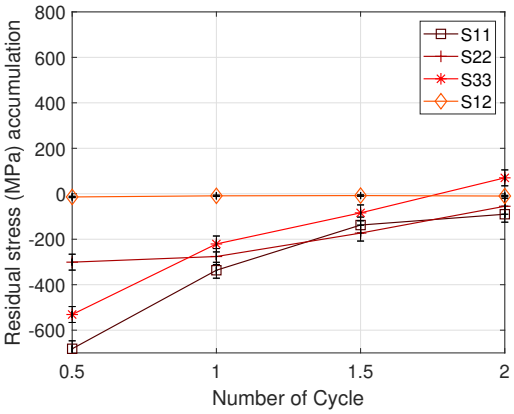


(c) (211) (β) (T-C load sequence)

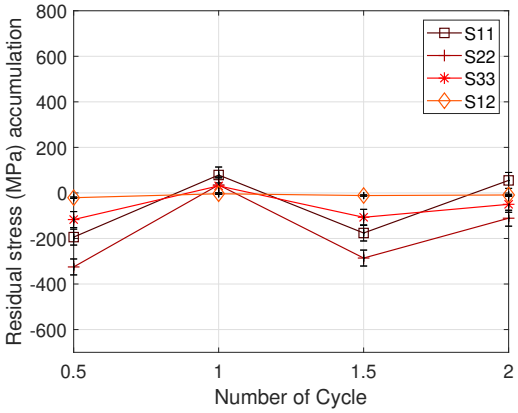
Figure 5.52: Residual stress accumulation in crystallographic planes in β phase at 200 °C during the T-C loading sequences, from load cycle 0.5 (Tension) to load cycle 2 (Compression). Each data point's uncertainty was estimated using the methodology outlined in Chapter 4.7.2, based on the synchrotron X-ray diffraction [141].



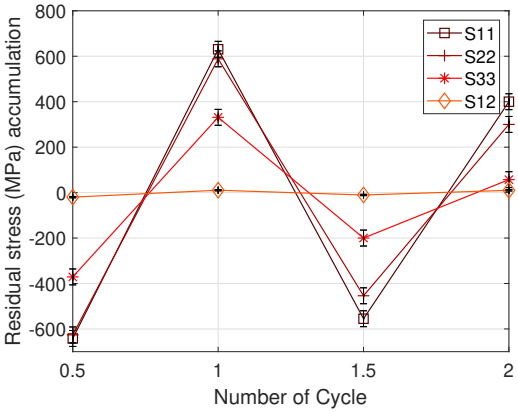
(a) Basal plane (0002) (α) (C-T load sequence)



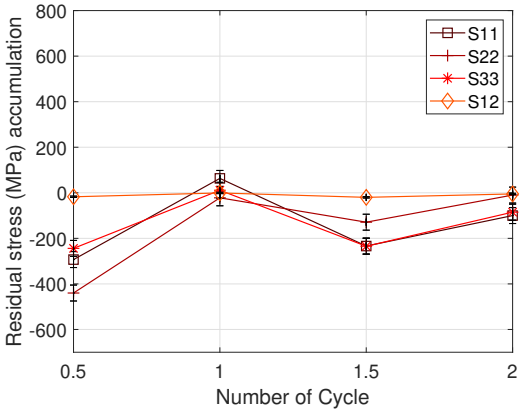
(b) Prismatic plane ($10\bar{1}0$) (α) (C-T load sequence)



(c) Pyramidal plane ($10\bar{1}1$) (α) (C-T load sequence)

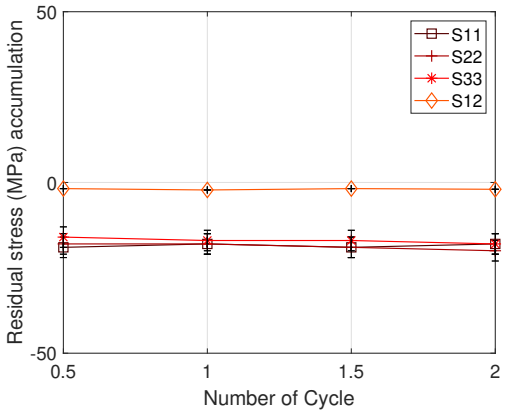


(d) Pyramidal plane ($20\bar{2}1$) (α) (C-T load sequence)

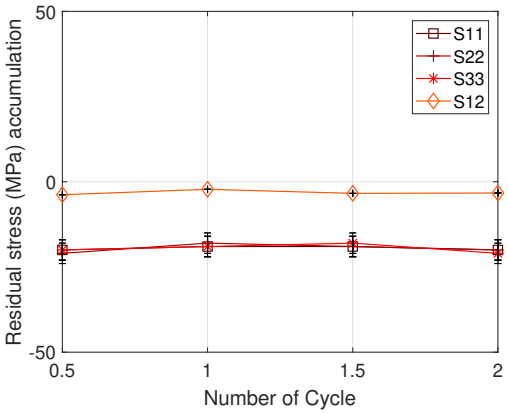


(e) Second-order Pyramidal plane ($11\bar{2}2$) (α) (C-T load sequence)

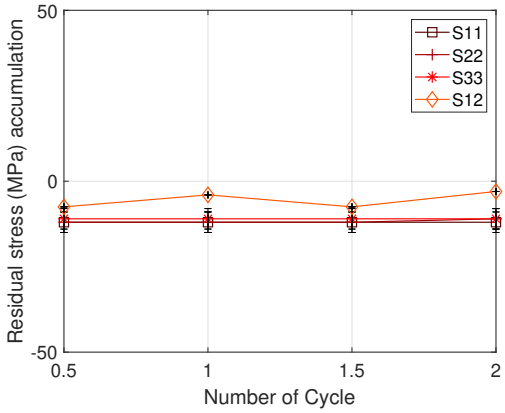
Figure 5.53: Residual stress accumulation in crystallographic planes in α phase at 200 °C during the C-T loading sequences, from load cycle 0.5 (Tension) to load cycle 2 (Compression). Each data point's uncertainty was estimated using the methodology outlined in Chapter 4.7.2, based on the synchrotron X-ray diffraction [141].



(a) (110) (β) (C-T load sequence)



(b) (200) (β) (C-T load sequence)



(c) (211) (β) (C-T load sequence)

Figure 5.54: Residual stress accumulation in crystallographic planes in β phase at 200 °C during the C-T loading sequences, from load cycle 0.5 (Tension) to load cycle 2 (Compression). Each data point's uncertainty was estimated using the methodology outlined in Chapter 4.7.2, based on the synchrotron X-ray diffraction [141].

5.6 Summary

During the low strain-rate reverse loading at elevated temperatures of 100 °C and 200 °C, the reverse loading response of forged Ti-6Al-4V is investigated across both loading sequences. At both temperatures, the material exhibited a persistent Bauschinger effect during the T-C load sequence; however, this effect nearly diminished during the C-T load sequence following the initial loading cycle. At 200 °C, the material withstood nearly three times the load compared to that at 100 °C before experiencing failure. The observed kinematic backstress in the T-C load sequence is noted to decrease with an increasing number of load cycles under both temperatures. Conversely, during the C-T load sequence, the kinematic backstress remains stable after the first loading cycle. The mean kinematic backstress is observed to decrease with increasing temperature (see Figure 5.8).

The microstructural behaviour of the material was analysed using interrupted specimens after each load step until load cycle 2. The microstructural analysis revealed the twinning-detwinning behaviour of twins, $\{10\bar{1}2\}$ and $\{10\bar{1}3\}$. Under both temperatures, during the T-C load sequence, both twins exhibited asymmetric fluctuations in the twinning-detwinning trend with the increasing number of load cycles. In contrast, during the C-T load sequence, the material experienced an overall detwinning trend as the number of load cycles increased at both temperatures. Overall, the detwinning rate is observed to increase with temperature. Furthermore, the Schmid factor behaviour for all slip systems demonstrated a fluctuating increasing-decreasing trend in the median Schmid factor values during

both loading sequences, except for the Prismatic slip system during the C-T load sequence, which exhibited a net constant median Schmid factor value at 100 °C, and a gradually increasing median Schmid factor value with the rise in load cycles at 200 °C. Interestingly, it was observed that, during the load step in which the twin boundary length decreases, indicating detwinning, the corresponding median Schmid factor for the prismatic slip system increases, indicating a greater propensity for slip. The interrupted unsectioned specimens were also analysed for the measurement of accumulated residual stress within the material using synchrotron X-ray diffraction. The residual stress accumulation across crystallographic planes in the material revealed an asymmetrical accumulation of residual stress in both loading sequences, with the exception of the Prismatic plane. Notably, the measurements indicated that the residual stress exhibited fluctuations in accumulation during the T-C load sequence. However, during the C-T load sequence, the residual stress was observed to gradually relax throughout under both temperature conditions.

6 | Behaviour of the Bauschinger effect as a Function of Strain-rate

6.1 Overview

In the previous chapter, a study was conducted to explore the impact of load direction on the Bauschinger response of forged Ti-6Al-4V when subjected to reverse loading at low strain-rate and elevated temperatures. The purpose of this chapter is to extend that analysis by examining how load direction and the effect of adiabatic self heating influence the Bauschinger response of the material during reverse loading at intermediate strain-rates, 1 s^{-1} and 10 s^{-1}, at room temperature. This chapter also analyses the *in situ* temperature rise of the material due to reverse loading at intermediate strain-rates. Furthermore, it quantifies the plastic work converted into heat in terms of the Taylor-Quinney coefficient. Additionally, the Bauschinger effect is analysed, and the behaviour of kinematic backstress is studied through successive loading cycles in both loading sequences at both strain-rates. To deepen the understanding of microstructural changes and the underlying causes of the Bauschinger effect under intermediate strain-rates, the reverse loading experiments are interrupted after each loading step, extending up to the second load cycle. This interruption facilitates a detailed examination of twin evolution, the distribution of the Schmid factor across the crystallographic planes, and the assessment of residual stress accumulation.

6.2 Experimental methodology

Uniaxial reverse loading experiments were performed at intermediate strain-rates, 1 s^{-1} and 10 s^{-1}, on the cylindrical dog-bone-shaped specimens, as shown in Figure 3.1. The gauge region of the specimens was speckled on one side, which faced the high-speed camera (Phantom, Vision Research) used to capture the deformation of the specimen during testing. The recorded video data were subsequently converted into image sequences and analysed using DaVis software to perform post-test Digital Image Correlation (DIC) for strain measurement. The opposite side of the specimens was painted with emissive paint, which has an emissivity of 0.95, and faced the thermal camera to measure the temperature rise during reverse loading. The tests were conducted using a hydraulic Instron machine 8850, as shown in Figure 6.1, capable of applying loads up to ±120 kN. For the intermediate strain-rate experiments, the ramp speed of the machine's cross-head was set to $\pm 3\,\mathrm{mm\,s^{-1}}$ to achieve a strain rate of 1 s^{-1}, and $\pm 30\,\mathrm{mm\,s^{-1}}$ for a strain rate of 10 s^{-1}. Also, this hydraulic Instron machine is equipped with an in-built displacement-controlled cross-head program, which in this study was set to operate within a range of ±0.45 mm. The engineering strain data was obtained by conducting post-test DIC analysis using the DaVis DIC software parameters, as shown in Table 6.1.

Table 6.1: DaVis DIC parameters for intermediate strain-rate reverse loading.

Parameter	Intermediate strain-rate reverse loading
Image properties: Image scale (pixels/mm)	142.53
Time-series settings: Correlation mode	Relative to first
Displacement-calculation settings: Subset size (pixels)	25
Displacement-calculation settings: Step size (pixels)	16
Calculation mode:	Gaussian 6th-order spline
Virtual extensometer characteristics: Strain formulation	Engineering strain

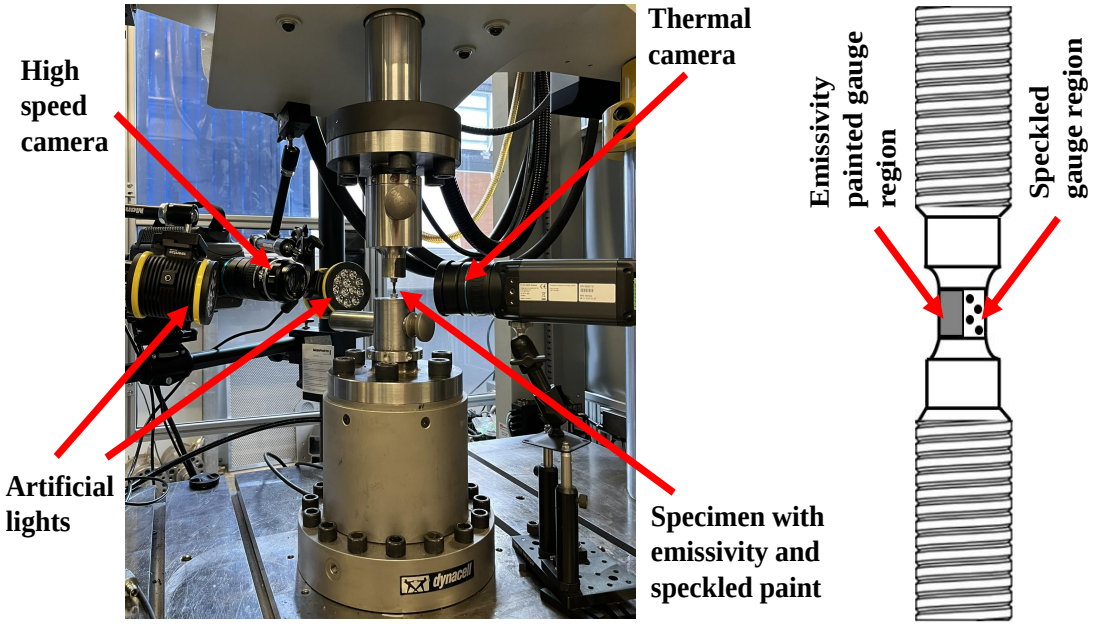


Figure 6.1: Set up to conduct reverse loading at intermediate strain rates of 1 s^{-1} and 10 s^{-1} at room temperature. A high-speed camera is positioned to face the speckled gauge region, capturing images of the speckled specimen for post-test Digital Image Correlation (DIC) strain measurements. Meanwhile, a thermal camera is oriented towards the emissive painted gauge region to monitor the temperature rise resulting from mechanical loading.

6.3 Experimental results

The stress-strain behaviour was examined at the strain-rates 1 s^{-1} and 10 s^{-1} in both loading sequences, as shown in Figures 6.2 and 6.3. During the reverse loading of the material, the maximum real-time temperature of the specimen was observed to exceed 200 °C in both loading sequences at a strain rate of 1 s^{-1}, as illustrated in Figure 6.4. The nature of the experiment was such that it allows the material sufficient time to cool down when the load is reversed. It was observed that the temperature of the specimen rises during loading and subsequently falls during the reversal of the load. The rise in temperature during loading occurs because, once plastic flow initiates, the external mechanical work partitions into (i) stored defect energy and (ii) an irreversible component that is dissipated immediately as heat [173, 174]. This dissipation arises from dislocation glide against obstacles and rate-dependent drag, dislocation reactions (junction formation/annihilation), thermally activated recovery (cross-slip and climb), and grain-boundary accommodation, among other dissipative microstructural processes [174–176]. At a strain rate of 1 s^{-1}, the heat generated during each loading half-cycle has some time to diffuse away to the grips and the surrounding air [174, 177], leading to an increase in surface temperature during loading and a slight decrease upon reversal before the next half-cycle.

In contrast, at the higher strain rate of 10 s^{-1}, as depicted in Figure 6.5, the maximum real-time temperature of the specimen rises above 450 °C in both loading sequences. Notably, the temperature continues to increase during loading,

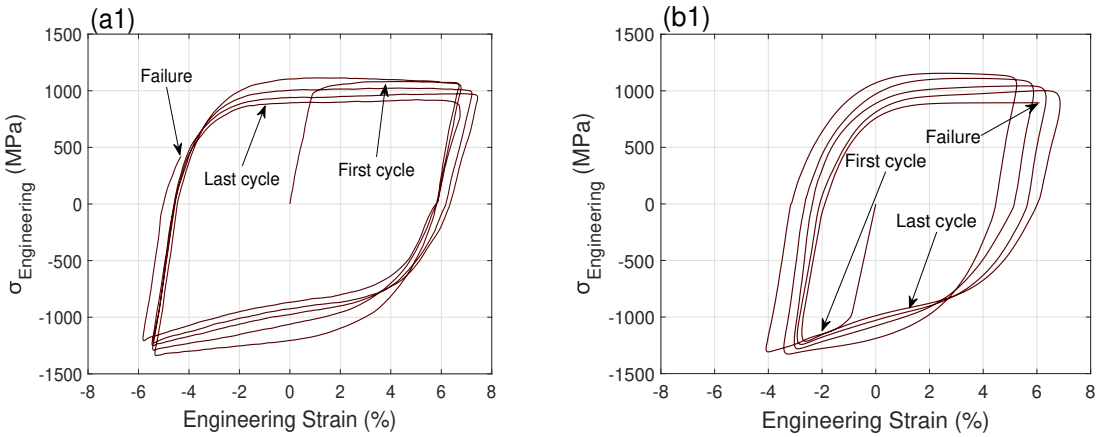


Figure 6.2: Engineering stress-strain response of forged Ti-6Al-4V during reverse loading: (a1) T-C load sequence and (b1) C-T load sequence, at a strain rate of $1\,\mathrm{s}^{-1}$.

and the specimen does not cool down during the reverse loading. This phenomenon indicates that the specimen does not have enough time to dissipate heat upon load reversal. At a rate of 10 s^{-1}, thermal diffusion cannot keep up, leading to nearly adiabatic conditions where heat accumulates from one cycle to the next [174,178]. However, towards the end of the test, a slight cooling of the specimen occurs due to the nucleation of micro-cracks just before failure.

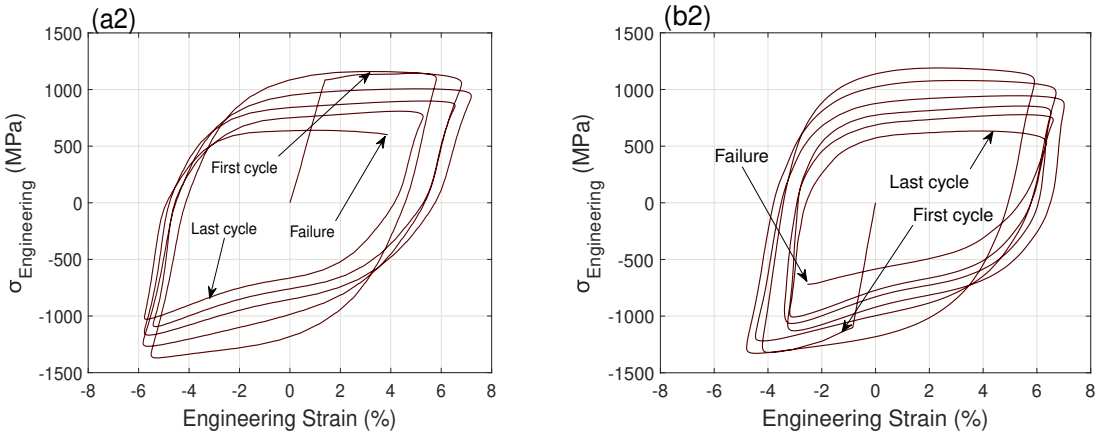


Figure 6.3: Engineering stress-strain response of forged Ti-6Al-4V during reverse loading: (a1) T-C load sequence and (b1) C-T load sequence, at a strain rate of $10\,\mathrm{s}^{-1}$.

To quantify the plastic work that is converted into heat dissipation under

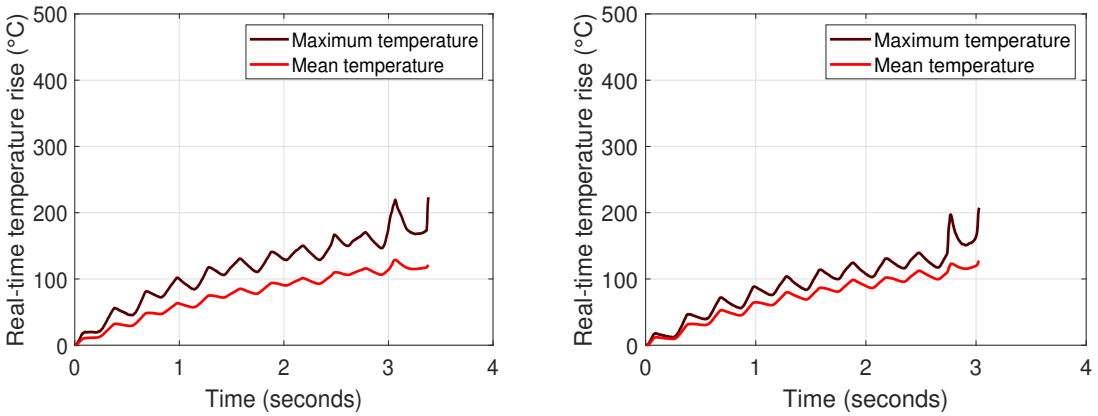


Figure 6.4: Real-time temperature rise of the material subjected to reverse loading in T-C (left) and C-T (right) load sequences at the strain-rate of 1 s^{-1}. The maximum temperature rise in the specimen is just above 200 °C in both loading sequences at a strain rate of 1 s^{-1}. The temperature of the specimen increases during loading and subsequently decreases during the reversal of loading. This behaviour suggests that the specimen has sufficient time to cool when the load is reversed.

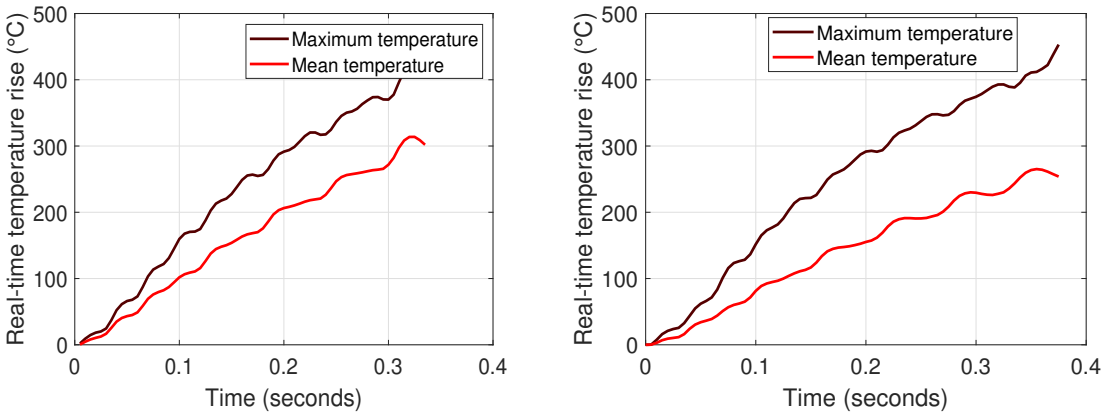


Figure 6.5: Real-time temperature rise of the material subjected to reverse loading in T-C (left) and C-T (right) load sequences at the strain-rate of 10 s^{-1}. The maximum temperature rise in the specimen is greater than 450 °C in both loading sequences. The temperature continues to increase during loading due to adiabatic heating, and the specimen does not cool down during the reverse loading. This phenomenon indicates that the specimen does not have enough time to dissipate heat upon load reversal.

adiabatic conditions, specifically at a strain rate of 10 s^{-1}, the Taylor-Quinney coefficient, β, is utilized, which represents the fraction of plastic work that is converted to heat is given by [173, 174, 178]:

$$\beta_{\text{int}} = \frac{\rho\, c_p\, \Delta T}{\int W_p} \tag{6.1}$$

Here, β_{int} is the Taylor-Quinney coefficient, $\int W_p$ represents the accumulated plastic work. The term ρ denotes the material density, c_p is the specific heat capacity at constant pressure, and ΔT is the measured temperature rise. Figure 6.6 illustrates the Taylor-Quinney behaviour as the number of load cycles increases at a strain rate of 10 s^{-1} for both loading sequences. The Taylor-Quinney coefficient β: the fraction of plastic work converted into heat, is observed to decrease with the increasing number of load cycles. During cyclic deformation at a rate of 10 s^{-1}, the temperature of the specimen increases, which facilitates thermally activated dislocation motion and recovery-driven rearrangements. This reduces the effective internal friction and increases the proportion of plastic work that is stored as internal energy [174,179,180], leading to a decrease in the value of β. Additionally, as the temperature rises, the amount of convective heat loss increases [181], and radiative heat loss grows approximately with T^4 [182]. These increasing losses diminish the net heat gain per cycle, causing the heating rate to decrease with the number of cycles, even though the absolute temperature continues to rise as long as the heat generated per cycle exceeds the heat losses.

As explained in Chapter 4, the 0.2% strain offset method to identify the Bauschinger effect by measuring the yield stresses at each load step during successive load cycles. Consequently, this study adopts the same methodology to examine the Bauschinger effect in both load sequences at both strain-rates. In

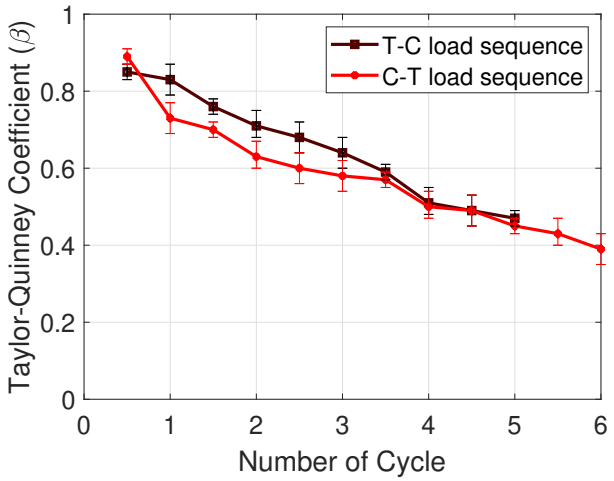


Figure 6.6: The behaviour of the Taylor-Quinny factor for the material is observed to gradually decrease with the increasing number of load cycles in both loading sequences at a strain rate of 10 s^{-1}. The error in this data was calculated using the propagation of error method [105, 106] in light of motivation from assessing error similar to Chapter 4.4.

Figure 6.7(a1), the Bauschinger effect is observed to persist throughout the T-C load sequence at a strain rate of 1 s^{-1}. In previous studies, Wielewski et al. (2015) measured the tensile yield stress of cross-rolled Ti-6Al-4V to be 1225 MPa. The material exhibits a strong basal (0001) texture. The test was conducted at a strain rate of 3.1×10^3 s^{-1}. Markovsky et al. (2020) reported a tensile yield stress of 988 MPa for the cast-and-wrought Ti-6Al-4V condition, measured under quasi-static loading at a strain rate of 10 s^{-1}.

In the C-T load sequence, the Bauschinger effect is only observed in the first, load cycle; after that, the effect diminishes, as illustrated in Figure 6.7(b1). In previous studies, Vinjamuri et al. (2020) measured the compressive yield stress of Ti-6Al-4V as 800 MPa. The test was conducted at the strain-rate of 100 s^{-1} and exhibited basal texture. Chen et al. (2024) measured the compressive yield stress of Ti-6Al-4V as 1200 MPa. The test was conducted at the strain-rate of

400 s^{-1}, and the material exhibited basal texture.

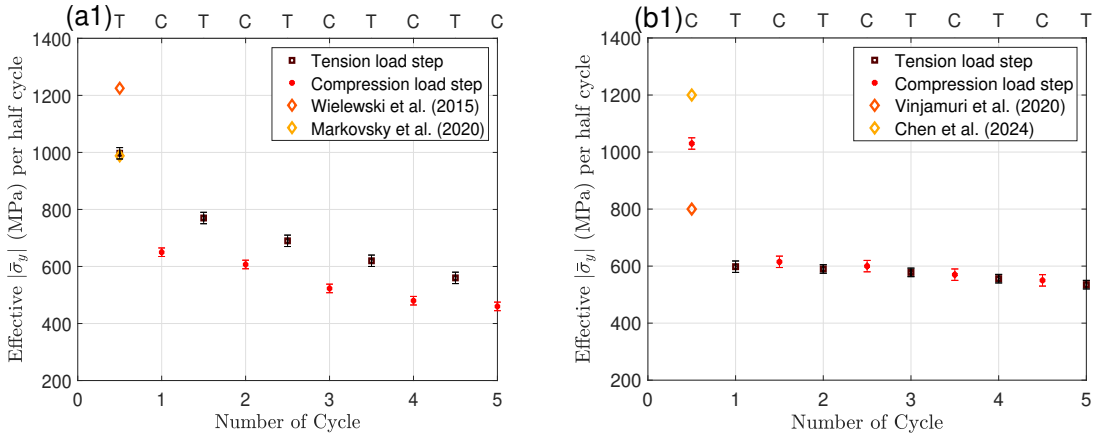


Figure 6.7: Behaviour of 0.2% effective yield strength determined from the stress-strain curve at each loading step during both the load sequences, (a1) T-C load sequence, (b1) C-T load sequence, at the strain-rate of 1 s^{-1}. During the T-C load sequence, the Bauschinger effect persists throughout until the material failure. During the C-T load sequence, the Bauschinger effect diminishes after the first load cycle. For each load step, the yield stress ($|\sigma_y|$) was averaged over repeated measurements, and the spread was quantified by the sample standard deviation ($S_{|\sigma_y|}$); error bars show $|\bar{\sigma}_y| \pm S_{|\sigma_y|}$ [113].

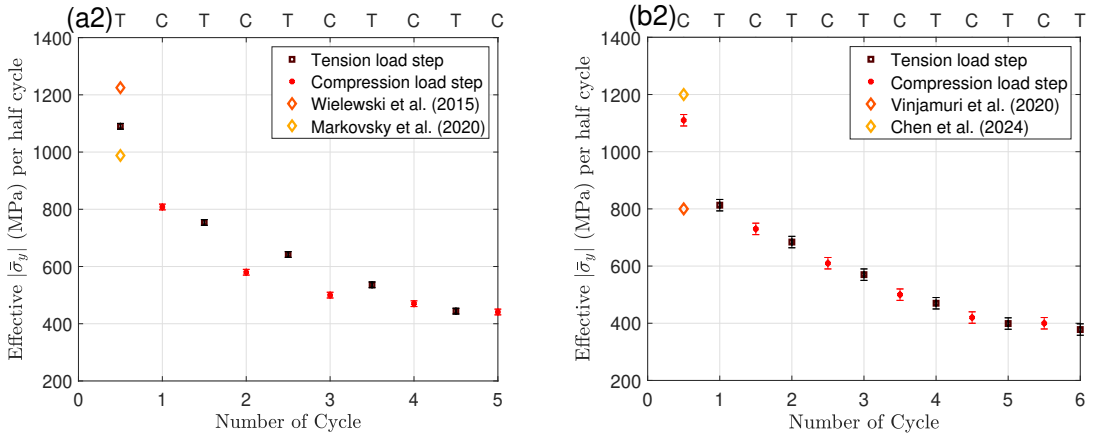


Figure 6.8: Behaviour of 0.2% effective yield strength determined from the stress-strain curve at each loading step during both the load sequences, (a2) T-C load sequence, (b2) C-T load sequence, at the strain-rate of 10 s^{-1}. During the T-C load sequence, the Bauschinger effect is observed but diminishes just before the material failure. During the C-T load sequence, the Bauschinger effect is noted to diminish after the first load cycle. For each load step, the yield stress ($|\sigma_y|$) was averaged over repeated measurements, and the spread was quantified by the sample standard deviation ($S_{|\sigma_y|}$); error bars show $|\bar{\sigma}_y| \pm S_{|\sigma_y|}$ [113].

In Figure 6.8(a2), during the T-C load sequence at a rate of 10 s^{-1}, the

Bauschinger effect is observed but diminishes just before failure. During the C-T load sequence, also shown in Figure 6.8(b2), the Bauschinger effect is noted to diminish after the first load cycle.

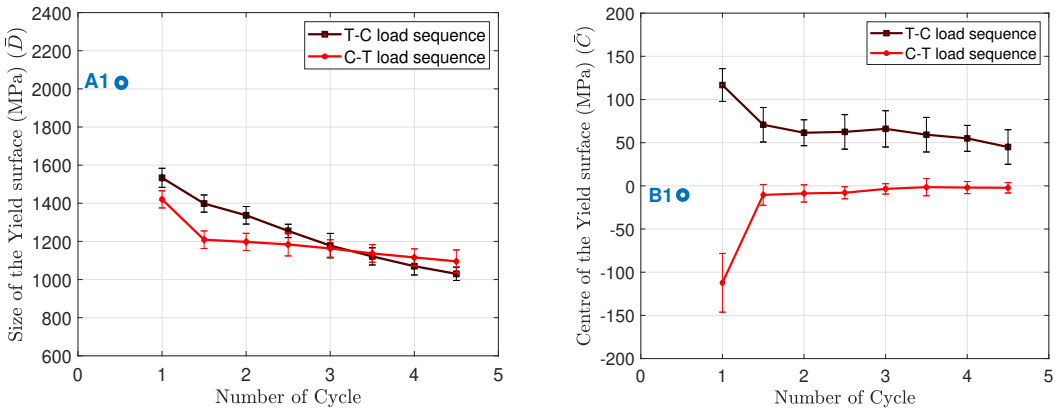


Figure 6.9: Isotropic hardening (Size of the yield surface) (on the left) and Kinematic hardening (Centre of the yield surface) (on the right) of both the loading sequences at the strain-rate of 1 s^{-1}. Point A1 shows the size of the yield surface (D) at load cycle 0.5 for both the T-C and C-T load sequences. The size of the yield surface decreases as the number of cycles increases in both load sequences. Point B1 shows the centre of the yield surface (C) at load cycle 0.5 for both the T-C and C-T load sequences. The centre of the yield surface gradually shifts downward with increasing load cycles during the T-C load sequence. In contrast, during the C-T load sequence, it moves significantly upwards towards zero before stabilising. For each condition, the Isotropic hardening (D) and Kinematic hardening (C) were averaged over repeated measurements, and the spread was quantified by the corresponding sample standard deviations (S_D and S_C); error bars show $\bar{D} \pm S_D$ and $\bar{C} \pm S_C$ [113].

During reverse loading in both loading sequences at both temperatures, the isotropic and kinematic hardening behaviour of the material is also explored in Figures 6.9 and 6.10. Isotropic and Kinematic hardening behaviours are determined with the same process as described in Chapter 4. At 1 s^{-1} (Figure 6.9), the size of the yield surface is observed to be gradually decreasing in both loading sequences. This contraction indicates that softening occurs within the material under fatigue loading [165]. Additionally, the centre of the yield surface is noted

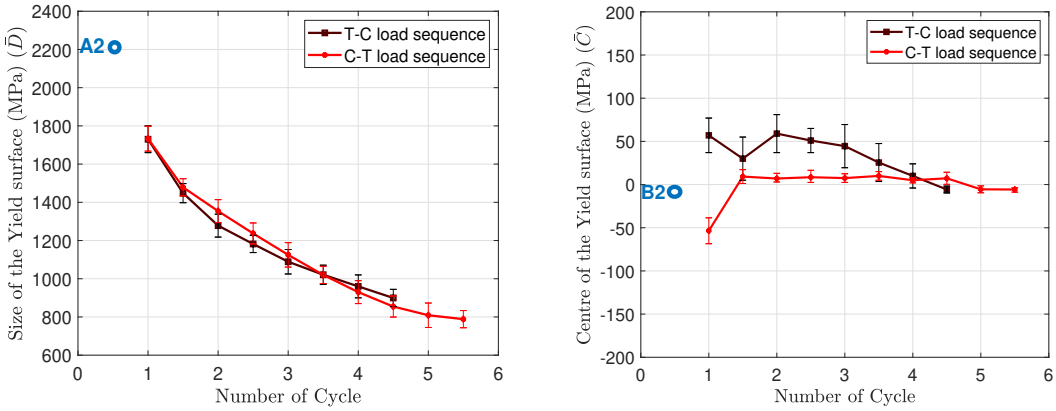


Figure 6.10: Isotropic hardening (Size of the yield surface) (on the left) and Kinematic hardening (Centre of the yield surface) (on the right) of both the loading sequences at the strain-rate of 10 s^{-1}. Point A2 shows the size of the yield surface (D) at load cycle 0.5 for both the T-C and C-T load sequences. The size of the yield surface decreases as the number of cycles increases in both load sequences. Point B2 shows the centre of the yield surface (C) at load cycle 0.5 for both the T-C and C-T load sequences. The centre of the yield surface varies throughout but globally decreases in the T-C load sequence. In contrast, during the C-T load sequence, it moves significantly upwards towards zero before stabilising. For each condition, the Isotropic hardening (D) and Kinematic hardening (C) were averaged over repeated measurements, and the spread was quantified by the corresponding sample standard deviations (S_D and S_C); error bars show $\bar{D} \pm S_D$ and $\bar{C} \pm S_C$ [113].

to gradually decrease during the T-C load sequence. In contrast, during the C-T load sequence, the centre of the yield surface remains close to zero after the first load cycle. At a rate of 10 s^{-1}, similar observations were noted regarding the size of the yield surface, which decreased with the increasing number of load cycles in both loading sequences. Additionally, the centre of the yield surface was observed to decrease, nearly reaching 0 MPa during the T-C load sequence. In contrast, the centre of the yield surface during the C-T load sequence remained close to 0 MPa after the first load cycle.

The behaviour of the mean kinematic hardening across both loading se-

quences and at both strain-rates is illustrated in Figure 6.11. In the T-C loading sequence, it is evident that the mean kinematic hardening decreases as the strain-rate increases. However, the change in the C-T load sequence is minimal. Notably, the accompanying temperature rise is self-generated during mechanical loading at elevated strain-rates (i.e. adiabatic or cyclic heating resulting from plastic work and energy dissipation), and the magnitude of this increase accumulates and intensifies with continued cyclic loading. This response is distinct from that observed in materials tested under a constant, externally imposed elevated temperature. The resultant *in-situ* heating at higher strain-rates accelerates thermally activated recovery and promotes backstress relaxation, ultimately leading to a reduction in average kinematic hardening [183].

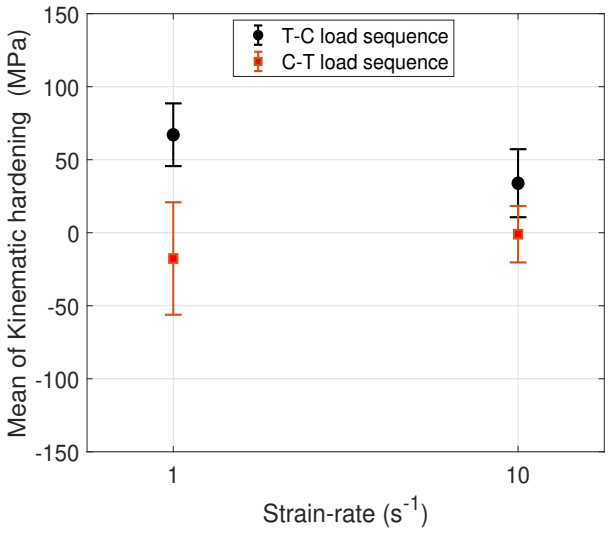


Figure 6.11: The kinematic hardening $\bar{C}$ behaviour at both strain-rates and loading sequences is demonstrated. In the T-C load sequence, the mean kinematic hardening decreases and approaches 0 MPa as the strain-rate increases. Similarly, in the C-T load sequence, the mean kinematic hardening also approaches 0 MPa (although the change is very minimal) with increasing strain-rate. For each condition, kinematic hardening (C) is averaged over repeated measurements and the spread was quantified by the sample standard deviation (S_C); error bars show $\bar{C} \pm S_C$ [113].

6.4 Microstructural analysis via Electron Backscatter Diffraction (EBSD) of sectioned interrupted specimens at $1\ s^{-1}$ and $10\ s^{-1}$ with increasing load cycles

To gain a better understanding of the Bauschinger response with increasing load cycles at $1\ s^{-1}$ and $10\ s^{-1}$, microstructural analysis using Electron Backscatter Diffraction (EBSD) was conducted on interrupted specimens from load cycle 0.5 to 2 in both loading sequences. The method used for this investigation is the same as described in Chapter 4.

6.4.1 Twin evolution in forged Ti-6Al-4V

The evolution of twin boundary length for $\{10\bar{1}2\}$ and $\{10\bar{1}3\}$ at a strain rate of $1\ s^{-1}$ under both T-C and C-T load sequences is illustrated in Figure 6.12 as the number of cycles increases. In the T-C sequence, both twin variants display a distinct asymmetric, non-monotonic response. Initially, there is a reduction in twin boundary length (detwinning) upon load reversal, which is followed by a partial reactivation of twinning. Subsequently, one observes a gradual attenuation of these fluctuations as cyclic deformation progresses. This behaviour suggests that both twinning and detwinning remain active beyond the initial transient response, although they progressively stabilise as the cycling continues. Conversely, in the C-T sequence, the most significant changes occur during the early transient stage.

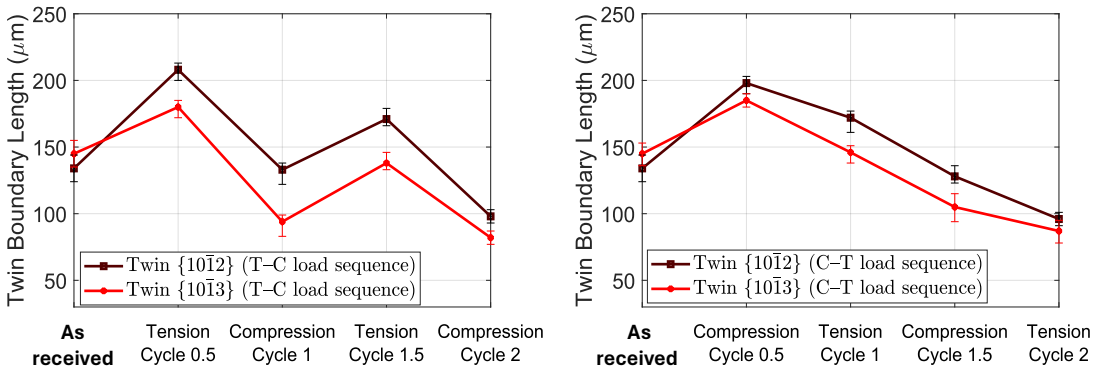


Figure 6.12: The evolution of twin boundary length for $\{10\bar{1}2\}$ and $\{10\bar{1}3\}$ twins during interrupted T-C (left) and C-T (right) loading demonstrates distinct behaviour under the two loading paths. Throughout the T-C cycle, twinning and detwinning exhibit asymmetric variations across successive cycles, with the twin boundary length in tension consistently greater than that in compression. Conversely, the C-T cycle displays marked changes during the initial load, followed by a gradual decrease in twin boundary length. The uncertainty was estimated from the EBSD scan spatial resolution, based primarily on the step size and the criteria used for twin boundary identification in OIM. The calculation of error is based on a methodology similar to the one described in Chapter 3.1.4.

After this point, both twin boundary lengths evolve more gradually, exhibiting a generally decreasing trend, which aligns with earlier microstructural stabilisation and reflects an increasing role of slip in accommodating subsequent deformation.

At 10 s^{-1} in Figure 6.13, a similar dependence on load sequence is observed, where the T-C sequence induces asymmetric fluctuations in the twin boundary length, indicative of repeated detwinning and re-twinning events occurring during the early cycles. These fluctuations are significantly more pronounced compared to those at lower strain rates. However, it is noted that the twin boundary length decreases more subsequently compared to the observations at 1 s^{-1}. In contrast, the C-T sequence demonstrates a response that is more dominated by transient effects, followed by a smoother evolution.

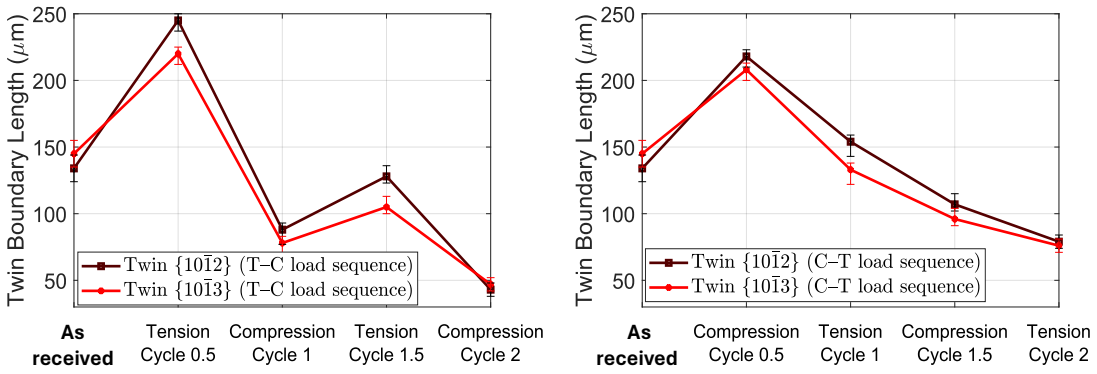


Figure 6.13: The development of twin boundary length for $\{10\bar{1}2\}$ and $\{10\bar{1}3\}$ twins during interrupted T-C loading (on the left) and C-T loading (on the right) demonstrates distinct behaviours in the two loading scenarios. Throughout the T-C cycle, both twinning and detwinning show asymmetric patterns across successive cycles, with the twin boundary length in tension consistently greater than in compression. It is also noted that the twin boundary length decreases more subsequently compared to the observations at 1 s^{-1}. Conversely, the C-T cycle exhibits significant changes during the initial loading phase, followed by a gradual reduction in twin boundary length. It is also observed that with increasing strain-rate, twin boundary length decreases. The uncertainty was estimated from the EBSD scan spatial resolution, based primarily on the step size and the criteria used for twin boundary identification in OIM. The calculation of error is based on a methodology similar to the one described in Chapter 3.1.4.

The strain-rate dependence observed aligns with the notion that twin activity becomes increasingly competitive during the initial loading phase at higher rates. As the flow stress escalates more rapidly, the thermally activated dislocation processes, such as cross-slip and climb, have diminished time to accommodate c-axis strain [184]. Consequently, the resolved shear stress can reach the critical twinning stress sooner than the more resistant $\langle c+a \rangle$ slip modes react, suggesting that twinning is favoured at elevated strain rates, consistent with the observed trends [184, 185].

6.4.2 Schmid factor evolution of crystallographic slip systems in α and β phases in forged Ti-6Al-4V

Similar to Chapter 4, the behaviour of the Schmid factor for the interrupted specimens is examined from load cycle 0.5 to load cycle 2 at the strain-rates of 1 s^{-1} and 10 s^{-1}. This analysis is conducted in both the α and β phases, as well as under two different load sequences, as illustrated in Figures 6.14 to 6.49. These figures depict the distribution of the Schmid factor, m, alongside its median, $\tilde{m}$, as the number of load cycles increases across the grains oriented in different directions.

The evolution of the median Schmid factor, $\tilde{m}$, for the α phase slip families during the T-C load sequence at a strain rate of 1 s^{-1} is shown in Figures 6.14 to 6.19. Across all families, $\tilde{m}$ exhibits asymmetric oscillations that follow the tension-compression reversals, indicating a cyclic redistribution of slip favourability rather than progressive stabilisation with cycle number. The basal slip system shows clear reversal sensitivity with a non-monotonic response across cycles. The prismatic slip system displays similarly strong asymmetric swings, highlighting a pronounced dependence on the loading direction. The pyramidal slip system exhibit smaller-amplitude oscillations with an overall mild reduction, consistent with more limited redistribution compared with basal and prismatic slip systems. The strongest reversal-driven redistribution occurs for the second-order pyramidal system, which show the largest asymmetric changes across reversals and only partial recovery with continued cycling. Overall, these trends demonstrate an asymmetric, cycle-

dependent re-weighting of deformation propensity among α-slip families during T-C cycling at 1 s^{-1}.

The evolution of the median Schmid factor, $\tilde{m}$, for the β phase slip families during the T-C load sequence at a strain rate of 1 s^{-1} is shown in Figures 6.20 to 6.22. Overall, the β phase exhibits only minor, transient changes in $\tilde{m}$ following the first loading step, after which the dominant $\{110\}\langle\bar{1}11\rangle$, $\{200\}\langle011\rangle$, and $\{211\}\langle\bar{1}11\rangle$ slip systems remain essentially stable up to load cycle 2. This near-constant behaviour indicates limited redistribution of slip favourability within the β phase during cyclic T-C loading at 1 s^{-1}.

The evolution of the median Schmid factor, $\tilde{m}$, for the α-phase slip families during the C-T load sequence at a strain rate of 1 s^{-1} is shown in Figures 6.23 to 6.28. The basal slip system shows modest, asymmetric oscillations with reversal. The prismatic slip system evolves smoothly and stabilises after the initial reversal, suggesting limited redistribution beyond the transient stage. In contrast, the pyramidal families exhibit stronger reversal sensitivity: the pyramidal slip system show clearer asymmetric swings with partial recovery on reloading, while the second-order pyramidal systems undergo the most pronounced redistribution with continued cycling and the weakest recovery, indicating the largest re-weighting of deformation propensity among the α-slip families under C-T loading at 1 s^{-1}.

The evolution of the median Schmid factor, $\tilde{m}$, for the β phase slip families during the C-T load sequence at a strain rate of 1 s^{-1} is illustrated in Figures 6.29 to 6.31. The β phase shows weak sensitivity to load reversal and cycle progression,

with $\tilde{m}$ remaining stable across the dominant slip systems $\{110\}\langle\bar{1}11\rangle$, $\{200\}\langle011\rangle$, and $\{211\}\langle\bar{1}11\rangle$.

The evolution of the median Schmid factor, $\tilde{m}$, for the α phase slip families during the T-C load sequence at a strain rate of 10 s^{-1} is shown in Figures 6.32 to 6.37. Overall, $\tilde{m}$ exhibits reversal-driven, asymmetric oscillations across all families, indicating a cyclic redistribution of slip favourability rather than progressive stabilisation with cycle number. The basal slip system shows clear reversal sensitivity with a non-monotonic response across cycles. The prismatic slip system displays similarly asymmetric swings, highlighting a pronounced dependence on loading direction. The pyramidal slip system shows smaller-amplitude oscillations with a mild overall reduction, consistent with more limited redistribution than basal and prismatic slip. The second-order pyramidal system exhibits the strongest redistribution among the pyramidal families, with more pronounced asymmetric changes across reversals and only partial recovery at later cycles. Collectively, these trends indicate an asymmetric, cycle-dependent re-weighting of deformation propensity among α-slip families during T-C cycling at 10 s^{-1}.

The evolution of the median Schmid factor, $\tilde{m}$, for β phase slip families during the T-C load sequence at a strain rate of 10 s^{-1} is illustrated in Figures 6.38 to 6.40. The β phase shows weak sensitivity to load reversal and cycle progression, with $\tilde{m}$ remaining stable across the primary slip systems $\{110\}\langle\bar{1}11\rangle$, $\{200\}\langle011\rangle$, and $\{211\}\langle\bar{1}11\rangle$.

The evolution of the median Schmid factor, $\tilde{m}$, for the α phase slip families

during the C-T load sequence at a strain rate of 10 s^{-1} is shown in Figures 6.41 to 6.46. The basal slip system shows clear reversal sensitivity with a non-monotonic response. In contrast, the prismatic slip system evolves smoothly with only minor changes, suggesting comparatively weak redistribution after the initial transient. The pyramidal slip systems exhibit clearer asymmetric swings with partial recovery on reloading. The second-order pyramidal slip system shows the strongest redistribution among the pyramidal families, with pronounced reversal-driven changes and only partial recovery at later cycles. Collectively, these trends indicate that C-T cycling at 10 s^{-1} preferentially redistributes deformation propensity among the pyramidal families, while prismatic slip remains comparatively less affected.

The evolution of the median Schmid factor, $\tilde{m}$, for the β phase slip families during the C-T load sequence at a strain rate of 10 s^{-1} is illustrated in Figures 6.47 to 6.49. The β phase shows minimal sensitivity to load reversal and cyclic progression, with $\tilde{m}$ remaining stable across the dominant $\{110\}\langle\bar{1}11\rangle$ and $\{211\}\langle\bar{1}11\rangle$ slip systems. Only minor, transient variations are seen in $\{200\}\langle011\rangle$ during early cycles, followed by recovery and stabilisation, indicating limited redistribution of slip favourability within the β phase during cyclic C-T loading at 10 s^{-1}.

In summary, the two strain-rates exhibit distinct behaviours in the prismatic slip system of the α phase. Specifically, the $\tilde{m}$ value varies during the T-C loading sequence but remains stable throughout the C-T loading sequence. This fluctuation in the $\tilde{m}$ value during the T-C sequence suggests that the favourability of slip is affected by the loading direction. Conversely, in the C-T loading

sequence, the $\tilde{m}$ values are consistent across different load directions, indicating that slip favourability is unaffected by the direction of the load. Additionally, no significant differences are observed in the β phase between the two loading sequences, and given its estimated area fraction of 2%, it is unlikely that the β phase significantly influences the observed behaviour.

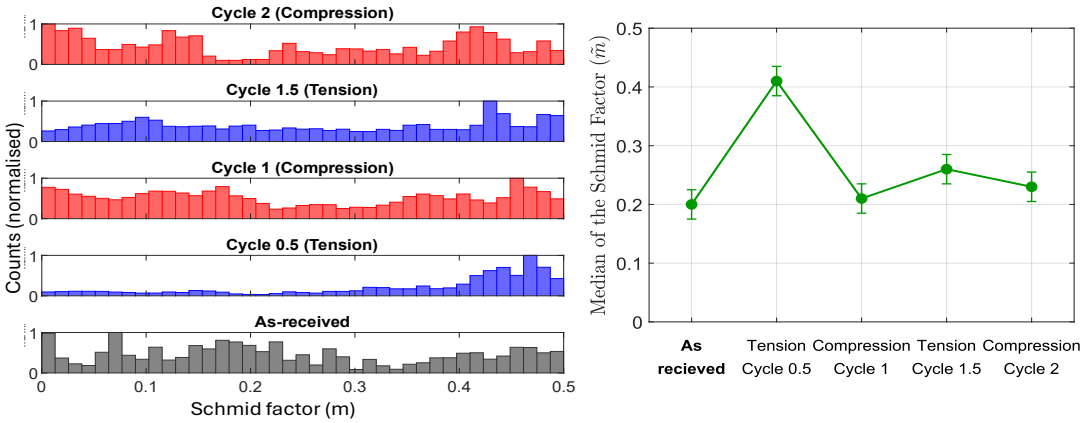


Figure 6.14: Basal slip system $\{0002\}\langle 11\bar{2}0\rangle$ (α) (T-C load sequence) at the strain-rate of 1 s^{-1}

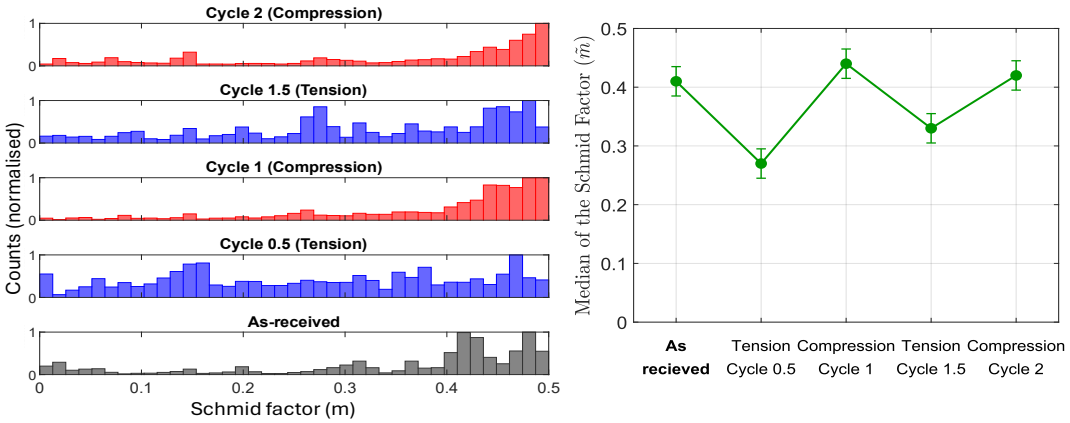


Figure 6.15: Prismatic slip system $\{10\bar{1}0\}\langle\bar{1}2\bar{1}0\rangle$ (α) (T-C load sequence) at the strain-rate of 1 s^{-1}

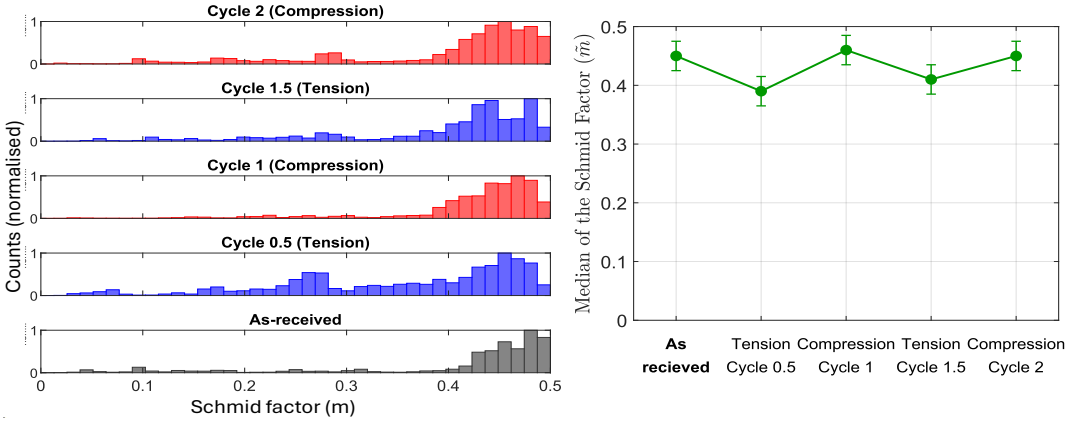


Figure 6.16: Pyramidal slip system $\{10\bar{1}1\}\langle\bar{1}2\bar{1}0\rangle$ (α) (T-C load sequence) at the strain-rate of 1 s^{-1}

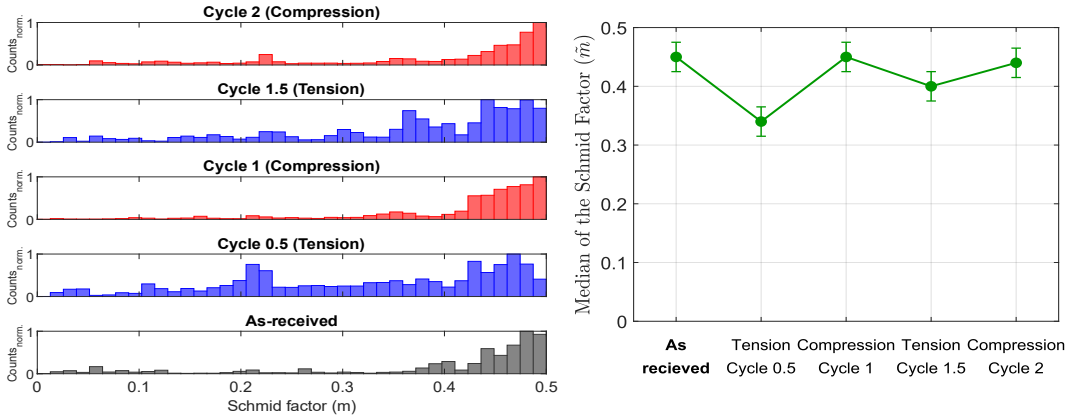


Figure 6.17: Pyramidal slip system $\{20\bar{2}1\}\langle\bar{1}2\bar{1}0\rangle$ (α) (T-C load sequence) at the strain-rate of 1 s^{-1}

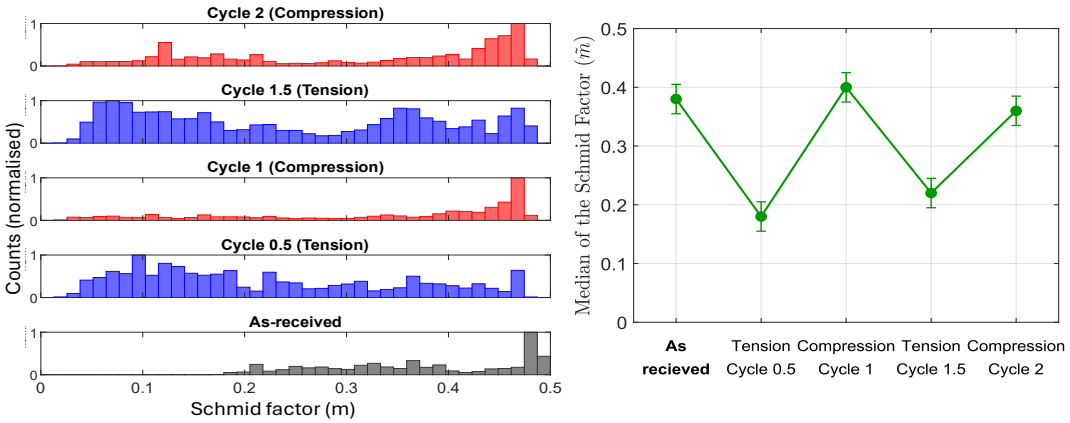


Figure 6.18: Second-order pyramidal slip system $\{11\bar{2}2\}\langle\bar{1}\bar{1}23\rangle$ (α) (T-C load sequence) at the strain-rate of 1 s^{-1}

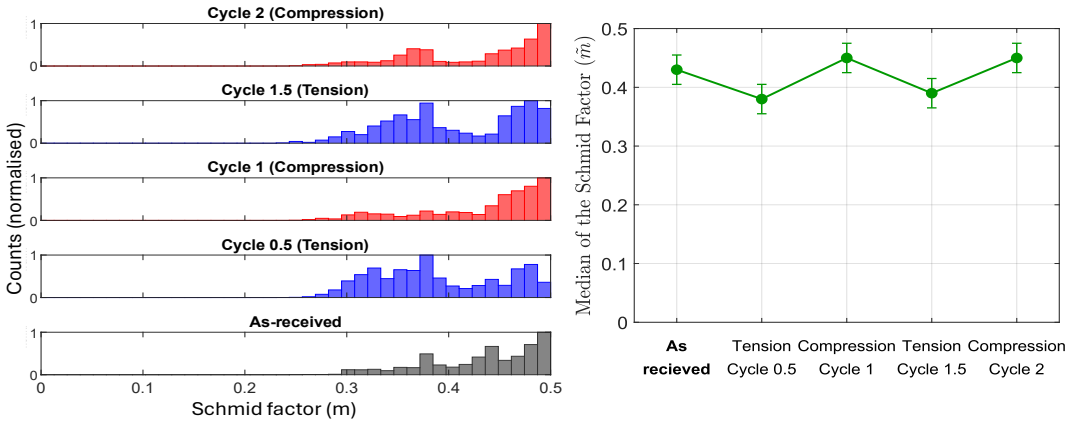


Figure 6.19: Pyramidal slip system $\{20\bar{2}2\}\langle\bar{1}\bar{1}23\rangle$ (α) (T-C load sequence) at the strain-rate of 1 s^{-1}

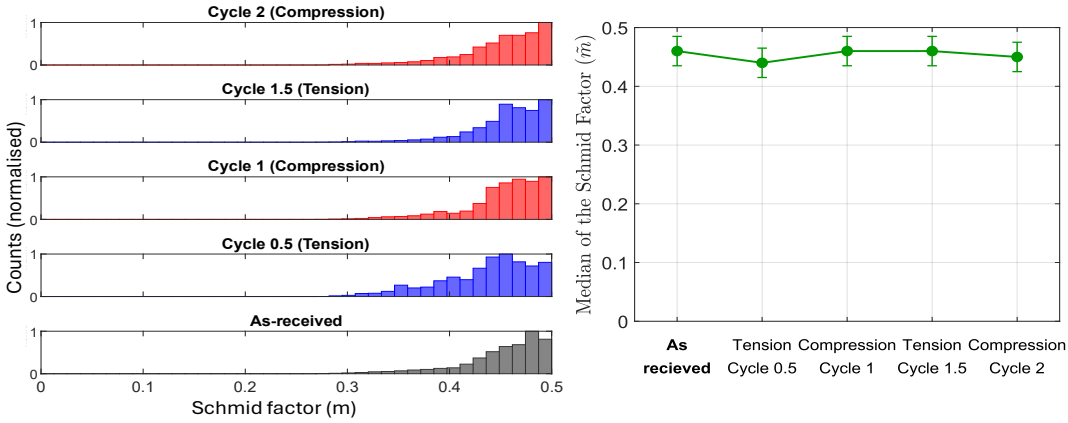


Figure 6.20: $\{110\}\langle\bar{1}11\rangle$ slip system (β) (T-C load sequence) at the strain-rate of 1 s^{-1}

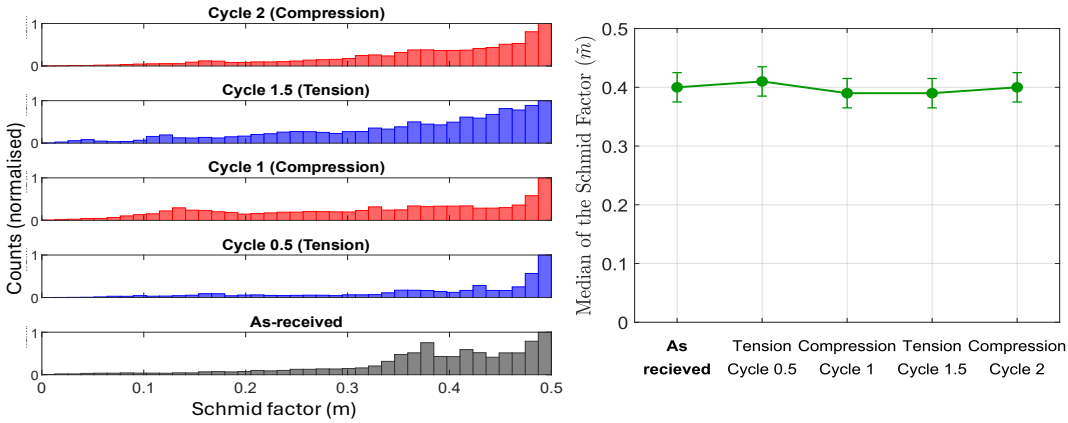


Figure 6.21: $\{200\}\langle011\rangle$ slip system (β) (T-C load sequence) at the strain-rate of 1 s^{-1}

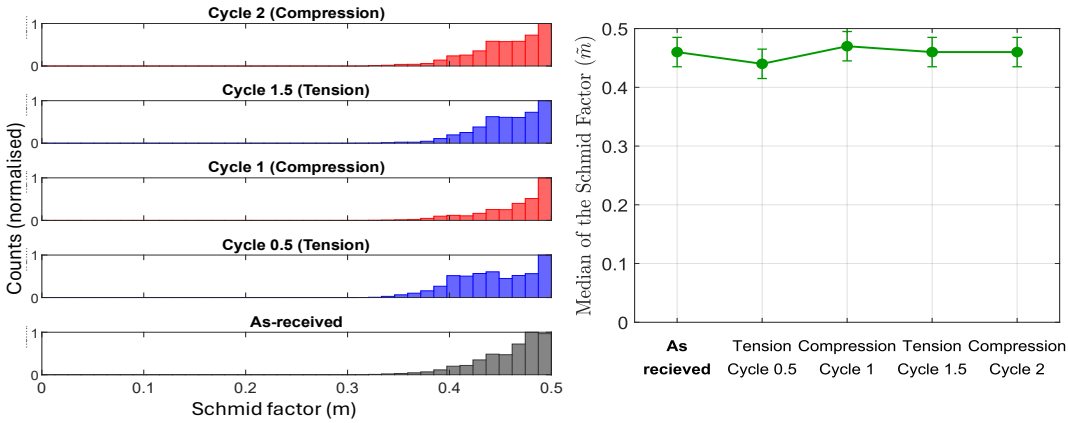


Figure 6.22: $\{211\}\langle\bar{1}11\rangle$ slip system (β) (T-C load sequence) at the strain-rate of 1 s^{-1}

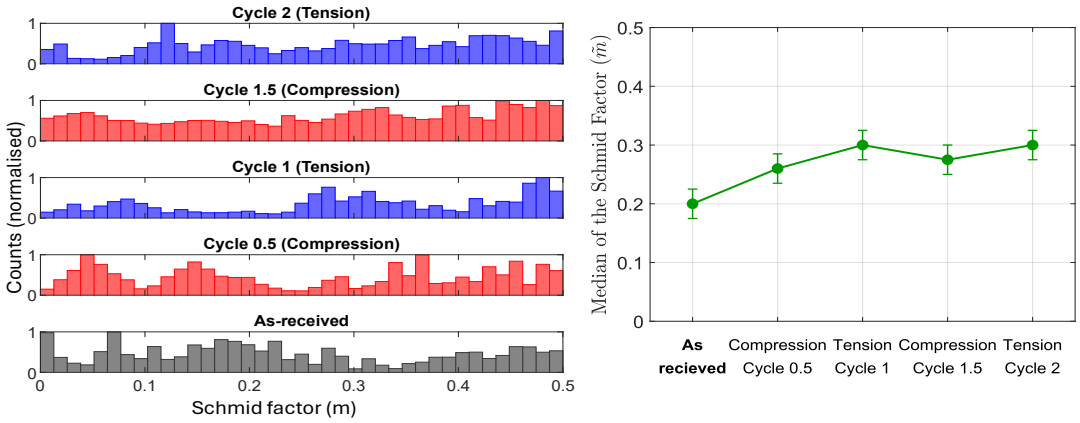


Figure 6.23: Basal slip system $\{0002\}\langle11\bar{2}0\rangle$ (α) (C-T load sequence) at the strain-rate of 1 s^{-1}

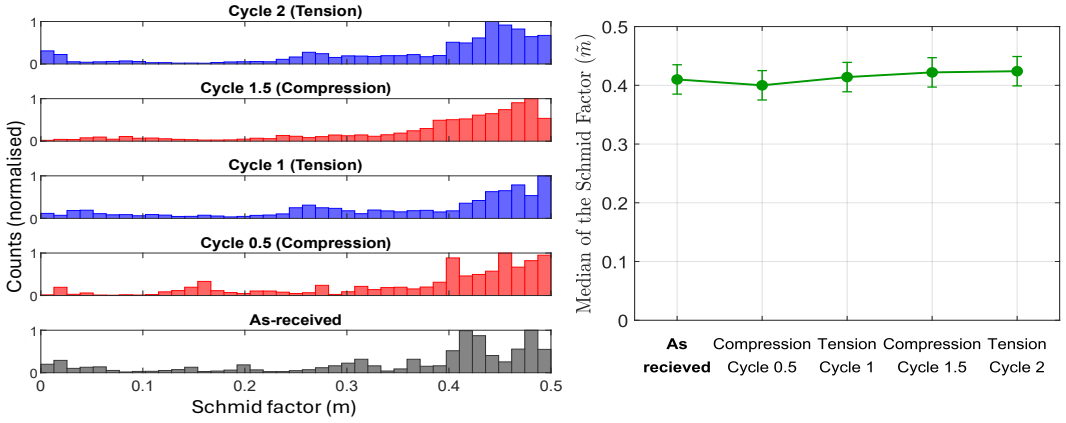


Figure 6.24: Prismatic slip system $\{10\bar{1}0\}\langle\bar{1}2\bar{1}0\rangle$ (α) (C-T load sequence) at the strain-rate of 1 s^{-1}

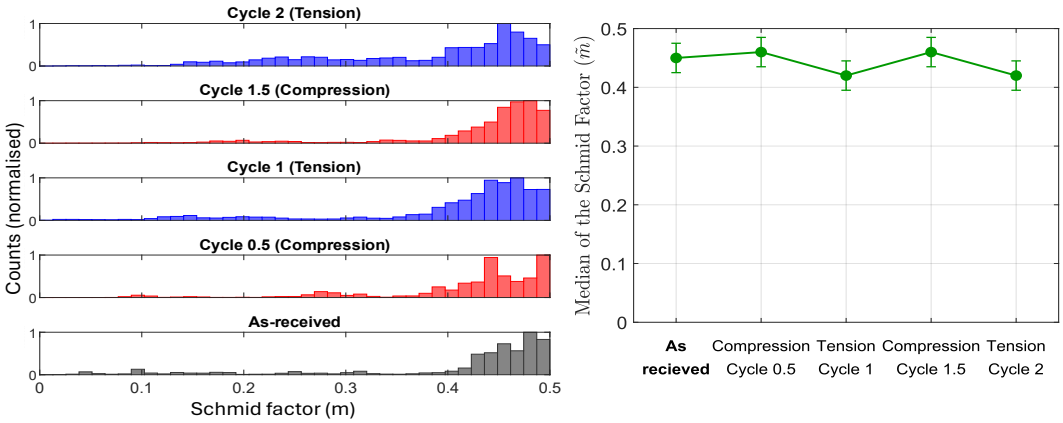


Figure 6.25: Pyramidal slip system $\{10\bar{1}1\}\langle\bar{1}2\bar{1}0\rangle$ (α) (C-T load sequence) at the strain-rate of 1 s^{-1}

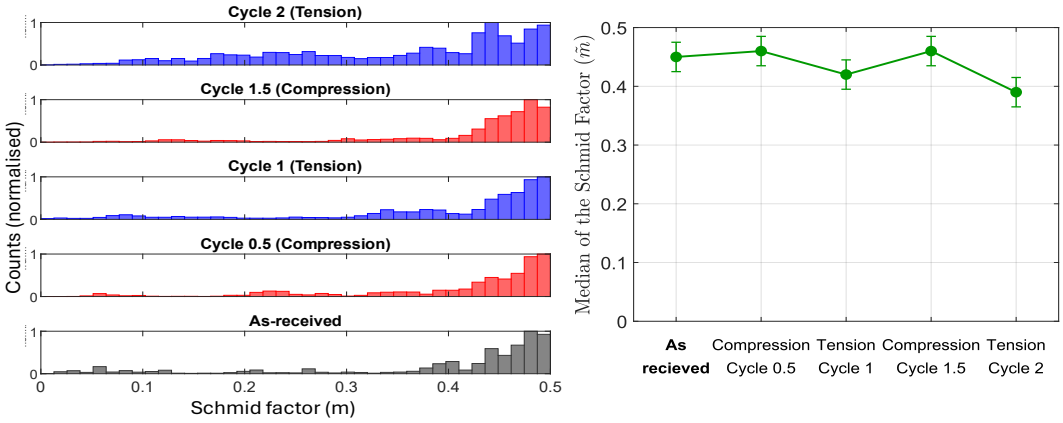


Figure 6.26: Pyramidal slip system $\{20\bar{2}1\}\langle\bar{1}2\bar{1}0\rangle$ (α) (C-T load sequence) at the strain-rate of 1 s^{-1}

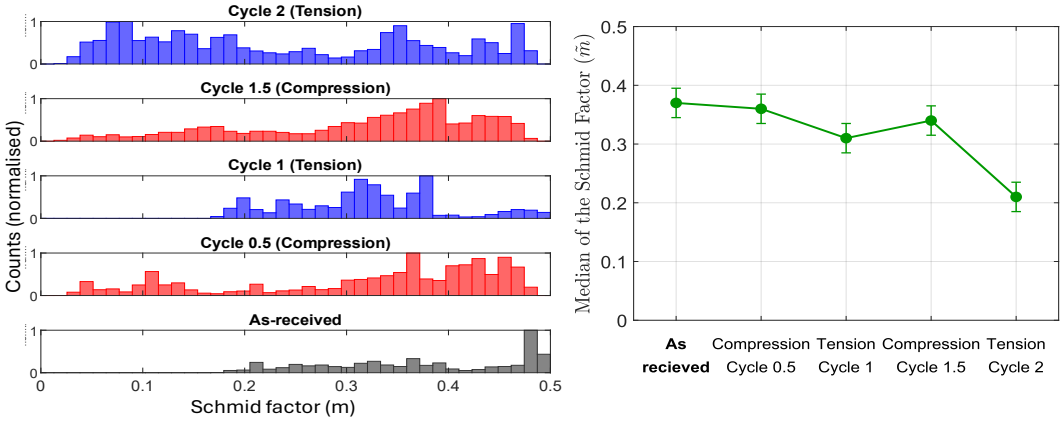


Figure 6.27: Second-order pyramidal slip system $\{11\bar{2}2\}\langle\bar{1}\bar{1}23\rangle$ (α) (C-T load sequence) at the strain-rate of 1 s^{-1}

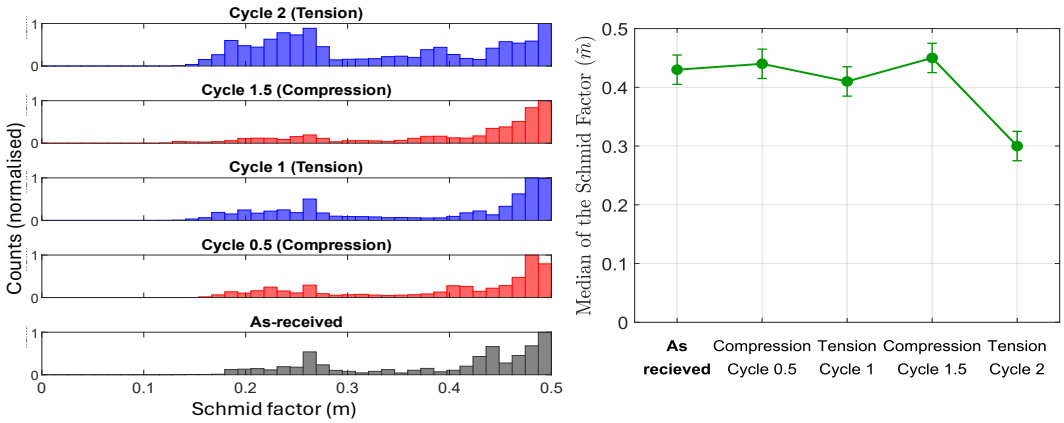


Figure 6.28: Pyramidal slip system $\{20\bar{2}2\}\langle\bar{1}\bar{1}23\rangle$ (α) (C-T load sequence) at the strain-rate of 1 s^{-1}

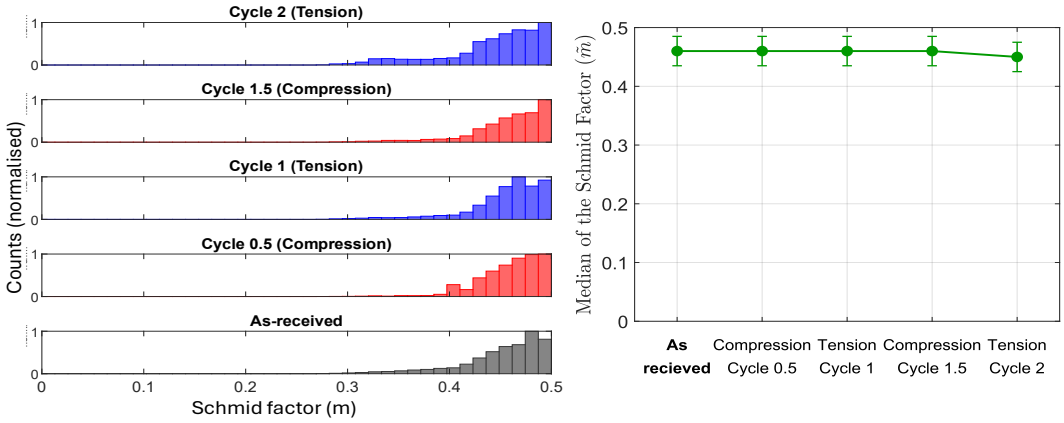


Figure 6.29: $\{110\}\langle\bar{1}11\rangle$ slip system (β) (C-T load sequence) at the strain-rate of 1 s^{-1}

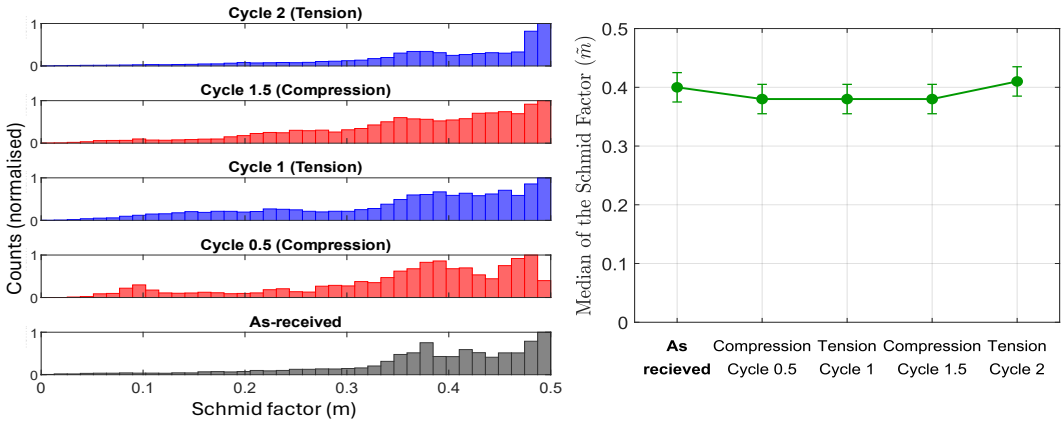


Figure 6.30: $\{200\}\langle011\rangle$ slip system (β) (C-T load sequence) at the strain-rate of 1 s^{-1}

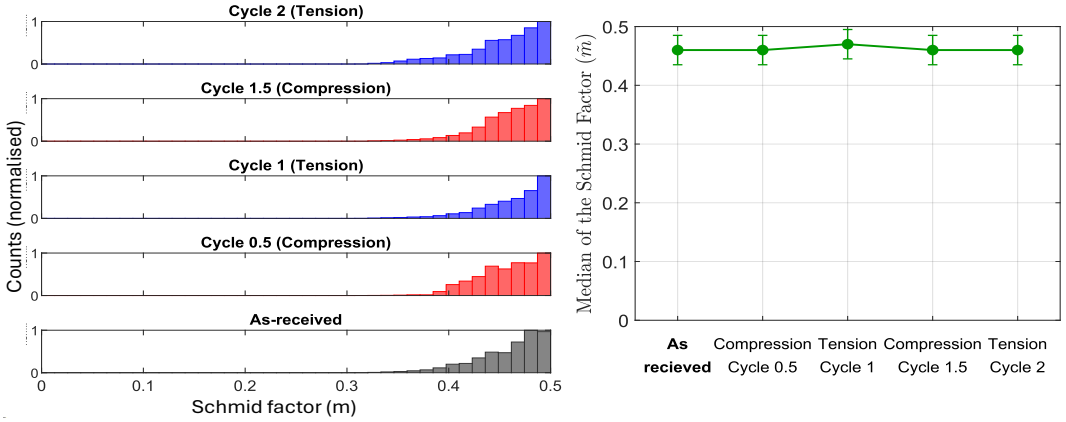


Figure 6.31: $\{211\}\langle\bar{1}11\rangle$ slip system (β) (C-T load sequence) at the strain-rate of 1 s^{-1}

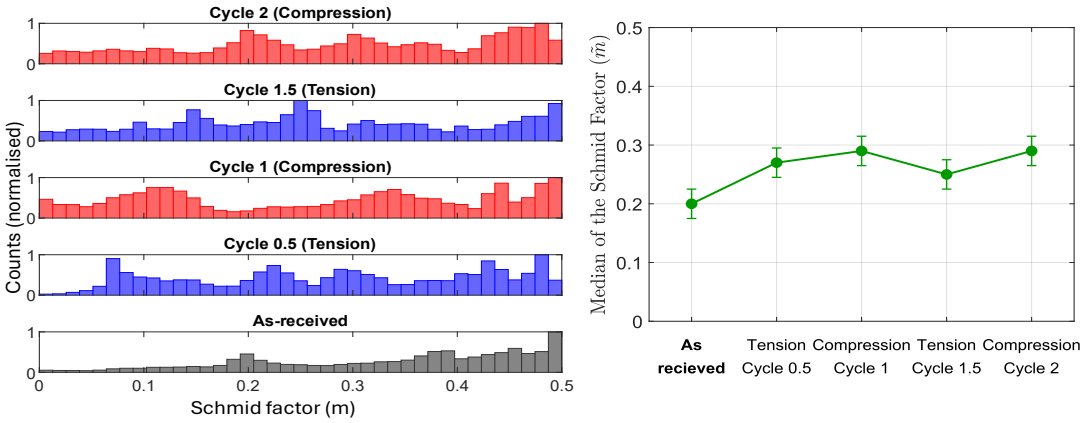


Figure 6.32: Basal slip system $\{0002\}\langle11\bar{2}0\rangle$ (α) (T-C load sequence) at the strain-rate of 10 s^{-1}

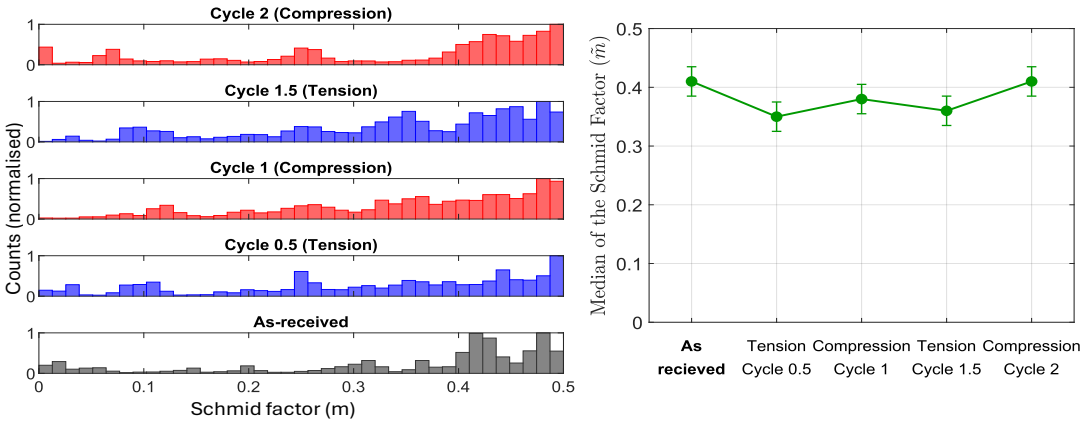


Figure 6.33: Prismatic slip system $\{10\bar{1}0\}\langle\bar{1}2\bar{1}0\rangle$ (α) (T-C load sequence) at the strain-rate of 10 s^{-1}

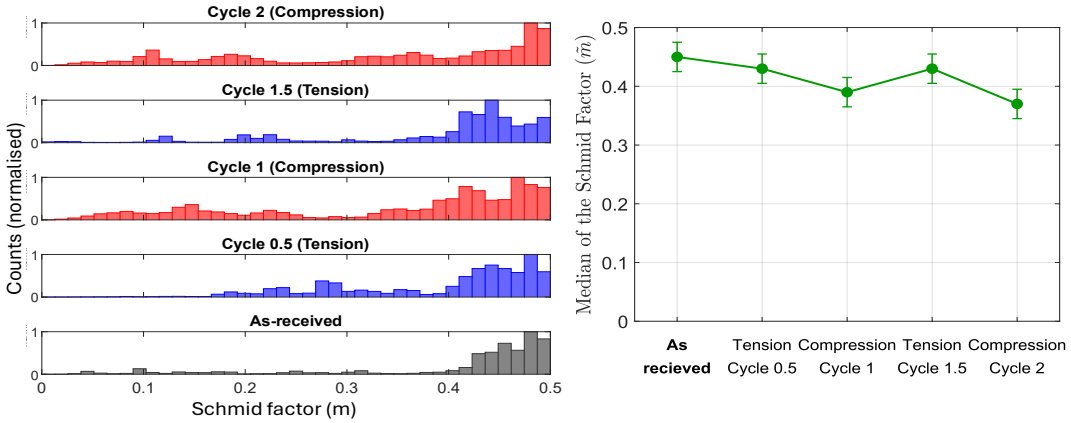


Figure 6.34: Pyramidal slip system $\{10\bar{1}1\}\langle\bar{1}2\bar{1}0\rangle$ (α) (T-C load sequence) at the strain-rate of 10 s^{-1}

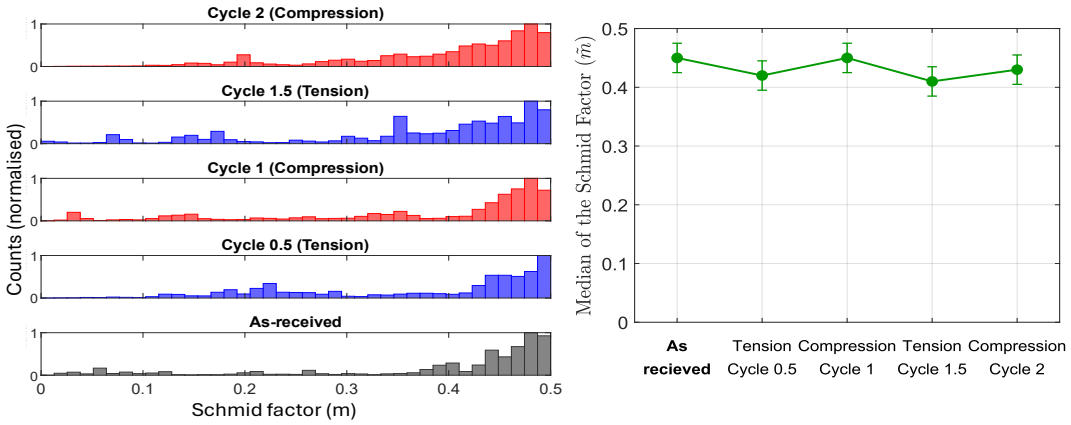


Figure 6.35: Pyramidal slip system $\{20\bar{2}1\}\langle\bar{1}2\bar{1}0\rangle$ (α) (T-C load sequence) at the strain-rate of 10 s^{-1}

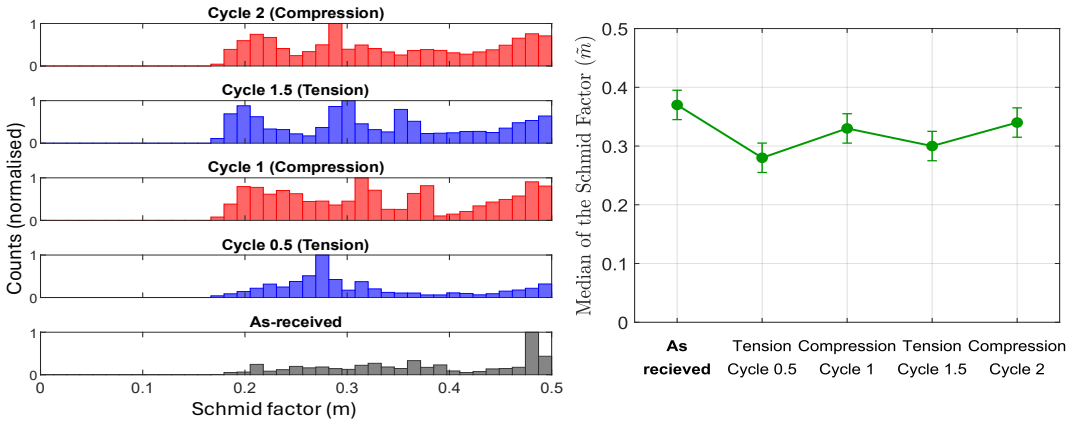


Figure 6.36: Second-order pyramidal slip system $\{11\bar{2}2\}\langle\bar{1}\bar{1}23\rangle$ (α) (T-C load sequence) at the strain-rate of 10 s^{-1}

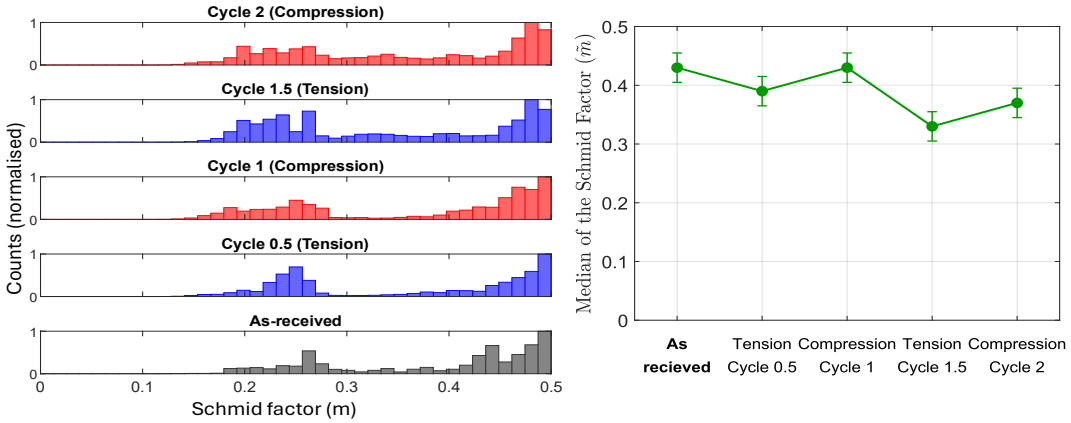


Figure 6.37: Pyramidal slip system $\{20\bar{2}2\}\langle\bar{1}\bar{1}23\rangle$ (α) (T-C load sequence) at the strain-rate of 10 s^{-1}

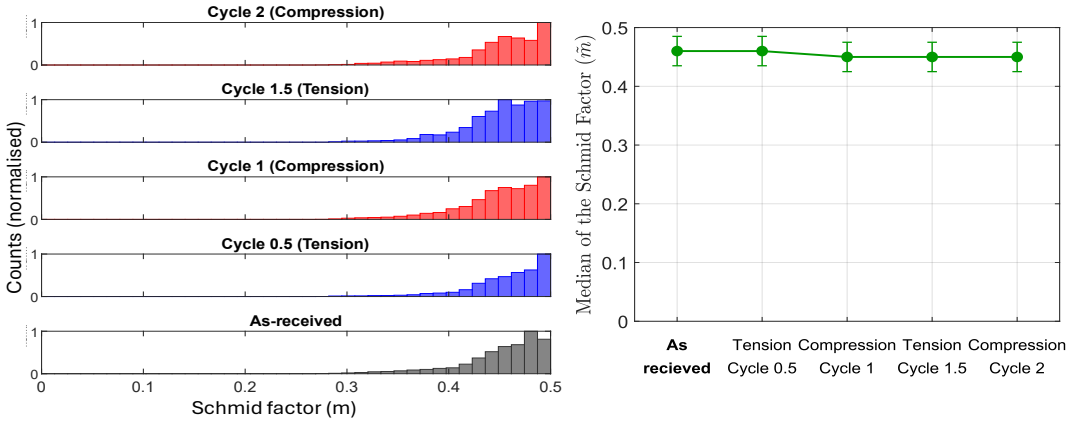


Figure 6.38: $\{110\}\langle\bar{1}11\rangle$ slip system (β) (T-C load sequence) at the strain-rate of 10 s^{-1}

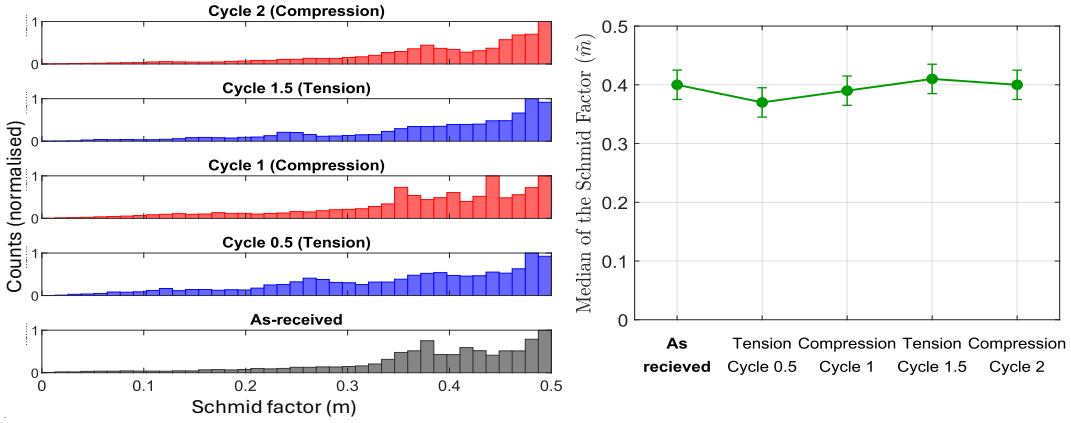


Figure 6.39: $\{200\}\langle011\rangle$ slip system (β) (T-C load sequence) at the strain-rate of 10 s^{-1}

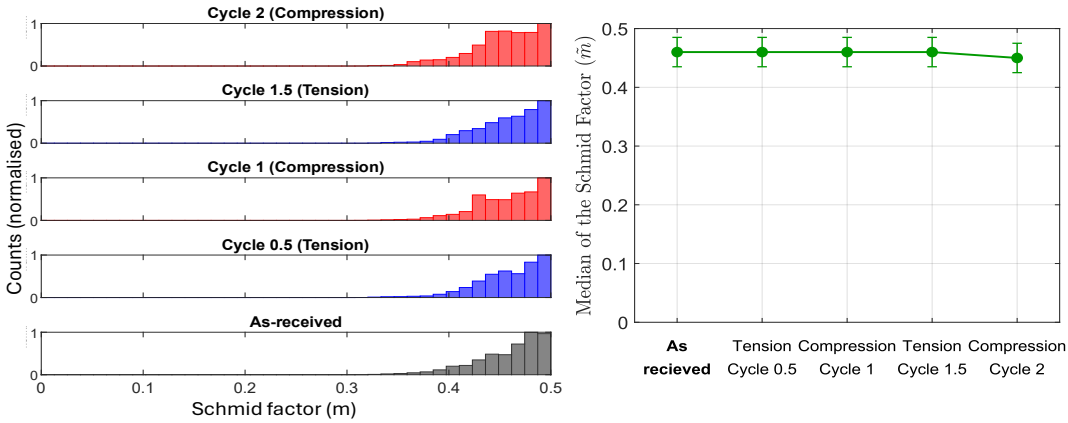


Figure 6.40: $\{211\}\langle\bar{1}11\rangle$ slip system (β) (T-C load sequence) at the strain-rate of 10 s^{-1}

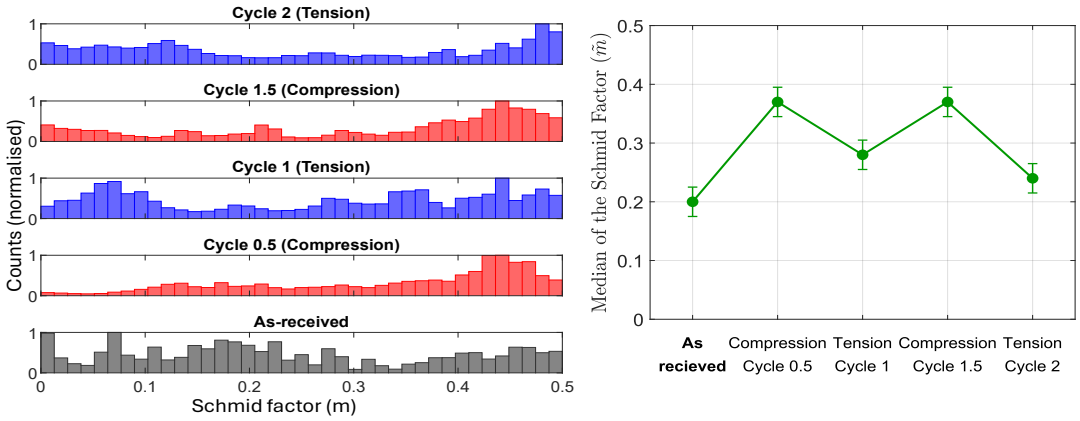


Figure 6.41: Basal slip system $\{0002\}\langle11\bar{2}0\rangle$ (α) (C-T load sequence) at the strain-rate of 10 s^{-1}

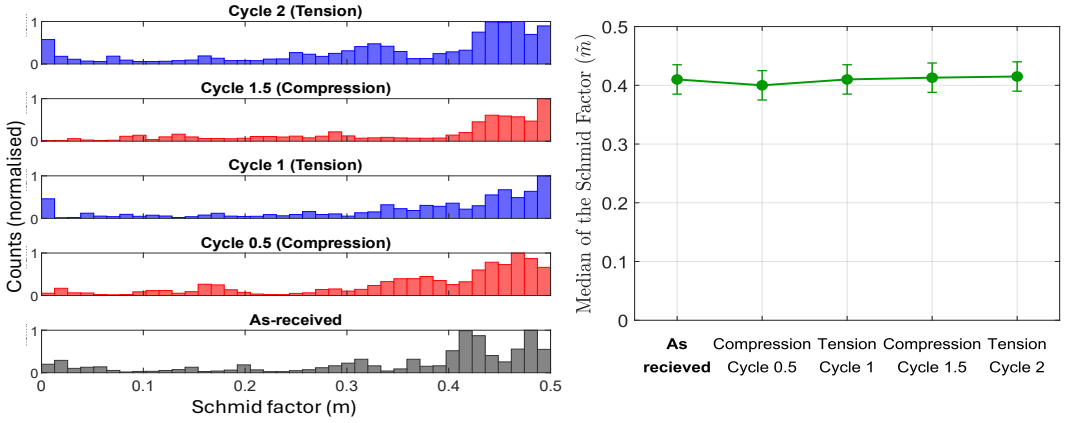


Figure 6.42: Prismatic slip system $\{10\bar{1}0\}\langle\bar{1}2\bar{1}0\rangle$ (α) (C-T load sequence) at the strain-rate of 10 s^{-1}

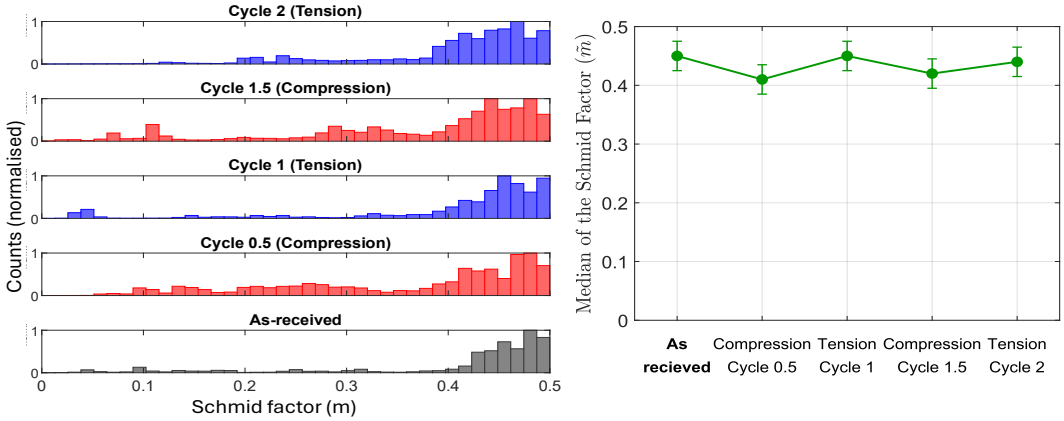


Figure 6.43: Pyramidal slip system $\{10\bar{1}1\}\langle\bar{1}2\bar{1}0\rangle$ (α) (C-T load sequence) at the strain-rate of 10 s^{-1}

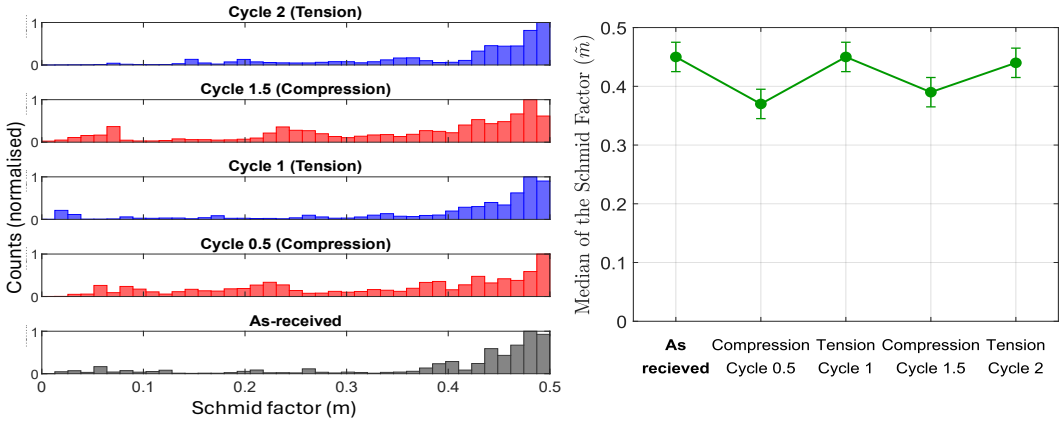


Figure 6.44: Pyramidal slip system $\{20\bar{2}1\}\langle\bar{1}2\bar{1}0\rangle$ (α) (C-T load sequence) at the strain-rate of 10 s^{-1}

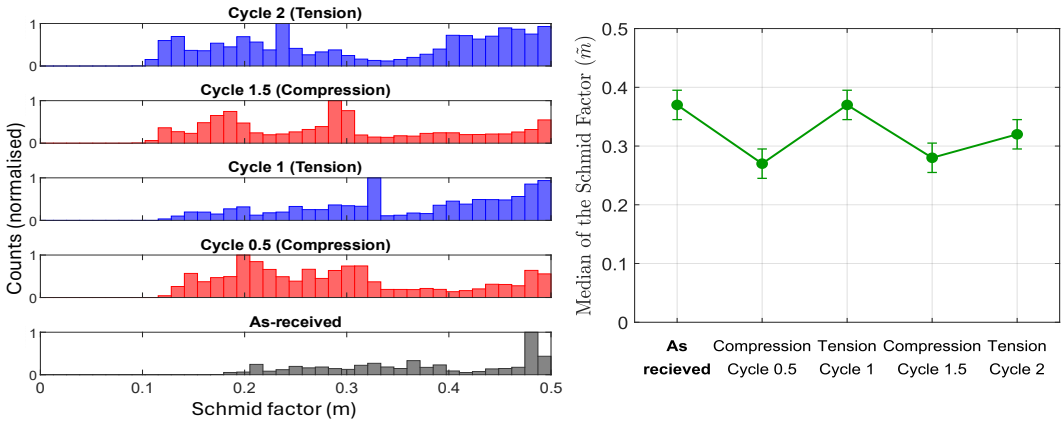


Figure 6.45: Second-order pyramidal slip system $\{11\bar{2}2\}\langle\bar{1}\bar{1}23\rangle$ (α) (C-T load sequence) at the strain-rate of 10 s^{-1}

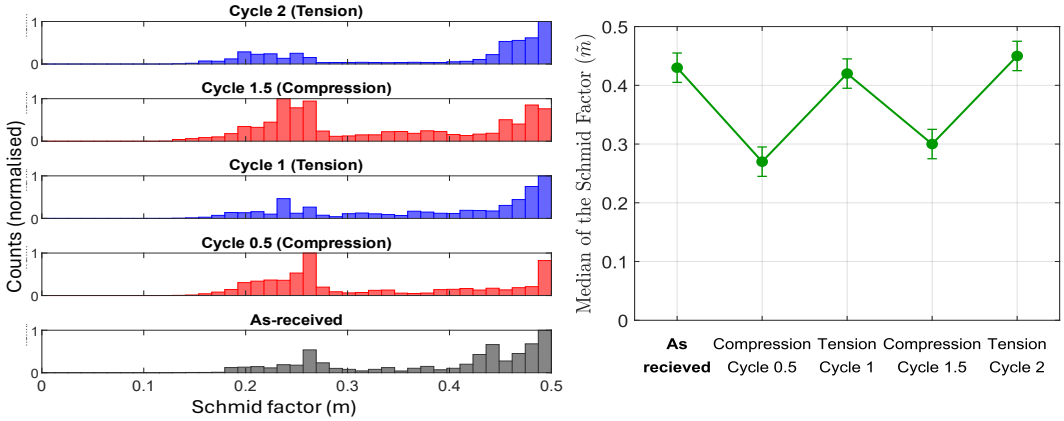


Figure 6.46: Pyramidal slip system $\{20\bar{2}2\}\langle\bar{1}\bar{1}23\rangle$ (α) (C-T load sequence) at the strain-rate of 10 s^{-1}

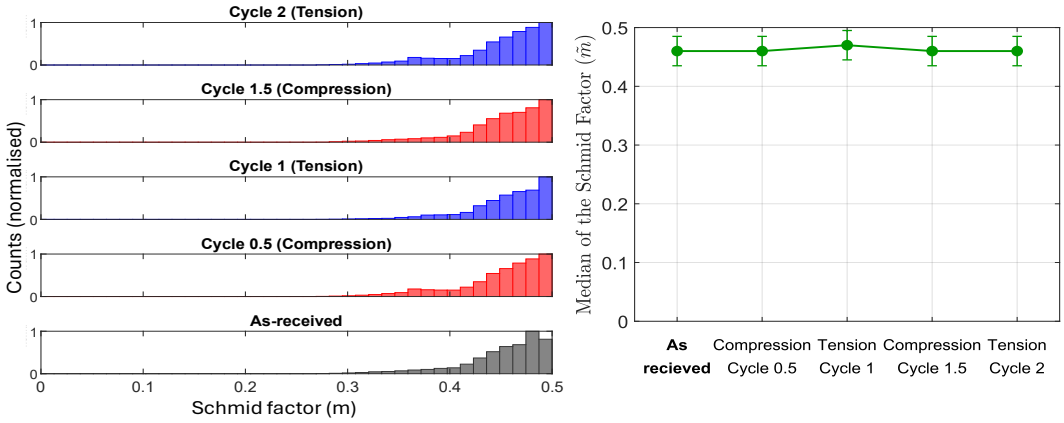


Figure 6.47: $\{110\}\langle\bar{1}11\rangle$ slip system (β) (C-T load sequence) at the strain-rate of 10 s^{-1}

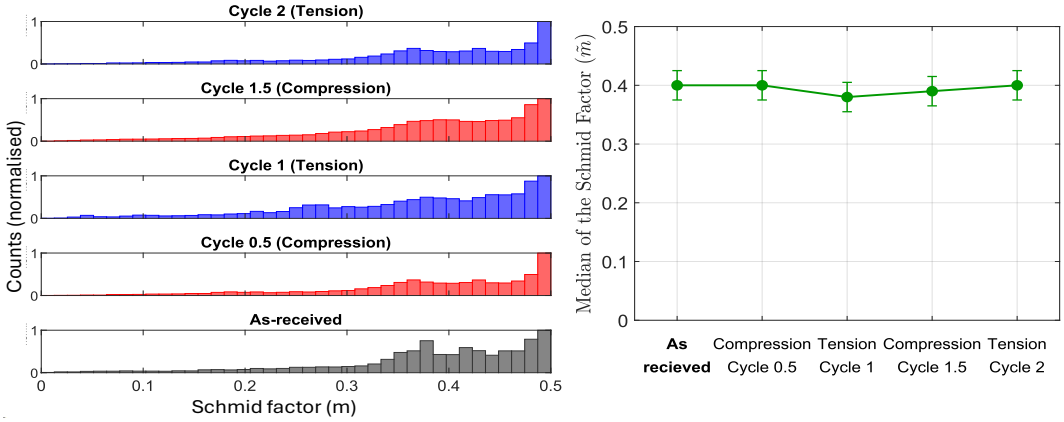


Figure 6.48: $\{200\}\langle011\rangle$ slip system (β) (C-T load sequence) at the strain-rate of 10 s^{-1}

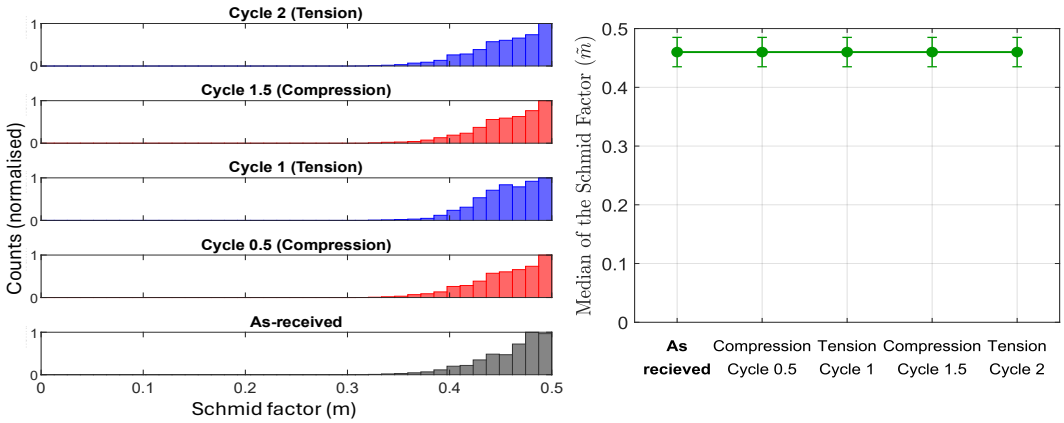


Figure 6.49: $\{211\}\langle\bar{1}11\rangle$ slip system (β) (C-T load sequence) at the strain-rate of 10 s^{-1}

6.5 Residual Stress accumulation in forged Ti-6Al-4V at $1\ s^{-1}$ and $10\ s^{-1}$

The evolution of residual stress accumulation in the crystallographic planes of the material during reverse loading at $1\ s^{-1}$ and $10\ s^{-1}$ was assessed through the evaluation of interrupted unsectioned specimens. These specimens were analysed after each load step, which ranged from 0.5 to 2 load cycles, in both loading sequences, using X-ray diffraction techniques.

6.5.1 Residual stress evolution of crystallographic planes in α and β phases present in forged Ti-6Al-4V

The interrupted, unsectioned specimens were analysed to measure the bulk residual stress after each loading step during the first two cycles of reverse loading for both loading sequences at the strain-rate of $1\ s^{-1}$ and at the strain-rate of $10\ s^{-1}$. Figures 6.50, 6.51, 6.52, 6.53, 6.54, 6.55, 6.56, and 6.57 demonstrate the evolution of the residual stress components, S_{11}, S_{22}, S_{33}, and S_{12}, within the crystallographic planes during the T-C loading in the α phase at $1\ s^{-1}$, during the T-C loading in the β phase at $1\ s^{-1}$, during the C-T loading in the α phase at $1\ s^{-1}$, during the C-T loading in the β phase at $1\ s^{-1}$, during the T-C loading in the α phase at $10\ s^{-1}$, during the T-C loading in the β phase at $10\ s^{-1}$, during the C-T loading in the α phase at $10\ s^{-1}$, and during the C-T loading in the β phase at $10\ s^{-1}$. The calculated values for S_{23} and S_{13} are zero in all the planes and are

therefore not shown in the plots.

The accumulation of residual stress in the α phase at 1 s^{-1} during the T-C loading sequence is illustrated in Figure 6.50. Figure 6.50(a) demonstrates an asymmetrical trend in the behaviour of residual stress components within the basal plane (0002) as the load cycle progresses from 0.5 to 2. In the prismatic plane $(10\bar{1}0)$, Figure 6.50(b) reveals that the residual stress components S_{11}, S_{22}, and S_{33} also exhibit an asymmetrical trend as the number of cycles increases, while S_{12} demonstrates minimal variation. In the pyramidal plane $(10\bar{1}1)$, as depicted in Figure 6.50(c), the accumulation of residual stress is more pronounced during compression load steps in comparison to tension load steps. For the pyramidal plane $(20\bar{2}1)$, illustrated in Figure 6.50(d), it is evident that all residual stress components during compression load steps are relatively greater than those in tension load steps. Finally, for the second-order pyramidal plane $(11\bar{2}2)$, Figure 6.50(e) indicates that the residual stress components exhibit an asymmetrical fluctuation trend as the number of cycles increases.

Given that the presence of the β phase in the sample is only 2%, the accumulation of residual stress within the crystallographic planes is significantly lower than that of the α phase. Figure 6.51 illustrates the accumulation of residual stress in the β phase at 1 s^{-1} during the T-C loading sequence. In the (110) plane, as depicted in Figure 6.51(a), all residual stress components remain nearly constant with the increasing number of load cycles. In the (200) plane, shown in Figure 6.51(b), all stress components also remain steady as the number of load cycles

increases. In the (211) plane, illustrated in Figure 6.51(c), the accumulation of residual stress in all components remains constant since the onset of loading.

As shown in Figure 6.52, in the α phase during the C-T loading sequence at 1 s^{-1}, the accumulation of residual stress in the basal plane (0002), depicted in Figure 6.52(a), exhibits an asymmetrical trend as well. Specifically, an increasing residual stress value is followed by a decreasing value, a trend that can be observed from load cycle 0.5 to cycle 2. In the prismatic plane $(10\bar{1}0)$, as illustrated in Figure 6.52(b), the residual stress components exhibit a relaxation of stress as the number of load cycles increases, transitioning from higher positive values toward zero. In contrast, S_{12} remains constant throughout. In the pyramidal plane $(10\bar{1}1)$, illustrated in Figure 6.52(c), the residual stress components show a similar trend, exhibiting both increasing and decreasing values as the number of load cycles increases. The pyramidal plane $(20\bar{2}1)$ shown in Figure 6.52(d) exhibits a similar trend in residual stress values, displaying more positive values during tension load steps and more negative values during compression load steps, as observed in S_{11} and S_{33}. A similar asymmetrical trend in residual stress values is observed in the second-order pyramidal plane, although residual stress values remain positive throughout in the $(11\bar{2}2)$, as illustrated in Figure 6.52(e).

In the β phase of the material during the C-T loading sequence at 1 s^{-1}, the accumulation of residual stress is illustrated in Figure 6.53. Across all planes, namely ((110), (200), and (211), as depicted in Figures 5.50(a), 6.53(b), and 6.53(c) respectively, the residual stress values remain almost constant until the

second load cycle.

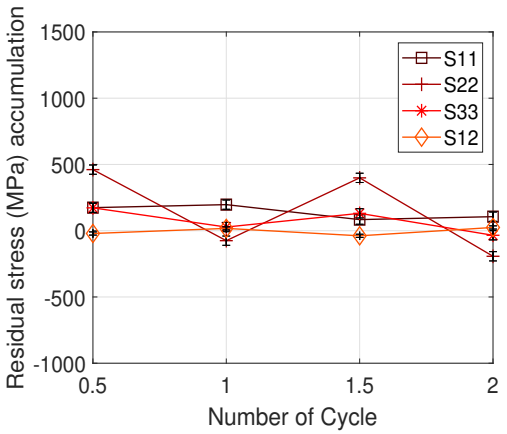
The accumulation of residual stress in the α phase at 10 s^{-1} during the T-C loading sequence is illustrated in Figure 6.54. Figure 6.54(a) demonstrates an asymmetrical trend in the behaviour of residual stress components within the basal plane (0002) as the load cycle progresses from 0.5 to 2. In the prismatic plane $(10\bar{1}0)$, Figure 6.54(b) reveals that the residual stress components S_{11}, S_{22}, and S_{33} also exhibit an asymmetrical trend as the number of cycles increases, while S_{12} demonstrates minimal variation. In the pyramidal plane $(10\bar{1}1)$, as depicted in Figure 6.54(c), the accumulation of residual stress is more pronounced during compression load steps in comparison to tension load steps. For the pyramidal plane $(20\bar{2}1)$, illustrated in Figure 6.54(d), it is evident that all residual stress components during compression load steps are relatively greater than those in tension load steps. Finally, for the second-order pyramidal plane $(11\bar{2}2)$, Figure 6.54(e) indicates that the residual stress components exhibit an asymmetrical fluctuation trend as the number of cycles increases.

Figure 6.55 illustrates the accumulation of residual stress in the β phase at 10 s^{-1} during the T-C loading sequence. In the (110) plane, as depicted in Figure 6.55(a), all residual stress components remain nearly constant with the increasing number of load cycles. In the (200) plane, shown in Figure 6.55(b), all stress components, except for S_{33}, also remain almost steady as the number of load cycles increases. In the (211) plane, illustrated in Figure 6.55(c), the accumulation of residual stress in all components remains almost constant since

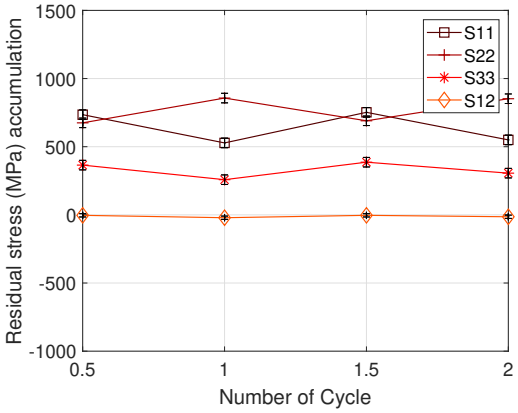
the onset of loading.

As shown in Figure 6.56, the α phase during the C-T loading sequence at 10 s^{-1}, the accumulation of residual stress in the basal plane (0002), depicted in Figure 6.56(a), exhibits an asymmetrical trend as well. Specifically, an increasing residual stress value is followed by a decreasing value, a trend that can be observed from load cycle 0.5 to cycle 2. In the prismatic plane $(10\bar{1}0)$, as illustrated in Figure 6.56(b), the residual stress components exhibit a relaxation of stress as the number of load cycles increases, transitioning from higher values toward zero. In contrast, S_{12} remains constant throughout. In the pyramidal plane $(10\bar{1}1)$, illustrated in Figure 6.56(c), the residual stress components show a similar trend, exhibiting both increasing and decreasing values as the number of load cycles increases. However, the accumulation of residual stress is more significant during compression load steps compared to tension load steps. The pyramidal plane $(20\bar{2}1)$ shown in Figure 6.56(d) exhibits a similar trend in residual stress values, displaying higher values during tension load steps than during compression load steps. A similar asymmetrical trend in residual stress values is observed in the second-order pyramidal plane $(11\bar{2}2)$, illustrated in Figure 6.56(e).

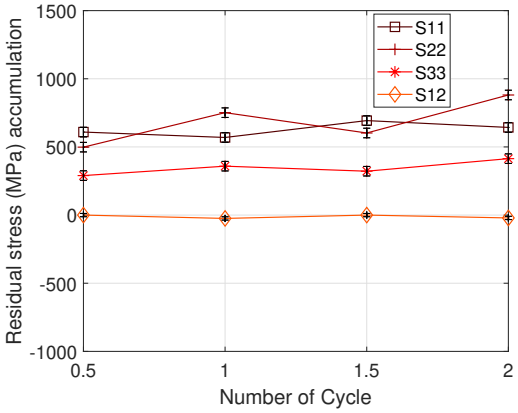
In the β phase of the material during the C-T loading sequence at 10 s^{-1}, the accumulation of residual stress is illustrated in Figure 6.57. Across all planes, namely (110), (200), and (211), as depicted in Figures 6.57(a), 6.57(b), and 6.57(c) respectively, the residual stress values remain almost constant until the second load cycle.



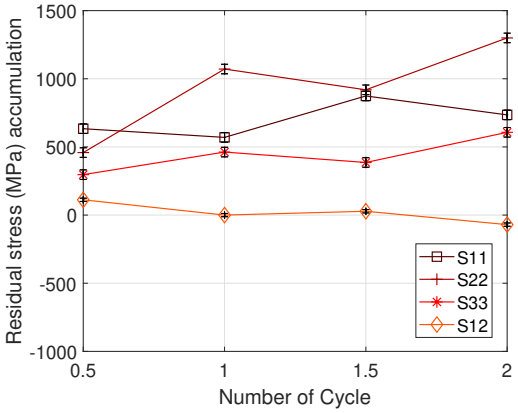
(a) Basal plane (0002) (α) (T-C load sequence)



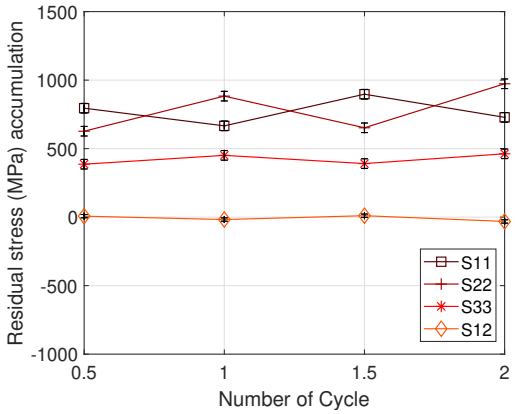
(b) Prismatic plane ($10\bar{1}0$) (α) (T-C load sequence)



(c) Pyramidal plane ($10\bar{1}1$) (α) (T-C load sequence)

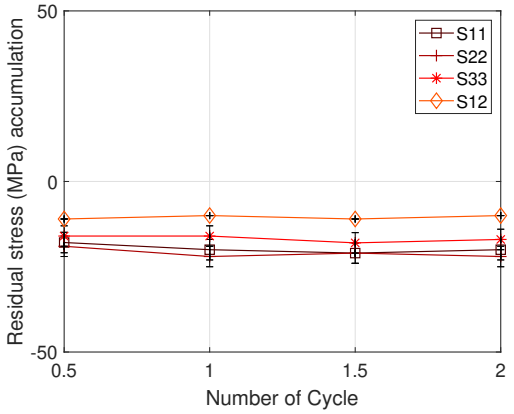


(d) Pyramidal plane ($20\bar{2}1$) (α) (T-C load sequence)

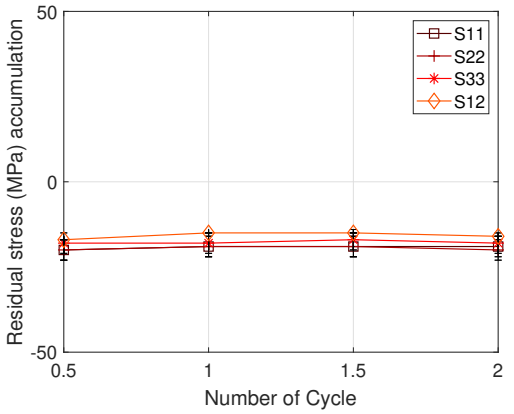


(e) Second-order Pyramidal plane ($11\bar{2}2$) (α) (T-C load sequence)

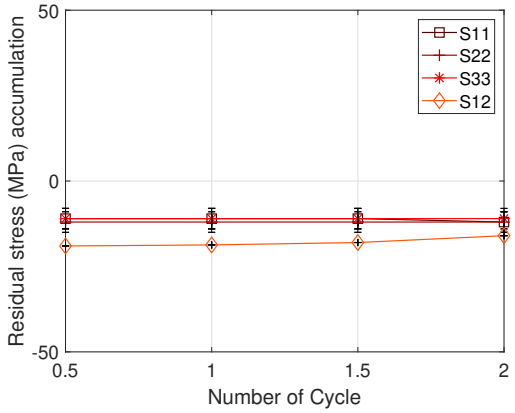
Figure 6.50: Residual stress accumulation in crystallographic planes in α phase at the strain-rate of 1 s^{-1} during the T-C loading sequences, from load cycle 0.5 (Tension) to load cycle 2 (Compression). Each data point's uncertainty was estimated using the methodology outlined in Chapter 4.7.2, based on the synchrotron X-ray diffraction [141].



(a) (110) (β) (T-C load sequence)

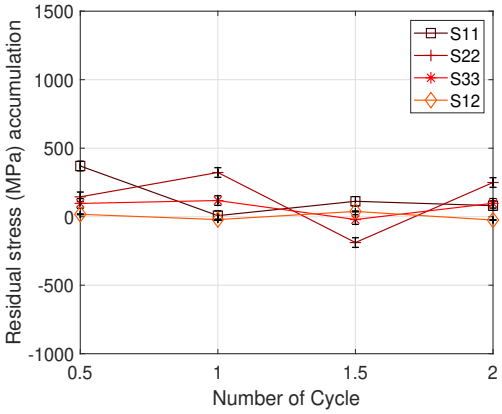


(b) (200) (β) (T-C load sequence)

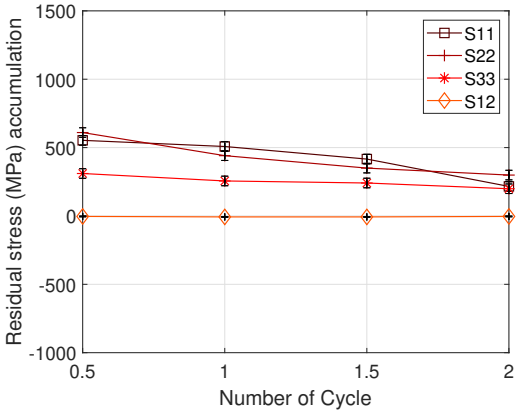


(c) (211) (β) (T-C load sequence)

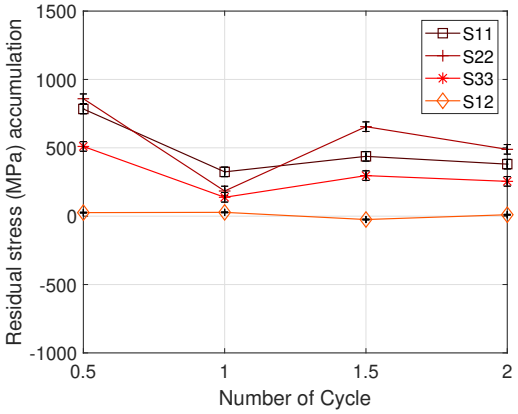
Figure 6.51: Residual stress accumulation in crystallographic planes in β phase at the strain-rate of 1 s^{-1} during the T-C loading sequences, from load cycle 0.5 (Tension) to load cycle 2 (Compression). Each data point's uncertainty was estimated using the methodology outlined in Chapter 4.7.2, based on the synchrotron X-ray diffraction [141].



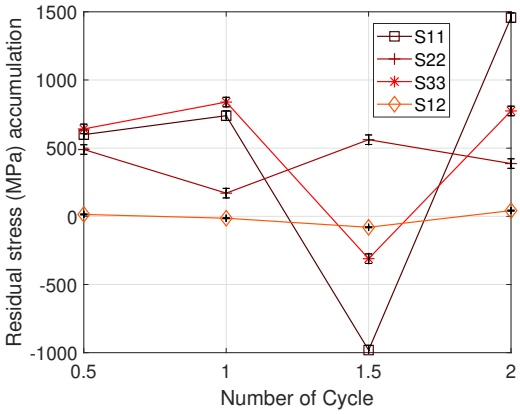
(a) Basal plane (0002) (α) (C-T load sequence)



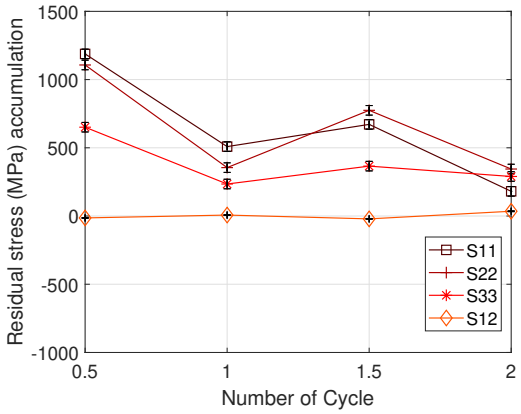
(b) Prismatic plane ($10\bar{1}0$) (α) (C-T load sequence)



(c) Pyramidal plane ($10\bar{1}1$) (α) (C-T load sequence)

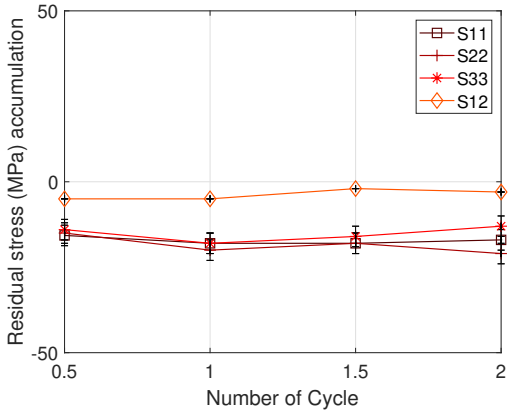


(d) Pyramidal plane ($20\bar{2}1$) (α) (C-T load sequence)

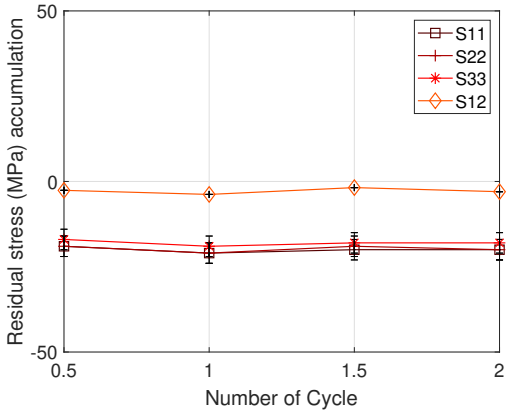


(e) Second-order Pyramidal plane ($11\bar{2}2$) (α) (C-T load sequence)

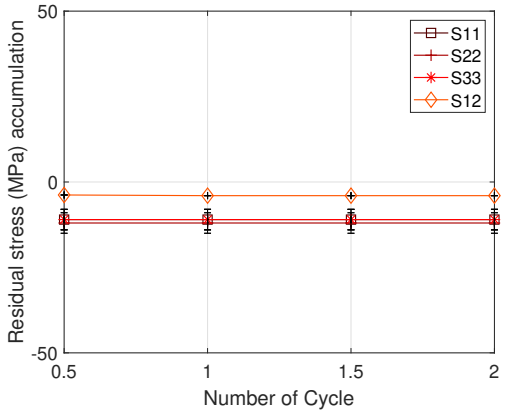
Figure 6.52: Residual stress accumulation in crystallographic planes in α phase at the strain-rate of 1 s^{-1} during the C-T loading sequences, from load cycle 0.5 (Tension) to load cycle 2 (Compression). Each data point's uncertainty was estimated using the methodology outlined in Chapter 4.7.2, based on the synchrotron X-ray diffraction [141].



(a) (110) (β) (C-T load sequence)

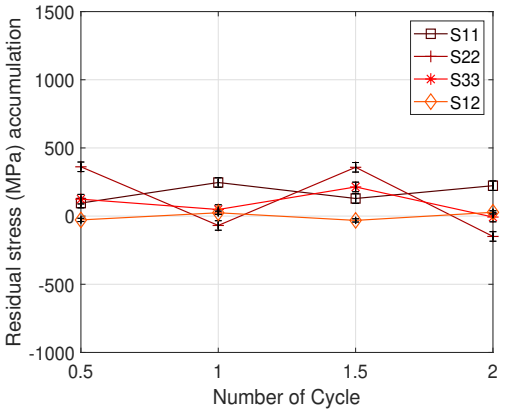


(b) (200) (β) (C-T load sequence)

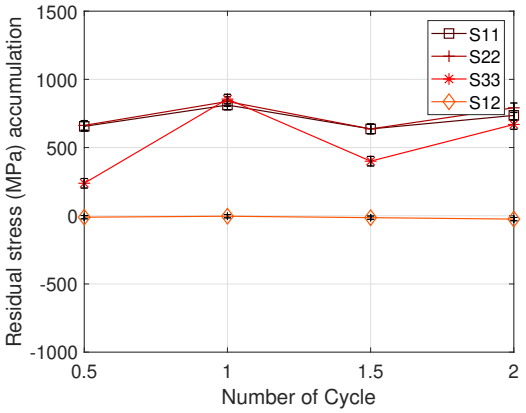


(c) (211) (β) (C-T load sequence)

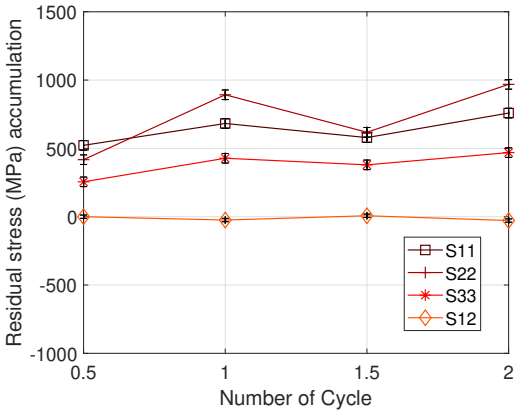
Figure 6.53: Residual stress accumulation in crystallographic planes in β phase at the strain-rate of 1 s^{-1} during the C-T loading sequences, from load cycle 0.5 (Tension) to load cycle 2 (Compression). Each data point's uncertainty was estimated using the methodology outlined in Chapter 4.7.2, based on the synchrotron X-ray diffraction [141].



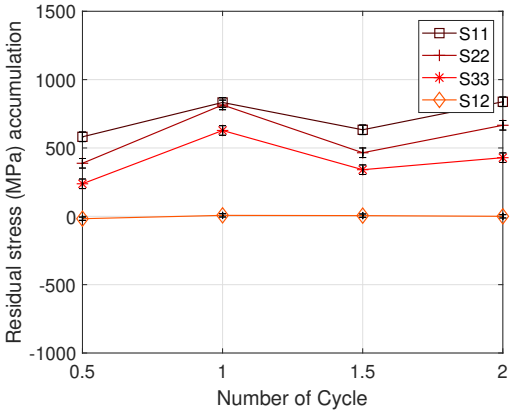
(a) Basal plane (0002) (α) (T-C load sequence)



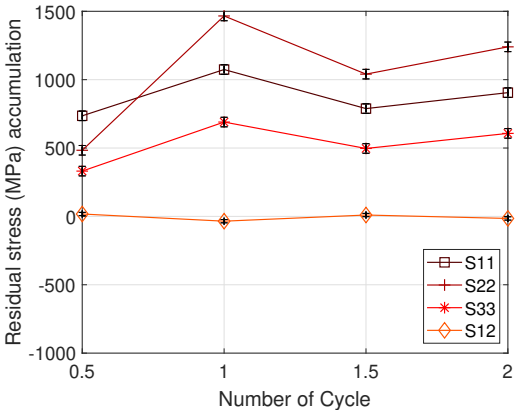
(b) Prismatic plane ($10\bar{1}0$) (α) (T-C load sequence)



(c) Pyramidal plane ($10\bar{1}1$) (α) (T-C load sequence)

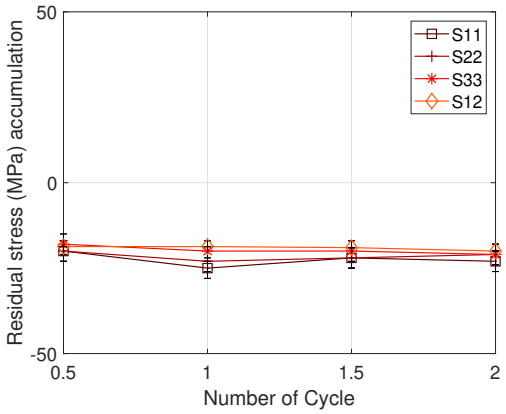


(d) Pyramidal plane ($20\bar{2}1$) (α) (T-C load sequence)

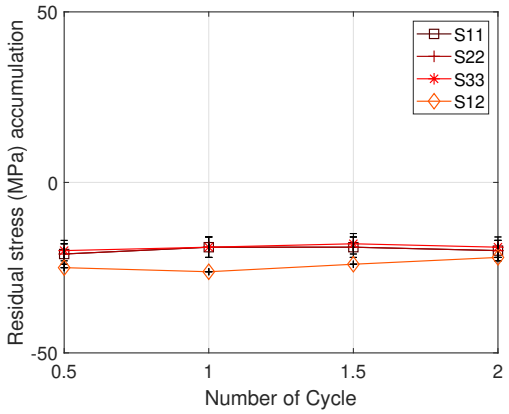


(e) Second-order Pyramidal plane ($11\bar{2}2$) (α) (T-C load sequence)

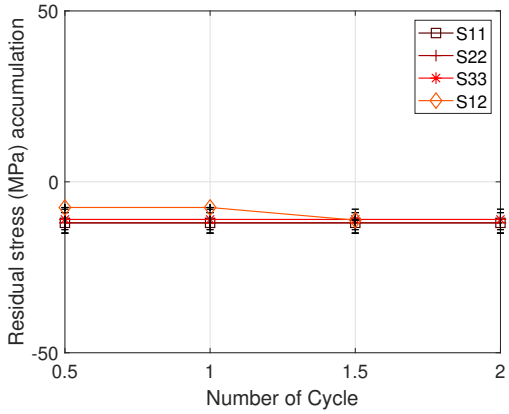
Figure 6.54: Residual stress accumulation in crystallographic planes in α phase at the strain-rate of 10 s^{-1} during the T-C loading sequences, from load cycle 0.5 (Tension) to load cycle 2 (Compression). Each data point's uncertainty was estimated using the methodology outlined in Chapter 4.7.2, based on the synchrotron X-ray diffraction [141].



(a) (110) (β) (T-C load sequence)

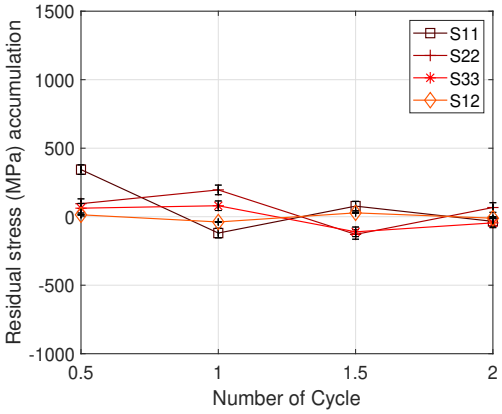


(b) (200) (β) (T-C load sequence)

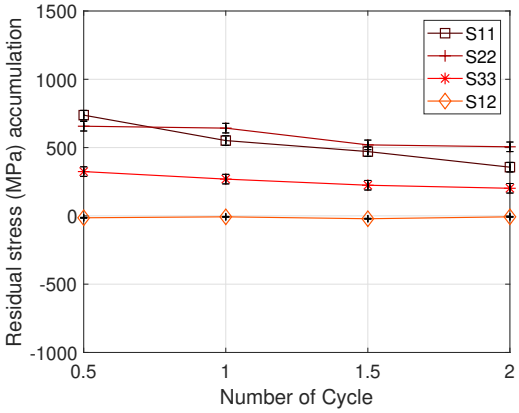


(c) (211) (β) (T-C load sequence)

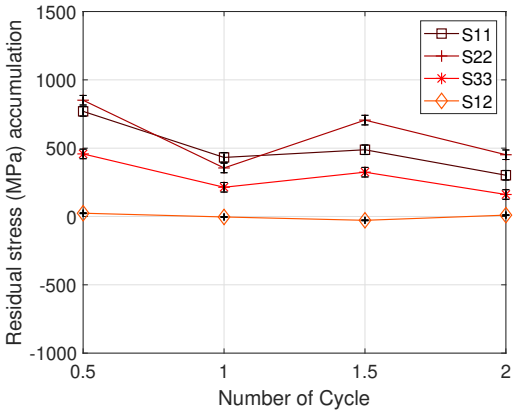
Figure 6.55: Residual stress accumulation in crystallographic planes in β phase at the strain-rate of 10 s^{-1} during the T-C loading sequences, from load cycle 0.5 (Tension) to load cycle 2 (Compression). Each data point's uncertainty was estimated using the methodology outlined in Chapter 4.7.2, based on the synchrotron X-ray diffraction [141].



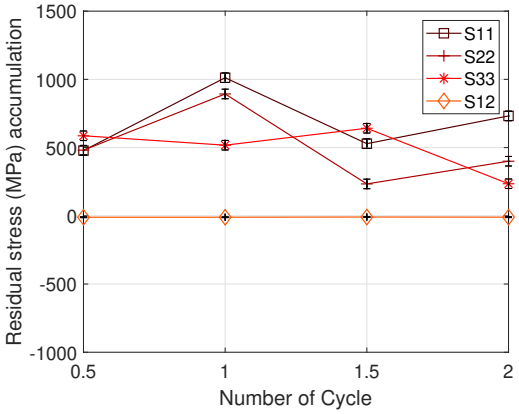
(a) Basal plane (0002) (α) (C-T load sequence)



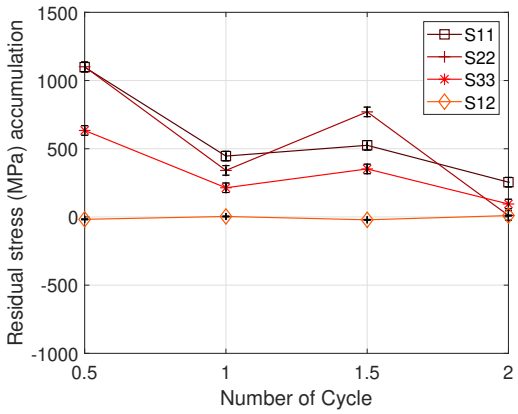
(b) Prismatic plane ($10\bar{1}0$) (α) (C-T load sequence)



(c) Pyramidal plane ($10\bar{1}1$) (α) (C-T load sequence)

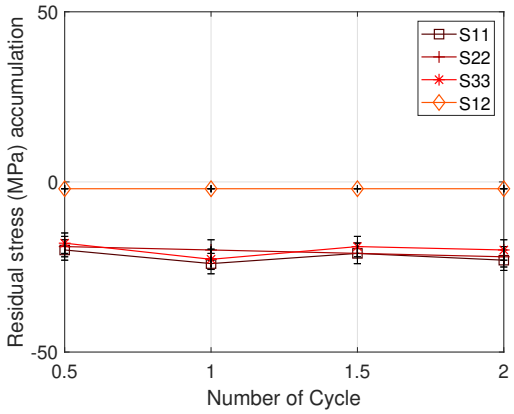


(d) Pyramidal plane ($20\bar{2}1$) (α) (C-T load sequence)

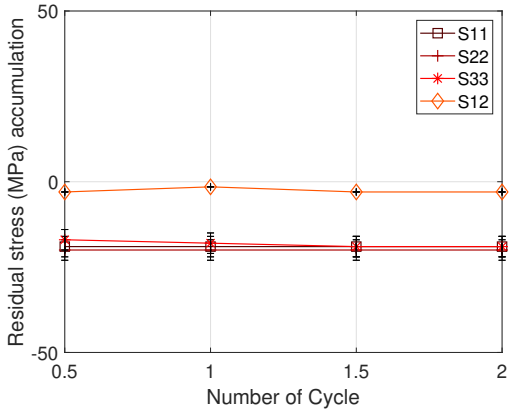


(e) Second-order Pyramidal plane ($11\bar{2}2$) (α) (C-T load sequence)

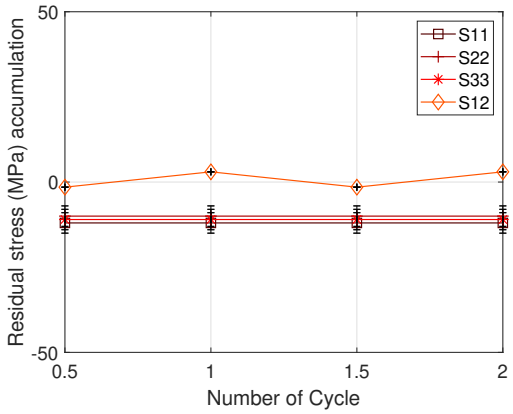
Figure 6.56: Residual stress accumulation in crystallographic planes in α phase at the strain-rate of 10 s^{-1} during the C-T loading sequences, from load cycle 0.5 (Tension) to load cycle 2 (Compression). Each data point's uncertainty was estimated using the methodology outlined in Chapter 4.7.2, based on the synchrotron X-ray diffraction [141].



(a) (110) (β) (C-T load sequence)



(b) (200) (β) (C-T load sequence)



(c) (211) (β) (C-T load sequence)

Figure 6.57: Residual stress accumulation in crystallographic planes in β phase at the strain-rate of 10 s^{-1} during the C-T loading sequences, from load cycle 0.5 (Tension) to load cycle 2 (Compression). Each data point's uncertainty was estimated using the methodology outlined in Chapter 4.7.2, based on the synchrotron X-ray diffraction [141].

6.6 Summary

During the intermediate strain-rates of 1 s^{-1} and 10 s^{-1} reverse loading at room temperature, the reverse loading response of forged Ti-6Al-4V is investigated across both loading sequences. During the reverse loading at 1 s^{-1}, the specimen had sufficient time to cool before reloading in the opposite direction, and hence it shows temperature increases during loading and decreases during unloading. At 10 s^{-1}, the temperature of the specimen increases due to the relatively fast loading. Adiabatic self-heating is maintained throughout the test, except for moments just before failure due to crack propagation.

At both strain-rates, the material exhibited a persistent Baushinger effect during the T-C load sequence, however, at 10 s^{-1}, the Bauschinger effect tends to diminish before the material failure. The magnitude of the Bauschinger effect is also observed to be slightly decreased with the increasing strain-rate. During the C-T load sequence, the Bauschinger effect diminishes after the first load cycle. The observed kinematic backstress in the T-C load sequence is noted to decrease with an increasing number of load cycles under both strain-rates. Conversely, during the C-T load sequence, the kinematic backstress remains close to 0 MPa after the first loading cycle. The mean kinematic backstress was observed to decrease with increasing strain-rate due to adiabatic self heating.

The microstructural behaviour of the material was analysed using interrupted specimens after each load step until load cycle 2. The microstructural

analysis revealed the twinning-detwinning behaviour of twins, $\{10\bar{1}2\}$ and $\{10\bar{1}3\}$. Under both strain-rates, during the T-C load sequence, both twins exhibited asymmetric fluctuations in the twinning-detwinning trend with the increasing number of load cycles. In contrast, during the C-T load sequence, the material experienced an overall detwinning trend as the number of load cycles increased within both temperatures. Overall, the detwinning rate is observed to increase with strain-rate. Furthermore, the Schmid factor behaviour for all slip systems demonstrated a fluctuating increasing-decreasing trend in the median Schmid factor values during both loading sequences, except for the Prismatic slip system during the C-T load sequence, which exhibited a gradual increase in the median of the Schmid factor value at 1 s^{-1} and 10 s^{-1}. The interrupted unsectioned specimens were also analysed for the measurement of accumulated residual stress within the material using synchrotron X-ray diffraction. The residual stress accumulation across crystallographic planes in the material revealed an asymmetrical accumulation of residual stress in both loading sequences, with the exception of the Prismatic plane. Notably, the measurements indicated that the residual stress exhibited fluctuations in accumulation during the T-C load sequence. However, during the C-T load sequence, the residual stress was observed to gradually relax throughout under both strain-rates.

7 | Discussion

7.1 Macroscopic characterisation of the Bauschinger effect

Reverse loading experiments in T-C and C-T load sequences on forged Ti-6Al-4V, conducted under controlled strain levels at low strain rates and room temperature, revealed that the Bauschinger effect was evident until the first cycle in both load sequences, as illustrated in Figure 4.8. However, this effect persists after load cycle 1 during the T-C load sequence (Figure 4.8(a)), while it diminishes during the C-T load cycle after load cycle 1 (Figure 4.8(b)).

Similarly, at low strain-rate and elevated temperatures of 100 °C and 200 °C, notable observations were made. At 100 °C, during the T-C load sequence, the Bauschinger effect persisted consistently throughout, as illustrated in Figure 5.4(a1). In contrast, during the C-T load sequence, this effect almost diminished after the first load cycle, as shown in Figure 5.4(b1). At 200 °C, the Bauschinger effect persisted during the T-C load sequence; however, its magnitude gradually decreased with an increasing number of load cycles compared to that at 100 °C, as evidenced in Figure 5.5(a2). This reduction can be attributed to the material's greater thermal softening, which lowers the yield stress and reduces the difference in yield stress observed during load reversal as the number of load cycles increases [186,187]. During the C-T load sequence, the magnitude of the Bauschinger effect nearly vanished after the first load cycle, as depicted in Figure 5.5(b2).

Interestingly, as the strain-rate increases at room temperature, different

behaviours are observed in the Bauschinger effect during load sequences. At the strain-rate of 1 s^{-1}, during the T-C load sequence, the Bauschinger effect remained persistent during the T-C load sequence as shown in Figure 6.7(a1), but in the C-T load sequence, it almost diminished after the first load cycle as shown in Figure 6.7(b1). At the strain-rate of 10 s^{-1}, the presence of the Bauschinger effect, as shown in Figure 6.8(a2), can be observed during the T-C load sequence with a relatively smaller magnitude than that at 1 s^{-1}. The reduction in magnitude of the Bauschinger effect at higher strain-rate is due to the adiabatic nature of the experiment at 10 s^{-1}, as observed in Figure 6.5 in which the temperature rise during the cyclic loading is only increasing with the increasing number of load cycles. This adiabatic self-heating facilitates thermal softening and recovery, which in turn reduces long-range backstresses [188, 189]. Consequently, the apparent magnitude of the Bauschinger effect decreases with increasing strain-rate. Under cyclic loading, the kinematic backstress typically saturates, resulting in cyclic softening and a gradual reduction in the Bauschinger stress drop as the number of cycles increases [190, 191]. This observation of adiabatic heating is consistent with dynamic tests on titanium alloys, which report significant temperature rises and adiabatic shear localisation at elevated strain-rates [67, 192]. During the C-T load sequence, the magnitude of the Bauschinger is very small during the first load cycle and almost diminished after the first load cycle as shown in Figure 6.8(b2).

7.2 Role of kinematic backstress

Further comparison of the mean kinematic hardening behaviour of the material as a function of temperature and strain-rate is illustrated in Figure 7.1. With respect to temperature, as shown in 7.1(a), during the low strain-rate T-C load sequence, the mean kinematic hardening is observed to decrease with the increase in temperature, from 58 MPa at 25 °C (room temperature) to 52 MPa at 100 °C, and further to 35 MPa at 200 °C. In contrast, during the C-T load sequence, the changes in mean kinematic hardening are minimal, from -8 MPa at 25 °C to -6 MPa at 100 °C, and remaining at -1 MPa at 200 °C. The reduction in mean kinematic hardening is due to elevated temperatures facilitating the recovery process and the relaxation of internal stress fields through mechanisms such as dislocation climb, rearrangement, and annihilation [166].

Regarding strain rate, as illustrated in 7.1(b), the behaviour of the material during the T-C load sequence indicates that the mean kinematic hardening value decreases with increasing strain rate. Specifically, the value is recorded at 67 MPa at $1\,s^{-1}$ and falls to 33 MPa at $10\,s^{-1}$. In contrast, the change observed in the C-T load sequence is minimal. The value is measured at -10 MPa at $1\,s^{-1}$ and -1 MPa at $10\,s^{-1}$. The reduction is exacerbated by adiabatic self-heating, which promotes thermal softening and recovery [188,189]. Notably, the accompanying temperature rise is self-generated during mechanical loading at elevated strain rates (i.e., adiabatic or cyclic heating resulting from plastic work and energy dissipation), and the magnitude of this increase accumulates and intensifies with continued cyclic

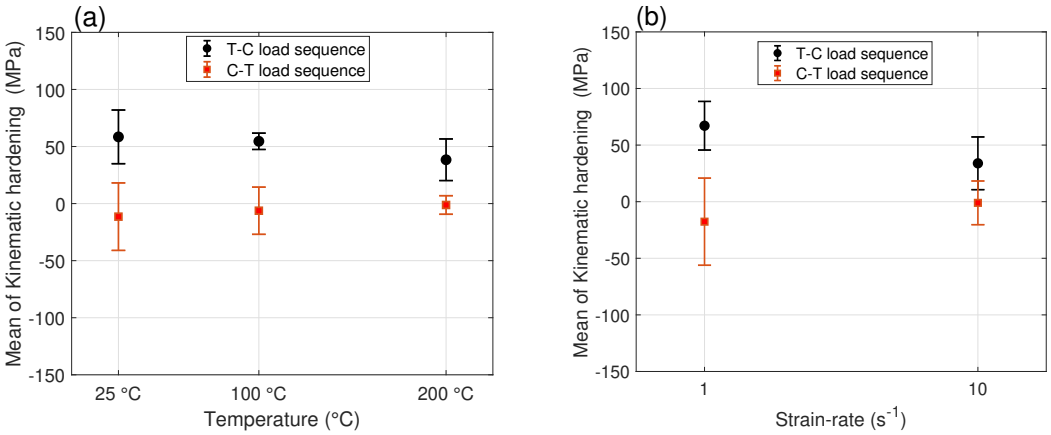


Figure 7.1: The behaviour of the mean of kinematic hardening $\bar{C}$ is examined as a function of temperature (a) and strain-rate (b). With the increase in temperature, T-C load sequence, the mean kinematic hardening is observed to decrease with the increase in temperature. In contrast, during the C-T load sequence, the changes in mean kinematic hardening are very minimal. The reduction is due to elevated temperatures facilitating the recovery process and the relaxation of internal stress fields through mechanisms such as dislocation climb, rearrangement, and annihilation [166]. Regarding strain-rate (b), the behaviour of the material during the T-C load sequence shows a decrease with increasing strain rate, whereas the change in the C-T load sequence is minimal. The reduction is exacerbated by adiabatic self-heating, which promotes thermal softening and recovery [188, 189]. For each condition, kinematic hardening (C) is averaged over repeated measurements and the spread was quantified by the sample standard deviation (S_C); error bars show $\bar{C} \pm S_C$ [113].

loading. This response is distinct from that observed in materials tested under a constant, externally imposed elevated temperature. The resultant in-situ heating at higher strain rates accelerates thermally activated recovery and promotes backstress relaxation, ultimately leading to a reduction in average kinematic hardening [183].

7.3 Role of twinning and detwinning

To gain a deeper understanding of how the evolution of microstructure contributes to the Bauschinger effect, the EBSD analysis of the interrupted specimens revealed that the asymmetrical fluctuation of twinning-detwinning activity is a contributing factor to the Bauschinger effect at low-strain-rate, as observed in previous literature [74, 131–134]. The findings of the current research align with existing literature at low strain-rates; however, this study indicates that twinning and detwinning behaviour also contribute to the Bauschinger effect at low strain-rates at elevated temperatures and at intermediate strain-rates at room temperature. At low strain-rate room temperature, the asymmetric fluctuation of Twin Boundary Length, specifically, the process of twinning followed by detwinning and then twinning again, as illustrated in Figure 4.10, with $\{10\bar{1}2\}$ and $\{10\bar{1}3\}$ in the T-C load sequence, is a contributing factor to the cause of the Bauschinger effect. Conversely, during the C-T load sequence, when these twinning activities cease to fluctuate, the Bauschinger effect begins to diminish, which is precisely what occurs after load cycle 1 in the C-T load sequence. This behaviour parallels the Bauschinger effect, as depicted in Figure 4.8.

Similar trend is observed in the behaviour of the Twin Boundary length as the number of load cycles increases for $\{10\bar{1}2\}$ and $\{10\bar{1}3\}$ at low strain rates under elevated temperatures, as well as at intermediate strain rates at room temperature. This is illustrated in Figures 5.9, 5.10, 6.12, and 6.13.

As illustrated in Figure 7.2, there is a significant reduction in the mean twin boundary length with increasing temperature and strain rate. Specifically, as a function of temperature during the T-C load sequence, the mean twin boundary length decreases from 140 μm at 25 °C (room temperature) to 132 μm at 100 °C, and further to 112 μm at 200 °C. In contrast, the changes in mean kinematic hardening during the C-T load sequence are minimal, with values recorded at 154 μm at 25 °C, decreasing to 148 μm at 100 °C, and remaining at 142 μm at 200 °C. This reduction in mean twin boundary length is attributed to elevated temperatures that enhance thermal dislocation glide and activate additional slip systems, thereby facilitating dynamic recovery [102, 193].

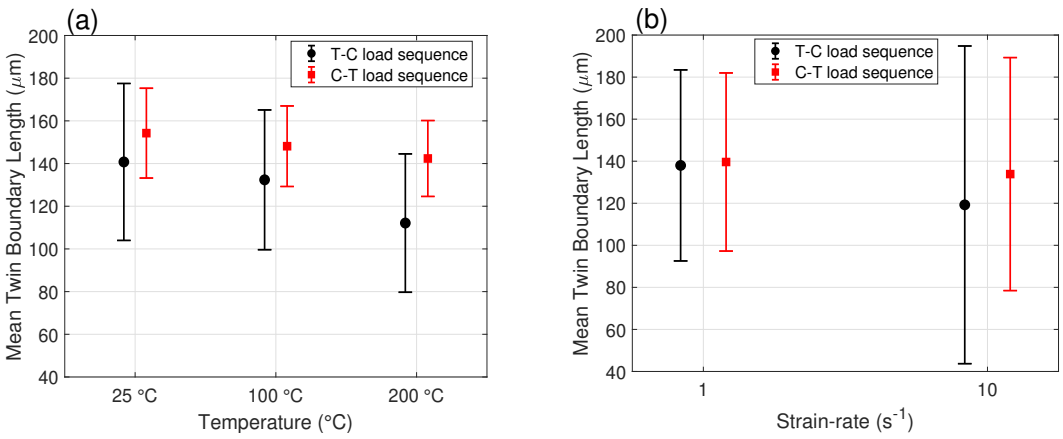


Figure 7.2: The behaviour of the mean twin boundary length is examined as a function of temperature (a) and strain rate (b). As the temperature (a) increases during the T-C loading sequence, the mean twin boundary length exhibits a decrease. In contrast, during the C-T loading sequence, the observed changes are minimal. This phenomenon is attributed to elevated temperatures that enhance thermal dislocation glide and activate additional slip systems, thereby facilitating dynamic recovery [102, 193]. With regard to strain rate (b), the mean twin boundary length in the T-C loading sequence also decreases with an increase in strain rate, while the changes observed during the C-T loading sequence remain minimal. This effect is attributed to adiabatic heating, which promotes the activation of thermally activated dislocations via the slip mechanism [64, 194]. For each condition, twin boundary length is averaged over repeated measurements and the spread was quantified by the sample standard deviation [113].

Regarding strain rate, as shown in 7.1(b), the material's behaviour during the T-C load sequence indicates a decrease in the mean kinematic hardening value with increasing strain rate. Specifically, the value is recorded at 140 μm at 1 s^{-1} and falls to 126 μm at 10 s^{-1}. Conversely, the change observed in the C-T load sequence is minimal, with values of 139 μm at 1 s^{-1} and 133 μm at 10 s^{-1}. This reduction is primarily due to the increase in strain rate, which significantly diminishes the twin formation sequence across the increasing number of cycles. This effect is attributed to adiabatic heating, which promotes the activation of thermally activated dislocations via the slip mechanism [64, 194].

7.4 Assessment of slip favourability

To further analyse the behaviour of the Schmid factor under all three conditions, the distribution of the Schmid factor, m, and its median, $\tilde{m}$, were plotted for all slip systems across both phases and loading directions. This assessment of slip favorability in the α phase during the T-C loading sequence across all three conditions: low strain rate at room temperature, low strain rate at elevated temperatures, and intermediate strain rates at room temperature, reveals that the median value of the Schmid factor, $\tilde{m}$, exhibits asymmetrical fluctuations in all the slip systems during the T-C load sequence. This fluctuating trend corresponds with the trend of the Bauschinger effect behaviour during the T-C load sequence, as shown in Figures 4.8, 5.4(a1), 5.5(a2), 6.7(a1), and 6.8(a2).

In contrast, during the C-T load sequence in the α phase, all slip systems exhibit an asymmetrical fluctuation trend, with the exception of the Prismatic slip system $\{11\bar{2}0\}\langle 1\bar{1}00\rangle$, which demonstrates favourable slip characteristics. This particular system either increases the Schmid factor or maintains a constant value of $\tilde{m}$ as the number of load cycles rises. The observed trend of the $\tilde{m}$ value in relation to the increasing number of load cycles correlates with the trend of the behaviour of the Bauschinger effect during the C-T load sequence across the three conditions, as illustrated in Figures 4.8, 5.4(b1), 5.5(b2), 6.7(b1), and 6.8(b2). Additionally, this trend aligns with the behaviour of the twin boundary fraction associated with the C-T load sequence, as shown in Figures 4.10, 5.9, 5.10, 6.12, and 6.13.

The β phase is present predominantly at grain boundaries and constitutes only a small volume fraction of approximately 2%. In addition, it exhibits minimal variation in Schmid factor with increasing loading cycles. It is therefore assumed to make only a limited contribution to the observed Bauschinger response.

7.5 Interference of twins with prismatic slip mechanism

The observed twinning-detwinning evolution reflects changes in the effective favourability for slip in the prismatic slip system $\{10\bar{1}0\}\langle\bar{1}2\bar{1}0\rangle$ during the T-C and C-T load sequences in all three conditions. In the initial tensile loading step of the

T-C sequence, the activation of $\{10\bar{1}2\}$ extension twins occurs, and in this study, $\{10\bar{1}3\}$ twins also form in favourably oriented grains. These twins reorient parts of the lattice and create twin boundaries that impede prismatic $\{10\bar{1}0\}\langle\bar{1}2\bar{1}0\rangle$ slip [195,196]. These boundaries promote dislocation pile-ups, resulting in a kinematic backstress [197], as observed in the T-C load sequence in Figures 4.9, 5.6, 5.7, 6.9, 6.10. When the loading reverses to compression, the retained backstress facilitates reverse prismatic glide (exhibiting a Bauschinger-type response), while detwinning accommodates part of the early reverse strain and progressively eliminates the barriers that previously hindered prismatic slip. Consequently, the compressive load steps lead to earlier yielding and exhibit different hardening characteristics [82,179,190].

In contrast, during the C-T load sequence, the first compressive load step results in the formation of $\{10\bar{1}2\}$ and $\{10\bar{1}3\}$ twins form in grains whose orientations and local constraints favour them; contraction twinning under compression in Titanium is well documented, while $\{10\bar{1}3\}$ is acknowledged as a rarer HCP twin mode [198, 199]. This formation introduces twin boundaries that shorten prismatic mean-free paths and generate backstress [200, 201]. Upon reversal to tension, these twins detwin, leading to a reduction in the twin boundary length, unpinning the prismatic sources, and diminishing the backstress, as observed in the C-T load sequence in Figures 4.9, 5.6, 5.7, 6.9, 6.10. As a result, prismatic slip can easily re-activates and demonstrates similar early hardening as observed in the preceding compressive load steps, indicating that the prismatic response is nearly symmetric in the C-T load sequence compared to that of the T-C load sequence.

Additionally, during the T-C loading sequence across all three conditions, a distinct inverse trend is observed: an increased twin boundary length, indicative of heightened twinning activity, corresponds with a reduced Schmid factor for prismatic slip, whilst a decreased twin boundary length, associated with detwinning, aligns with a heightened prismatic Schmid factor. This trend is clearly illustrated by the comparison of the twin boundary images in Figures 4.10, 5.9, 5.10, 6.12, and 6.13 with the corresponding prismatic Schmid factors in Figures 4.12, 5.12, 5.30, 6.15, and 6.33. Given that twin boundaries can obstruct, redirect, and localise prismatic dislocation motion, this inverse relationship implies that, as twinning activity diminishes or detwinning transpires during cyclic reversal, prismatic slip may accommodate a larger proportion of the plastic strain [197, 202, 203]. In this manner, the interaction between deformation twinning and prismatic slip may contribute to the Bauschinger effect through the development of internal backstresses and local heterogeneity in slip resistance during forward loading, thus facilitating earlier yielding upon load reversal.

Furthermore, the twin-slip interference during the T-C load sequence changes with both an increase in temperature and strain-rate. As illustrated in Figure 7.2, the formation of twins diminishes with increasing temperature and decreases significantly with higher strain rates. Consequently, the interference of twin-prismatic slip would be lessened, leading to a reduction in backstress formation with temperature and a pronounced decrease with strain-rate, as depicted in Figure 7.1.

7.6 Residual stress accumulation - Consequence of the twin-prismatic slip interference

Additionally, the interrupted specimens in all three conditions underwent further analysis to examine the accumulation of residual stress in both phases and directions within the material. During the T-C load sequence in the α phase, the residual stress accumulation is observed to be asymmetrical in Basal plane (0002), Prismatic plane $(10\bar{1}0)$, Pyramidal planes $(10\bar{1}1)$ and $(20\bar{2}1)$, and Second-order Pyramidal plane $(11\bar{2}2)$, in all three conditions. This fluctuating trend in the Prismatic plane $(10\bar{1}0)$, corresponds with the trend of the Bauschinger effect behaviour during the T-C load sequence, as shown in Figures 4.8, 5.4(a1), 5.5(a2), 6.7(a1), and 6.8(a2)

In contrast, all the aforementioned planes exhibit asymmetrical residual accumulation during the C-T load sequence, with the exception of the Prismatic plane $(10\bar{1}0)$. This trend of the residual stress accumulation behaviour in the Prismatic plane also aligns well with the trend of the Bauschinger response of the material under C-T load sequence across all three conditions, as shown in Figures 4.8, 5.4(b1), 5.5(b2), 6.7(b1), and 6.8(b2). As the number of load cycles increases at 100 °C and 200 °C, it is observed that the negative (compressive) residual stress accumulation relaxes, approaching zero, as illustrated in Figures 5.49(b) and 5.53(b). Concurrently, at intermediate strain rates of 1 s^{-1} and 10 s^{-1}, the tensile residual stress gradually relaxes, as shown in Figures 6.52(b) and 6.56(b). This indicates that during the C-T load sequence, the pattern of residual stress

accumulation remains consistent and non-fluctuating.

These observations indicate a close relationship between the generation of kinematic backstress and the evolution of residual stress during cyclic deformation. In the present study, residual stress accumulates when deformation is accommodated heterogeneously, and decreases or redistributes when deformation occurs more uniformly. Such behaviour is consistent with the development and evolution of internal stress fields associated with deformation incompatibility during cyclic loading [204, 205].

7.7 Two-tailed correlation analysis of kinematic hardening behaviour and twin boundary length evolution

To assess whether the macroscale mechanical response was statistically associated with microstructural evolution, the relationship between kinematic hardening and twin boundary length was examined using a two-tailed Spearman rank correlation test. Kinematic hardening served as the macroscale mechanical variable, whilst twin boundary length was employed as the microstructural variable.

The null hypothesis was:

$$H_0 : \rho_s = 0 \tag{7.1}$$

meaning that there is no correlation between kinematic hardening and twin boundary length.

The alternative hypothesis was:

$$H_1 : \rho_s \neq 0 \tag{7.2}$$

meaning that the correlation between kinematic hardening and twin boundary length is significantly different from zero.

The Spearman rank correlation coefficient was calculated as [206]:

$$\rho_s = 1 - \frac{6 \sum d_i^2}{n(n^2 - 1)} \tag{7.3}$$

where ρ_s is the Spearman rank correlation coefficient, d_i is the difference between the rank of twin boundary length and the rank of kinematic hardening for the i^{th} paired data point, and n is the number of paired data points. The test was two-tailed because the aim was to determine whether the correlation coefficient was significantly different from zero, without assuming beforehand whether the relationship should be positive or negative.

For the dataset, the two-tailed Spearman rank correlation test gave:

$$\rho_s = 0.543, \quad p = 0.0134 \tag{7.4}$$

The positive value of ρ_s suggests that a greater length of twin boundaries correlates

with increased kinematic hardening. Conversely, a shorter twin boundary length is associated with reduced kinematic hardening. This pattern aligns with the interpretation that enhanced development of twin boundaries bolsters the back-stress-like contribution to kinematic hardening, while a reduction in twin boundary length diminishes this back-stress effect.

Given that $p < 0.05$, the null hypothesis was rejected at the 5% significance level. This indicates that the positive relationship between twin boundary length and kinematic hardening is statistically significant.

Overall, this statistically significant positive correlation reinforces the interpretation that the development of twin boundaries is linked to the macroscale kinematic hardening response. Specifically, an increase in twin boundary length corresponds with greater kinematic hardening, while a decrease in twin boundary length leads to a weaker back-stress-like response during reversed loading.

7.8 Summary of maximum MRD values obtained from pole figures for the α and β phases

Table 7.1 summarises the maximum MRD values derived from the pole figures for the α and β phases in the as-received and tested conditions. For the as-received material, the maximum MRD values are 2.308 for the α phase and 1.575 for the β phase. Following testing, the maximum MRD values remain within a relatively narrow range, from 1.565 to 2.843, indicating that no substantial increase

Table 7.1: Maximum MRD values obtained from pole figures for the α and β phases under as-received and tested conditions.

Condition	**Phase**	**As-received**	**T-C**	**C-T**
As-received	α	2.308	–	–
As-received	β	1.575	–	–
Low strain-rate	α	–	2.843	2.381
Low strain-rate	β	–	1.731	1.597
Low strain-rate, 100°C	α	–	2.706	2.291
Low strain-rate, 100°C	β	–	1.614	1.569
Low strain-rate, 200°C	α	–	2.432	2.170
Low strain-rate, 200°C	β	–	1.796	1.565
Intermediate strain-rate, 1 s^{-1}	α	–	2.336	2.347
Intermediate strain-rate, 1 s^{-1}	β	–	1.621	1.861
Intermediate strain-rate, 10 s^{-1}	α	–	2.424	2.437
Intermediate strain-rate, 10 s^{-1}	β	–	1.588	1.678

in texture intensity is observed under the applied loading paths, strain-rates or temperatures. Overall, MRD values remain within the weak-to-moderate texture range across all tested conditions. The pole-figure results therefore suggest that the applied loading paths and testing temperatures do not produce a major change in overall texture intensity.

To improve readability and reduce repetition in the main thesis chapters, the EBSD pole figures have been moved to Appendix B.

8 | Conclusion

The behaviour of the Bauschinger effect in forged Ti-6Al-4V is examined under various conditions: low strain-rate at room temperature, low strain-rate at elevated temperatures, and intermediate strain rates. The material was cyclically subjected to uniaxial loading. The Bauschinger effect was characterised through the stress-strain behaviour of the material, while the kinematic hardening behaviour was also analysed using the stress-strain response. Additionally, sectioned interrupted specimens underwent EBSD analysis, which included investigations into texture, twin behaviour, and Schmid factor, as well as the increasing number of load cycles, to comprehend the microscopic behavior of the material under cyclic loading in different conditions. Furthermore, unsectioned specimens that experienced the same type of loading were analysed using high-energy X-ray diffraction to examine residual stress accumulation behaviour with the increasing number of load cycles.

1. This study suggests that twinning and detwinning behaviour, together with twin-prismatic slip interference, contribute to the Bauschinger effect, while the deformation incompatibility arising from this interaction promotes the development and evolution of residual stress.

2. It was observed that, as temperature increases, the mean kinematic backstress diminishes, and a similar reduction is evident with rising strain-rate. A corresponding decrease in the mean twin boundary length is noted under these same conditions. This suggests a strong relationship between twin activity and kinematic backstress, with the Bauschinger effect becoming less

pronounced as temperature and strain rate-rise.

3. **The affect of load direction on the Bauschinger response at low strain-rate:** The Bauschinger effect persists throughout the T-C load sequence but exhibits significantly weaker characteristics in the C-T sequence. This effect is attributed to the growing interference between deformation twins and prismatic slip, which generates a pronounced kinematic backstress with the increasing number of load cycles during the T-C load sequence. In contrast, backstress is near zero during the C-T sequence, where twinning is less involved and slip becomes more homogeneous. The residual stress evolves from incompatible plastic strains created when deformation is constrained (due to twinning-prismatic slip interference) and subsequently relaxes as plastic flow becomes more uniform. Consequently, the twin-slip interference present during the T-C sequence accumulates residual stress in the prismatic plane and are observed to be increasing with the increasing number of load cycles, while the more uniform slip during the C-T load sequence leads to less residual stress accumulation.

4. **Role of increasing temperature on the Bauschinger Response at low strain-rate:** In this study, the Bauschinger effect persists throughout the T-C load sequence at temperatures of 100 °C and 200 °C; however, it diminishes during the C-T load sequence. During the T-C load sequence, as the temperature increases, the interference between deformation twinning and prismatic slip gradually reduces due to the thermal softening of

the material. Additionally, the slow nature of the experiment facilitates the rearrangement of dislocations and promotes dislocation motion, resulting in a decrease in the kinematic backstress during the T-C transition. Consequently, the accumulation of residual stress in prismatic plane diminishes, owing to the reduction in interference between twin and prismatic slip, which fosters dislocation motion at elevated temperatures.

5. **Behaviour of the Bauschinger effect as a function of Strain-rate:** In this case, the Bauschinger effect remains pronounced in the T-C load sequence but is diminished in the C-T load sequence at 1 s^{-1} and 10 s^{-1}. During the T-C load sequence, the magnitude of the Bauschinger effect decreases sharply with increasing strain rate due to adiabatic self-heating (resulting from plastic work and energy dissipation), which promotes thermally activated recovery and dislocation rearrangement. As load cycle progresses, this self-heating facilitates dislocation motion and reduces twin-prismatic slip interference, resulting in a substantial decrease in the kinematic backstress at intermediate strain-rates. This phenomenon is reflected in the residual stress accumulation in the prismatic plane, which diminishes with the increase in load cycles.

The strain-rate estimate presented in Appendix A suggests that leading-edge deformation during bird impact can occur at approximately $\dot{\varepsilon} \sim 10^4$ s^{-1}. In contrast, the present thesis investigates strain-rates up to $\dot{\varepsilon} = 10$ s^{-1}. The estimated bird-strike strain-rate is therefore around three orders of magnitude higher than the

maximum strain-rate investigated experimentally in this work. Consequently, the present results should not be interpreted as directly reproducing bird-strike loading. Instead, they provide a low-to-moderate strain-rate mechanistic baseline for understanding the core objective of the current research, which is how and why the Bauschinger effect evolves as a function of loading direction with increasing strain-rate and temperature under controlled reverse-loading conditions.

The applicability of the presented strain-rate data to aeroengine impact conditions is therefore limited by the difference in strain-rate regime, as well as by the simplified nature of the present loading path compared with real fan-blade impact. Bird-strike deformation is highly transient, localised and multiaxial, whereas the present experiments provide controlled reverse-loading data designed to isolate the roles of strain-rate, adiabatic heating, and thermal softening. Nevertheless, this baseline is important because it establishes the trend that the Bauschinger effect decreases with increasing strain-rate and temperature within the investigated range. Future split Hopkinson pressure bar testing could extend the work by enabling reverse-loading experiments at strain-rates closer to those estimated for leading-edge bird-strike deformation, including compression followed by tension sequences for up to two loading cycles. Such testing would allow the evolution of the Bauschinger effect to be assessed under more adiabatic conditions and would clarify whether thermal softening becomes dominant at impact-relevant strain-rates, and whether the Bauschinger effect continues to decrease, persists, or becomes negligible under these conditions.

9 | Future Work

Following the characterisation of the Bauschinger effect and the analysis of microstructure evolution in interrupted specimens up to load cycle 2 at various conditions, low strain rates at room temperature, low strain rates at elevated temperatures, and intermediate strain rates at room temperature, it is beneficial to explore the Bauschinger effect at higher strain rates and different temperatures. Consequently, the proposed design for a reverse loading split Hopkinson bar is illustrated in Figure 9.1, which aims to cyclically load a specimen through two cycles: Compression-Tension-Compression-Tension.

This proposed design builds on the previous test rig developed by Sivasubramaniam Sathianathan [207], who was one of the earlier DPhil students in the Impact and Shock Mechanics Laboratory at the University of Oxford. The earlier design was capable of cyclically loading the specimen through just one cycle: Compression followed by Tension.

As shown in Figure 9.1, the gas-gun impactor accelerates a two-part striker separated by a narrow slit; the front segment (Striker 1) initiates the first impact, while the rear segment (Striker 2) follows after a delay determined by the slit length. A transfer flange with a short incident tube couples the striker to the input bar, ensuring the first pulse enters the input bar in compression. This bar transmits waves to the specimen and houses the strain gauges. The specimen is securely threaded into the bar-end fixtures, maintaining its alignment and integrity during load reversals. A compact reaction mass reinforces the input-side fixture for timing stability. The output bar carries the transmitted waves away, and a downstream

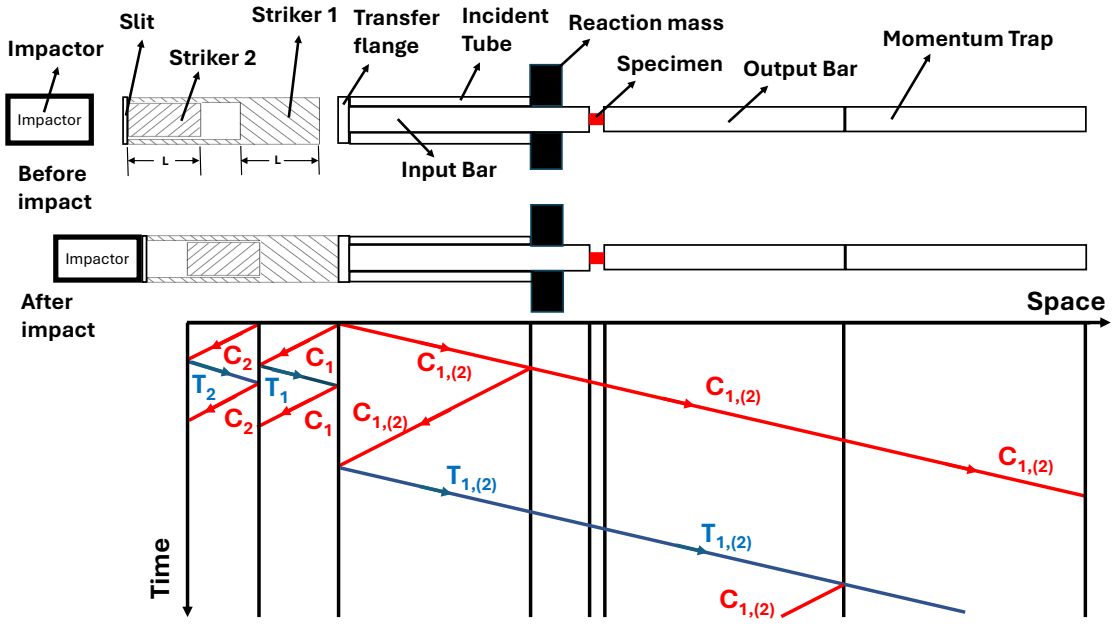


Figure 9.1: Geometry of the specimens used to conduct reverse loading in the C-T load sequence.

momentum trap absorbs late compressive returns to prevent unintended re-loading. All interfaces are carefully aligned and impedance-matched to minimise bending and spurious reflections.

In the Lagrangian (spacetime) diagram, red (compression) and blue (tension) wave paths, labelled 1 and 2, illustrate the Compression-Tension-Compression-Tension history during a high-rate shot, as shown in Figure 9.1. Upon the first impact, Striker 1 generates a compressive pulse in the input bar, loading the threaded specimen in compression, C_1. This setup produces the first tensile reversal at the specimen, T_1, through the designed reflection/transfer path on the input side, while the output-side momentum trap suppresses significant compressive return. After a slit-controlled delay, Striker 2 impacts again, repeating the pattern with a compressive loading, C_2, followed by a controlled tensile reversal, T_2.

A | Appendix

Strain-rate Estimate for Fan Blade Bird Impact During Real-time Aeroplane Operation

Bird-strike events serve as a valuable engineering context for estimating the strain rates associated with fan-blade impacts. A detailed order-of-magnitude calculation is provided. This section summarizes the engineering foundation for this estimate and explains the application of a simplified leading-edge bending approximation.

Jain et al. investigated the effects of a 0.9 kg bird striking pre-stressed rotating fan blades through an explicit finite-element hydrodynamic framework, treating the bird as a hydrodynamic projectile [208]. Their model for the bird was designed with an initial velocity of $140\,\mathrm{m\,s^{-1}}$, a density of $1000\,\mathrm{kg\,m^{-3}}$, a length of 166 mm, and a diameter of 84 mm. Similarly, Wu et al. employed a Smoothed Particle Hydrodynamics (SPH) model in LS-DYNA to analyse bird impacts on rotating aero-engine fan blades, taking into account parameters such as the location of the impact, orientation of the bird, initial velocity, rotational speed of the fan, bearing stiffness, and bearing damping [209]. The application of a local leading-edge bending estimate aligns with aerospace bird-ingestion certification standards. According to 14 CFR §33.76, the requirement for ingestion by a large flocking bird dictates that the bird must impact the first exposed rotating stage or stages at a blade airfoil height of no less than 50%, measured from the leading edge [210].

The FAA Advisory Circular AC 33.76-1B further clarifies that, for the majority of contemporary turbofan engines, the critical parameter for ingestion is the stress at the leading edge of the fan blade; however, this may shift to blade-root stress depending on factors such as bird velocity, mass, slice mass, and blade geometry. Additionally, this advisory circular specifies that the target point on the first exposed rotating stage must not be less than 50% of the airfoil height, taken from the leading edge of the fan blade [211]. Consequently, the local bending assumption at the leading edge used in the present Euler-Bernoulli estimate is consistent with the relevant certification impact location, engine operating conditions, and critical damage parameters.

For an estimate of order of magnitude, the fan blade is modelled as a cantilevered Euler-Bernoulli beam experiencing localised leading-edge bending during the initial bird impact. This modelling approach is suitable for approximating the local bending strain rate, rather than capturing the complete three-dimensional response to impact. The justification for employing a local leading-edge deformation model comes from the findings of Jain and Ramachandra, who noted that the maximum strain occurs on the suction side at the leading edge. Additionally, Sinha characterised the dynamic loading due to bird strikes on a fan blade as predominantly localised at the sharp leading edge, with peak load occurring within approximately 0.1 ms of initial contact [208, 212].

In Euler-Bernoulli beam theory [213], plane cross-sections are assumed to remain plane and normal to the neutral axis after bending. Consider a small beam

element bent into a circular arc with radius of curvature ρ. The neutral axis has arc length

$$ds = \rho d\phi \tag{A.1}$$

where $d\phi$ is the small change in angle over the element. A fibre located a distance y from the neutral axis has radius

$$\rho_y = \rho - y \tag{A.2}$$

for one side of the neutral axis, or equivalently $\rho+y$ for the opposite side, depending on the sign convention. Its arc length is therefore

$$ds_y = (\rho - y)d\phi. \tag{A.3}$$

The axial strain in that fibre is the change in length divided by the original neutral-axis length:

$$\varepsilon = \frac{ds_y - ds}{ds}. \tag{A.4}$$

Substituting the arc lengths gives

$$\varepsilon = \frac{(\rho - y)d\phi - \rho d\phi}{\rho d\phi} \tag{A.5}$$

$$\varepsilon = -\frac{y}{\rho}. \tag{A.6}$$

Since curvature is defined as

$$\kappa = \frac{1}{\rho}, \tag{A.7}$$

the bending strain is

$$\varepsilon = -y\kappa. \tag{A.8}$$

The sign only indicates whether the fibre is in tension or compression. Therefore, the magnitude of bending strain is

$$|\varepsilon| = y\kappa. \tag{A.9}$$

The maximum bending strain occurs at the outer surface of the section, where the distance from the neutral axis is

$$y = \frac{h}{2} \tag{A.10}$$

for a local blade section of thickness h. Hence, the maximum surface bending strain is

$$\varepsilon_{\max} = \frac{h}{2}\kappa. \tag{A.11}$$

This derivation follows the standard Euler-Bernoulli beam-theory assumption that normals to the neutral surface remain normal during deformation, giving the axial strain relation $\varepsilon = -y/\rho = -y\kappa$ [214, 215].

The local curvature is approximated as the change in local rotation over a characteristic bending length:

$$\kappa \approx \frac{\theta}{l_c}, \tag{A.12}$$

where θ is the local impact-induced rotation and l_c is the characteristic local bending length. Substituting this into the bending strain expression gives

$$\varepsilon_{\max} \approx \frac{h\theta}{2l_c}. \tag{A.13}$$

The corresponding bending strain rate is then obtained by dividing the strain by the characteristic local deformation time t_c:

$$\dot{\varepsilon} \approx \frac{\varepsilon_{\max}}{t_c}. \tag{A.14}$$

Therefore,

$$\dot{\varepsilon} \approx \frac{h\theta}{2l_c t_c} \tag{A.15}$$

This expression is used to estimate the local leading-edge bending strain-rate during bird strike.

The numerical values used in this estimate are selected from bird-strike-specific studies where possible, and otherwise derived from cited values. A bird velocity of $140\,\mathrm{m\,s^{-1}}$, bird density of $1000\,\mathrm{kg\,m^{-3}}$, bird length of 166 mm, and bird diameter of 84 mm were used in the fan-blade impact analysis [208]. Jain et al. reported that the fully nonlinear analysis was conducted up to 300 μs with a time step of 1 μs [208]. Importantly, after 220 μs, the maximum and minimum principal strains in the blade were 0.071 and 0.043, respectively, showing that significant blade strain develops very early in the impact event.

Wu et al. used bird impact velocities of $253\,\mathrm{m\,s^{-1}}$, $225\,\mathrm{m\,s^{-1}}$, and $116\,\mathrm{m\,s^{-1}}$

and fan rotational speed cases of $600\,\mathrm{rad\,s^{-1}}$, $395\,\mathrm{rad\,s^{-1}}$, and $88\,\mathrm{rad\,s^{-1}}$ in their aero-engine fan-blade bird-strike simulations [209]. Their simulations showed that the bird-impact process produces severe blade loading, with impact force reaching $359\,\mathrm{kN}$ for the $253\,\mathrm{m\,s^{-1}}$ case and von Mises stress reaching $1238\,\mathrm{MPa}$ for the $225\,\mathrm{m\,s^{-1}}$ case . These bird-strike-specific values indicate that the relevant local impact velocity at the blade is of the order of $10^2\ \mathrm{m\,s^{-1}}$, and that local blade deformation develops over microsecond-to-sub-millisecond time scales.

For the current Euler-Bernoulli estimate, it is assumed that local deformation occurs specifically at the blade's leading edge, rather than along the entire span of the blade. Jain et al. explicitly stated that variable-thickness shell elements were employed for the fan blade, as the blade thickness changes from tip to base and from leading edge to trailing edge. Consequently, a representative local blade thickness of $h = 4\,\mathrm{mm}$ (or 0.004 m) is adopted for the local region of the leading edge. This value is not intended to represent an exact measurement from the blade's design; instead, it is chosen as a literature-based local effective thickness for estimating leading-edge bending. Yella et al. utilized a blade-level fan-blade model measuring $550\,\mathrm{mm} \times 1050\,\mathrm{mm} \times 7.5\,\mathrm{mm}$, reflecting the dimensions of a real fan blade, and they included a titanium alloy cap at the leading edge [216]. They also observed that the actual thickness of the blade varies in both span-wise and chord-wise directions, although their model employed a constant thickness approximation. Therefore, the value $h = 4\,\mathrm{mm}$ is less than the full blade-level thickness of $7.5\,\mathrm{mm}$ used by Yella et al., and is thus used here as a simplified local effective thickness specifically for the thinner leading-edge region, rather than as

a representation of the entire blade's thickness.

The characteristic local bending length is derived from the effective local leading-edge thickness rather than selected independently. Since the effective local leading-edge thickness used above is $h = 4$ mm, the characteristic local bending length is taken to be slightly larger than the local thickness:

$$l_c \approx 1.25h \tag{A.16}$$

$$l_c = 1.25(4\,\text{mm}) = 5\,\text{mm} = 0.005\,\text{m}.$$

This choice provides an empirical Saint-Venant-type length scale over which local boundary and bending effects are assumed to decay, rather than a separate fitted parameter. It defines a local curvature-development zone with the same physical scale as the leading-edge structure. The use of a leading-edge-based local length scale is motivated by the leading-edge nature of the impact: Sinha notes that bird-strike loading on the fan blade is generally localised at the sharp leading edge, and that blade leading-edge thickness at the impact point is an important parameter controlling the damage response [212]. This also avoids using the full bird diameter of 84 mm from Jain et al., which would represent a much more global contact length rather than the initial local leading-edge curvature zone [208].

The local rotation is estimated from bird-strike simulation results rather than selected independently. In a rotating fan-blade simulation, a maximum forward axial deflection of approximately 32 mm was predicted at the leading edge, while the corresponding experimental rotating fan-blade result showed approxi-

mately 30 mm leading-edge axial deflection. A bird diameter of 84 mm was also used [208]. A simple geometric estimate of local rotation can therefore be obtained from the ratio of leading-edge deflection to bird diameter:

$$\theta \approx \tan^{-1}\left(\frac{30}{84}\right) \tag{A.17}$$

$$\theta \approx 0.35\,\text{rad}.$$

Therefore, the value used in the present Euler-Bernoulli estimate is $\theta = 0.35\,\text{rad}$.

Significant leading-edge principal strains were reported after 220 μs, further supporting the use of a finite local rotation during the early impact response [208]. The local deformation time is estimated using a local interaction distance This is chosen as half of the effective local blade thickness,

$$s = \frac{h}{2} = \frac{4\,\text{mm}}{2} = 2\,\text{mm}, \tag{A.18}$$

which is consistent with the Euler-Bernoulli strain expression because the maximum surface strain is evaluated at $y = h/2$. The value $s = 2\,\text{mm}$ therefore represents the time for the bird front to sweep across the outer-fibre deformation scale of the leading-edge section, rather than across the full bird length. This choice is consistent with the localised leading-edge loading description given by Sinha [212]. Using the bird's velocity, $V_b = 140\,\text{m}\,\text{s}^{-1}$, reported by Jain and Ramachandra, the local deformation time is

$$t_c \approx \frac{s}{V_b} \tag{A.19}$$

$$t_c = \frac{0.002}{140} \approx 14.3\,\mu\text{s}.$$

This value is below 0.1 ms, consistent with Sinha's statement that the dynamic bird-strike loading on the fan blade generally peaks less than approximately 0.1 ms of initial contact [212]. Substituting these values into the Euler-Bernoulli strain-rate expression gives

$$\dot{\varepsilon} \approx \frac{h\theta}{2l_c t_c} \tag{A.20}$$

$$\dot{\varepsilon} = \frac{0.004 \times 0.35}{2 \times 0.005 \times 1.43 \times 10^{-5}} \quad \approx 1.0 \times 10^4\ \text{s}^{-1}.$$

for local leading-edge bending during bird strike.

This value is also consistent with the higher bird velocities used by Wu et al [209]. In their simulations, bird velocities of $225\,\text{m}\,\text{s}^{-1}$ to $253\,\text{m}\,\text{s}^{-1}$ were considered for rotating aero-engine fan-blade impact. If the same local interaction distance $s = 2\,\text{mm}$ is used, the corresponding local deformation time becomes

$$t_c = \frac{0.002}{225} = 8.89 \times 10^{-6}\ \text{s} \tag{A.21}$$

for the $225\,\text{m}\,\text{s}^{-1}$ case, and

$$t_c = \frac{0.002}{253} = 7.91 \times 10^{-6}\ \text{s} \tag{A.22}$$

for the $253\,\text{m}\,\text{s}^{-1}$ case. Using the same Euler-Bernoulli parameters, $h = 0.004\,\text{m}$,

$\theta = 0.35\,\text{rad}$, and $l_c = 0.005\,\text{m}$, gives

$$\dot{\varepsilon} = \frac{0.004 \times 0.35}{2 \times 0.005 \times 8.89 \times 10^{-6}} = 1.57 \times 10^4\ \text{s}^{-1} \tag{A.23}$$

for $V_b = 225\,\text{m}\,\text{s}^{-1}$, and

$$\dot{\varepsilon} = \frac{0.004 \times 0.35}{2 \times 0.005 \times 7.91 \times 10^{-6}} = 1.77 \times 10^4\ \text{s}^{-1} \tag{A.24}$$

for $V_b = 253\,\text{m}\,\text{s}^{-1}$. Therefore, using the above bird-strike-specific velocities, a strain-rate range of approximately $\dot{\varepsilon} \approx 1.0 \times 10^4$ to $1.8 \times 10^4\ \text{s}^{-1}$ is obtained from the Euler-Bernoulli local bending estimate.

These estimates provide an approximation of the real-time strain-rate scale that could be encountered during a bird strike on a rotating fan blade. The calculations indicate that the strain-rate in the local impact zone can be on the order of $10^4\ \text{s}^{-1}$, but this figure should be regarded as an estimate rather than an exact measurement or verification of the experimental loading conditions employed in this thesis. Consequently, the aim of the calculations is to provide context regarding impact duration and to encourage further studies focused on strain-rate dependence under more representative high-rate loading conditions. This does not suggest that the experiments carried out in this thesis directly replicate a fan-blade bird-strike event. Instead, the experimental programme yields material-level data on the behaviour of forged Ti-6Al-4V under controlled reverse-loading conditions at elevated temperatures and imposed strain rates. These data enhance the under-

standing of strain-rate-dependent deformation, the Bauschinger effect, and cyclic reverse-loading behaviour, and may be utilised in future research to inform constitutive modelling and experimental investigations of aeroengine materials under impact-relevant loading conditions.

B | Appendix

Supplementary EBSD Pole Figures

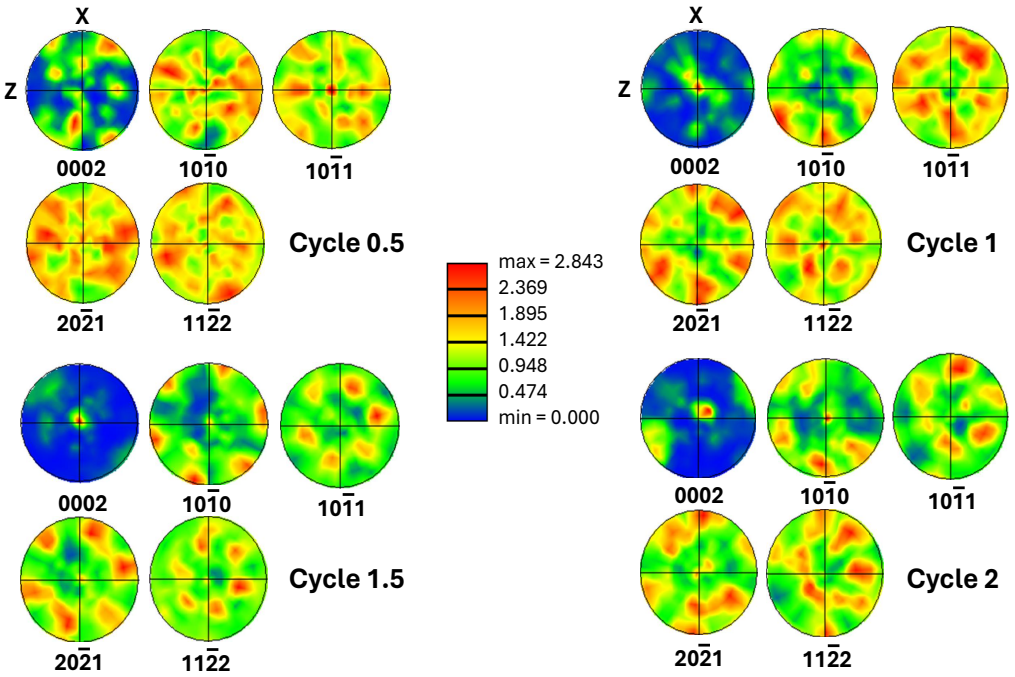


Figure B.1: Pole figures for crystallographic planes in the α phase at low strain-rate during interrupted T-C loading show a weak-to-moderate, diffuse texture.

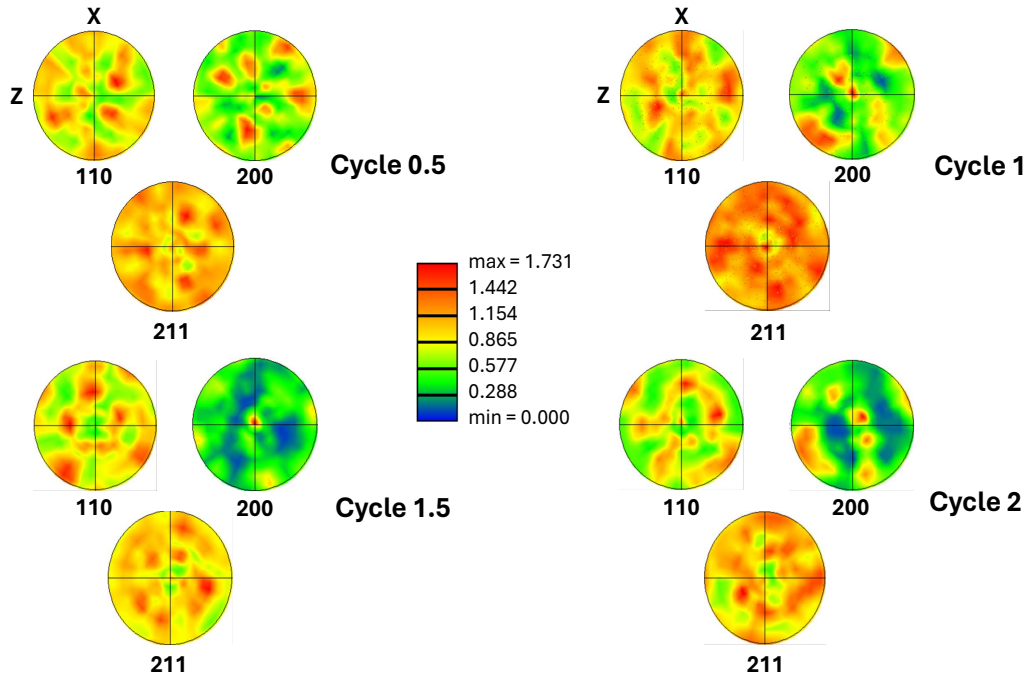


Figure B.2: Pole figures for crystallographic planes in the β phase at low strain-rate during interrupted T-C loading exhibit a weak diffuse texture.

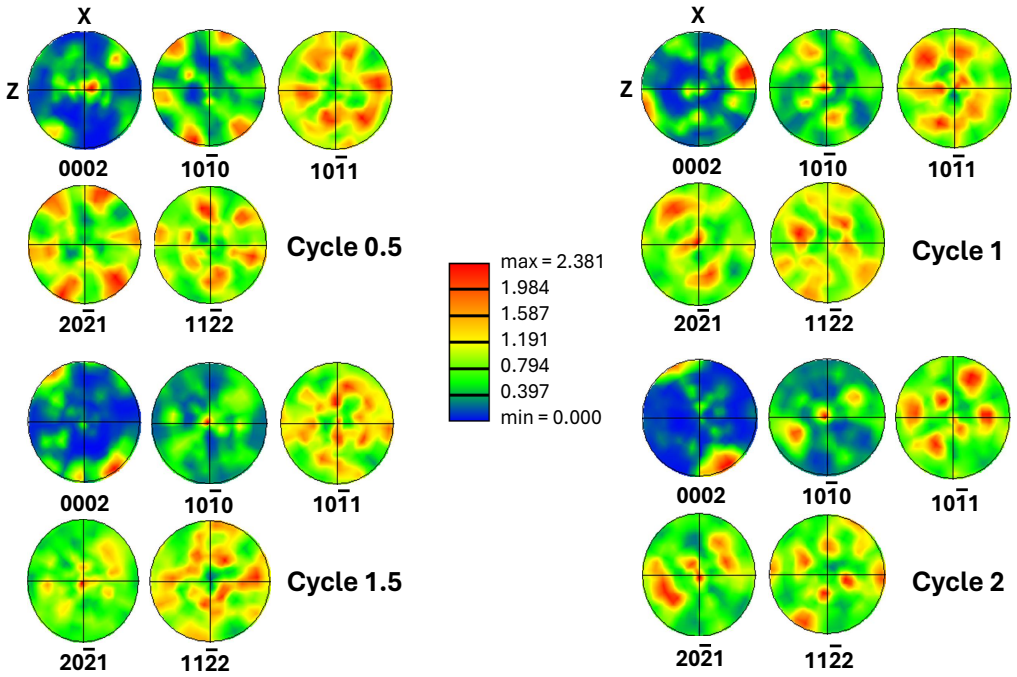


Figure B.3: Pole figures for crystallographic planes in the α phase at low strain-rate during interrupted C-T loading show a weak to moderate diffuse texture.

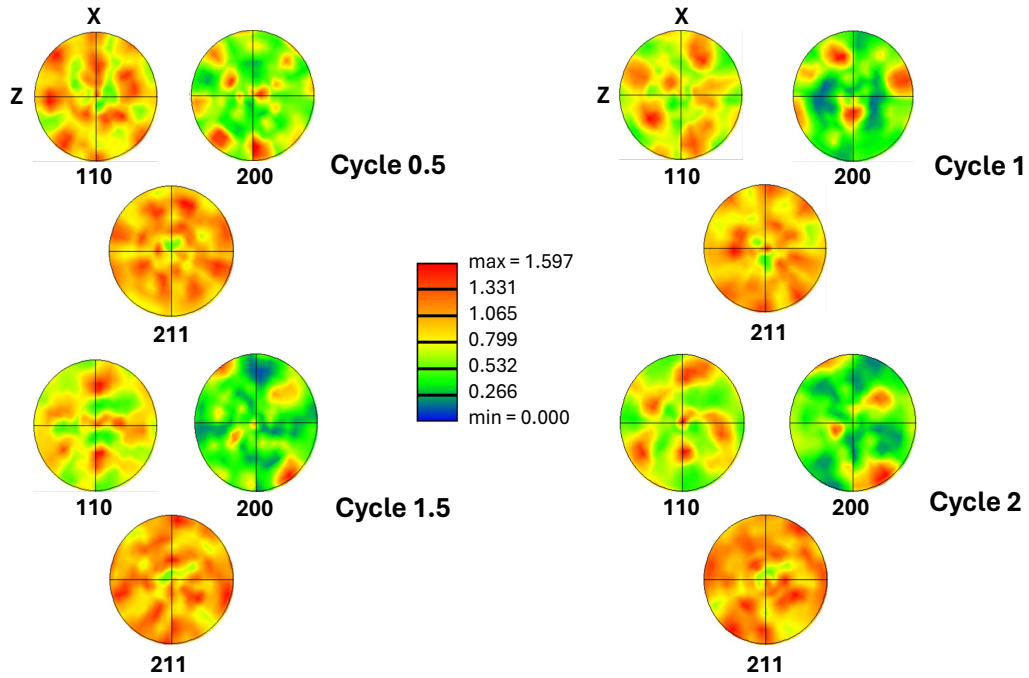


Figure B.4: Pole figures for crystallographic planes in the β phase at low strain-rate during the C-T load sequence reveal a weak diffuse texture.

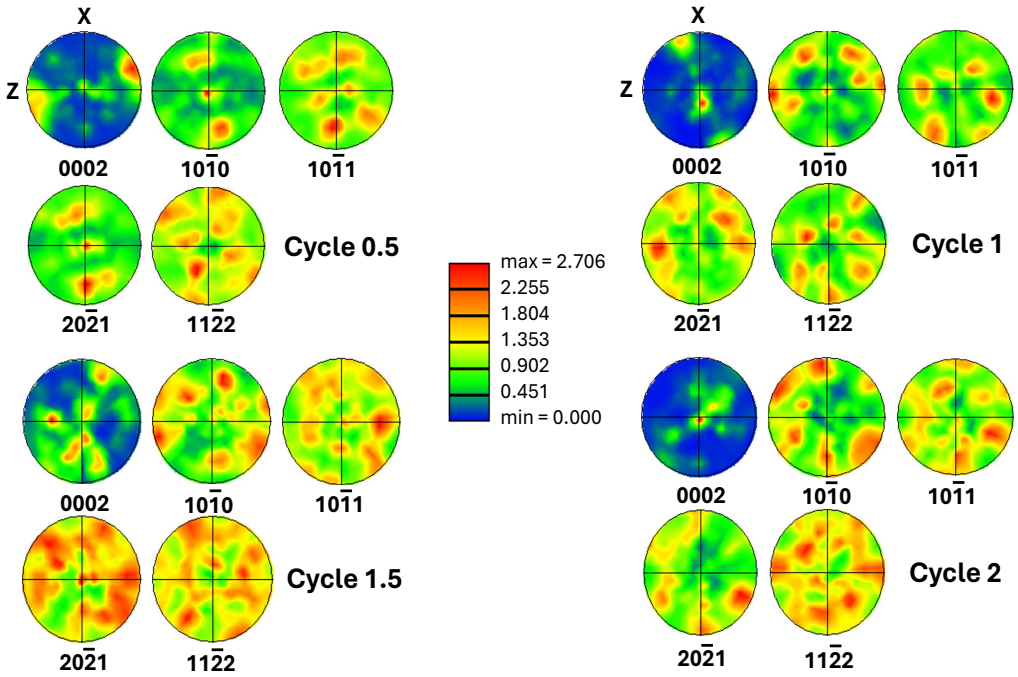


Figure B.5: Pole figures for crystallographic planes in the α phase at 100 °C during interrupted T-C loading show a weak-to-moderate, diffuse texture.

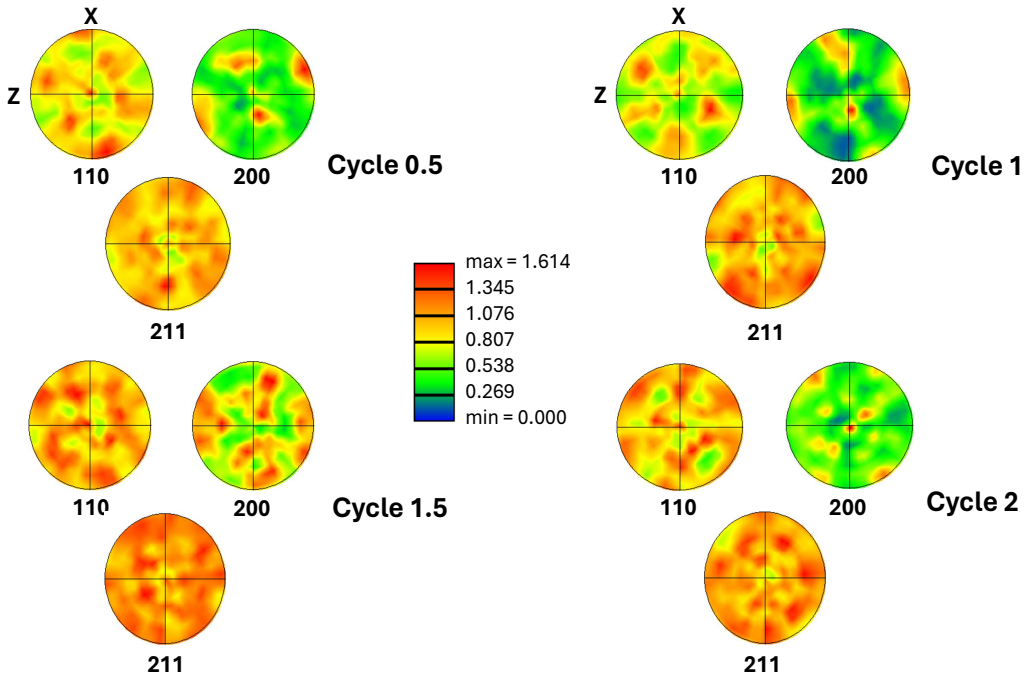


Figure B.6: Pole figures for crystallographic planes in the β phase at 100 °C during interrupted T-C loading reveal a weak, diffuse texture.

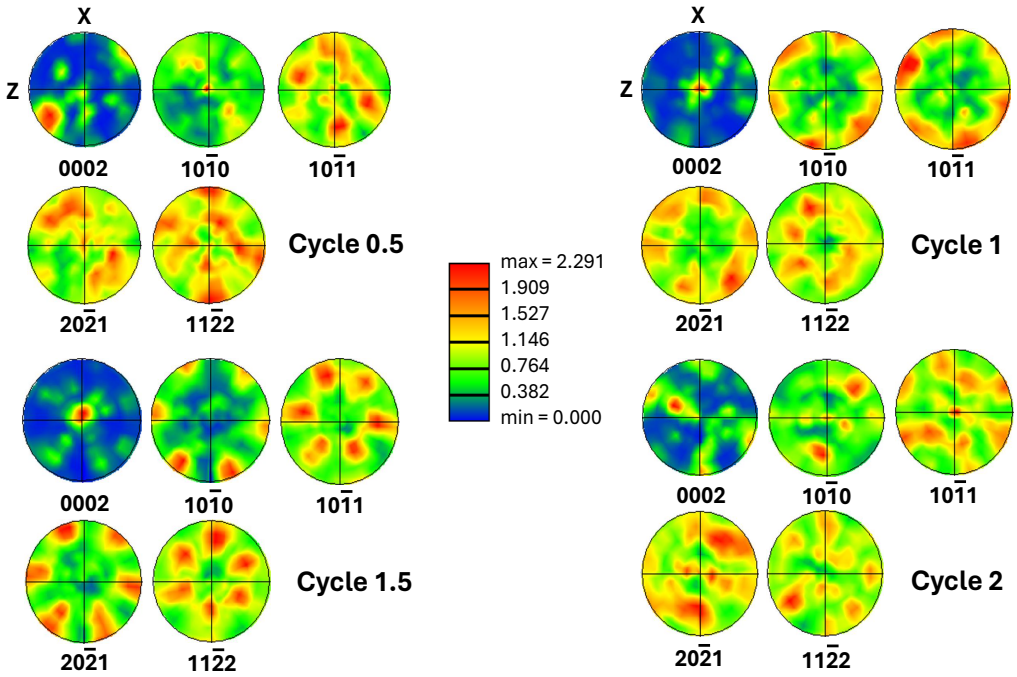


Figure B.7: Pole figures for crystallographic planes in the α phase at 100 °C during interrupted C-T loading show a weak-to-moderate, diffuse texture.

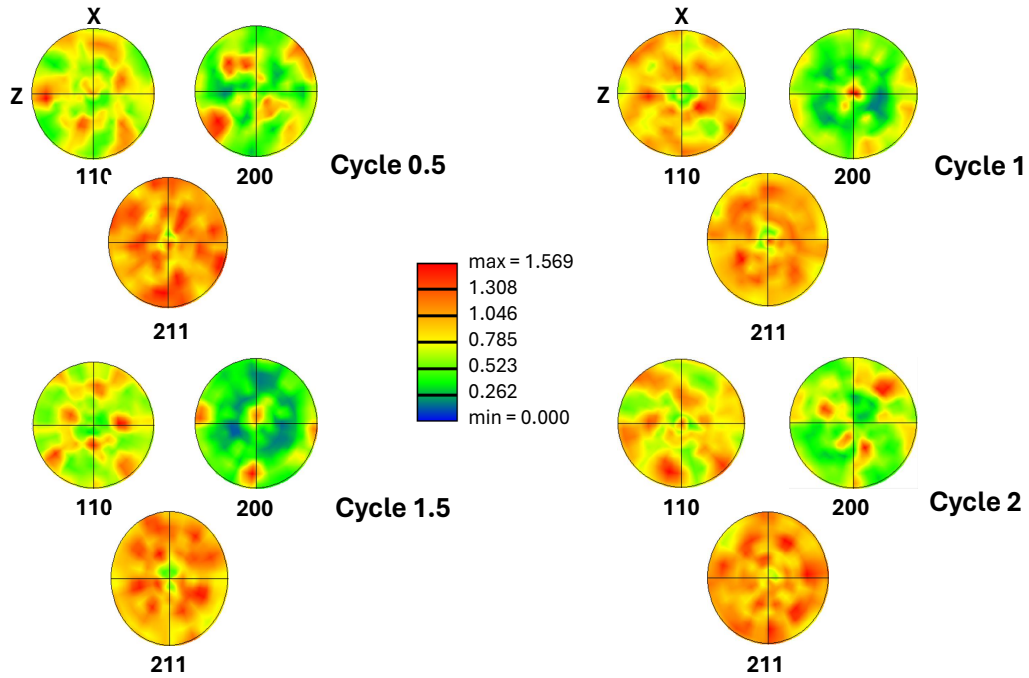


Figure B.8: Pole figures for crystallographic planes in the β phase at 100 °C during interrupted C-T loading show a weak and diffuse texture.

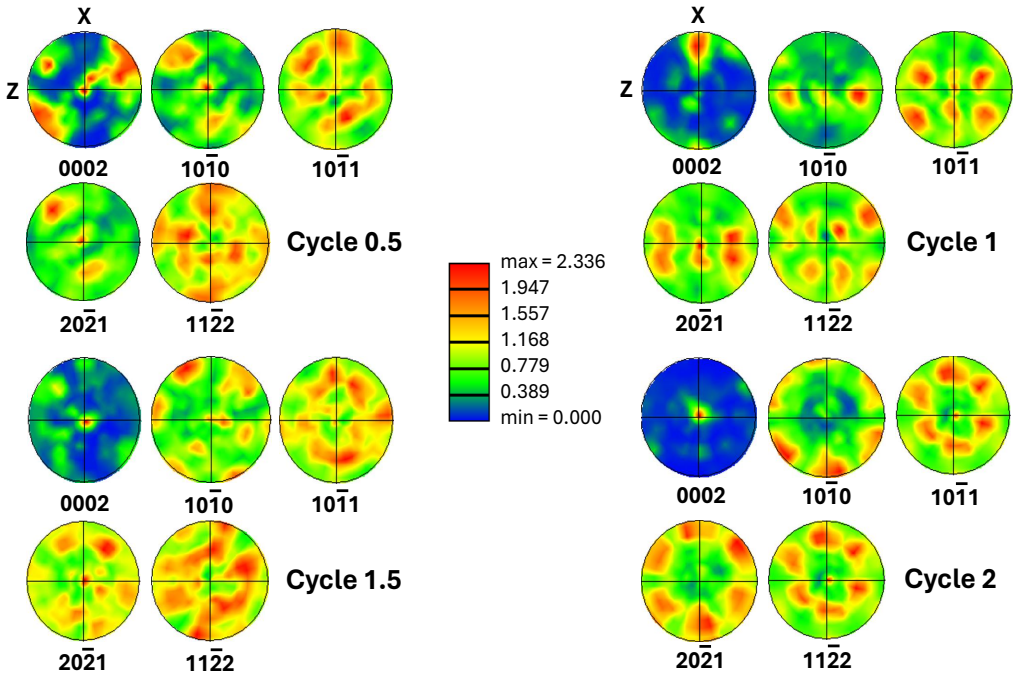


Figure B.9: Pole figures for crystallographic planes in the α phase at a strain rate of $1\,s^{-1}$ during interrupted T-C loading show a weak-to-moderate diffuse texture.

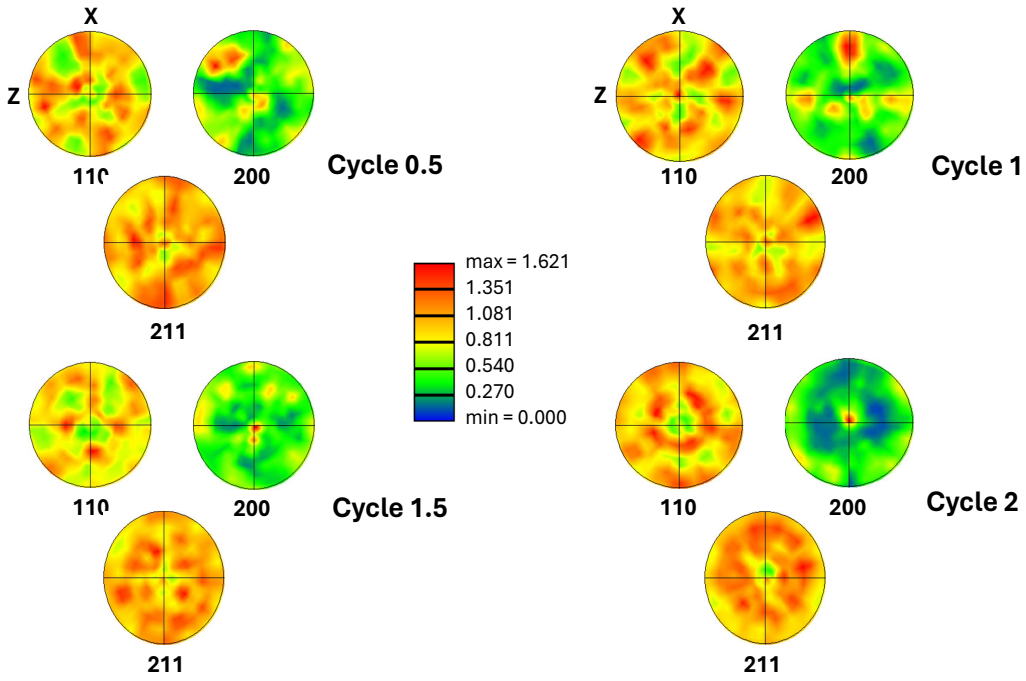


Figure B.10: Pole figures for crystallographic planes in the β phase at a strain rate of $1\,\mathrm{s}^{-1}$ during interrupted T-C loading show a weak and diffuse texture.

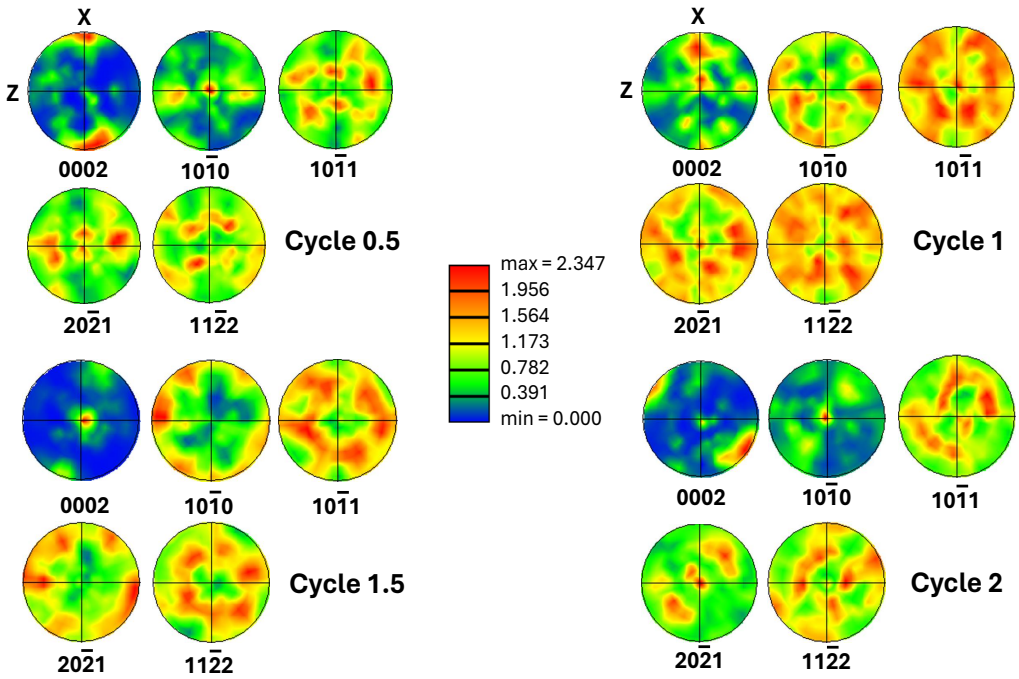


Figure B.11: Pole figures for crystallographic planes in the α phase, measured at a strain rate of $1\,\mathrm{s}^{-1}$ during interrupted C-T loading, show a weak-to-moderate diffuse texture.

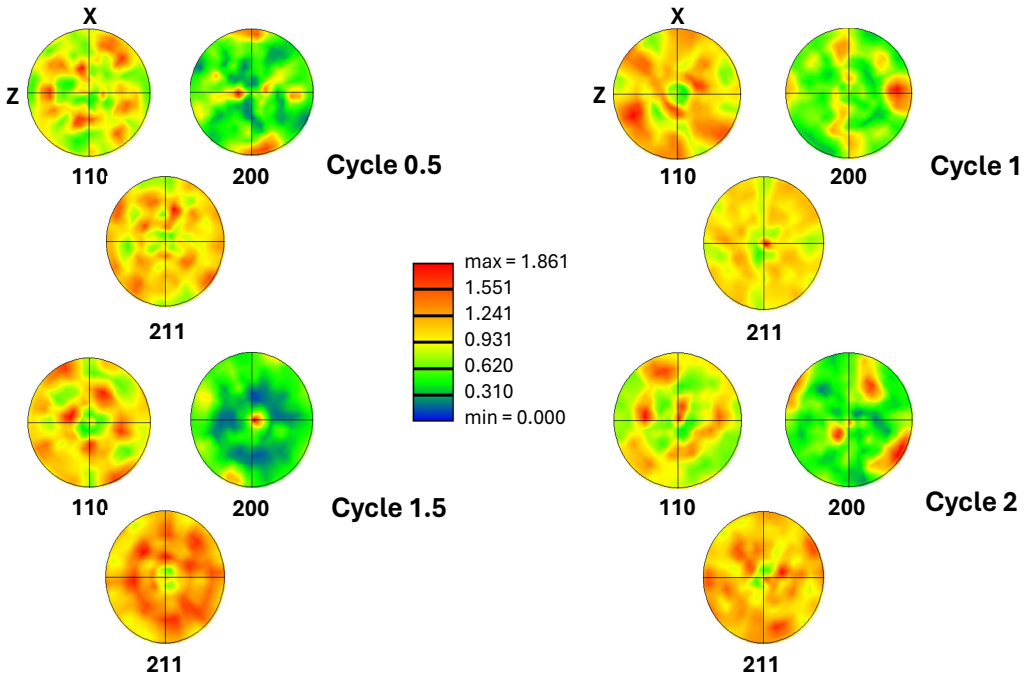


Figure B.12: $1\,s^{-1}$ during interrupted C-T loading show a weak diffuse texture .

Bibliography

[1] M. J. Donachie, Titanium: A Technical Guide, ASM international, 2000.

[2] R. R. Boyer, A An overview on the use of titanium in the aerospace industry, Tech. rep. (1996).

[3] B. Fehrm, Bjorn's corner; Turbofan engine challenges; Part 2 (11 2016).

[4] K. P. Duffy, Overview of NASA GRC Research on Damping of Jet Engine Blades, Tech. rep., NASA Glenn Research Center (2009).

[5] R. M. Coroneos, L. Berke, N. Jaunky, Structural Analysis and Optimization of a Composite Fan Blade Sized for a Large Civil Aircraft Engine, Tech. rep., NASA (2012).

[6] Irish Aviation Authority, Guidance Regarding ATM/ANS Provision in the Vicinity of Volcanic Ash (2025).

[7] C. L. Ryder, Aircraft engine dust ingestion at global airports (2024).

[8] R. A. Dolbeer, M. J. Begier, P. R. Miller, J. R. Weller, W. Major, A. L. Anderson, Wildlife Strikes to Civil Aircraft in the United States, 1990–2024 (6 2025).

[9] TNN, Mid-air scare: Bird strike forces Bengaluru-bound IndiGo flight to land in Varanasi (2026).

[10] J. Piercy, Emergency landing at Eppley due to bird strike, officials say (2026).

[11] Y. Jiang, P. Kurath, CHARACTERISTICS OF THE ARMSTRONG-FREDERICK TYPE PLASTICITY MODELS, Tech. Rep. 3 (1996).

[12] G. E. Dieter, Mechanical metallurgy, McGraw-Hill series in materials science and engineering, McGraw-Hill, New York, 1986.
URL `https://catalog.hathitrust.org/Record/000384843https://hdl.handle.net/2027/mdp.39015036225079https://hdl.handle.net/2027/mdp.39015048125523https://hdl.handle.net/2027/mdp.39015048076981`

[13] J. L. Chaboche, A review of some plasticity and viscoplasticity constitutive theories, International Journal of Plasticity 24 (10) (2008) 1642–1693. `doi:10.1016/j.ijplas.2008.03.009`.

[14] X. Gao, T. Zhang, J. Zhou, S. M. Graham, M. Hayden, C. Roe, On stress-state dependent plasticity modeling: Significance of the hydrostatic stress,

the third invariant of stress deviator and the non-associated flow rule, International Journal of Plasticity 27 (2) (2011) 217–231. doi:10.1016/j.ijplas.2010.05.004.

[15] L. E. Malvern, Introduction to the Mechanics of a Continuous Medium, Prentice-Hall, 1969.

[16] B. Holmedal, Bauschinger effect modelled by yield surface distortions, International Journal of Plasticity 123 (2019) 86–100. doi:10.1016/j.ijplas.2019.07.009.

[17] R. Hill, The Mathematical Theory of Plasticity, Oxford University Press, 1950.

[18] R. von Mises, Mechanik der festen K{\"o}rper im plastisch-deformablen Zustand, Nachrichten von der Gesellschaft der Wissenschaften zu G{\"o}ttingen, Mathematisch-Physikalische Klasse (1913) 582–592.

[19] D. C. Drucker, W. Prager, Soil mechanics and plastic analysis or limit design, Quarterly of Applied Mathematics 10 (2) (1952) 157–165.

[20] J. Lemaitre, J.-L. Chaboche, Mechanics of Solid Materials, Cambridge University Press, 1990.

[21] H. Ziegler, A Modification of Prager's Hardening Rule, Quarterly of Applied Mathematics 17 (1) (1959) 55–65.

[22] P. J. Armstrong, C. O. Frederick, A Mathematical Representation of the Multiaxial Bauschinger Effect, Tech. rep., Central Electricity Generating Board (1966).

[23] J. Bauschinger, Ueber die Veranderung der Elasticitatsgrenze und des Elasticitatsmoduls verschuedener Metalle, Zivilingenieur 27 (1881) 289–348.
URL https://cir.nii.ac.jp/crid/1573105974583453056.bib?lang=en

[24] M. A. Meyers, Dynamic behavior of materials, Wiley, 1994.

[25] M. E. Kassner, P. Geantil, L. E. Levine, Long range internal stresses in single-phase crystalline materials: An experimental overview, International Journal of Plasticity 45 (2013) 44–60.

[26] K. C. Le, T. M. Tran, Thermodynamic dislocation theory: Bauschinger effect, Physical Review E 97 (2018). doi:10.1103/PhysRevE.97.043002.

[27] B. Babu, Physically Based Model for Plasticity and Creep of Ti-6Al-4V,

Tech. rep., Lule{\aa} University of Technology (2008).

[28] L. M. Brown, W. M. Stobbs, The Work-hardening of Copper-Silica, Philosophical Magazine 23 (185) (1971) 1201–1233. doi:10.1080/14786437108217406.

[29] D. V. Wilson, Reversible Work Hardening in Alloys of Cubic Metals, Acta Metallurgica 13 (7) (1965) 807–814. doi:10.1016/0001-6160(65)90145-8.

[30] J. D. Embury, Plastic Flow in Dispersion Hardened Materials, Metallurgical Transactions A 16A (1985) 2191–2200.

[31] M. Kreins, S. Schilli, T. Seifert, A. H. Iyer, M. H. Colliander, S. Wesselmecking, U. Krupp, Bauschinger effect and latent hardening under cyclic microbending of Ni-base Alloy 718 single crystals: Part I. Experimental analysis of single and multi slip plasticity, Materials Science and Engineering: A 827 (10 2021). doi:10.1016/j.msea.2021.142027.

[32] A. Rajput, S. K. Paul, Bauschinger Effect Analysis in Polycrystalline Copper: an Atomistic Simulation, Transactions of the Indian National Academy of Engineering 7 (1) (2022) 235–242. doi:10.1007/s41403-021-00266-3.

[33] J. Hu, B. Chen, D. J. Smith, P. E. Flewitt, A. C. Cocks, On the evaluation of the Bauschinger effect in an austenitic stainless steel - The role of multi-scale residual stresses, International Journal of Plasticity 84 (2016) 203–223. doi:10.1016/j.ijplas.2016.05.009.

[34] D. W. Kim, S. S. Sohn, W. K. Kim, K. S. Kim, S. Lee, Study of Bauschinger effect of acicular ferrite and polygonal ferrite through ex-situ interrupted bending tests in API X80 linepipe steels, Scientific Reports 8 (1) (12 2018). doi:10.1038/s41598-018-34046-x.

[35] J. Fajoui, D. Gloaguen, V. Legrand, G. Oum, J. Kelleher, W. Kockelmann, Bauschinger Effect in an Austenitic Steel: Neutron Diffraction and a Multiscale Approach, Metallurgical and Materials Transactions A: Physical Metallurgy and Materials Science 47 (5) (2016) 2024–2036. doi:10.1007/s11661-016-3362-5.

[36] A. A. Mamun, R. J. Moat, J. Kelleher, P. J. Bouchard, Origin of the Bauschinger effect in a polycrystalline material, Materials Science and Engineering: A 707 (2017) 576–584. doi:10.1016/j.msea.2017.09.091.

[37] J. D. Atkinson, L. M. Brown, W. M. Stobbs, The work-hardening of copper-silica: IV. The Bauschinger effect and plastic relaxation, Philosophical Magazine 30 (6) (1974) 1247–1280. doi:10.1080/14786437408207280.

[38] D. Ugi, K. Zoller, K. Lukács, Z. Fogarassy, I. Groma, S. Kalácska, K. Schulz, P. D. Ispánovity, Irreversible evolution of dislocation pile-ups during cyclic microcantilever bending, Materials and Design 238 (2 2024). doi:10.1016/j.matdes.2024.112682.

[39] F. Li, X. Zhao, H. Zhang, W. He, H. Chen, H. Guo, Bauschinger Effect of Mn18Cr18N Austenitic Stainless Steel, Journal Wuhan University of Technology, Materials Science Edition 35 (2) (2020) 399–406. doi:10.1007/s11595-020-2270-0.

[40] A. Ellermann, B. Scholtes, The Bauschinger Effect in Different Heat Treatment Conditions of 42CrMo4, Tech. Rep. 1 (2011).

[41] J. N. Hu, A. C. Cocks, Effect of creep on the Bauschinger effect in a polycrystalline austenitic stainless steel, Scripta Materialia 128 (2017) 100–104. doi:10.1016/j.scriptamat.2016.10.005.

[42] S. Gao, K. Yoshino, D. Terada, Y. Kaneko, N. Tsuji, Significant Bauschinger effect and back stress strengthening in an ultrafine grained pure aluminum fabricated by severe plastic deformation process, Scripta Materialia 211 (4 2022). doi:10.1016/j.scriptamat.2022.114503.

[43] M. Buttard, T. Lenoir, B. Chéhab, C. Josserond, A. Deschamps, J. J. Blandin, G. Martin, Bauschinger effect in an aluminium alloy designed for laser powder bed fusion, Materialia 34 (5 2024). doi:10.1016/j.mtla.2024.102093.

[44] Nil Constans Sole, An investigation on the Bauschinger effect in titanium alloys for aerospace, Tech. rep., University of Oxford, Oxford (2021).

[45] V. V. Stolyarov, Structure Refinement and Bauschinger Effect in fcc and hcp Metals, Metals 13 (7) (7 2023). doi:10.3390/met13071307.

[46] X. Yu, H. Ji, H. Zhang, D. Xu, Experimental and numerical investigation on the Bauschinger effect during cold forming of TC4 ELI alloy, International Journal of Material Forming 15 (2) (3 2022). doi:10.1007/s12289-022-01666-8.

[47] J. D. Paul, R. Hoppe, F. Appel, On the Bauschinger effect in TiAl alloys, Acta Materialia 104 (2016) 101–108. doi:10.1016/j.actamat.2015.10.036.

[48] J. Ma, H. Yang, H. Li, Z. J. Tao, G. J. Li, Springback prediction of titanium tube bending considering Bauschinger effect and Young's modulus variation, in: Journal of Physics: Conference Series, Vol. 734, Institute of Physics Publishing, 2016. doi:10.1088/1742-6596/734/3/032113.

[49] H. Mughrabi, Dislocation clustering and long-range internal stresses in monotonically and cyclically deformed metal crystals, Revue de Physique Appliquée 23 (4) (1988) 367–379. doi:10.1051/rphysap:01988002304036700.

[50] constanssole_1070388_MSc_thesis.

[51] J. Zhou, J. Shen, F. A. Essa, J. Yu, Twins and grain boundaries-dominated the reverse Bauschinger effect and tension-compression asymmetry, Journal of Materials Research and Technology 18 (2022) 15–28. doi:10.1016/j.jmrt.2022.02.080.

[52] Y. Saleht, H. Margolin, BAUS˜HING˜R EFFECT DURING CYCLIC STRAINING OF TWO DUCTILE PHASE ALLOYS", Tech. rep.

[53] R. r. p. PURUSHOTTAM RAJ PUROHIT, S. LHADI, N. GEY, O. CASTELNAU, T. RICHETON, L. GERMAIN, S. BERBENNI, Stress partitioning in a near-β Titanium alloy induced by elastic and plastic phase anisotropies: experimental and modeling, MATEC Web of Conferences 321 (2020) 11090. doi:10.1051/matecconf/202032111090.

[54] J. Shen, J. Zhou, G. Zhao, C. Gong, J. Yu, Z. Xia, F. Xian, Attenuation of the Bauschinger effect and enhancement of tension-compression asymmetry in single crystal aluminum by temperature, RSC Advances 12 (33) (2022) 21235–21246. doi:10.1039/d2ra03051a.

[55] R. L. Woolley, The Bauschinger effect, Philosophical Magazine 44 (1953) 597–618.

[56] Y. Saleh, H. Margolin, Bauschinger effect during cyclic straining of two ductile phase alloys, Acta Metallurgica 27 (1979) 535–544.

[57] M. D. Atkinson, Measurement of local plastic strain during uniaxial reversed

loading of nickel alloy 625, Materials Characterization 168 (2020).

[58] J. Toribio, Analysis of the Bauschinger Effect in Cold Drawn Pearlitic Steels, Metals 10 (2020).

[59] D. Ryu, Y. Kim, S. Nahm, L. Kang, Recent Developments in Plastic Deformation Behavior of Titanium and Its Alloys During the Rolling Process: A Review (12 2024). doi:10.3390/ma17246060.

[60] J. C. Tseng, W. C. Huang, W. Chang, A. Jeromin, T. F. Keller, J. Shen, A. C. Chuang, C. C. Wang, B. H. Lin, L. Amalia, N. T. Tsou, S. J. Shih, E. W. Huang, Deformations of Ti-6Al-4V additive-manufacturing-induced isotropic and anisotropic columnar structures: Insitu measurements and underlying mechanisms, Additive Manufacturing 35 (10 2020). doi:10.1016/j.addma.2020.101322.

[61] Y. Fu, Y. Gao, W. Jiang, W. Xiao, X. Zhao, C. Ma, A Review of Deformation Mechanisms, Compositional Design, and Development of Titanium Alloys with Transformation-Induced Plasticity and Twinning-Induced Plasticity Effects (1 2024). doi:10.3390/met14010097.

[62] P. S. Follansbee, G. T. Gray, An Analysis of the Low Temperature, Low and High Strain-Rate Deformation of Ti-6AI-4V, Tech. rep.

[63] L. Lei, Q. Zhao, Q. Zhu, M. Yang, W. Yang, W. Zeng, Y. Zhao, Twinning-induced high impact toughness of titanium alloy at cryogenic temperature, Materials Science and Engineering: A 860 (2022) 144258. doi:https://doi.org/10.1016/j.msea.2022.144258.
URL https://www.sciencedirect.com/science/article/pii/S0921509322016380

[64] G. Tsukamoto, T. Kunieda, S. Yamasaki, M. Mitsuhara, H. Nakashima, Effects of temperature and grain size on active twinning systems in commercially pure titanium, Journal of Alloys and Compounds 884 (2021) 161154. doi:https://doi.org/10.1016/j.jallcom.2021.161154.
URL https://www.sciencedirect.com/science/article/pii/S0925838821025639

[65] L. Lilensten, F. Sun, A. Hocini, G. Dirras, P. Vermaut, F. Prima, 332<113> mechanical detwinning as a deformation mechanism in the β-metastable

Ti-15Mo alloy during cyclic loading, Scripta Materialia 232 (2023) 115503. doi:https://doi.org/10.1016/j.scriptamat.2023.115503.
URL https://www.sciencedirect.com/science/article/pii/S1359646223002270

[66] R. Zhang, X. Li, H. Huang, X. Zhao, Research Progress on Slip Behavior of \alpha-Ti under Quasi-Static Loading: A Review, Metals 12 (2022).

[67] S.-c. Liao, J. Duffy, Adiabatic shear bands in a TI-6Al-4V titanium alloy, Journal of the Mechanics and Physics of Solids 46 (11) (1998) 2201–2231. doi:https://doi.org/10.1016/S0022-5096(98)00044-1.
URL https://www.sciencedirect.com/science/article/pii/S0022509698000441

[68] K. D. Karantza, D. E. Manolakos, A Review on the Adiabatic Shear Banding Mechanism in Metals and Alloys Considering Microstructural Characteristics, Morphology and Fracture (12 2023). doi:10.3390/met13121988.

[69] P. Wang, P. Mao, Z. Wei, L. Zhou, Z. Wang, F. Wang, H. Yi, Z. Liu, Detwinning behavior of TA2 pure titanium during in-situ tensile, Journal of Alloys and Compounds 1026 (2025) 180234. doi:https://doi.org/10.1016/j.jallcom.2025.180234.
URL https://www.sciencedirect.com/science/article/pii/S092583882501792X

[70] B. Qian, M. Yang, L. Lilensten, P. Vermaut, F. Sun, F. Prima, In-situ observations of a hierarchical twinningdetwinning process in stress-induced α-martensite of Ti-12Mo alloy, Materials Research Letters 10 (2) (2022) 45–51. doi:10.1080/21663831.2021.2013967.

[71] C. Zhang, D. Li, X. Li, Y. Li, C. . Zhang, C. . Li, D. . Li, X. . Li, metals An Experimental Study of the Tension-Compression Asymmetry of Extruded Ti-6.5Al-2Zr-1Mo-1V under Quasi-Static Conditions at High Temperature (2021). doi:10.3390/xxxxx.
URL https://doi.org/10.3390/xxxxx

[72] M. R. Winstone, M. L. Wright, R. D. Rawlings, The strength differential in some titanium alloys, Scripta Metallurgica 7 (12) (1973) 1265–1268. doi:https://doi.org/10.1016/0036-9748(73)90074-4.

URL https://www.sciencedirect.com/science/article/pii/0036974873900744

[73] Y. Yuan, Y. Zhang, Y. Qiao, J. Xie, Q. Xu, Y. Qi, W. Zhang, P. Chen, Effect of build orientation on dynamic compressive behaviour of Ti-6Al-4V alloy fabricated by selective laser melting, Materials Science and Engineering: A 862 (2023) 144440. doi:https://doi.org/10.1016/j.msea.2022.144440.
URL https://www.sciencedirect.com/science/article/pii/S0921509322018202

[74] C. Ma, H. Wang, T. Hama, X. Guo, X. Mao, J. Wang, P. Wu, Twinning and detwinning behaviors of commercially pure titanium sheets, International Journal of Plasticity 121 (2019) 261–279. doi:10.1016/j.ijplas.2019.06.010.

[75] J. B. Jordon, M. F. Horstemeyer, K. Solanki, Y. Xue, Damage and stress state influence on the Bauschinger effect in aluminum alloys, Mechanics of Materials 39 (10) (2007) 920–931. doi:10.1016/j.mechmat.2007.03.004.

[76] E. Maawad, H. G. Brokmeier, Z. Y. Zhong, N. Al-Hamdany, M. Salih, L. Wagner, N. Schell, Determination of polycrystal diffraction elastic constants of Ti-2.5Cu by using in situ tensile loading and synchrotron radiation, Materials Science and Engineering: A 594 (2014) 62–67. doi:10.1016/j.msea.2013.11.053.

[77] T. Mishurova, K. Artzt, S. Cabeza, G. Requena, G. Bruno, J. Haubrich, Creative Commons CC-BY-NC licence https://creativecommons.org/licenses/by-nc/4.0/ Subsurface Residual Stress Analysis in Ti-6Al-4V Additive Manufactured Parts by Synchrotron X-ray Diffraction, Tech. rep.
URL http://www.ndt.net/?id=22781

[78] J. R. Cho, S. Tin, R. C. Reed, Measurements of residual strains and stresses in laser formed plates of Ti-6Al-4V using synchrotron X-ray diffraction, Materials Science and Technology 20 (4) (2004) 465–472. doi:10.1179/026708304225010299.

[79] J. D. H. Paul, R. Hoppe, M. Oehring, F. Appel, On the evolution of internal stresses and glide resistance during Bauschinger

tests performed on a γ(TiAl) alloy, Materialia 40 (2025) 102398. doi:https://doi.org/10.1016/j.mtla.2025.102398.
URL https://www.sciencedirect.com/science/article/pii/S2589152925000651

[80] J. Peirs, P. Verleysen, J. Degrieck, Study of the dynamic Bauschinger effect in Ti6Al4V by torsion experiments, in: EPJ Web of Conferences, Vol. 26, 2012. doi:10.1051/epjconf/20122601023.

[81] V. Tuninetti, G. Gilles, O. Milis, T. Pardoen, A. M. Habraken, Anisotropy and tensioncompression asymmetry modeling of the room temperature plastic response of Ti6Al4V, International Journal of Plasticity 67 (2015) 53–68. doi:https://doi.org/10.1016/j.ijplas.2014.10.003.
URL https://www.sciencedirect.com/science/article/pii/S0749641914001971

[82] X. X. Guan, L. Lu, S. N. Luo, D. Fan, In situ observations of detwinning and strain localization in pure titanium, Materials Science and Engineering: A 813 (5 2021). doi:10.1016/j.msea.2021.141073.

[83] O. M. Badr, F. Barlat, B. Rolfe, M.-G. Lee, P. Hodgson, M. Weiss, Constitutive modelling of high strength titanium alloy Ti-6Al-4ăV for sheet forming applications at room temperature, International Journal of Solids and Structures 80 (2016) 334–347. doi:https://doi.org/10.1016/j.ijsolstr.2015.08.025.
URL https://www.sciencedirect.com/science/article/pii/S0020768315003807

[84] A. J. Ring, E. H. Baker, J. A. Salem, J. C. Thesken, Yield Behavior of Solution Treated and Aged Ti-6Al-4V, Tech. rep. (2014).
URL http://www.sti.nasa.gov

[85] A. S. Khan, S. Yu, Deformation induced anisotropic responses of Ti-6Al-4V alloy. Part I: Experiments, International Journal of Plasticity 38 (2012) 14–26. doi:10.1016/j.ijplas.2012.03.015.

[86] A. Fitzner, D. G. Prakash, J. Q. Da Fonseca, M. Thomas, S. Y. Zhang, J. Kelleher, P. Manuel, M. Preuss, The effect of aluminium on twinning in binary alpha-titanium, Acta Materialia 103 (2016) 341–351. doi:10.1016/

j.actamat.2015.09.048.

[87] D. Koreček, P. Solfronk, J. Sobotka, A Deformational Analysis of a Titanium Alloy Supported by the Mathematical Modelling of the Sheet Metal Forming Process via Numerical Simulation, Materials 18 (7) (4 2025). doi:10.3390/ma18071598.

[88] T. Neeraj, M. F. Savage, J. Tatalovich, L. Kovarik, R. W. Hayes, M. J. Mills, Observation of Tension-Compression Asymmetry in α and α/β Titanium Alloys, in: Philosophical Magazine, Vol. 85, 2005, pp. 279–295. doi:10.1080/14786430412331315707.

[89] Struers, Metallographic preparation of titanium and titanium alloys, Tech. rep. (2026).

[90] F. P. S. Afonso, L. Lagoeiro, H. Fossen, P. F. Barbosa, C. B. Pinto, C. G. P. De Souza, Application of the EBSD Technique in the Study of Porosity and Permeability in Deformation Bands in Sandstone, Microscopy and Microanalysis 30 (4) (2024) 692–702. doi:10.1093/mam/ozae070.

[91] B. Adams, S. I. Wright, K. Kunze, Orientation Imaging: The Emergence of a New Microscopy, Metallurgical Transactions A 24A (4 1993).

[92] E. Nieto-Valeiras, E. Ganju, N. Chawla, J. LLorca, Assessment of slip transfer criteria for prismatic-to-prismatic slip in pure Ti from 3D grain boundary data, Acta Materialia 262 (1 2024). doi:10.1016/j.actamat.2023.119424.

[93] C. Liu, R. Thomas, T. Sun, J. Donoghue, X. Zhang, T. L. Burnett, J. Q. da Fonseca, M. Preuss, Multi-dimensional study of the effect of early slip activity on fatigue crack initiation in a near-α titanium alloy, Acta Materialia 233 (7 2022). doi:10.1016/j.actamat.2022.117967.

[94] M. Ninomi, S. Akiyama, M. Ikeda, M. Hagiwara, K. Maruyama The, Three-Dimensional Characterization and Mesoscale Mechanical Modeling of a Beta Titanium Alloy, Tech. rep. (2007).

[95] C. Lavogiez, C. Dureau, Y. Nadot, P. Villechaise, S. Hémery, Crack initiation mechanisms in Ti-6Al-4V subjected to cold dwell-fatigue, low-cycle fatigue and high-cycle fatigue loadings, Acta Materialia 244 (1 2023). doi:10.1016/j.actamat.2022.118560.

[96] Y. Yamabe-Mitarai, N. Motohashi, S. Kuroda, P. V. Cobbinah, Microstruc-

ture Evolution and Fatigue Properties of Ti Alloy Forged by 1500 t Forging Simulator, Materials 18 (7) (4 2025). doi:10.3390/ma18071436.

[97] L. Germain, Y. Samih, P. Delaleau, J. Gilgert, N. Gey, Analysis of cold dwell fatigue crack initiation site in a β-forged Ti-6242 disk in relation with local texture, Metals 10 (7) (2020) 1–14. doi:10.3390/met10070951.

[98] F. J. Humphreys, Review Grain and subgrain characterisation by electron backscatter diffraction, Tech. rep.

[99] B. Adams, S. I. Wright, K. Kunze, Orientation Imaging: The Emergence of a New Microscopy, METALLURGICALTRANSACTIONSA 24 (1992).

[100] Erich Schmid, Walter Boas, Mit besonderer Berücksichtigung der Metalle, Julius Springer, Berlin 17 (1935).

[101] T. C. Chu, W. F. Ranson, M. A. Sutton, W. H. Peters, Applications of Digital.Image-Correlation Techniques to Experimental Mechanics.
URL ExperimentalMechanics

[102] A. Orozco-Caballero, D. Lunt, J. D. Robson, J. Quinta da Fonseca, How magnesium accommodates local deformation incompatibility: A high-resolution digital image correlation study, Acta Materialia 133 (2017) 367–379. doi:10.1016/j.actamat.2017.05.040.

[103] T. E. Edwards, F. Di Gioacchino, H. P. Springbett, R. A. Oliver, W. J. Clegg, Stable Speckle Patterns for Nano-scale Strain Mapping up to 700ă°C, Experimental Mechanics 57 (9) (2017) 1469–1482. doi:10.1007/s11340-017-0317-8.

[104] Y. B. Das, A. N. Forsey, T. H. Simm, K. M. Perkins, M. E. Fitzpatrick, S. Gungor, R. J. Moat, In situ observation of strain and phase transformation in plastically deformed 301 austenitic stainless steel, Materials and Design 112 (2016) 107–116. doi:10.1016/j.matdes.2016.09.057.

[105] Philip R Bevington, D. Keith Robinson, Data Reduction and Error Analysis for the Physical Sciences, McGraw Hill Higher Education, 2003.

[106] John R. Taylor, An Introduction to Error Analysis, University Science Books, California.

[107] M. A. Sutton, Image Correlation for Shape, Motion and Deformation Measurements: Basic Concepts, Theory and Applications, Springer, 2009.

[108] J. Zhao, C. Shield, C. French, T. Posbergh, Effect of Servovalve/Actuator Dynamics on Displacement Controlled Testing, in: Proceedings of the 13th World Conference on Earthquake Engineering, Vancouver, Canada, 2004.

[109] M. V. Sivaselvan, A. M. Reinhorn, X. Shao, S. Weinreber, Dynamic Force Control with Hydraulic Actuators Using Added Compliance and Displacement Compensation, Earthquake Engineering and Structural Dynamics (2009).

[110] M. Poschmann, M. Asta, D. C. Chrzan, Effect of non-Schmid stresses on a-type screw dislocation core structure and mobility in titanium, Computational Materials Science 161 (2019) 261–264. doi:10.1016/j.commatsci.2019.01.052.

[111] W. Roberts, J. Gong, A. J. Wilkinson, E. Tarleton, Tensioncompression asymmetry of c+a slip in Ti6Al, Scripta Materialia 178 (2020) 119–123. doi:10.1016/j.scriptamat.2019.11.002.

[112] I. P. Jones, W. B. Hutchinson, Stress-State Dependence of Slip in Titanium-6Al-4V and Other H.C.P. Metals, Acta Metallurgica 29 (1981) 951–968.

[113] D. C. Montgomery, G. C. Runger, Applied statistics and probability for engineers, Wiley, 2003.

[114] P. Serrano, L. Toualbi, P. Kanoute, A. Couret, Cyclic deformation of TiAl generic microstructures at room and high temperature: Bauschinger effect & strain rate sensitivity, Intermetallics 122 (7 2020). doi:10.1016/j.intermet.2020.106816.

[115] B. L. Boyce, X. Chen, J. O. Peters, J. W. Hutchinson, R. O. Ritchie, Mechanical relaxation of localized residual stresses associated with foreign object damage, Materials Science and Engineering A 349 (2003) 48–58.
URL https://doi.org/10.1016/S0921-5093(02)00543-9

[116] B. J. Hayes, B. W. Martin, B. Welk, S. J. Kuhr, T. K. Ales, D. A. Brice, I. Ghamarian, A. H. Baker, C. V. Haden, D. G. Harlow, H. L. Fraser, P. C. Collins, Predicting tensile properties of Ti-6Al-4V produced via directed energy deposition, Acta Materialia 133 (2017) 120–133. doi:10.1016/j.actamat.2017.05.025.

[117] M. Zhang, J. Qiu, C. Fang, M. Zhang, Z. Yang, J. Lei, Effect of texture on

the room temperature tensile and creep properties of Ti6Al4V plate with large thickness, Journal of Materials Research and Technology 30 (2024) 2311–2321. doi:10.1016/j.jmrt.2024.03.212.

[118] S. Kim, D.-H. Kam, K.-A. Lee, High-temperature strength and microstructural evolution of Ti-6Al-4V alloy fabricated by wire Arc additive manufacturing under elevated temperature, Scientific Reports (12 2025). doi:10.1038/s41598-025-31895-1.
URL https://www.nature.com/articles/s41598-025-31895-1

[119] E. Wielewski, M. R. Arthington, C. R. Siviour, N. Petrinic, Characterising the Effects of Strain Rate, Crystallographic Texture and Direction of Loading on the Mechanical Behaviour of Ti-6Al-4V, Journal of Dynamic Behavior of Materials 1 (4) (2015) 462–471. doi:10.1007/s40870-015-0040-4.

[120] Y. Xiao, H. Zhou, P. Liu, L. Chen, Gleeble-Simulated Ultra-Fast Cooling Unlocks StrengthDuctility Synergy in Fully Martensitic Ti-6Al-4V, Materials 18 (19) (10 2025). doi:10.3390/ma18194572.

[121] C. S. White, C. A. Bronkhorst, L. Anand, An Improved Isotropic-Kinematic Hardening Model for Moderate Deformation Metal plasticity, Mechanics of Materials 10 (1990) 127–147.

[122] K. Prasad, V. Kumar, Effect of Temperature and Hold Time on Internal Hardening Behavior of a near α Titanium Alloy Under Cyclic Deformation, Materials and Design 31 (6) (2010) 2716–2724. doi:10.1016/j.matdes.2010.01.031.

[123] R. Biswal, X. Zhang, M. Shamir, A. Al Mamun, M. Awd, F. Walther, A. Khadar Syed, Interrupted fatigue testing with periodic tomography to monitor porosity defects in wire + arc additive manufactured Ti-6Al-4V, Additive Manufacturing 28 (2019) 517–527. doi:10.1016/j.addma.2019.04.026.

[124] I. Altenberger, R. K. Nalla, Y. Sano, L. Wagner, R. O. Ritchie, On the effect of deep-rolling and laser-peening on the stress-controlled low- and high-cycle fatigue behavior of Ti-6Al-4V at elevated temperatures up to 550 °c, International Journal of Fatigue 44 (2012) 292–302. doi:10.1016/j.ijfatigue.2012.03.008.

[125] F. Liu, H. Cui, C. Liu, X. Song, Z. Cui, R. Xin, Understanding the interaction of {1012} twins and Mg17Al12 precipitates in magnesium alloys via high-resolution electron microscopy, Journal of Materials Research and Technology 27 (2023) 7129–7137. doi:10.1016/j.jmrt.2023.11.177.

[126] L. Tan, X. Huang, Y. Wang, Q. Sun, Y. Zhang, J. Tu, Z. Zhou, Activation Behavior of {10-12}-{10-12} Secondary Twins by Different Strain Variables and Different Loading Directions during Fatigue Deformation of AZ31 Magnesium Alloy, Metals 12 (9) (9 2022). doi:10.3390/met12091433.

[127] L. Li, W. Liu, F. Qi, D. Wu, Z. Zhang, Effects of deformation twins on microstructure evolution, mechanical properties and corrosion behaviors in magnesium alloys - A review (9 2022). doi:10.1016/j.jma.2022.09.003.

[128] W. Mei, H. Pang, Q. Li, X. Chen, Effect of Sm on twinning behavior of Mg-Gd-Y-Zr alloy at room temperature compression, Journal of Materials Research and Technology 25 (2023) 2545–2555. doi:10.1016/j.jmrt.2023.06.113.

[129] B. L. Henrie, Thomas A. Mason, John F. Bingert, Automated twin identification technique for use with electron backscatter diffraction, Materials Science Forum, Trans Tech Publications Ltd 495 (2005) 191–196.

[130] L. Song, B. Wu, L. Zhang, X. Du, Y. Wang, C. Esling, M. J. Philippe, Detwinning-related Bauschinger effect of an extruded magnesium alloy AZ31B, Materials Characterization 148 (2019) 63–70. doi:10.1016/j.matchar.2018.12.005.

[131] T. Hama, N. Yi, A. Kobuki, S. Uchida, H. Fujimoto, H. Takuda, Work-hardening behavior of commercially pure titanium JIS grade 1 sheet upon reverse loading, in: AIP Conference Proceedings, Vol. 1769, American Institute of Physics Inc., 2016. doi:10.1063/1.4963619.

[132] S. Sinha, N. P. Gurao, In situ electron backscatter diffraction study of twinning in commercially pure titanium during tension-compression deformation and annealing, Materials and Design 116 (2017) 686–693. doi:10.1016/j.matdes.2016.10.060.

[133] J. Wang, Crystal Plasticity Modeling to Understand Interactions Between Slip and Deformation Twinning in Hexagonal Close Packed Alloys, Ph.D.

thesis, University of California Santa Barbara (6 2022). doi:https://escholarship.org/uc/item/89w656jm.
URL https://escholarship.org/uc/item/89w656jm

[134] M. Wroński, M. A. Kumar, R. J. McCabe, K. Wierzbanowski, C. N. Tomé, Deformation behavior of CP-titanium under strain path changes: Experiment and crystal plasticity modeling, International Journal of Plasticity 148 (1 2022). doi:10.1016/j.ijplas.2021.103129.

[135] H. Abdolvand, J. Wright, A. J. Wilkinson, Strong grain neighbour effects in polycrystals, Nature Communications 9 (1) (12 2018). doi:10.1038/s41467-017-02213-9.

[136] Y. Guo, H. Abdolvand, T. B. Britton, A. J. Wilkinson, Growth of {112ŕ2} twins in titanium: A combined experimental and modelling investigation of the local state of deformation, Acta Materialia 126 (2017) 221–235. doi:10.1016/j.actamat.2016.12.066.

[137] Y. Guo, T. B. Britton, A. J. Wilkinson, Slip band-grain boundary interactions in commercial-purity titanium, Acta Materialia 76 (2014) 1–12. doi:10.1016/j.actamat.2014.05.015.

[138] R. M. Gray, D. L. Neuhoff, Quantization, IEEE Transactions on Information Theory 44 (1998) 2325–2383.

[139] H. Xu, D. Ye, L. Mei, A study of the back stress and the friction stress behaviors of Ti-6Al-4V alloy during low cycle fatigue at room temperature, Materials Science and Engineering: A 700 (2017) 530–539. doi:10.1016/j.msea.2017.06.051.

[140] A. Ismaeel, X. Li, D. Xu, J. Zhang, L. Weining, C. Wang, R. Yang, Effect of slip and twinning on texture evolution mechanisms in dual-phase titanium alloys, Journal of Materials Research and Technology 35 (2025) 4882–4894. doi:10.1016/j.jmrt.2025.02.102.

[141] M. Drakopoulos, T. Connolley, C. Reinhard, R. Atwood, O. Magdysyuk, N. Vo, M. Hart, L. Connor, B. Humphreys, G. Howell, S. Davies, T. Hill, G. Wilkin, U. Pedersen, A. Foster, N. De Maio, M. Basham, F. Yuan, K. Wanelik, I12: The Joint Engineering, Environment and Processing (JEEP) beamline at Diamond Light Source, Journal of Synchrotron Ra-

diation 22 (2015) 828–838. doi:10.1107/S1600577515003513.

[142] D. C. Pagan, K. E. Nygren, M. P. Miller, Analysis of a Three-Dimensional Slip Field in a Hexagonal Ti Alloy from in-situ High-Energy X-ray Diffraction Microscopy Data, Tech. rep. (2021).
URL https://www.elsevier.com/open-access/userlicense/1.0/

[143] R. E. Lim, D. C. Pagan, D. E. Boyce, J. V. Bernier, P. A. Shade, A. D. Rollett, Grain-resolved temperature-dependent anisotropy in hexagonal Ti-7Al revealed by synchrotron X-ray diffraction, Materials Characterization 174 (4 2021). doi:10.1016/j.matchar.2021.110943.

[144] W. Li, H. Sharma, P. Kenesei, J.-S. Park, S. Ravi, O. K. Celebi, D. You, T. B. Celebi, H. Sehitoglu, A. Bucsek, Intragranular evolution of slip system strength and activity in titanium using point-focused high-energy diffraction microscopy, Tech. rep.
URL https://ssrn.com/abstract=5151306

[145] J. Filik, A. W. Ashton, P. C. Y. Chang, P. A. Chater, S. J. Day, M. Drakopoulos, M. W. Gerring, M. L. Hart, O. V. Magdysyuk, S. Michalik, A. Smith, C. C. Tang, N. J. Terrill, M. T. Wharmby, H. Wilhelm, Processing two-dimensional X-ray diffraction and small-angle scattering data in DAWN 2, Journal of Applied Crystallography 50 (3) (2017) 959–966. doi:10.1107/S1600576717004708.
URL https://doi.org/10.1107/S1600576717004708

[146] S. L. R. da Silva, L. O. Kerber, L. Amaral, C. A. dos Santos, X-ray diffraction measurements of plasma-nitrided Ti-6Al-4V, Surface and Coatings Technology 116-119 (1999) 342–346. doi:https://doi.org/10.1016/S0257-8972(99)00204-2.

[147] M. I. Jamaludin, Development of Porous TI-6AL-4V Mix with Palm Stearin Binder By Metal Injection Moulding Technique, Ph.D. thesis, Universiti Teknologi Mara (2015).

[148] S. J. Lainé, K. M. Knowles, D. Rugg, Very high strain rate deformation twinning behaviour of Ti6Al4V, Materialia 12 (8 2020). doi:10.1016/j.mtla.2020.100762.

[149] M. Nishida, A. Chiba, S. Ando, K. Imamura, H. Minato, Microstructural

Modifications in an Explosively Welded Ti/Ti Clad Material: II. Deformation Structures around Bonding Interface, Metallurgical Transactions A 24A (3 1993). doi:https://doi.org/10.1007/BF02656642.

[150] C. Suryanarayana and M. Grant Norton, Practical Aspects of X-ray Diffraction, in: X-Ray Diffraction: A Practical Approach, Springer US, Boston, MA, 1998, pp. 97–237. doi:10.1007/978-1-4899-0148-4{_}3.

[151] J. Bolze, M. Gateshki, Highly versatile laboratory X-ray scattering instrument enabling (nano-)material structure analysis on multiple length scales by covering a scattering vector range of almost five decades, Review of Scientific Instruments 90 (12) (12 2019). doi:10.1063/1.5130061.

[152] J. E. Huber, F. Hofmann, S. Barhli, T. J. Marrow, C. Hildersley, Observation of crack growth in a polycrystalline ferroelectric by synchrotron X-ray diffraction, Scripta Materialia 140 (2017) 23–26. doi:10.1016/j.scriptamat.2017.06.053.

[153] J. F. Cárdenas-García, S. Ekwaro-Osire, J. M. Berg, W. H. Wilson, Nonlinear least-squares solution to the moiré hole method problem in orthotropic materials. Part I: Residual stresses, Experimental Mechanics 45 (4) (2005) 301–313. doi:10.1177/0014485105056080.

[154] Fitzpatrick M.E., Fry A.T., Holdway. P, Kandil F.A., Shackleton J., Suominen. L, Determination of Residual Stresses by X-ray Diffraction Issue 2, Tech. rep., National Physical Laboratory (9 2005).

[155] P. J. Withers, H. K. D. H. Bhadeshia, Residual stress Part 1-Measurement techniques, Materials Science and Technology 17 (355) (2001).

[156] Daymond Mark R., The determination of a continuum mechanics equivalent elastic strain from the analysis of multiple diffraction peaks, Journal of Applied Physics 8 (96) (2004) 4263–4272.

[157] S. Ivanov, M. Gushchina, A. Artinov, M. Khomutov, E. Zemlyakov, Effect of Elevated Temperatures on the Mechanical Properties of a Direct Laser Deposited Ti-6Al-4V, Materials 14 (6432) (2021). doi:https://doi.org/10.3390/ma14216432.

[158] B. Rehmer, F. Bayram, L. A. Ávila Calderón, G. Mohr, B. Skrotzki, Elastic modulus data for additively and conventionally manufactured variants of

Ti-6Al-4V, IN718 and AISI 316 L, Scientific Data 10 (1) (12 2023). doi:10.1038/s41597-023-02387-6.

[159] E. Nes, K. Marthinsen, Y. Brechet, On the mechanisms of dynamic recovery, Scripta Materialia 47 (2002) 607–611.
URL www.actamat-journals.com

[160] D. June, J. R. Mayeur, P. Gradl, A. Wessman, K. Hazeli, Effects of size, geometry, and testing temperature on additively manufactured Ti-6Al-4V titanium alloy, Additive Manufacturing 80 (1 2024). doi:10.1016/j.addma.2024.103970.

[161] W. Chen, C. J. Boehlert, E. A. Payzant, J. Y. Howe, The effect of processing on the 455 °C tensile and fatigue behavior of boron-modified Ti-6Al-4V, International Journal of Fatigue 32 (3) (2010) 627–638. doi:10.1016/j.ijfatigue.2009.04.013.

[162] M. Paghandeh, A. Zarei-Hanzaki, H. R. Abedi, Y. Vahidshad, J. Kawalko, D. Dietrich, T. Lampke, Compressive/tensile deformation behavior and the correlated microstructure evolution of Ti-6Al-4V titanium alloy at warm temperatures, Journal of Materials Research and Technology 10 (2021) 1291–1300. doi:10.1016/j.jmrt.2020.12.110.

[163] J. Ayllón, V. Miguel, A. Martínez-Martínez, J. Coello, J. A. Naranjo, F. García-Sevilla, Compression behavior of sheets metals of pure titanium 2 and Ti6Al4V alloy under high temperature: Evaluation of the tensioncompression asymmetry, Metals 11 (1) (2021) 1–25. doi:10.3390/met11010168.

[164] S. Zherebtsov, G. Salishchev, R. Galeyev, K. Maekawa, Mechanical Properties of Ti-6Al-4V Titanium Alloy with Submicrocrystalline Structure Produced by Severe Plastic Deformation, Materials Transactions 46 (2005) 2020–2025. doi:https://doi.org/10.2320/matertrans.46.2020.

[165] P. Kubaschinski, A. Gottwalt, U. Tetzlaff, H. Altenbach, M. Waltz, Calibration of a combined isotropic-kinematic hardening material model for the simulation of thin electrical steel sheets subjected to cyclic loading, Materialwissenschaft und Werkstofftechnik 53 (4) (2022) 422–439. doi:10.1002/mawe.202100341.

[166] M. Ruiz De Sotto, P. Longère, V. Doquet, J. Papasidero, A constitutive

model for a rate and temperature-dependent, plastically anisotropic titanium alloy, International Journal of Plasticity 134 (11 2020). doi:10.1016/j.ijplas.2020.102777.

[167] A. Orozco-Caballero, F. Li, D. Esqué-de los Ojos, M. D. Atkinson, J. Quinta da Fonseca, On the ductility of alpha titanium: The effect of temperature and deformation mode, Acta Materialia 149 (2018) 1–10. doi:10.1016/j.actamat.2018.02.022.

[168] Y. Qin, J. Liang, X. Long, N. Zhang, M. Chen, J. Tang, L. Wang, Q. Kong, W. Liu, Q. Li, D. Ren, L. Chen, D. Yan, J. Zhu, M. Yin, Temperature dependence tensile deformation behaviors of laser powder bed fusion GH3230 Ni-based superalloy, Materials Characterization 225 (7 2025). doi:10.1016/j.matchar.2025.115177.

[169] M. Kopec, M. Łazińska, J. Janiszewski, High strain rate response of CP-titanium under low-temperature conditions: experiment and modeling, Archives of Civil and Mechanical Engineering 25 (5-6) (10 2025). doi:10.1007/s43452-025-01317-0.

[170] George E. Totten, Deformation and Recrystallization of Titanium and Its Alloys, Vol. 4E, ASM International, 2016.

[171] H. Lv, D. Li, X. Li, Y. Zhang, Y. Li, Mechanical properties and microstructure evolutions of deposited Ti6Al4V titanium alloy under short-term stress relaxation at elevated temperatures, Journal of Materials Research and Technology 30 (2024) 866–878. doi:10.1016/j.jmrt.2024.03.117.

[172] Y. Wang, Wei Cai, Stress-dependent Activation Entropy in Thermally Activated Cross-slip of Dislocations, in: Proceedings of the National Academy of Sciences, United States of America, 2023.

[173] . Q. H. Taylor, G. I., The Latent Energy Remaining in a Metal after Cold Working, in: Proceedings of the Royal Society of London. Series A, Containing Papers of a Mathematical and Physical Character, Royal Society of London, 307-326, 1934. doi:http://www.jstor.org/stable/96095.

[174] D. Rittel, L. H. Zhang, S. Osovski, The dependence of the TaylorQuinney coefficient on the dynamic loading mode, Journal of the Mechanics and Physics of Solids 107 (2017) 96–114. doi:10.1016/j.jmps.2017.06.016.

[175] G. I. Taylor, R. Society, H. Qu In N E Y, The Latent Energy Remaining in a Metal after Cold Working, Proceedings of the Royal Society of London. Series A, Containing Papers of a Mathematical and Physical Character 143 (1934) 307–326. doi:https://doi.org/10.1098/rspa.1934.0004.
URL https://royalsocietypublishing.org/

[176] A. E. Chrysochoos, H. E. Louche, An infrared image processing to analyse the calorific effects accompanying strain localisation, International Journal of Engineering Science 38 (2000) 1759–1788.
URL www.elsevier.com/locate/ijengsci

[177] M. B. Bever and D. L. Holt and A. L. Titchener, The Stored Energy of Cold Work, Progress in Materials Science 17 (1973).

[178] D. Rittel, On the conversion of plastic work to heat during high strain rate deformation of glassy polymers, Mechanics of Materials 31 (1999) 131–139.

[179] T. B. Britton, F. P. Dunne, A. J. Wilkinson, On the mechanistic basis of deformation at the microscale in hexagonal close-packed metals (6 2015). doi:10.1098/rspa.2014.0881.

[180] Q. Guo, F. Zaïri, W. Yang, Evaluation of intrinsic dissipation based on self-heating effect in high-cycle metal fatigue, International Journal of Fatigue 139 (10 2020). doi:10.1016/j.ijfatigue.2020.105653.

[181] I. Newton, Scala graduum Caloris. Calorum Descriptiones & signa, Philosophical Transactions of the Royal Society of London 22 (1701) 824–829.

[182] L. Boltzmann, Ableitung des Stefanschen Gesetzes, betreffend die Abh{\"a}ngigkeit der W{\"a}rmestrahlung von der Temperatur aus der electromagnetischen Lichttheorie, Annalen der Physik und Chemie 258 (6) (1884) 291–294.

[183] C. Fischer, S. Schackert, T. Seifert, C. Schweizer, M. Fuchs, Experiments and Modeling on the Stain-Controlled Time- and Temperature-Dependent Cyclic Ratchetting Plasticity of the Nickel-Based Superalloy IN100, Materials 16 (5) (3 2023). doi:10.3390/ma16051888.

[184] M. Deguchi, S. Yamasaki, M. Mitsuhara, H. Nakashima, G. Tsukamoto, T. Kunieda, Tensile Deformation Behaviors of Pure Ti with Different Grain Sizes under Wide-Range of Strain Rate, Materials 16 (2) (1 2023). doi:

10.3390/ma16020529.

[185] T. Wang, B. Li, M. Li, Y. Li, Z. Wang, Z. Nie, Effects of strain rates on deformation twinning behavior in α-titanium, Materials Characterization 106 (2015) 218–225. doi:10.1016/j.matchar.2015.05.016.

[186] M. Brandes, M. J. Mills, Static recovery in titanium alloys at lower temperatures, Materials Science and Engineering: A (2004).

[187] X. Hou, Z. Liu, B. Wang, W. Lv, X. Liang, Y. Hua, Stress-Strain Curves and Modified Material Constitutive Model for Ti-6Al-4V over the Wide Ranges of Strain Rate and Temperature, Materials 11 (2018).

[188] A. Sela, G. Ortiz-de Zarate, D. Soler, G. Germain, L. Gallegos, P. J. Arrazola, Adiabatic self-heating determination for Ti6Al4V at different temperatures, International Journal of Heat and Mass Transfer 204 (5 2023). doi:10.1016/j.ijheatmasstransfer.2022.123747.

[189] G. Gour, D. Thomson, K. R. Ramakrishnan, D. Townsend, N. Petrinic, A. Pellegrino, Influence of Strain History on Dynamic Strain Localization and Stress State During High-Rate Tensile Loading of Titanium Alloys: Experiments, Modeling, and Analytical Methods, Journal of Applied Mechanics 90 (2) (11 2022). doi:10.1115/1.4056136.
URL https://doi.org/10.1115/1.4056136

[190] A. K. Syed, D. Parfitt, D. Wimpenny, E. Muzangaza, B. Chen, Cyclic plasticity and damage mechanisms of Ti-6Al-4V processed by electron beam melting, International Journal of Fatigue 160 (7 2022). doi:10.1016/j.ijfatigue.2022.106883.

[191] A. S. Beranger, X. Feaugas, M. Clavel, Low cycle fatigue behavior of an α + β titanium alloy: Ti6246, Materials Science and Engineering: A 172 (1) (1993) 31–41. doi:https://doi.org/10.1016/0921-5093(93)90423-C.
URL https://www.sciencedirect.com/science/article/pii/092150939390423C

[192] F. Hao, Y. Du, P. Li, Y. Mao, D. Lin, J. Wang, X. Gao, K. Wang, X. Liu, H. Song, Y. Feng, J. Li, W. Y. Wang, Effect of high strain rate on adiabatic shearing of α+b dual-phase Ti alloy, Materials 14 (8) (4 2021). doi:10.3390/ma14082044.

[193] H. Li, C. Li, D. Chen, Y. Liu, Z. Zhao, B. Zhang, M. Qi, J. Liu, Q. Wang, Temperature-Dependent Deformation Mechanisms in Ti65 Alloy: An In Situ Tensile Study, Materials 18 (14) (7 2025). doi:10.3390/ma18143270.

[194] S. Nemat-Nasser, W.-G. Guo, V. F. Nesterenko, S. S. Indrakanti, Y.-B. Gu, Dynamic response of conventional and hot isostatically pressed Tiś6Alś4V alloys: experiments and modeling, Tech. rep.
URL www.elsevier.com/locate/mechmat

[195] M. Arul Kumar, M. Wroński, R. J. McCabe, L. Capolungo, K. Wierzbanowski, C. N. Tomé, Role of microstructure on twin nucleation and growth in HCP titanium: A statistical study, Acta Materialia 148 (2018) 123–132. doi:10.1016/j.actamat.2018.01.041.

[196] B. Ahmadikia, L. Wang, M. A. Kumar, I. J. Beyerlein, Grain boundary slip twin transmission in titanium, Acta Materialia 244 (1 2023). doi:10.1016/j.actamat.2022.118556.

[197] P. Chen, J. Ombogo, B. Li, Dislocation twin transmutations during interaction between prismatic slip and {101ŕ1} twin in magnesium, Acta Materialia 186 (2020) 291–307. doi:10.1016/j.actamat.2020.01.010.

[198] F. Coghe, W. Tirry, L. Rabet, D. Schryvers, P. Van Houtte, Importance of twinning in static and dynamic compression of a Ti-6Al-4V titanium alloy with an equiaxed microstructure, Materials Science and Engineering: A 537 (2012) 1–10. doi:10.1016/j.msea.2011.12.047.

[199] C. D. Barrett, H. El Kadiri, Impact of deformation faceting on { 1 0 1 2 }, { 1 0 1 1 } and { 1 0 1 3 } embryonic twin nucleation in hexagonal close-packed metals, Acta Materialia 70 (2014) 137–161. doi:10.1016/j.actamat.2014.02.018.

[200] Y. He, B. Li, C. Wang, S. X. Mao, Direct observation of dual-step twinning nucleation in hexagonal close-packed crystals, Nature Communications 11 (1) (12 2020). doi:10.1038/s41467-020-16351-0.

[201] Y. Liu, N. Li, S. Shao, M. Gong, J. Wang, R. J. McCabe, Y. Jiang, C. N. Tomé, Characterizing the boundary lateral to the shear direction of deformation twins in magnesium, Nature Communications 7 (6 2016). doi:10.1038/ncomms11577.

[202] C. Xin, Q. Wang, J. Ren, Y. Zhang, J. Wu, J. Chen, L. Zhang, B. Sang, L. Li, Plastic Deformation Mechanism and Slip Transmission Behavior of Commercially Pure Ti during In Situ Tensile Deformation, Metals 12 (5) (5 2022). doi:10.3390/met12050721.

[203] M. Arul Kumar, B. Clausen, L. Capolungo, R. J. McCabe, W. Liu, J. Z. Tischler, C. N. Tomé, Deformation twinning and grain partitioning in a hexagonal close-packed magnesium alloy, Nature Communications 9 (1) (12 2018). doi:10.1038/s41467-018-07028-w.

[204] P. J. Withers, Residual stress and its role in failure, Reports on Progress in Physics 70 (12) (2007) 2211–2264. doi:10.1088/0034-4885/70/12/R04.

[205] M.-S. . Pham, S. R. Holdsworth, M.-S. Pham, Evolution of Relationships Between Dislocation Microstructures and Internal Stresses of AISI 316L During Cyclic Loading at 293 K and 573 K (20 °C and 300 °C), METALLURGICAL AND MATERIALS TRANSACTIONS A 75 A (2014). doi:10.3929/ethz-b-000081146.
URL https://doi.org/https://doi.org/10.3929/ethz-b-000081146

[206] C. Spearman, The Proof and Measurement of Association between Two Things, The American Journal of Psychology 15 (1904) 72–101.

[207] S. Sathianathan, The development of Reverse Loading Split Hopkinson Pressure Bar systems for the study of the Dynamic Bauschinger Effect, Tech. rep. (2010).

[208] R. Jain, K. Ramachandra, Bird Impact Analysis of Pre-Stressed Fan Blades Using Explicit Finite Element Code, International Gas Turbine Congress, Tokyo, 2003.

[209] B. Wu, R. Hedayati, Z. Li, M. Aghajanpour, G. Zhang, J. Zhang, J. Lin, Effect of Impact and Bearing Parameters on Bird Strike with Aero-Engine Fan Blades, Applied Sciences (Switzerland) 12 (1) (1 2022). doi:10.3390/app12010007.

[210] Electronic Code of Federal Regulations, 14 CFR \S 33.76 – Bird ingestion (2026).

[211] Federal Aviation Administration, Bird ingestion, 14 C.F.R. § 33.76 (2026).

[212] S. K. Sinha, 5 th International LS-DYNA ® Users Conference Transient

Dynamics of Slicing-Impact Loading on Jet Engine Fan Blades during a Bird-strike Event, 15th International LS-DYNA® Users Conference, 2018.

[213] O. A. Bauchau, J. I. Craig, Euler-Bernoulli Beam Theory, in: Structural Analysis, Vol. 163, Springer, 2009.

[214] S. P. Timoshenko, J. M. Gere, Mechanics of Materials, Van Nostrand Reinhold, 1972.

[215] J. M. Gere, B. J. Goodno, Mechanics of Materials, 8th Edition, Cengage Learning, 2012.

[216] G. Yella, P. Jadhav, C. Lande, Bird-Strike Analysis on Hybrid Composite Fan Blade: Blade-Level Validation, Aerospace 10 (5) (5 2023). doi:10.3390/aerospace10050435.